

University of Denver

Digital Commons @ DU

Electronic Theses and Dissertations

Graduate Studies

1-1-2016

Relaxation of Metals and Their Impact on Nitroxides

Priyanka Aggarwal
University of Denver

Follow this and additional works at: <https://digitalcommons.du.edu/etd>



Part of the [Chemistry Commons](#)

Recommended Citation

Aggarwal, Priyanka, "Relaxation of Metals and Their Impact on Nitroxides" (2016). *Electronic Theses and Dissertations*. 1182.

<https://digitalcommons.du.edu/etd/1182>

This Dissertation is brought to you for free and open access by the Graduate Studies at Digital Commons @ DU. It has been accepted for inclusion in Electronic Theses and Dissertations by an authorized administrator of Digital Commons @ DU. For more information, please contact jennifer.cox@du.edu, dig-commons@du.edu.

Relaxation of Metals and Their Impact on Nitroxides

Abstract

Pulsed and continuous wave electron spin resonance were used to characterize the relaxation rates of selected paramagnetic metals at 5 to 15 K or 80 K, measure the impact of these rapidly relaxing metals on the relaxation rates of nitroxide radicals in glassy mixtures and in discrete complexes, and characterize novel iron-sulfur proteins.

Spin echoes were observed at 5 to 7 K in 1:1 water:glycerol for Er(diethylenetriamine pentaacetic acid)²⁻ (Er(DTPA)²⁻), Co(DTPA)³⁻ and aquo Co²⁺ with relaxation times that are strongly temperature dependent. Deep proton modulation was present on spin echo decays (Ch. 3). For Gd³⁺ and Gd(DTPA)²⁻ in 1:1 water:glycerol at 80 K T₁ is 1.5 to 2 μs and T₂ is about 0.5 μs. When Gd³⁺ is loaded into P22 viral capsids with local concentrations up to about 180 mM the relaxation rates at 80 K are dramatically increased (Ch. 6).

Relaxation rates for 0.2 mM nitroxide radical in mixtures with rapidly relaxing metal ions in 1:1 water:glycerol glasses were measured at temperatures between 20 and 200 K (Ch. 4). The enhancement of the relaxation rate of the nitroxide increases in the order Co²⁺ < Er³⁺ < Dy³⁺ < Tm³⁺. The maximum spin-lattice relaxation enhancement occurs at about 35 K for Dy³⁺, 40 K for Er³⁺, and 80 K for Co²⁺. Changes in T₁ are a much larger fraction of the non-interacting values than for T₂.

Complexes were prepared in which an ethylenediamine tetraacetic acid (EDTA) metal binding site was separated via linkers of varying lengths from a nitroxide radical. Energy minimization calculations found distances of 1.6, 2.4, and 3.4 nm between the metal binding and nitroxide N-O groups. The interaction between a paramagnetic metal bound to the EDTA and the nitroxide were characterized by measuring relaxation times and continuous wave power saturation.

The temperature dependence of the electron spin-lattice relaxation rates for iron-sulfur clusters from Pyruvate Formate Lyase- Activating Enzyme, hydrogenase and Mycofactin C protein were studied (Ch. 7). Compared to other iron-sulfur proteins the relaxation rates were relatively slow.

Document Type

Dissertation

Degree Name

Ph.D.

Department

Chemistry and Biochemistry

First Advisor

Sandra S. Eaton, Ph.D.

Second Advisor

Susan Sadler

Third Advisor

Martin Margittai

Keywords

Relaxation rates, Electron Spin-lattice

Subject Categories

Chemistry

Publication Statement

Copyright is held by the author. User is responsible for all copyright compliance.

Relaxation of Metals and their Impact on Nitroxides

A Dissertation

Presented to

the Faculty of Natural Sciences and Mathematics

University of Denver

In Partial Fulfillment

of the Requirements for the Degree

Doctor of Philosophy

by

Priyanka Aggarwal

August 2016

Advisor: Dr. Sandra S. Eaton

Author: Priyanka Aggarwal
Title: Relaxation of Metals and their Impact on Nitroxides
Advisor: Dr. Sandra S. Eaton
Degree Date: August 2016

Abstract

Pulsed and continuous wave electron spin resonance were used to characterize the relaxation rates of selected paramagnetic metals at 5 to 15 K or 80 K, measure the impact of these rapidly relaxing metals on the relaxation rates of nitroxide radicals in glassy mixtures and in discrete complexes, and characterize novel iron-sulfur proteins.

Spin echoes were observed at 5 to 7 K in 1:1 water:glycerol for Er(diethylenetriamine pentaacetic acid)²⁻ (Er(DTPA)²⁻), Co(DTPA)³⁻ and aquo Co²⁺ with relaxation times that are strongly temperature dependent. Deep proton modulation was present on spin echo decays (Ch. 3). For Gd³⁺ and Gd(DTPA)²⁻ in 1:1 water:glycerol at 80 K T₁ is 1.5 to 2 μs and T₂ is about 0.5 μs. When Gd³⁺ is loaded into P22 viral capsids with local concentrations up to about 180 mM the relaxation rates at 80 K are dramatically increased (Ch. 6).

Relaxation rates for 0.2 mM nitroxide radical in mixtures with rapidly relaxing metal ions in 1:1 water:glycerol glasses were measured at temperatures between 20 and 200 K (Ch. 4). The enhancement of the relaxation rate of the nitroxide increases in the order Co²⁺ < Er³⁺ < Dy³⁺ < Tm³⁺. The maximum spin-lattice relaxation enhancement

occurs at about 35 K for Dy^{3+} , 40 K for Er^{3+} , and 80 K for Co^{2+} . Changes in T_1 are a much larger fraction of the non-interacting values than for T_2 .

Complexes were prepared in which an ethylenediamine tetraacetic acid (EDTA) metal binding site was separated via linkers of varying lengths from a nitroxide radical. Energy minimization calculations found distances of 1.6, 2.4, and 3.4 nm between the metal binding and nitroxide N-O groups. The interaction between a paramagnetic metal bound to the EDTA and the nitroxide were characterized by measuring relaxation times and continuous wave power saturation.

The temperature dependence of the electron spin-lattice relaxation rates for iron-sulfur clusters from Pyruvate Formate Lyase- Activating Enzyme, hydrogenase and Mycofactin C protein were studied (Ch.7). Compared to other iron-sulfur proteins the relaxation rates were relatively slow.

Acknowledgements

I would like to thank Professors Gareth and Sandra Eaton for allowing me the privilege of pursuing my doctorate in their lab. They have been great mentors and it has been an honor to learn under them. I would also like to thank all the committee members who took their precious time and helped me in the defense.

The work described in this dissertation was in collaboration with Dr. Eric Shepard and Dr. Robert Usselman at the University of Montana and Dr. John Latham at University of Denver. I would like to thank them for giving me a chance to be a part of their projects.

Finally, I would like to thank my friends and family for all their support and understanding throughout my graduate career. In particular I need to thank my mom, dad and brother. Without their help, none of this would have been possible.

Table of Contents

Chapter 1	1
Introduction.....	1
1.1 Study Overview.....	1
1.2 Thesis Outline	1
Chapter 2.....	3
Electron Paramagnetic Resonance (EPR).....	4
2.1 Introduction	4
2.2 Continuous Wave (CW) experiment.....	6
2.3 Pulse experiments.....	8
2.3.1 Spin-spin or transverse relaxation time (T_2).....	8
2.3.2 Spin-lattice or longitudinal relaxation time (T_1).....	10
2.4 Design of EPR spectrometer	11
2.4.1 Source	11
2.4.2 Circulator	12
2.4.3 Resonator	12
2.4.4 Electromagnet.....	13
2.4.5 Detector	13
Chapter 3.....	15
EPR of Lanthanides and Cobalt Ions	15
3.1 Introduction	15
3.1.1 Lanthanides Magnetism.....	15
3.2 Experimental Methods	17
3.2.1 Continuous Wave	17
3.2.2 Pulsed EPR measurement.....	18

3.3 EPR spectra of Dy ³⁺ , Er ³⁺ , Gd ³⁺ , Tm ³⁺ and Co ²⁺ and their complexes.....	19
3.3.1 Dy ³⁺ and its complexes.....	19
3.3.2 Er ³⁺ and its complexes.....	21
3.3.3 Tm ³⁺ and its complexes.....	28
3.3.4 Co ²⁺ and its complexes.....	30
3.3.5 Gd ³⁺ and its complexes.....	39
 Chapter 4	 47
Effect of Lanthanides and Cobalt Ions on Nitroxide in Mixtures.....	49
4.1 Introduction.....	49
4.1.1 Intermolecular Effect of Lanthanides and Cobalt ions on the relaxation of nitroxide.....	49
4.2 Experimental Details.....	56
4.2.1 Preparation of samples.....	56
4.2.2 Pulsed EPR measurement of electron spin relaxation times at 10 to 80 K.....	57
4.3 Effect of the lanthanides on the relaxation of tempone.....	57
4.3.1 Effect of the rapidly relaxing metals on the spin-lattice relaxation of tempone.....	57
4.3.2 Effect of the rapidly relaxing metal ions on the spin-spin relaxation of tempone.....	63
4.3.3 Effect of Lanthanides and their complexes on the spin-lattice relaxation of nitroxide at X-band and Q-band.....	70
4.3.4 Effect of Lanthanides and their complexes on the spin-spin relaxation of nitroxide at X-band and Q-band.....	72
4.3.5 Effect of the more slowly relaxing Gd ³⁺ ion on the spin-lattice relaxation of tempone.....	72
4.3.6 Effect of the more slowly relaxing Gd ³⁺ ion on the spin-spin relaxation of tempone.....	77
4.4 Prediction of signal-to-noise (S/N) improvement for DEER.....	78
 Chapter 5.....	 83
Distance between lanthanide and nitroxide	83
5.1 Introduction.....	83
5.2 Experimental Details.....	87

5.2.1 Preparation of Tetraethylester of EDTA (Et ₄ EDTA)	87
5.2.2 Preparation of Triethylester of EDTA (Et ₃ EDTA).....	89
5.2.3 Preparation of N-hydroxy succinimide (NHS) ester of Et ₃ EDTA	91
5.2.4 Coupling of Et ₃ EDTA with N-terminus of alanine to make Et ₃ EDTA-A.....	93
5.2.5 Spin labeling of Et ₃ EDTA-A at the C-terminus of alanine to make Et ₃ EDTA-A-T.....	95
5.2.6 Cleavage of ethyl esters from Et ₃ EDTA–A-T to make EDTA-A-T	97
5.2.7 Complexation of lanthanides (La, Gd, Dy and Er) to EDTA-A-T to make MEAT	98
5.2.8 Coupling of Et ₃ EDTA with N-terminus of peptide triglycine to make Et ₃ EDTA-G	101
5.2.9 Spin labeling of Et ₃ EDTA-G at the peptide C-terminus to form Et ₃ EDTA-G-T	102
5.2.10 Cleavage of ethyl esters from Et ₃ EDTA-G-T to make EDTA-G-T	104
5.2.11 Complexation of lanthanides (La, Gd, Dy and Er) with EDTA-G-T to make MEGT	104
5.2.12 Coupling of Et ₃ EDTA with N-terminus of peptide APPPPPP (alanine with six prolines) to make Et ₃ EDTA-P	106
5.2.13 Spin labeling of Et ₃ EDTA-P at the peptide C-terminus to make Et ₃ EDTA-P-T	109
5.2.14 Cleavage of ethyl esters from Et ₃ EDTA-P-T to make EDTA-P-T	110
5.2.15 Complexation of lanthanides (La, Gd, Dy and Er) to EDTA-P-T to make MEPT.....	111
5.2.16 Conversion of trans polyproline to cis and monitoring the conversion using Circular Dichroism (CD)	112
5.2.17 Distance calculations using Discovery Studio 2.5.....	113
5.2.18 EPR spectroscopy	115
5.2.19 Pulsed EPR measurements of electron spin relaxation times at 30 to 80 K.	116
5.3 Results	117
5.3.1 Conversion of trans-MEPT to cis-MEPT	117
5.3.2 Tumbling correlation times (τ_B) of spin-labeled molecules	119
5.3.3 Effect of lanthanides on P _{1/2} values of nitroxide at 80 and 120 K	120
5.3.4 Intensity loss for spin echo detected spectra	123
5.3.5 Relaxation enhancement for nitroxides in the metal complexes	127

Chapter 6.....	136
Gadolinium- loaded P22 virus capsids	136
6.1 Introduction	136
6.2 Experimental Details	141
6.2.1 Continuous Wave Q-band EPR Spectra at 80 and 150 K.....	141
6.2.2 Power saturation at 80 K	142
6.2.3 Pulsed EPR measurement of Gd ³⁺ electron spin relaxation times at 80 K.....	142
6.3 Results	143
6.3.1 Continuous Wave Q-band EPR Spectra at 80 and 150 K.....	143
6.3.2 Power saturation at 80 K	145
6.3.3 Pulsed EPR measurement of Gd ³⁺ electron spin relaxation times at 80 K.....	146
6.4 Discussion	147
 Chapter 7.....	 148
Iron-Sulfur Clusters	148
7.1 Introduction	148
7.2 PFL-AE, HydE and HydF samples	151
7.2.1 Experimental Details	151
7.2.2 CW and Field Swept Echo Detected Spectra	153
7.2.3 Electron Spin Relaxation.....	164
7.2.4 Discussion.....	169
7.3 MtfC SAM enzyme	170
7.3.1 Experimental Details	170
7.3.2 Results	172
7.3.3 Discussion.....	176
7.3.4 Comparison of [4Fe-4S] ⁺ cluster in HydF ^{ΔEG} Reduced and MtfC	177
 Chapter 8.....	 178
Conclusion and Future Work	178
8.1 Conclusion.....	178
8.2 Future work	180

References..... 182

List of Figures

Figure 2.1 Energy level diagram for unpaired electron spin states under the influence of an external magnetic field (B).....	5
Figure 2.2 Energy level diagram for unpaired electron spin states interacting with one proton in the presence of an external magnetic field (B).....	7
Figure 2.3 Pulse sequence for Hahn-echo to measure spin-spin relaxation time.	8
Figure 2.4 Stepwise graphical illustration of magnetic spin vector at particular positions in the two-pulse sequence depicted in Figure 2.3.	8
Figure 2.5 Pulse sequence for inversion recovery to measure spin-lattice relaxation time	9
Figure 2.6 Stepwise graphical illustration of magnetic spin vector at particular positions in the spin-lattice relaxation sequence.	9
Figure 2.7 Schematic diagram of a basic EPR instrument.....	13
Figure 3.1 CW spectrum at X-band of 30 mM aquo Dy ³⁺	20
Figure 3.2 CW spectra at X-band of 30 mM Dy(DTPA) ²⁻	21
Figure 3.3 CW spectrum at X-band of 30 mM aquo Er ³⁺ at 5 K.....	22
Figure 3.4 CW spectra at X-band of 30 mM aquo Er ³⁺ at 10 K.....	23
Figure 3.5 CW spectra at X-band of 30 mM Er(DTPA) ²⁻	25
Figure 3.6 T ₂ echo decays of 30 mM aquo Er(DTPA) ²⁻	26
Figure 3.7 Two-pulse field-swept echo-detected spectrum of 30 mM Er(DTPA) ²⁻ at 5K	27
Figure 3.8 Two-pulse field-swept echo detected spectrum of 30 mM Er(DTPA) ²⁻ at 7 K.	28
Figure 3.9 CW spectrum at X-band of 30 mM aquo Tm ³⁺	29
Figure 3.10 Two-pulse field-swept echo detected spectrum of 20 mM aquo Tm ³⁺	30
Figure 3.11 CW spectrum at X-band of 30 mM aquo Co ²⁺	32
Figure 3.12 CW spectrum at X-band of 30 mM Co(DTPA) ³⁻	33
Figure 3.13 Two-pulse field-swept echo-detected spectra at X-band of 30 mM aquo Co ²⁺	34
Figure 3.14 Two-pulse field-swept echo-detected spectra at X-band of 30 mM Co(DTPA) ³⁻	35
Figure 3.15 T ₂ decays at five field positions at X-band of 30 mM aquo Co ²⁺	36
Figure 3.16 T ₂ decays at five field positions at X-band of 30 mM Co(DTPA) ³⁻	37
Figure 3.17 Spin-lattice relaxation rates (1/T ₁) for aquo Co ²⁺ as a function of field.	38
Figure 3.18 Spin-lattice relaxation rate (1/T ₁) for Co(DTPA) ³⁻ as a function of field.....	39
Figure 3.19 Q-band (33.97 GHz) CW spectrum of 1 mM Gd ³⁺	42
Figure 3.20 Q-band (33.95 GHz) CW spectrum of 2 mM Gd(DTPA) ²⁻	43
Figure 3.21 X-band (9.84 GHz) CW spectrum of 5 mM Gd ³⁺ in water at room temperature.	44
Figure 3.22 X-band (9.84 GHz) CW spectrum of 5 mM Gd(EDTA) ⁻ in water at room temperature.	45

Figure 3.23 X-band (9.84 GHz) CW spectrum of 2 mM Gd(DTPA) ²⁻ in water at room temperature.	46
Figure 3.24 X-band (9.84 GHz) CW spectrum of 1 mM Gd(DPA) ₃ in water at room temperature.	47
Figure 4.1 Effect of metals on the spin-lattice relaxation rate for 0.2 mM tempone.	60
Figure 4.2 Concentration dependence of the effect of Dy ³⁺ on the spin-lattice relaxation for 0.2 mM tempone as a function of temperature at X-band.	60
Figure 4.3 Concentration dependence of the effect of Er ³⁺ on the spin-lattice relaxation for 0.2 mM tempone as a function of temperature at X-band.	61
Figure 4.4 Concentration dependence of the effect of Tm ³⁺ on the spin-lattice relaxation for 0.2 mM tempone as a function of temperature at X-band.	62
Figure 4.5 Concentration dependence of the effect of Co ²⁺ on the spin-lattice relaxation for 0.2 mM tempone as a function of temperature at X-band.	63
Figure 4.6 Effect of metals on the spin-spin relaxation rate for 0.2 mM tempone.	65
Figure 4.7 Concentration dependence of the effect of Dy ³⁺ on the spin-spin relaxation for 0.2 mM tempone as a function of temperature at X-band.	66
Figure 4.8 Concentration dependence of the effect of Er ³⁺ on the spin-spin relaxation for 0.2 mM tempone as a function of temperature at X-band.	67
Figure 4.9 Concentration dependence of the effect of Tm ³⁺ on the spin-spin relaxation for 0.2 mM tempone at X-band.	68
Figure 4.10 Concentration dependence of the effect of Co ²⁺ on the spin-spin relaxation for 0.2 mM tempone as a function of temperature at X-band.	69
Figure 4.11 Effect of Dy ³⁺ and its complex on spin-lattice relaxation rate of nitroxide at X- and Q-band as a function of temperature.	71
Figure 4.12 Effect of Er ³⁺ and its complex on spin-lattice relaxation rate of nitroxide at X- and Q-band as a function of temperature.	72
Figure 4.13 Effect of Dy ³⁺ and its complex on spin-spin relaxation rate of nitroxide at X- and Q-band as a function of temperature.	74
Figure 4.14 Effect of Er ³⁺ and its complex on spin-spin relaxation rate of nitroxide at X- and Q-band as a function of temperature.	75
Figure 4.15 Concentration dependence of the effect of Gd ³⁺ on the spin-lattice relaxation for 0.2 mM tempone as a function of temperature at X-band.	76
Figure 4.16 Concentration dependence of the effect of Gd ³⁺ on the spin-spin relaxation for 0.2 mM tempone as a function of temperature at X-band.	77
Figure 4.17 Predicted DEER S/N improvement with a 2 μs spacing between pulses.	80
Figure 4.18 Predicted DEER S/N improvement for metals and their complexes for nitroxide attached to syntaxin for a constant pulse spacing of 2 μs.	82
Figure 5.1 NMR of Et ₄ EDTA in deuterated chloroform.	88
Figure 5.2 Mass spectrum of Et ₄ EDTA obtained with an Agilent 6100 LCMS system in ESI ionization mode.	89
Figure 5.3 NMR of Et ₃ EDTA in deuterated chloroform.	90

Figure 5.4 Mass spectrum of Et ₃ EDTA.	91
Figure 5.5 NMR of NHS ester of Et ₃ EDTA in deuterated chloroform.	92
Figure 5.6 Mass spectrum of NHS ester of Et ₃ EDTA.	93
Figure 5.7 NMR of NHS ester of Et ₃ EDTA.	94
Figure 5.8 Mass spectrum of Et ₃ EDTA-A.....	95
Figure 5.9 Mass spectrum of Et ₃ EDTA-A-T.....	97
Figure 5.10 Mass spectrum of LaEAT.....	100
Figure 5.11 Mass spectrum of Et ₃ EDTA-G.....	102
Figure 5.12 Mass spectrum of Et ₃ EDTA-G-T.....	103
Figure 5.13 Mass spectrum of LaEGT (a) (LaEGT + H) ⁺ and (b) (LaEGT + K) ⁺	106
Figure 5.14 Mass spectrum of Et ₃ EDTA-P.....	108
Figure 5.15 Mass spectrum of Et ₃ EDTA-P-T.....	110
Figure 5.16 Mass spectrum of LaEPT.....	112
Figure 5.17 CD spectrum of polyproline.	118
Figure 5.18 Percentage of nitroxide spins detectable in (a) MEAT, (b) MEGT AND (c) MEPT complexes at 30 to 80 K using τ of 100 ns.....	125
Figure 5.19 Temperature dependence of spin-lattice relaxation rates for nitroxide in (a) MEAT, (b) MEGT and (c) MEPT complexes at 30 to 80 K.	129
Figure 5.20 The width of distribution of spin-lattice times in the UPEN curve.	130
Figure 5.21 Temperature dependence of spin-spin relaxation rates for nitroxide in MEAT complexes at 30 to 80 K.....	134
Figure 6.1 Schematic of polymeric P22 particles with spatially confined Gd ³⁺ ions.....	139
Figure 6.2 Q-band EPR spectra of the $m_s = \pm 1/2$ transitions for P22-Gd ³⁺	144
Figure 7.1 X-band (9.42 GHz) CW spectra of PFL-AE at 10 - 70 K.....	154
Figure 7.2 X-band (9.424 GHz) two-pulse field-swept echo-detected spectra of PFL-AE at 10 – 50 K.....	155
Figure 7.3 Comparison of field-swept echo-detected spectra and integrals of CW spectra at 10 to 70 K for PFL-AE.....	156
Figure 7.4 CW spectra at X-band of the [2Fe-2S] ⁺ in Ca HydE, at 30 -70 K.	158
Figure 7.5 X-band (9.43 GHz) two-pulse field-swept echo-detected spectra of the [2Fe-2S] ⁺ in Ca HydD at 10 – 70 K.....	159
Figure 7.6 X-band (9.24 GHz) two-pulse field-swept echo-detected spectra of HydF ^{ΔEG} + DTT at 10 – 70 K.....	160
Figure 7.7 X-band CW spectra of HydF ^{ΔEG} Reduced at 10-20 K.....	161
Figure 7.8 X-band (9.43 GHz) CW spectra of HydF ^{ΔEG} Reduced at 10 – 40 K.....	162
Figure 7.9 X-band (9.43 GHz) two-pulse field swept echo detected spectra of HydF ^{ΔEG} Reduced at 10 – 40 K.....	163
Figure 7.10 X-band (9.43 GHz) two-pulse field-swept echo-detected spectra of HydF ^{ΔEG} Reduced at 10 – 20 K.....	164
Figure 7.11 Temperature dependence of X-band spin-spin relaxation rates at $g = 2.006$ for [2Fe-2S] ⁺ in the different proteins.	166

Figure 7.12 Temperature dependence of X-band spin-lattice relaxation rates at $g = 2.006$ for $[2\text{Fe-2S}]^+$ in the different proteins.....	167
Figure 7.13 X-band spectra of reduced MtfC.....	173
Figure 7.14 Spectra for reduced sample of MtfC after subtracting oxidized spectra at 20, 30 and 40 K.....	174

List of Tables

Table 3.1 Concentration dependence of T_1 and T_2 for aquo Gd^{3+} and $Gd(DTPA)^{2-}$ at 80 K and 34 GHz in 1:1 water: glycerol.....	41
Table 3.2 Temperature dependence of T_1 and T_2 for aquo Gd^{3+} at 9.5 GHz in 1:1 water: glycerol.	48
Table 3.3 Overview of Relaxation Times for $Dy(EDTA)^{2-}$, $Er(DTPA)^{2-}$, Co^{2+} and $Co(DTPA)^{3-}$ at 5 to 12 K.....	48
Table 4.1 Concentration and temperature dependence of stretched exponential parameter x for solutions of 0.2 mM tempone and Dy^{3+}	66
Table 4.2 Concentration and temperature dependence of stretched exponential parameter x for solutions of 0.2 mM tempone and Er^{3+}	67
Table 4.3 Concentration and temperature dependence of stretched exponential parameter x for solutions of 0.2 mM tempone and Tm^{3+}	68
Table 4.4 Concentration and temperature dependence of stretched exponential parameter x for solutions of 0.2 mM tempone and Co^{2+}	69
Table 4.5 Concentration and temperature dependence of stretched exponential parameter x for solutions of 0.2 mM tempone and Co^{2+}	78
Table 4.6 T_2 values of spin label on syntaxin with and without metal ions at 30 to 80 K.81	
Table 4.7 T_1 values of spin label on syntaxin with and without metal ions at 30 to 80 K.....	81
Table 5.1 The structure and distances of molecules obtained using Discovery Studio 2.5 software.....	114
Table 5.2 Correlation times in water for tempamine attached to different molecules, calculated using the Kivelson model of tumbling.....	120
Table 5.3 $P_{1/2}$ (mW) for nitroxide in complexes with La^{3+} , Gd^{3+} , Dy^{3+} and Er^{3+} in 1:1 water: glycerol at 80 and 120 K.....	121
Table 5.4 Comparison of percentage of spins detectable for different probes in 1:1 water: glycerol at 80 K and 120 K by comparing the intensity of normalized integral with respective La analog.	123
Table 5.5 Nitroxide spins detected at τ of 100 ns or 200 ns in 1:1 water: glycerol at 80 K.	126
Table 5.6 Nitroxide spins detected for MEGT complexes at τ of 100 ns or 200 ns in 1:1 water: glycerol at 70 K in field-swept echo-detected spectra.	126
Table 5.7 Widths of distribution of spin-lattice times (ms) for nitroxide in different probes as a function of temperature.	131

Table 5.8 The ratio of the distribution width to the central value of spin-lattice time in probes as a function of temperature..	132
Table 6.1 P22 cage Gd^{3+} loading factors, Gd^{3+} concentrations inside P22 cages, P22 cage concentrations and global Gd^{3+} concentrations	141
Table 6.2 Average EPR line widths at 80 and 150 K for samples with varying Gd^{3+} concentrations in the P22 cages	145
Table 6.3 Power saturation of Gd^{3+} EPR signals at 80 K.	146
Table 7.1 T_2 and T_1 at $g = 2.006$ ($[2Fe-2S]^+$) and at $g = 2.02$ ($[3Fe-4S]^+$) in PFL-AE	167
Table 7.2 T_2 and T_1 at $g = 2.006$ ($[2Fe-2S]^+$) and 1.89 ($[4Fe-4S]^+$) in HydF $^{\Delta EG}$ Reduced.	168
Table 7.3 T_2 at $g = 1.93$ for reduced MtfC sample.	175
Table 7.4 T_1 at $g = 1.93$ for Reduced MtfC.	176

List of abbreviations

AEMA	Aminoethyl methacrylate
ATRP	Atom transfer radical polymerization
CAs	Contrast agents
CD	circular dichorism
CCMV	Cowpea chlorotic virus
CPMV	Cowpea mosaic virus
CW	Continuous Wave
DEER	Double electron- electron resonance
DPA	Dipicolinic acid
DOTA	1,4,7,10-tetraazacyclododecane-1,4,7,10-tetraacetic acid
DTPA	diethylenetriaminepentaacetic acid
EDTA	Ethylenediaminetetraacetic acid
EEDQ	1-ethoxycarbonyl-2-ethoxy-1, 2-dihydroquinoline
EPR	Electron paramagnetic resonance
ES	Empty shell
EX	Expanded shell
Fe-S	Iron-sulfur proteins
HydE and HydF	hydrogenase related enzymes
MEAT	Metal-EDTA-Alanine-Tempamine complex
MEGT	Metal-EDTA-Triglycine-Tempamine complex

MEPT complex	Metal-EDTA-Peptide (Alanine with six proline)-Tempamine
MRI	Magnetic resonance imaging
MtfC	Mycofactin
NAD ⁺	Nicotinamide adenine dinucleotide
NHS	N- hydroxy succinimide
NMR	Nuclear magnetic resonance
NMRD	Nuclear magnetic resonance dispersion
OD	Outer Diameter
P _{1/2} saturation	microwave power at which EPR signal is half of the signal without saturation
PC	Procapsid
PFL-AE	pyruvate–formate lyase activating enzyme
SAM	S-adenosyl methionine
T ₂	Spin- spin relaxation time
T ₁	Spin- lattice relaxation time
UPEN method	Uniform penalty method
WB	Wiffleball
ZFS	Zero field splitting

Chapter 1

Introduction

1.1 Study Overview

Understanding the relaxation effect of paramagnetic lanthanides and of cobalt(II) on nitroxides is the central goal of this dissertation. In addition, the electron paramagnetic resonance (EPR) spectra of FeS clusters have been studied to help characterize several proteins. The magnetic properties of lanthanides and transition metals and some fundamentals of EPR and its application to measuring distances between spins have been discussed in detail in Refs. [1-6].

1.2 Thesis Outline

The thesis has three main parts. In the first part relevant aspects of EPR are introduced (Chapter 2). The second part contains information about the paramagnetic properties of lanthanides (Chapter 3) and interactions of lanthanides and cobalt with nitroxides, both intermolecular (Chapter 4) and intramolecular (Chapter 5). A study of gadolinium (Gd^{3+}) in capsids is in Chapter 6. The third part is about Fe-S clusters in some proteins (Chapter 7).

Chapter 2 of the thesis concisely describes relevant theory of the continuous wave (CW) and pulsed EPR used in these studies. The EPR instrument used is also described.

Chapter 3 provides general background concerning paramagnetic properties of lanthanides, and cites some papers and reviews illustrating applications of lanthanides in techniques such as NMR. The chapter includes a brief discussion of the g-values of lanthanides and how they relate to the relaxation of lanthanides.

Chapter 4 discusses the intermolecular dipolar interactions between lanthanides and cobalt(II) ions and nitroxide in glassy solvent mixtures at temperatures below 200 K. The concentration and temperature dependent effect of metals with differing relaxation rates on the slowly relaxing nitroxide is the focus of this chapter.

Chapter 5 builds on the interactions in mixtures to understand the intramolecular interactions between lanthanides and nitroxide in discrete complexes that contain both a paramagnetic metal and a nitroxide. The goal of this chapter is to measure the relaxation enhancement of the nitroxide by the lanthanide at three interspin distances.

In Chapter 6, the intermolecular interaction between Gadolinium diethylenetriaminepentaacetic acid ($\text{Gd}(\text{DTPA})^{2-}$) in a viral capsule P22 was studied by EPR. This study helped in the understanding of Gd^{3+} loaded P22 viral capsid as a contrast agent in MRI (Magnetic Resonance Imaging).

Chapter 7 describes EPR studies of FeS clusters in three proteins: pyruvate – formate lyase activating enzyme (PFL-AE), enzymes of hydrogenase clusters (HydE and HydF) and Mycofactocin (Mft) in Mycobacterium Tuberculosis.

Chapter 8 is a brief discussion of suggestions for future work.

Chapter 2

Electron Paramagnetic Resonance (EPR)

2.1 Introduction

Electron paramagnetic resonance (EPR) is a branch of magnetic resonance spectroscopy, used for studying paramagnetic molecules or atoms that have an unpaired electron. The unpaired electron in a molecular species has magnetic moment (μ) due to its own orbital magnetic moment and spin magnetic moment. The movement of the electron around the nucleus corresponds to an orbital magnetic moment and the spin magnetic moment is a quantum mechanical property that is metaphorically described as if it were generated from the movement of the electron on its own axis. The two spin states (m_s) of an unpaired electron have degenerate energies when no external field is applied. These spin states of an electron split into different energies (lower and higher energy) under the influence of the external magnetic field (B) due to the Zeeman Effect. The splitting is called Zeeman splitting. When the magnetic moment of an electron is aligned in the direction of the applied magnetic field, the lower energy state ($m_s = -1/2$) occurs and when it goes against the applied magnetic field, the higher energy state ($m_s = +1/2$) occurs as shown in Figure 2.1. The energy difference between the two spin states is proportional to the product of magnetic moment (μ) and applied magnetic field (B). The

magnetic moment (μ) is equal to $m_s g \beta$, where g is the Zeeman splitting constant and β is the electron Bohr magneton. The energy difference equation is,

$$\Delta E = gB\beta \quad 2.1$$

EPR spectroscopy also depends on absorption of electromagnetic radiation. Radiation would be absorbed if

$$\Delta E = h\nu \quad 2.2$$

where, h is Planck's constant and ν is the frequency of the radiation.

The transition between two spin states (Figure 2.1) is possible only if

$$\Delta E = h\nu = gB\beta \quad 2.3$$

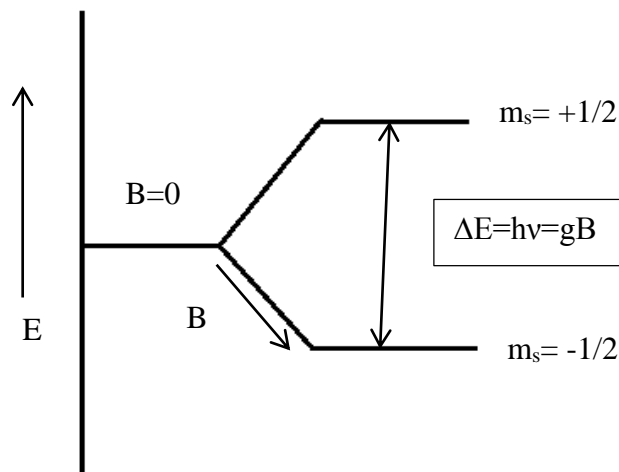


Figure 2.1 Energy level diagram for unpaired electron spin states under the influence of an external magnetic field (B).

According to the Boltzmann equation, the population of electrons in the two different energy levels in the applied magnetic field at thermal equilibrium, is given by the equation:

$$n_h/n_l = e^{-\Delta E/kT} \quad 2.4$$

where, n_h = spin population of higher energy level, n_l = spin population of lower energy level, ΔE = energy difference between the two levels, k = Boltzmann constant and T = absolute temperature. Substituting ΔE from equation 2.1, equation 2.4 can be rewritten as:

$$n_h/n_l = e^{-gB\beta/kT} \quad 2.5$$

At 298 K and at the field of 3000 G, $n_h/n_l = 0.9986$. The lower energy level has a little more population than the higher energy level, which gives rise to the absorption spectra in EPR. The two most common kinds of EPR experiments are continuous wave (CW) where microwave radiation is applied continuously to the sample and pulse experiments where a series of pulses of microwaves is applied to the sample. A brief introduction about CW and pulse experiment is given in this chapter and details can be found in Refs. [3, 7-10].

2.2 Continuous Wave (CW) experiment

In a CW experiment, microwave radiation is applied to the sample continuously at fixed frequency and the strength of the magnetic field is swept to record the spectrum. CW experiments are the most common EPR experiments. In this experiment, a derivative

spectrum is obtained instead of an absorption spectrum. The line width and the line shape of the signals give information about the size of the molecule, concentration of the molecule and many other things (Weil and Bolton [3], Eaton and Eaton [10]). The interaction between the unpaired electron and nearby nuclei split the EPR signal which is called hyperfine splitting. The hyperfine splitting gives information about the number of nuclei in the vicinity of the unpaired electron (Figure 2.2) [3,7-10]. The anisotropic contribution to the hyperfine depends on the distance between nuclei and electron. The number of hyperfine lines can be calculated using:

$$2nI+1 \qquad 2.6$$

where, n is the number of equivalent nuclei and I is the nuclear spin of the nuclei. An isotropic EPR spectrum is obtained for a species that is tumbling sufficiently rapidly to average anisotropy. An anisotropic spectrum is obtained for samples in rigid lattices such as glasses, powders, or single crystals.

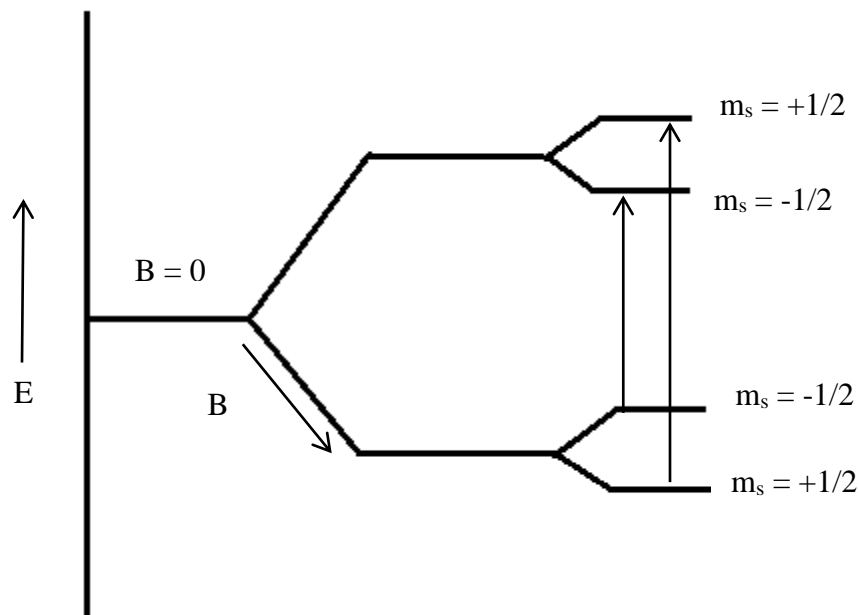


Figure 2.2 Energy level diagram for unpaired electron spin states interacting with one proton in the presence of an external magnetic field (B).

2.3 Pulse experiments

In pulse experiments, microwave radiation is applied to the sample in the form of short or long pulses at constant field and frequency. The pattern of pulses, the length of the pulses and the time between the pulses define different experiments. Pulse experiments can measure electron relaxation times. Changes in relaxation reflect interactions between the unpaired electron and its surroundings. There are mainly two types of relaxation times which can be measured by different pulse sequences – spin-spin relaxation or transverse (T_2) and spin-lattice relaxation or longitudinal (T_1) time.

2.3.1 Spin-spin or transverse relaxation time (T_2)

The spin-spin relaxation time is the constant for return to equilibrium of magnetization in the x-y plane or the decay of an echo. A pulse sequence that is used to

measure this relaxation process is $\pi/2 - \tau - \pi - \tau - \text{echo}$, where $\pi/2$ and π are 90° and 180° pulses and τ is the time interval between the two pulses (Figure 2.3). The echo is called a Hahn echo because it was described by Hahn in 1950 [11]. When the 90° excitation pulse is applied to the net spin vector in z-direction, the vector is rotated into the x-y plane (Figure 2.4). The spins start to dephase. They become out of phase with each other in time period τ . The 180° pulse flips the spins precession in the opposite direction in the transverse plane, which is the x-y plane. The spins start refocusing and produce an echo at time τ .

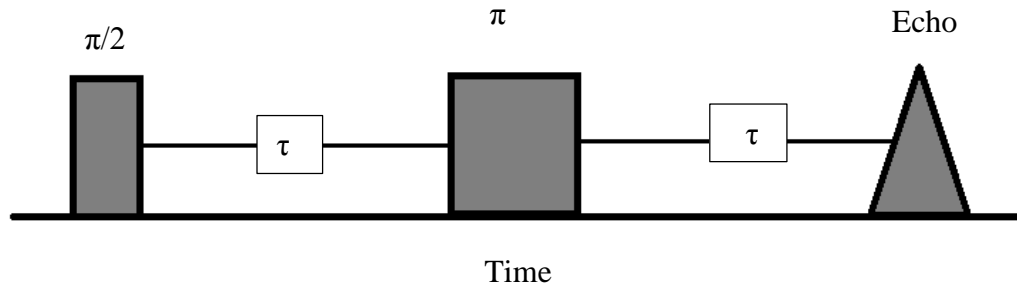


Figure 2.3 Pulse sequence for Hahn-echo to measure spin-spin relaxation time.

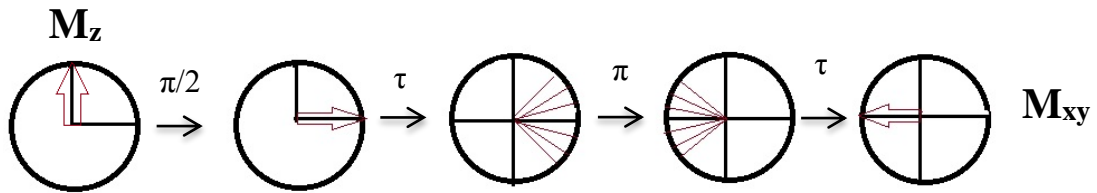


Figure 2.4 Stepwise graphical illustration of magnetic spin vector at particular positions in the two-pulse sequence depicted in Figure 2.3.

2.3.2 Spin-lattice or longitudinal relaxation time (T_1)

The spin-lattice relaxation time constant is the time required to lose the energy that was absorbed from the pulse to the lattice. The spin-lattice relaxation time can be measured using a 3-pulse inversion recovery experiment (Figure 2.5). The pulse sequence for this relaxation experiment is $\pi - T - \pi/2 - \tau - \pi - \tau - \text{echo}$, where $\pi/2$ and π are the 90° and 180° pulses, T is the delay time and τ is the time interval between the two pulses of the spin-echo detection sequence. As the 180° excitation pulse is applied to the net spin vector that is in z -direction, the spins move to the $-z$ direction. Spins start recovering in that direction during delay time T . The 90° excitation pulse is applied to the spin vector that puts the spins in the x - y plane. The spins start to dephase in the x - y plane. The 180° pulse that is applied after a constant time τ flips the spins in the opposite direction. The spins start refocusing in the time period τ to give the desired recovered echo (Figure 2.6) [8-10].

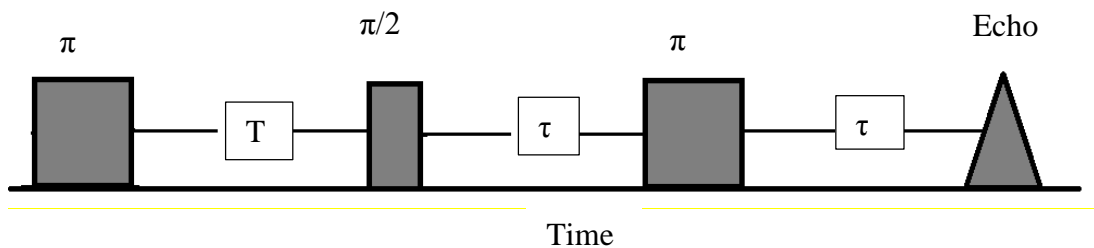


Figure 2.5 Pulse sequence for inversion recovery to measure spin-lattice relaxation time.

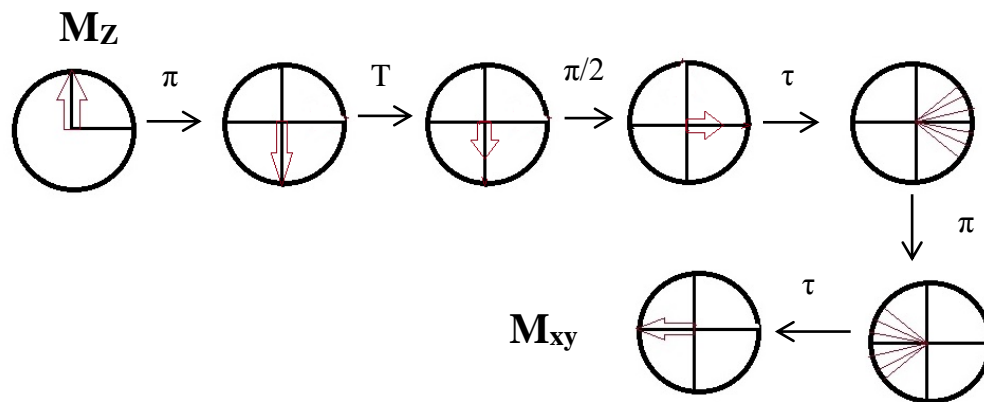


Figure 2.6 Stepwise graphical illustration of magnetic spin vector at particular positions in the spin-lattice relaxation sequence.

2.4 Design of EPR spectrometer

The basic requirements for an EPR spectrometer are a source for microwave radiation with a particular frequency, coaxial cables or waveguides to transmit the radiation, a circulator to direct waves, and a resonant cavity that includes the sample, an electromagnet and a detector (Figure 2.7).

2.4.1 Source

A Gunn diode or a klystron is the source of a particular frequency that is absorbed by the sample and provides the spectrum. The required frequency depends on the specific strength of magnetic field and the characteristics of the unpaired electrons. The source can be tuned mechanically or by voltages applied to it, to determine the particular frequency. The radiation is then propagated through a wave guide or coaxial cables. The

dimensions of the wave guide depend on the wavelength of the radiation. Coaxial cables are less efficient for transmitting the radiation, but are not frequency specific.

2.4.2 Circulator

The circulator is used to propagate the waves to the resonant cavity and the detector. Part of the radiation to the resonator is absorbed by the spin system. Part of the radiation is reflected back from the resonator and goes to the detector through the circulator. The reflected radiation goes to a detector that produces a DC output.

2.4.3 Resonator

The resonator holds the sample. It can be a rectangular cavity or other more compact structure [12]. The dimensions of a cavity or other resonator depend on the frequency of the source. The sample is placed in the middle of the resonator where it can absorb the maximum radiation. An important property of a resonator is defined by the Q-factor, which shows how much energy can be stored.

$$Q = \frac{2\pi \text{ Energy stored}}{\text{Energy dissipated per cycle}} \quad 2.7$$

$$Q = (v_{\text{res}}/\Delta v) \quad 2.8$$

where, v_{res} is the resonant frequency and Δv is the width at half height of the resonance. The resonator efficiency Ω is the proportionality between incident power, P and the microwave magnetic field, B_1 .

$$B_1 = \Omega\sqrt{P} \quad 2.9$$

2.4.4 Electromagnet

The electromagnet creates a range of magnetic field strengths. As the field is swept, electromagnets produce heat due to the current in the coils. Electromagnets are cooled by the continuous flow of water from the cooling system.

2.4.5 Detector

The reflected waves from the circulator as described in section 2.4.2 are sent to the detector to convert the microwave input to a DC output. The detector is often a silicon crystal diode that converts microwave power to current. The absorption of microwave radiation by the sample can be detected by the change in the detector current. The detector current varies as the square root of power [10].

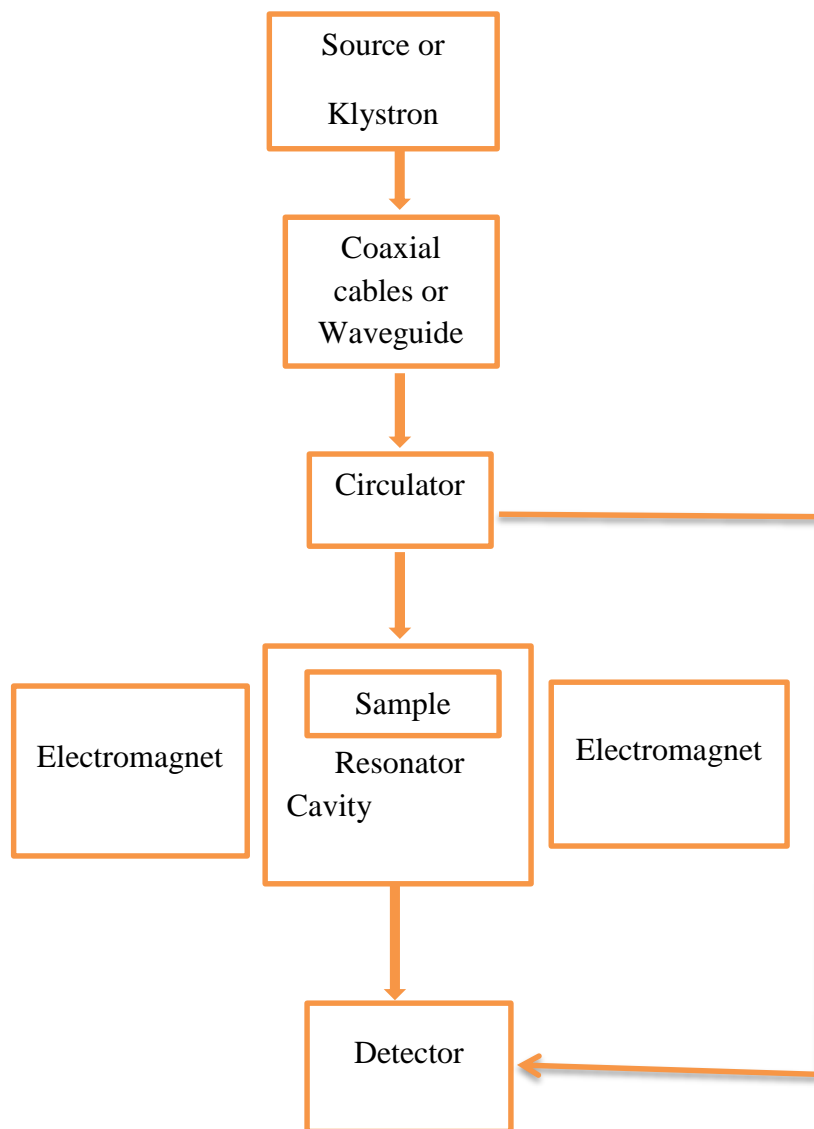


Figure 2.7 Schematic diagram of a basic EPR instrument.

Chapter 3

EPR of Lanthanide and Cobalt Ions

3.1 Introduction

3.1.1 Lanthanides Magnetism

Lanthanides have unique magnetic properties because of their paramagnetism (except for La^{3+} and Lu^{3+} , which are diamagnetic) and their physio-chemical properties. Lanthanides have much larger spin-orbit coupling than crystal field splitting, which makes them different from transition metals. Their orbital angular momentum is also large because of the number of unpaired electrons. In lanthanides, the magnetic moment formula takes spin as well as orbital angular momentum into consideration [1, 2, 13]. The magnetism of the lanthanides is very complicated. In addition, we have to consider spin quantum number and include the value of M_s , with $-S \leq M_s \leq S$. Hence, in the zero fields also, there can be some orientation dependence of magnetic moment [2,13,14]. The large spin-orbit coupling makes their anisotropy larger too. The large anisotropy contributes to a fast relaxation rate. Most of the lanthanides have fast electron spin relaxation as discussed in this chapter, except Gd^{3+} that has an S-state with half-filled f orbital. Hence, most of the lanthanides can only be studied by EPR at very low temperature.

Lanthanides have been used as paramagnetic relaxation enhancers in Nuclear magnetic resonance (NMR) [15,16,17] and in dynamic nuclear polarization [18,19] and in EPR. La^{3+} , Nd^{3+} and Pr^{3+} were used with nitroxyl radical to see the paramagnetic g-shift [13]. Dy^{3+} was used as a relaxer for galvinoxyl, benzosemiquinone and free radicals in tissues at 77 K [20]. $\text{Ho}(\text{EDTA})^{2-}$ and Dy^{3+} were used to enhance relaxation of semiquinone radicals in ubiquinone cytochrome c oxidoreductase [21]. Dy^{3+} has been used to decrease the power saturation of Fe^{3+} in cytochromes [22]. Dy^{3+} has also been used for relaxation enhancement studies, including measurement of interspin distances [23-25]. Gd^{3+} has been used in studying distances in proteins by Double Electron-Electron Resonance (DEER) at 95 GHz [25].

The lanthanide complexes (except for Gd^{3+}) also relax very quickly because the difference between their ground state and excited state is relatively small. Due to their fast relaxation, it is hard to measure their relaxation times directly except at low temperature. Hence their relaxation times are sometimes measured indirectly by looking at their effect on the relaxation of another slow relaxing species [27]. In this chapter, I focus on the lanthanides and their complexes that I have studied using CW EPR and pulse measurements of relaxation times, including Dysprosium (Dy^{3+}), Erbium (Er^{3+}), Gadolinium (Gd^{3+}), Thulium (Tm^{3+}) and the transition metal Cobalt (Co^{2+}). These metal ions were chosen after looking at the effect of different metals on relaxation of spins in melanin at X-band at -150 °C in Hyde and Sarna et. al. (1976) [28]. They did CW power saturation measurements, and observed that $P_{1/2}$ (the microwave power at which the EPR signal is half of the original signal without saturation) for Dy^{3+} and Tm^{3+} is the highest so

they concluded that $2\pi\nu T_{1m} \approx 1$ for these ions at $-150\text{ }^\circ\text{C}$. It was concluded that Gd^{3+} and Ho^{3+} have $2\pi\nu T_{1m} \gg 1$ and Er^{3+} , Nd^{3+} , Sm^{3+} and Pr^{3+} have $2\pi\nu T_{1m} \ll 1$ at $150\text{ }^\circ\text{C}$. The metals that have $2\pi\nu T_{1m} \approx 1$ and $2\pi\nu T_{1m} \ll 1$ have more effect on the spin-lattice relaxation of the neighboring species than the metals having $2\pi\nu T_{1m} \gg 1$.

3.2 Experimental Methods

3.2.1 Continuous Wave

X-band ($\sim 9.5\text{ GHz}$) and Q-band ($\sim 34\text{ GHz}$) continuous wave (CW) EPR spectra were recorded on a Bruker E580 spectrometer with an ER4118X-MS5 split ring resonator, an Oxford CF935 liquid helium cryostat, and an Oxford ITC503 temperature controller. Stock solutions (100 mM) of lanthanides $\text{DyCl}_3 \cdot 6\text{H}_2\text{O}$, $\text{GdCl}_3 \cdot 6\text{H}_2\text{O}$, $\text{TmCl}_3 \cdot 6\text{H}_2\text{O}$ and $\text{Er}(\text{NO}_3)_3 \cdot 5\text{H}_2\text{O}$ or transition metal $\text{CoCl}_2 \cdot 6\text{H}_2\text{O}$ were prepared by dissolving in a 1:1 glycerol: water mixture (v/v). Different concentrations of lanthanide or transition metal ions were prepared by diluting the stock solution with a 1:1 glycerol: water mixture. The metal complexes of $(\text{DTPA})^{2-}$ (diethylenetriaminepentaacetic acid) were formed by mixing equal moles of Dy^{3+} , Gd^{3+} , Er^{3+} or Co^{2+} and DTPA^{2-} solutions in 1:1 glycerol: water (v/v) with pH maintained at 5.5-6 using 0.1 mM NaOH and stirring it overnight. The $\text{Gd}(\text{dipicolinate})_3$ ($\text{Gd}(\text{DPA})_3$) complex was prepared by mixing Gd^{3+} chloride and DPA in 1:3.5 ratio and NaOH was added to deprotonate the DPA with pH adjusted to 5 at the end. Samples were put into 4 mm OD quartz tubes for X-band experiments. Samples were transferred into quartz capillaries and centrifuged for 4 min at 1000 X g for Q-band experiments. CW spectra were acquired with 0.4 mT or 0.3 mT

magnetic field modulation amplitude at 100 kHz and 2.3 to 6.9 mW microwave power. Resonator tuning at low temperature is more difficult than at ambient temperature, so selection of power was based on incomplete power saturation information. The g-values were estimated directly from the spectra without simulations.

3.2.2 Pulsed EPR measurement

X-band (~ 9.5 GHz) pulsed EPR experiments were performed on a Bruker E-580 spectrometer. Electron spin-spin relaxation times (T_2) were measured by two-pulse spin echo using pulse length of 40 and 80 ns. The initial time for data acquisition was 200 ns, which is limited by the resonator ring-down. Electron spin-lattice relaxation times (T_1) were measured by inversion recovery using 80-40-80 ns pulses. The attenuation of the power from the 2 KW TWT (Travelling Wave Tube) amplifier was selected to give 180 and 90° pulses. 2-Dimensional echo decay experiments and inversion recovery experiments were done for Co^{2+} , $\text{Co}(\text{DTPA})^{3-}$ and $\text{Er}(\text{DTPA})^{2-}$ in which the second dimension was variation in field. These experiments measured the relaxation time as a function of position in the spectrum. The relaxation times T_2 and T_1 were obtained by fitting single or double exponentials to the data using the Bruker E-580 XEPR software. For $\text{Er}(\text{DTPA})^{2-}$ echo envelope modulation was observed in the two-pulse decay, so T_2 was calculated using the EXPON program and fitting to the peaks of the modulation, which were selected manually. Field-swept echo detected spectra were obtained by holding the time between pulses constant and stepping the magnetic field.

3.3 EPR spectra of Dy³⁺, Er³⁺, Gd³⁺, Tm³⁺ and Co²⁺ and their complexes

3.3.1 Dy³⁺ and its complexes

Dy³⁺ has 9 electrons in its 4f shell. The total magnetic angular quantum number for Dy is 15/2, the spin quantum number is 5/2, the orbital quantum number is 5, and the spectral term for the ground state is ⁶H_{15/2} [1]. The effective magnetic moment of Dy³⁺ is 10.3 to 10.6 Bohr magneton [13,29,30]. The g-value of Dy³⁺ is orientation dependent and can vary from 15 to 2 for magnetically dilute samples [31]. The g-value obtained from the peak in the first-derivative CW spectrum at 10 K is 13.7 (Figure 3.1). The g-value reported for Dy-EDTA in Refs. [22,32] is 14 to 15, which is similar to the value of 13.7 for the aquo ion. The g-value for Dy(DTPA)²⁻ is 15.8 to 16 at 10 and 15 K (Figure 3.2). The g-value depends on the type and symmetry of the ligand. The full-width half maximum line width (ΔB_{FWHM}) for aquo Dy³⁺ is 300 to 384 G at 10 K and for Dy(DTPA)²⁻ (Figure 3.2) is 100 G at 10 K, 146 G at 15 K, 244 G to 390 G at 20 K, which are similar to 473 G reported for Dy(EDTA)²⁻ at 9 K [32]. The relaxation time for Dy(EDTA)³⁺ at 10 K was estimated from line broadening to be about 2×10^{-10} s [32]. The ΔB_{FWHM} increases by a factor of 1.5 and the amplitude of signal decreases by a factor of 2 between 10 and 15 K. The broadening is attributed to decreasing T₂ that is driven by the rapidly changing T₁, with T₁ = T₂ at temperatures higher than 20 K. The CW signals for Dy³⁺ and Dy(DTPA)²⁻ were observable only at temperature up to 20 K because it is a very fast relaxing ion. Reported relaxation values include T₁ of about 2×10^{-11} s at 123 K, where $2\pi\nu T_1 \sim 1$ at X-band [28] and 10^{-13} s at room temperature [30,33,34]. An electron

spin echo was not seen for Dy^{3+} or $\text{Dy}(\text{DTPA})^{2-}$ at 5 to 10 K, which means that T_2 is less than about $0.2 \mu\text{s}$ at these temperatures. The inability to detect an echo at 5 K is consistent with the report that the relaxation rate for Dy^{3+} in $\text{YCl}_3 \cdot 6\text{H}_2\text{O}$ is strongly temperature dependent above about 2 K, with a T^7 dependence [35].

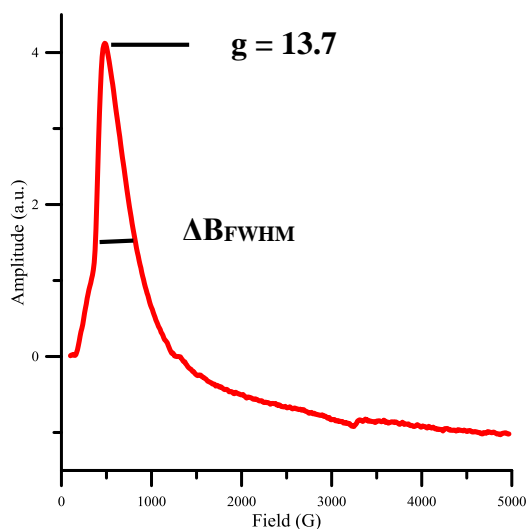


Figure 3.1 CW spectrum at X-band of 30 mM aquo Dy^{3+} .

The sample was dissolved in 1:1 H_2O : glycerol pH 6 at 10 K. The spectrum was obtained with 5.9 mW power, 4 G modulation amplitude and 5000 G sweep

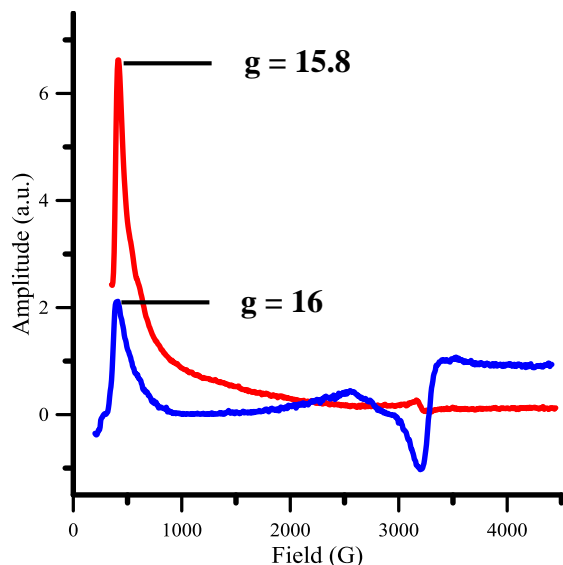


Figure 3.2 CW spectra at X-band of 30 mM Dy(DTPA)₂⁻.

The sample was dissolved in 1:1 H₂O: glycerol pH 6. The spectra were obtained at 10 K (red) and 15 K (blue) with 2.3 mW power, 3 G modulation amplitude and 4500 G sweep width. The signal at about 3000 G is due to a Cu(II) impurity in the resonator and appears larger at 15 K relative to the signal from Dy(DTPA)₂⁻ than at 10 K because of the broadening of the signal from Dy(DTPA)₂⁻.

3.3.2 Er³⁺ and its complexes

Er³⁺ has 11 electrons in the 4f shell. The total magnetic angular quantum number for Er³⁺ is 15/2, the spin quantum number is 3/2, the orbital quantum number is 6, and the spectral term for the ground state is ⁴I_{15/2} [1]. The effective magnetic moment of Er³⁺ is 8.9 – 9.4 Bohr magneton [13,29,30]. The g-value obtained from the CW spectrum of aquo Er³⁺ is 7 at 5 K (Fig 3.3) which is in agreement with g = 6.7 reported in Refs. [36, 37] and lower than the g = 11 at observed at 10 K (Figure 3.4). The much broader spectrum at 5 K than at 10 K (Figure 3.3 and 3.4 respectively) is not typical of unsaturated signals. The broadening at 5 K (Figure 3.3) may be due to the power

saturation or the signal may be a mixture of the absorption and dispersion. At 5 K values of T_1 for Er^{3+} in ionic lattices are strongly dependent on lattice (see Appendix 2 of Standley and Vaughn [38]). The spectrum at 5 K is included here for comparison, but requires further evaluation. The g -values for $\text{Er}(\text{DTPA})^{2-}$ are 11.5 and 4.6 at 10 to 30 K (Figure 3.5). The ΔB_{FWHM} for Er^{3+} is 341 G to 344 G at 10 to 15 K and for $\text{Er}(\text{DTPA})^{2-}$ is 99 G at 10 K, 150 G at 20 K and 293 G at 30 K. The temperature dependence of ΔB_{FWHM} is attributed to the temperature dependence of T_1 , with $T_1 = T_2$ at temperatures higher than 30 K.

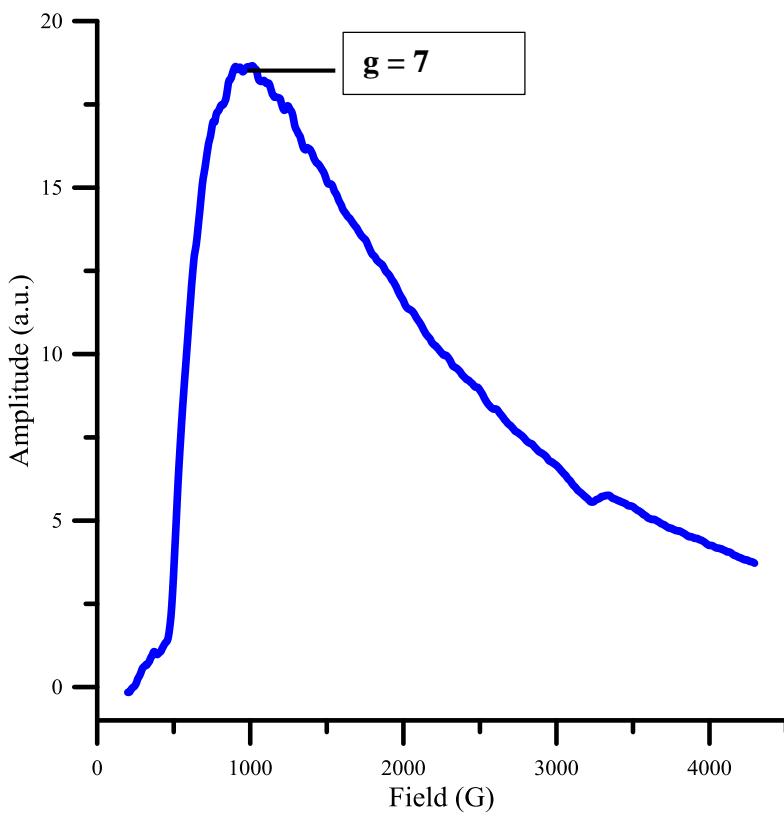


Figure 3.3 CW spectrum at X-band of 30 mM aquo Er^{3+} .

The sample was dissolved in 1:1 H_2O : glycerol pH 6. The spectrum was obtained at about 5 K with 6.9 mW power, 3 G modulation amplitude and 4500 G sweep width. It is so wide because of the mixture of absorption and dispersion.

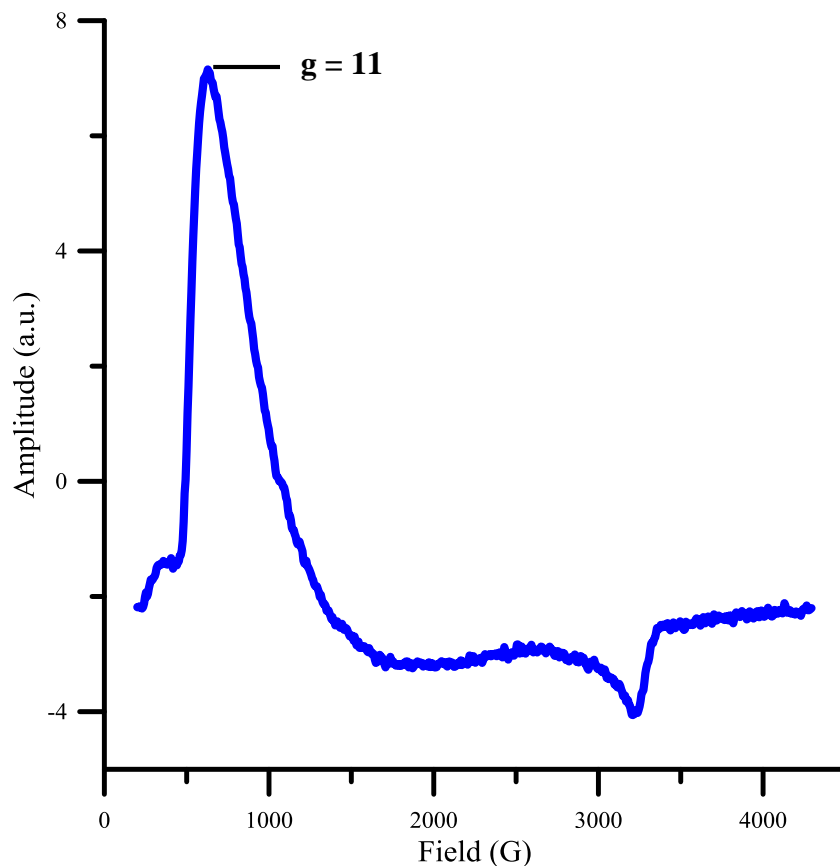


Figure 3.4 CW spectra at X-band of 30 mM aquo Er^{3+} .

The sample was dissolved in 1:1 H_2O : glycerol pH 6. The spectrum was obtained at about 10 K with 6.9 mW power, 3 G modulation amplitude and 4500 G sweep width.

The amazing difference between aquo Er^{3+} and $\text{Er}(\text{DTPA})^{2-}$ was in the pulse experiments. In the case of aquo Er^{3+} , an echo was not seen at 5 K at X-band between 500 to 6000 G. The inability to detect an echo may be due to the large number of water molecules coordinated directly to the Er^{3+} ion that can produce deep proton modulation and make T_2^* very short. However, for $\text{Er}(\text{DTPA})^{2-}$, an echo was observed at 5-7 K. Proton echo modulation is clearly seen in the T_2 decays (Figure 3.6). There was no echo detected for higher g-values because the modulation becomes deeper at lower magnetic

fields (higher g-values). The modulation is due to the electron-nuclear coupling. The depth of proton modulation is inversely proportional to the distance between the unpaired electron and the proton, so it is larger when water is directly attached to the Er^{3+} than for more distant protons [39]. The modulation frequency changes with magnetic field because the proton resonance frequency is changing. The period of the modulation in T_2 echo decay is about 103 ns at 2373 G, 97 ns at 2760 G and 98 ns at 2825 G. These correspond to modulation frequencies of 9.7 MHz to 11 MHz, respectively, which are consistent with the expected proton modulation frequencies of 10 or 12 MHz at these magnetic fields respectively. There is a possibility of interactions with both protons of a water molecule which can give rise to modulation at both ν_H and $2\nu_H$, and makes it more difficult to estimate the modulation frequency. Fitting to all data points with the Bruker Xepr software gave $T_2 = 298$ ns and $T_1 = 28$ and 5.4 μs when fitted bi-exponentially at 5 K. T_2 relaxation times obtained using the peak picking method in EXPON are 168 ns at 2373 G, 223 ns at 2760 G and 238 ns at 2825 G. At 7 K T_2 is 107 μs including all data points and fitting with Xepr and 93 μs by the peak picking method and T_1 is 1.32 μs . In the field-swept echo spectra at 5 K (Figure 3.7), the maximum signal was seen at 1968 G and 2760 G when the constant τ was 100 ns, at 2373 G when the constant τ was 200 ns and at 1823 G and 2825 G when constant τ was 142 ns. The maxima in the field-swept echo-detected spectra are due in part to the variation in the proton modulation frequency with field. At 7 K, (Figure 3.8) the maximum intensity peaks were seen at 2513 G and 3201 G in the field-swept echo, at constant τ of 100 ns. The CW signal of Er^{3+} and the CW and echo spectra for $\text{Er}(\text{DTPA})^{2-}$ were observed only at temperature ≤ 15 K. This

observation is consistent with the literature reports that it is a very fast relaxing ion with T_1 of about 10^{-13} s in water at room temperature, measured by NMR linewidths [30,40].

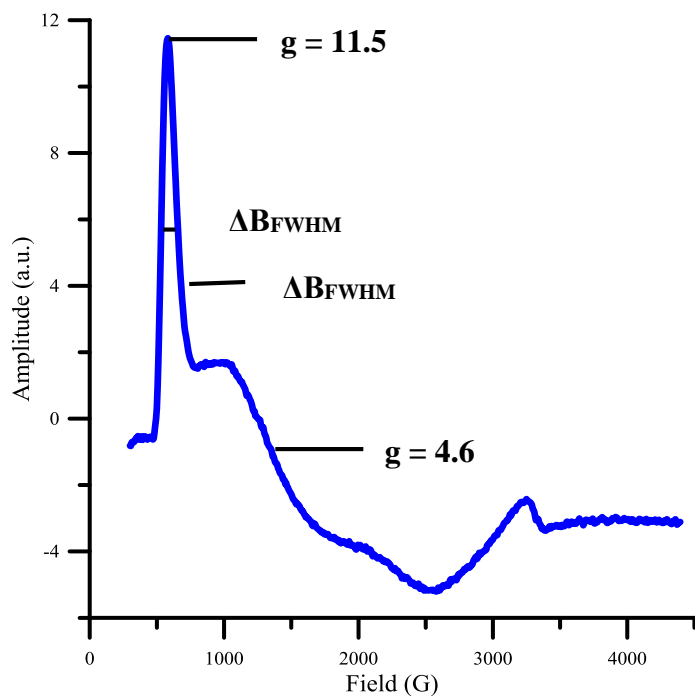


Figure 3.5 CW spectra at X-band of 30 mM $\text{Er}(\text{DTPA})^{2-}$.

The sample was dissolved in 1:1 H_2O : glycerol pH 6. The spectrum was obtained at about 10 K with 2.3 mW power, 3 G modulation amplitude and 4500 G sweep width.

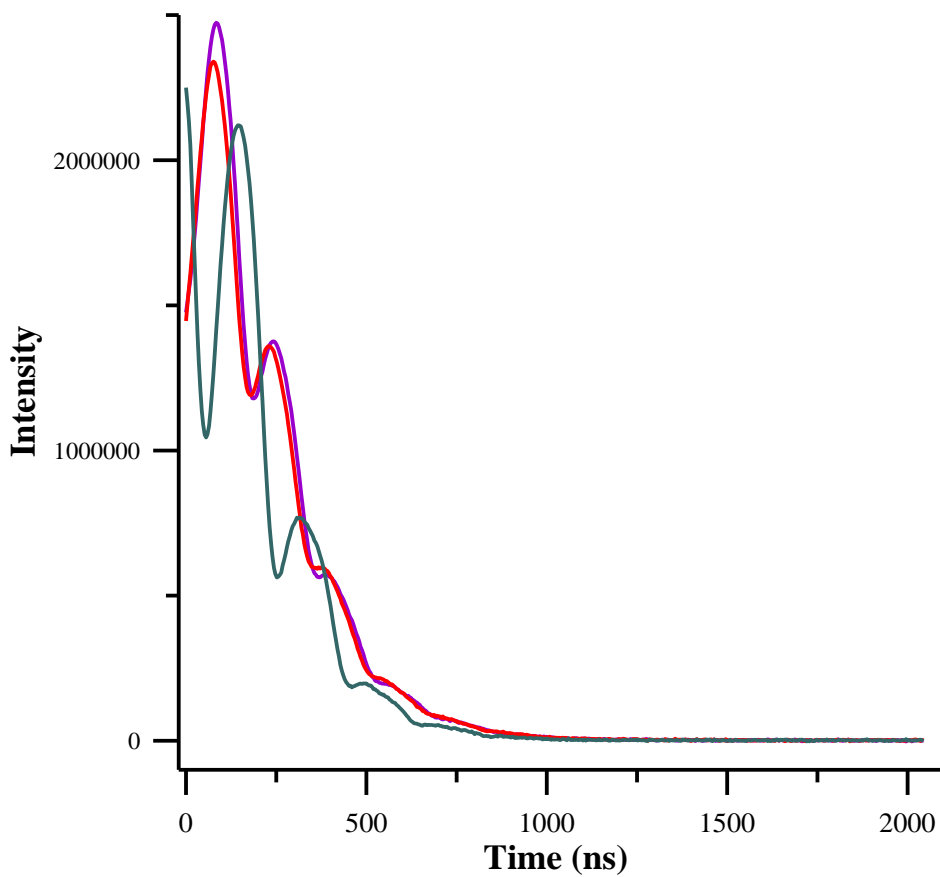


Figure 3.6 T_2 echo decays of 30 mM aquo $\text{Er}(\text{DTPA})^{2-}$.

The spectra were obtained at X-band in 1:1 H_2O : glycerol pH 6 at about 5 K using 40 ns 90° pulses with an initial τ value of 200 ns at three field positions: 2373 G (green trace), 2760 G (red trace) and 2825 G (purple trace). The time (x) axis is 2τ .

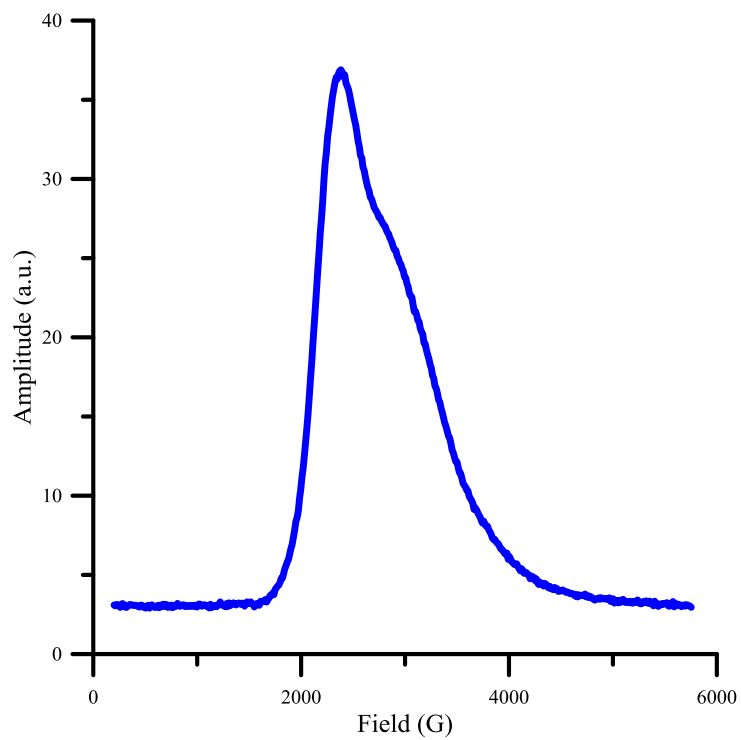


Figure 3.7 Two-pulse field-swept echo-detected spectrum of 30 mM Er (DTPA)²⁻. The spectrum was obtained at X-band in 1:1 H₂O: glycerol pH 6 at about 5 K, using 40 ns 90° pulses at 28 dB attenuation. The constant τ value was 200 ns.

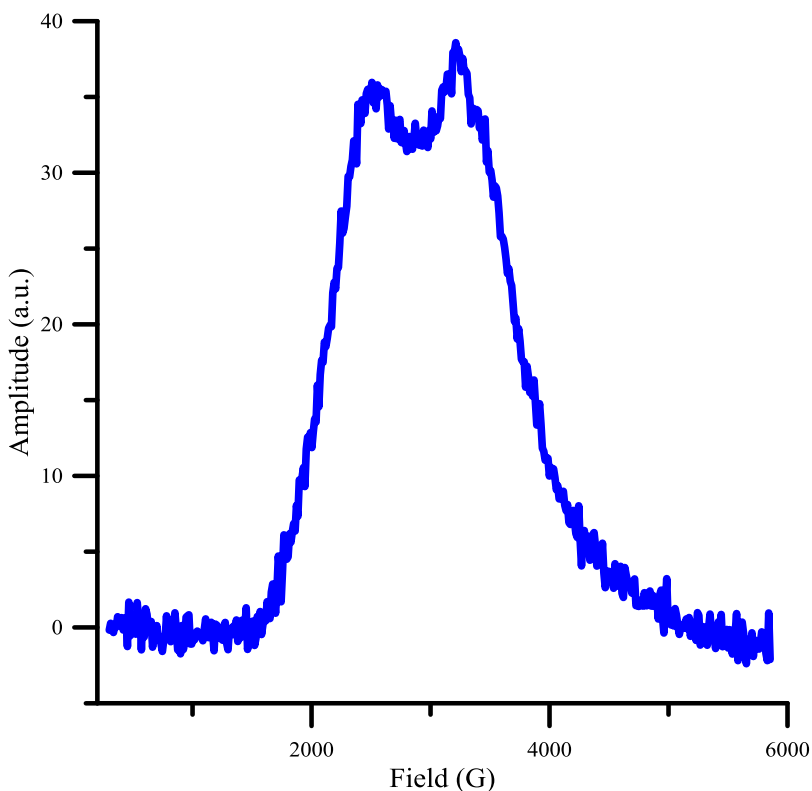


Figure 3.8 Two-pulse field-swept echo detected spectrum of 30 mM Er(DTPA)²⁻.

The spectrum was obtained at X-band in 1:1 H₂O: glycerol pH 6 at about 7 K, using 40 ns 90° pulses at 25 dB attenuation. The constant τ value was 100 ns.

3.3.3 Tm³⁺ and its complexes

Tm³⁺ has 12 electrons in the 4f shell. The total magnetic angular quantum number for Tm³⁺ is 6, spin quantum number is 1, orbital quantum number is 5, and the spectral term for ground state is ³H₆ [1]. The CW spectrum at 10 K (Figure 3.9) looks like a saturated spectrum and it also may have a mixture of absorption and dispersion, but looks similar to the spectrum at 4 K in Refs. [41]. In Table IV of Ref. [21] a g value of 9.2 is listed. The field swept echo spectra at 7 to 15 K (Figure 3.10) show the impact of varying proton modulation across the swept field. The temperature dependence of the fields at

which maximum echo amplitude is observed is not understood. These spectra need to be replicated. The CW signal and echo for Tm^{3+} were observed only at temperatures lower than 15 K, which shows that it is a very fast relaxing species. The intensity of the echo decreased as temperature was increased from 7 to 15 K, which means that the relaxation rate increases with temperature. The value of T_1 is about 10^{-13} s in water at room temperature. Since g -value depends on both the S and J , spectra extend over many Gauss.

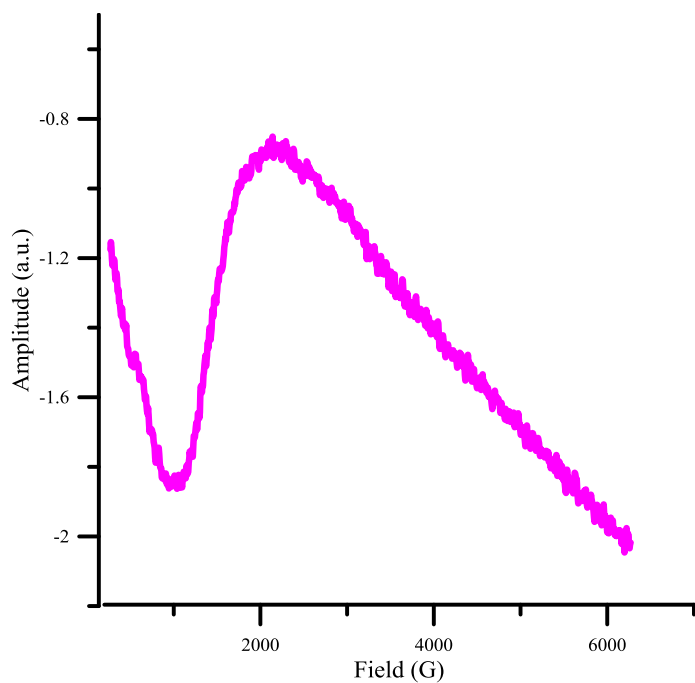


Figure 3.9 CW spectrum at X-band of 30 mM aquo Tm^{3+} .

The sample was dissolved in 1:1 H_2O : glycerol pH 6. The spectrum was obtained at about 10 K, with 6.9 mW power, 3 G modulation amplitude and 6000 G sweep width.

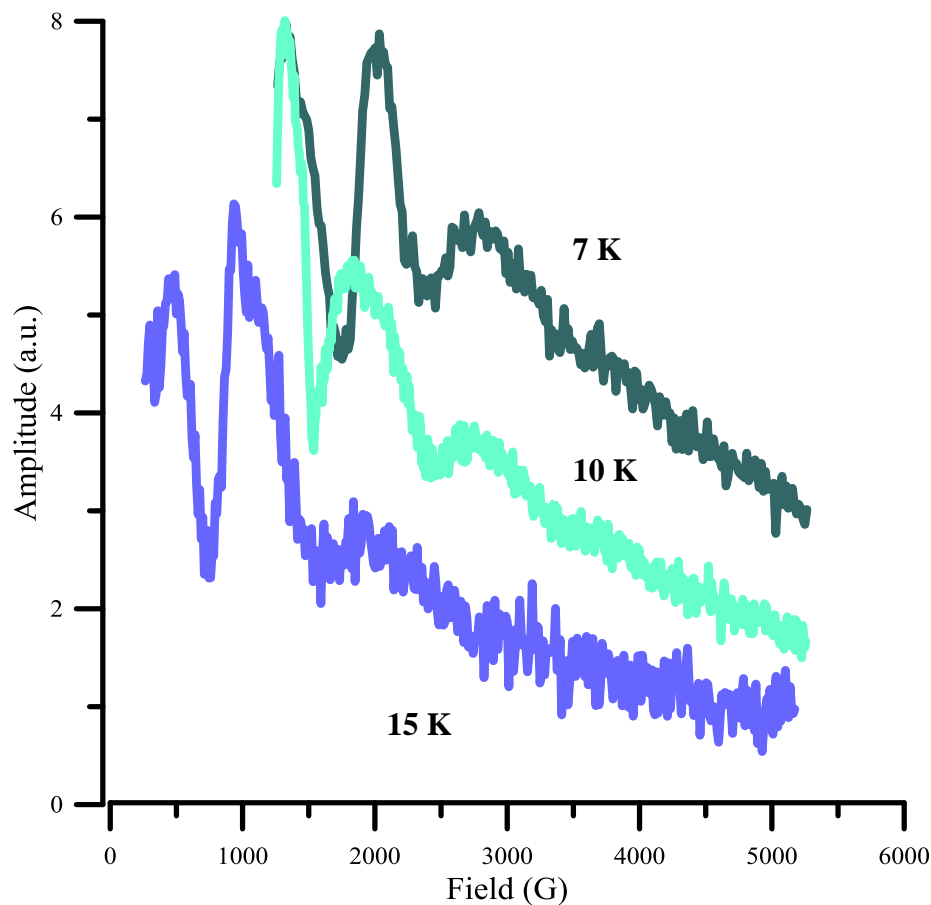


Figure 3.10 Two-pulse field-swept echo detected spectrum of 20 mM aquo Tm^{3+} . The sample was dissolved in 1:1 H_2O : glycerol pH 6. The spectrum was obtained at about 7, 10 and 15 K, using 40 ns 90° pulses at 31 dB with a constant τ value of 200 ns at X-band.

3.3.4 Co^{2+} and its complexes

$\text{Co}(\text{II})$ has a d^7 electron configuration in its high spin configuration. The g -value obtained from the CW spectrum at 10 K is 5 for aquo Co^{2+} (Figure 3.11) and 5.2 for $\text{Co}(\text{DTPA})^{3-}$ (Figure 3.12) which are similar to the g -values in Refs. [39,42] for aquo Co^{2+} and $\text{Co}(\text{DTPA})^{3-}$. The linewidth for Co^{2+} is 1000 G (Figure 3.11) and Co -DTPA is 1400 G (Figure 3.12). For aquo Co^{2+} and $\text{Co}(\text{DTPA})^{3-}$, a field swept echo spectrum was seen at 5 K to 10 K for Co^{2+} (Figure 3.13) and for $\text{Co}(\text{DTPA})^{3-}$ (Figure 3.14) with

maximum intensity at 2249 G and 2860 G for Co^{2+} and 2794 G and 3029 G for Co(DTPA)^{3-} when the constant τ is 100 ns. The amplitudes of the field-swept echo-detected spectra decrease with the increase in temperature for both Co^{2+} and Co(DTPA)^{3-} . This occurs because the difference in Boltzmann populations of the two levels decreases and because T_2 decreases with increasing temperature. No echo was detected for lower field positions which is attributed to the deep proton modulation that can be clearly seen in T_2 decay plots (Figure 3.15 for Co^{2+} and Figure 3.16 for Co(DTPA)^{3-}). Also, T_2 is shorter at lower field (Figure 3.15). The modulation is due to the electron-proton interaction, analogous to what was observed for Er(DTPA)^{2-} . It was hard to calculate T_2 because of the deep proton modulation, but T_2 was very short at 10 K and T_1 approached T_2 above 10 K. At 5 K T_2 for Co^{2+} is $1.0 \mu\text{s} \pm 0.2 \mu\text{s}$ if calculated in XEPR using all data points and $0.8 \pm 0.1 \mu\text{s}$ if calculated using the peak picking method in EXPON. At 5 K T_2 for Co(DTPA)^{3-} is $1.2 \mu\text{s} \pm 0.2 \mu\text{s}$ using XEPR with all points and $0.9 \pm 0.1 \mu\text{s}$ using the peak picking method in EXPON. The proton modulation was field dependent (Figure 3.15 and 3.16), with deeper modulation at lower field than at higher field. The period of the modulation for aquo Co^{2+} is about 89 ns at 2974 G (Figure 3.15), which corresponds to a frequency of 11 MHz. Since the modulation is relatively shallow this is in reasonable agreement with the expected ^1H modulation frequency of 13 MHz. The period decreases with increasing field, as expected. For Co(DTPA)^{3-} the modulation period is 97 ns at 2000 G (Figure 3.16), which corresponds a modulation frequency of 10.3 MHz, which is in reasonable agreement with the 8.5 MHz ^1H frequency at this field. The $1/T_1$ rate increased with increasing temperature for both Co^{2+} and Co(DTPA)^{3-} and was not

strongly field dependent (Fig. 3.17 and 3.18). The average T_1 obtained for Co^{2+} at 5 K was $228 \pm 70 \mu\text{s}$, $17 \pm 3 \mu\text{s}$ at 7 K and $1.5 \pm 0.5 \mu\text{s}$ at 10 K. The average T_1 obtained for $\text{Co}(\text{DTPA})^{3-}$ at 5 K was $241 \pm 52 \mu\text{s}$, $25 \pm 6 \mu\text{s}$ at 7 K and $2.7 \pm 0.7 \mu\text{s}$ at 10 K. These values are different from the T_1 values of 1.6 ms at 6.5 K, $25 \mu\text{s}$ at 8.2 K and $8 \mu\text{s}$ at 10 K in Ref. [39]. There can be 2 reasons for the differences. Firstly, my samples were 6 times more concentrated than the samples in Ref. [39] and secondly, T_1 in Ref. [39] was measured using saturation recovery rather than inversion recovery that was used to measure T_1 in these experiments.

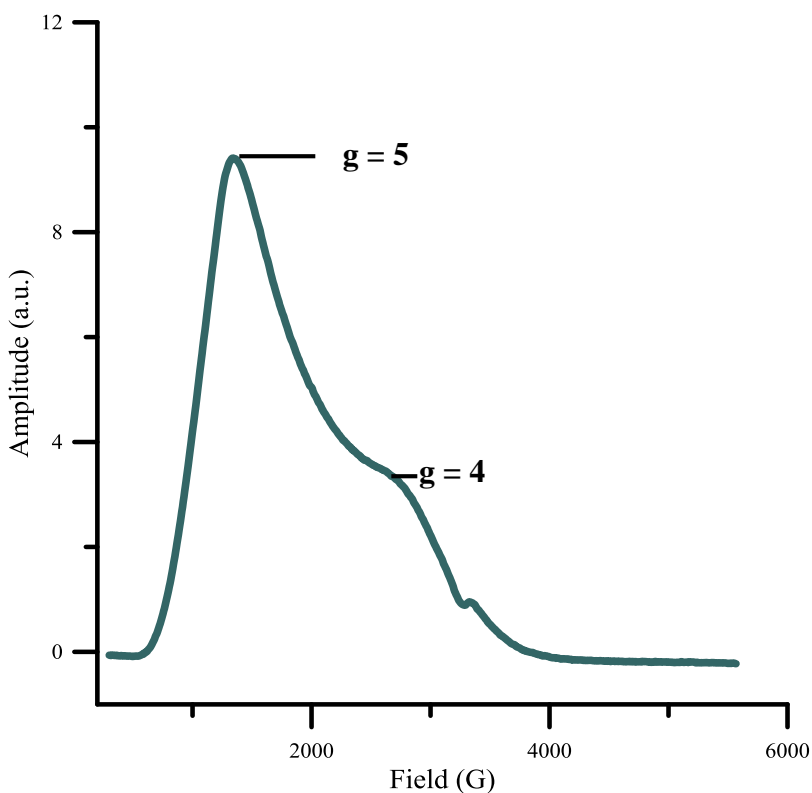


Figure 3.11 CW spectrum at X-band of 30 mM aquo Co^{2+} .

The sample was dissolved in 1:1 H_2O : glycerol pH 6. The spectrum was obtained at 10 K with 2.3 mW power, 3 G modulation amplitude and 5700 G sweep width. This is a derivative spectrum that exhibits passage effects and looks more like an absorption spectrum.

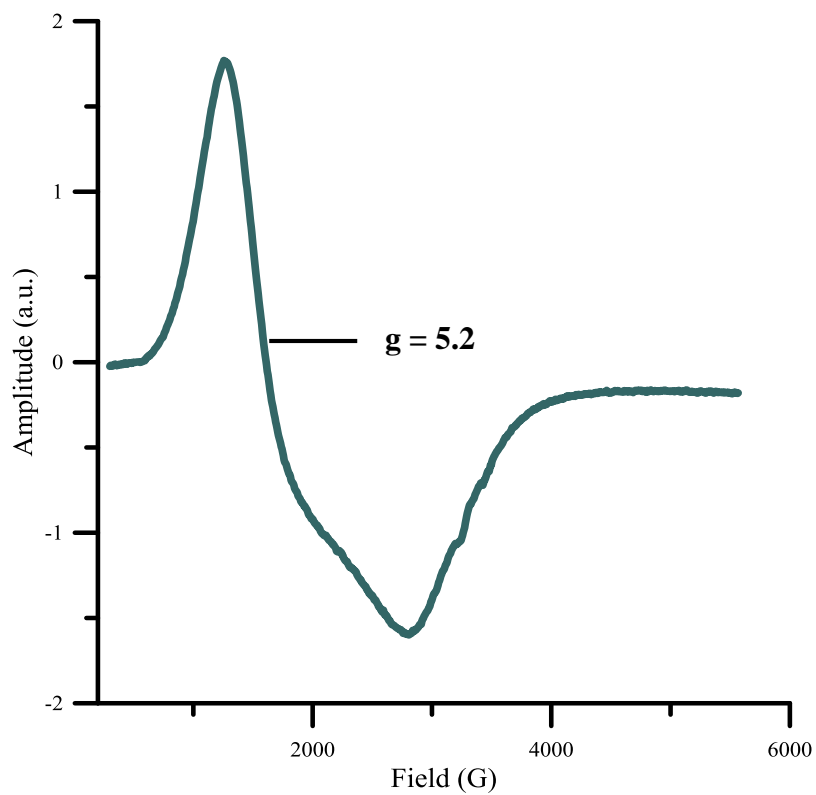


Figure 3.12 CW spectrum at X-band of 30 mM $\text{Co}(\text{DTPA})^{3-}$.

The sample was dissolved in 1:1 H_2O : glycerol pH 6. The spectrum was recorded at about 10 K, with 2.3 mW power, 3 G modulation amplitude and 6000 G sweep width.

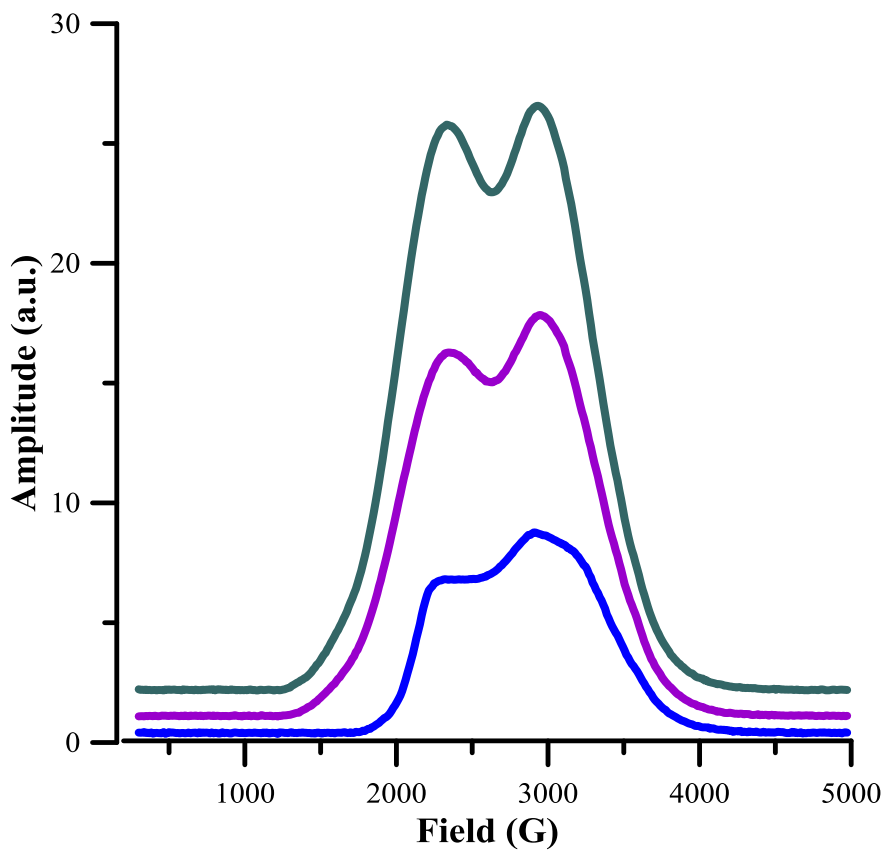


Figure 3.13 Two-pulse field-swept echo-detected spectra at X-band of 30 mM aquo Co^{2+} .

The sample was dissolved in 1:1 H_2O : glycerol pH 6. Spectra were recorded at about 5 K (green), 7 K (purple) and 10 K (blue) with 5000 G sweep width using 40 ns 90° pulses at 20 dB attenuation. Shot repetition time was 510 μs and 1 scan was taken for each spectrum. Shots/point was 64.

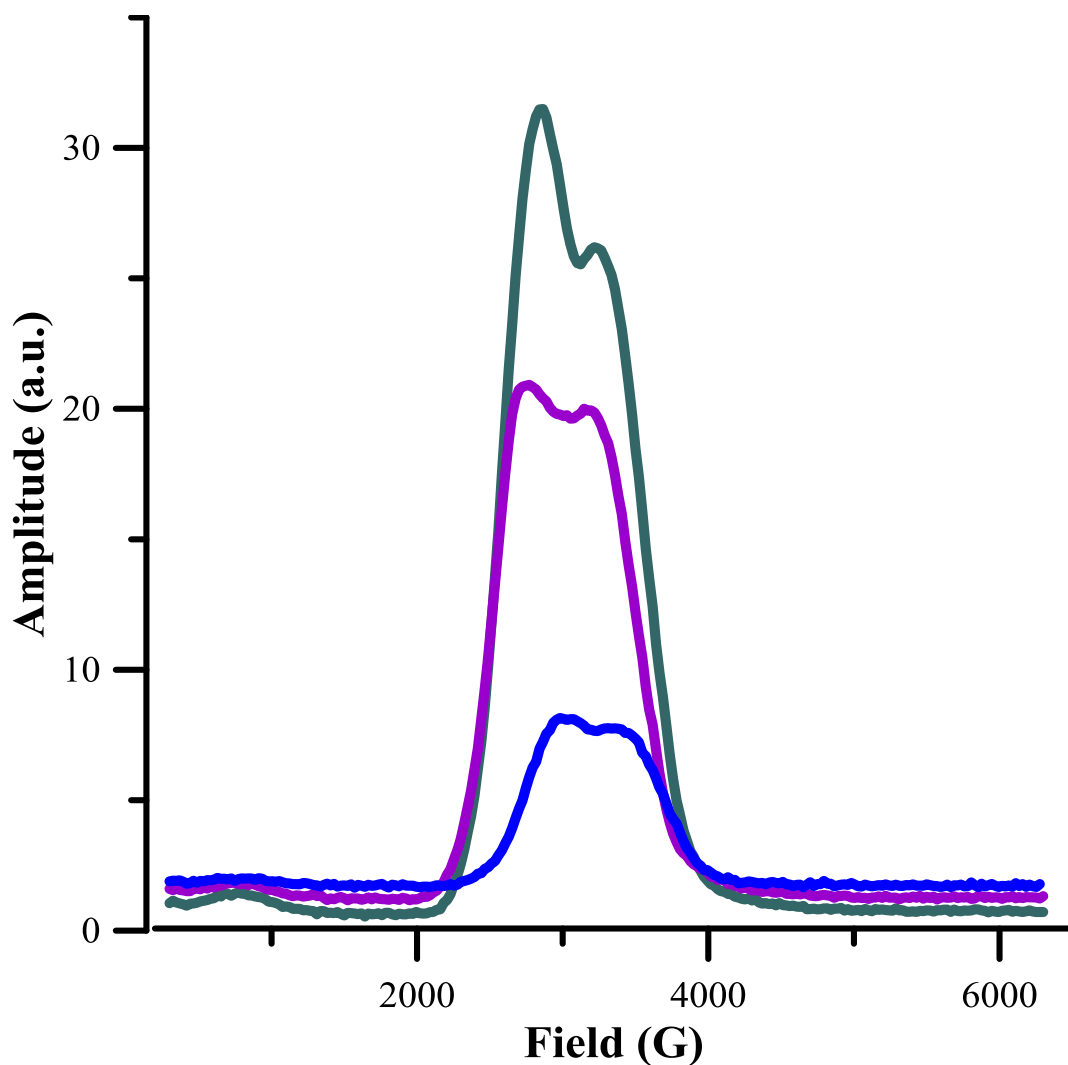


Figure 3.14 Two-pulse field-swept echo-detected spectra at X-band of 30 mM $\text{Co}(\text{DTPA})^{3-}$.

The sample was dissolved in 1:1 H_2O : glycerol pH 6. Spectra were obtained at about 5 K (green), 7 K (purple) and 10 K (blue) with 6500 G sweep widths using 40 ns 90° pulses at 22 dB attenuation. The shot repetition time was 1000 μs for each spectrum and amplitude was normalized for 1 scan. The shots/point was 64.

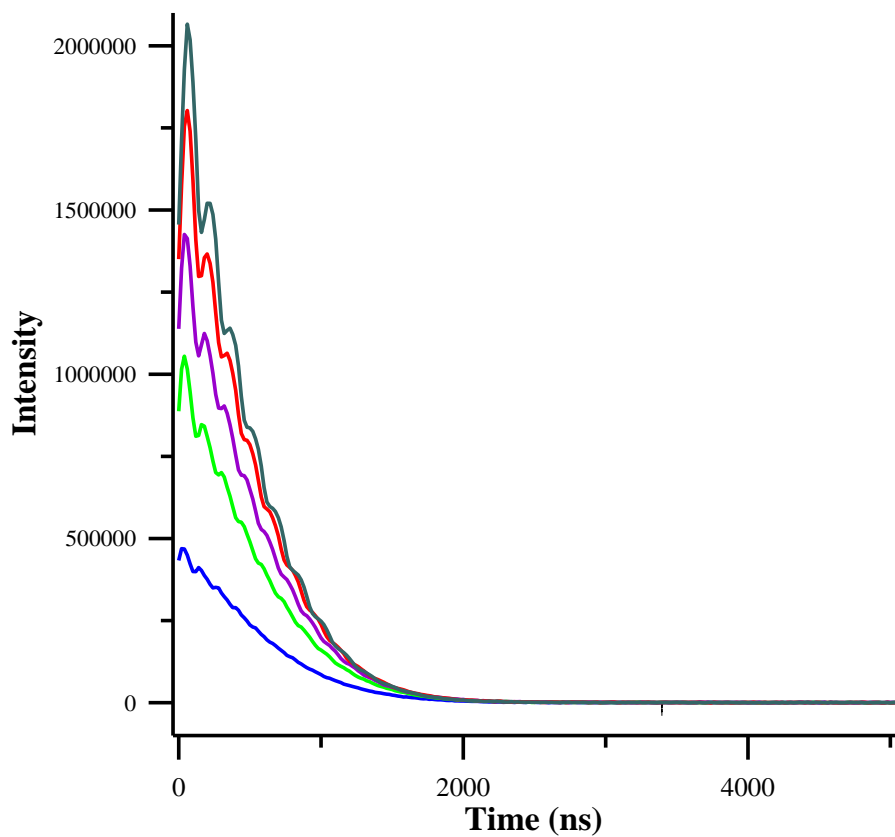


Figure 3.15 T_2 decays at five field positions at X-band for 30 mM aquo Co^{2+} .

The sample was dissolved in 1:1 H_2O : glycerol pH 6. Decays were recorded at about 7 K. The field positions are 3500 G (blue), 3289 G (green), 3184 G (purple), 3079 G (red) and 2974 G (dark green). The time (x) axis is 2τ .

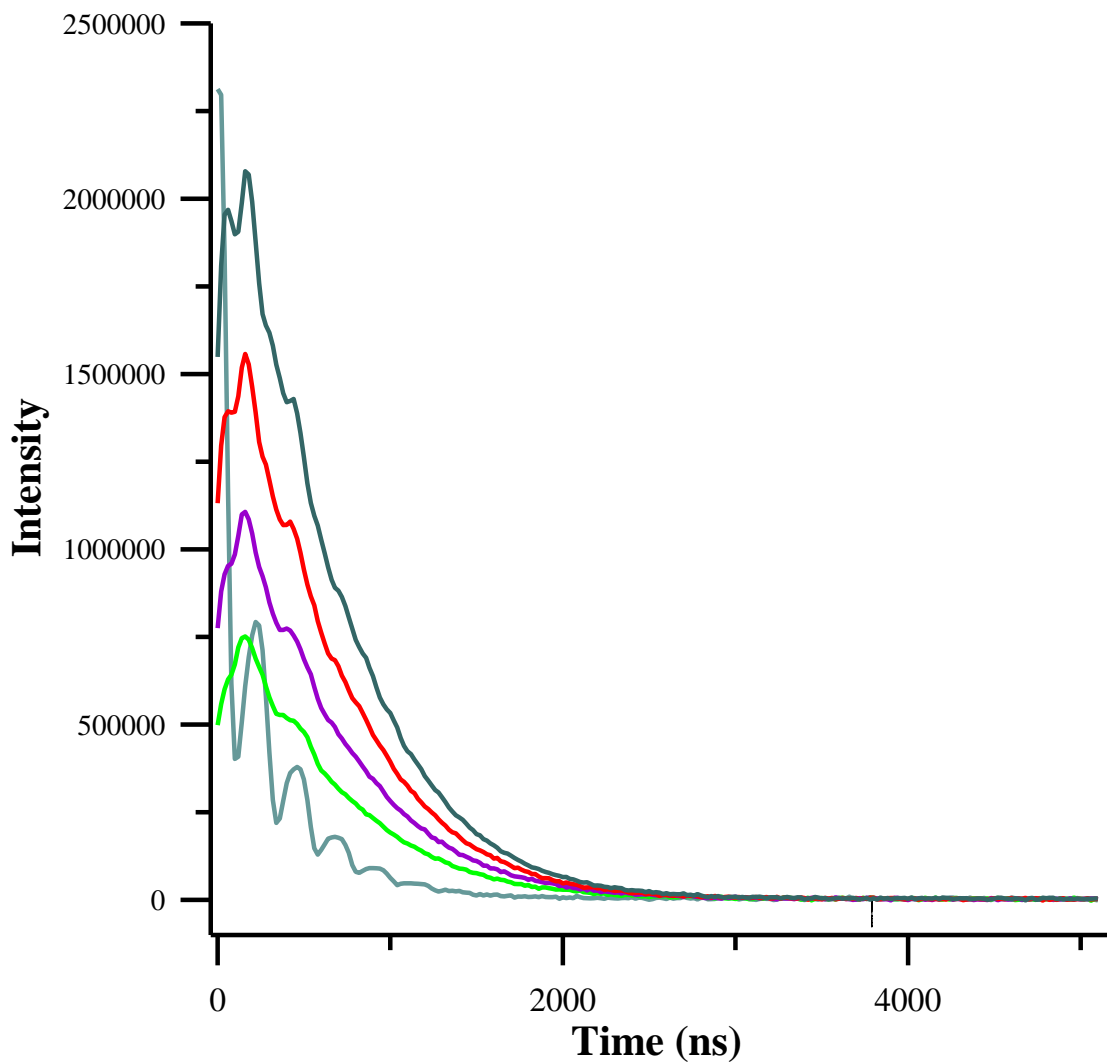


Figure 3.16 T_2 decays at five field positions at X-band for 30 mM Co(DTPA)^{3-} . The sample was dissolved in 1:1 H_2O : glycerol pH 6. Decays were recorded at about 7 K, using 40 ns 90° pulse. The field positions are 2000 G (grey), 3684 G (light green), 3579 G (purple), 3474 G (red) and 3368 G (dark green). The time (x) axis is 2τ .

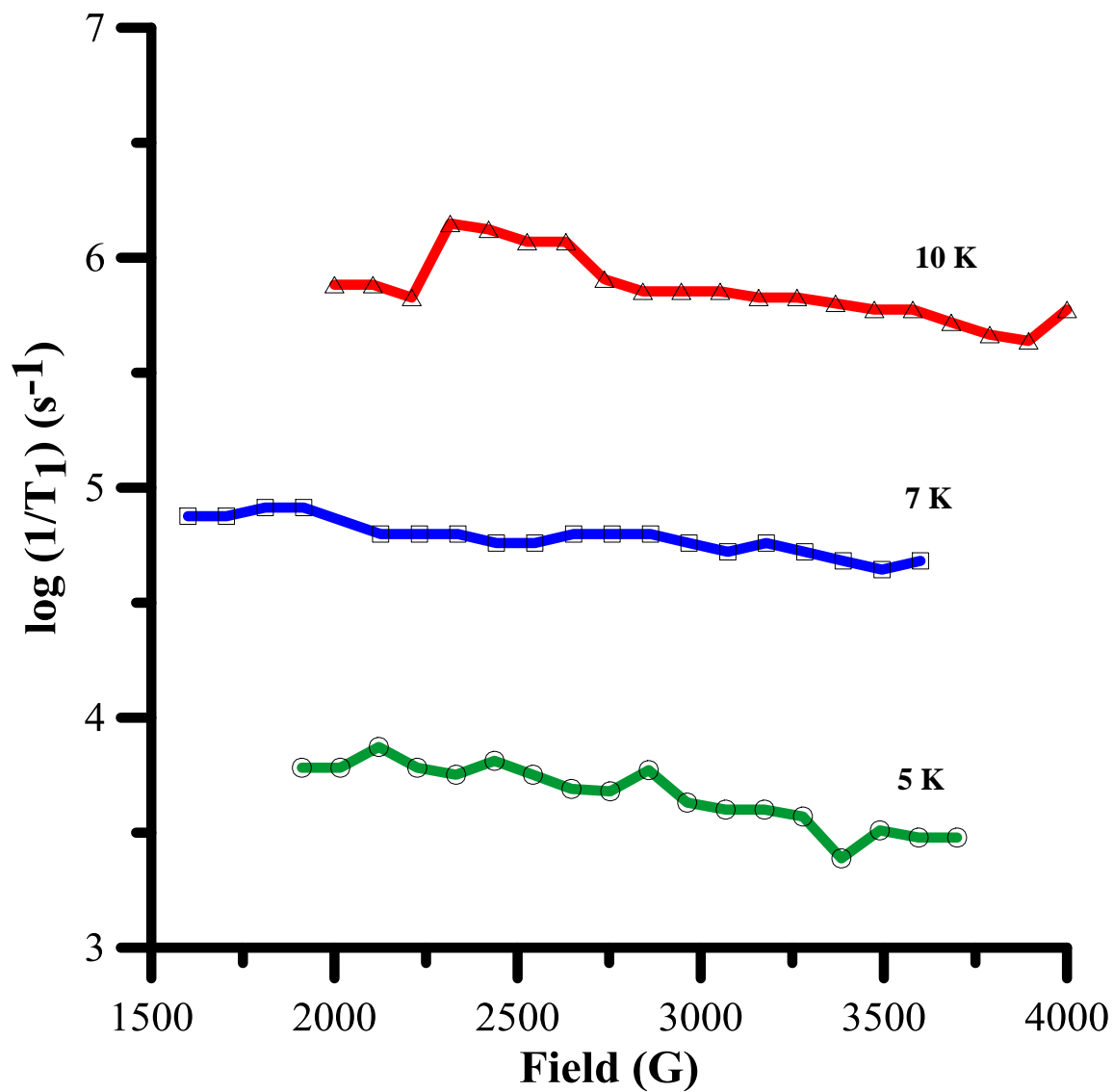


Figure 3.17 Spin-lattice relaxation rates ($1/T_1$) for aquo Co^{2+} as a function of field. The rates were measured at 5 K (green line), 7 K (blue line) and 10 K (red line). Uncertainty is about 4- 6%.

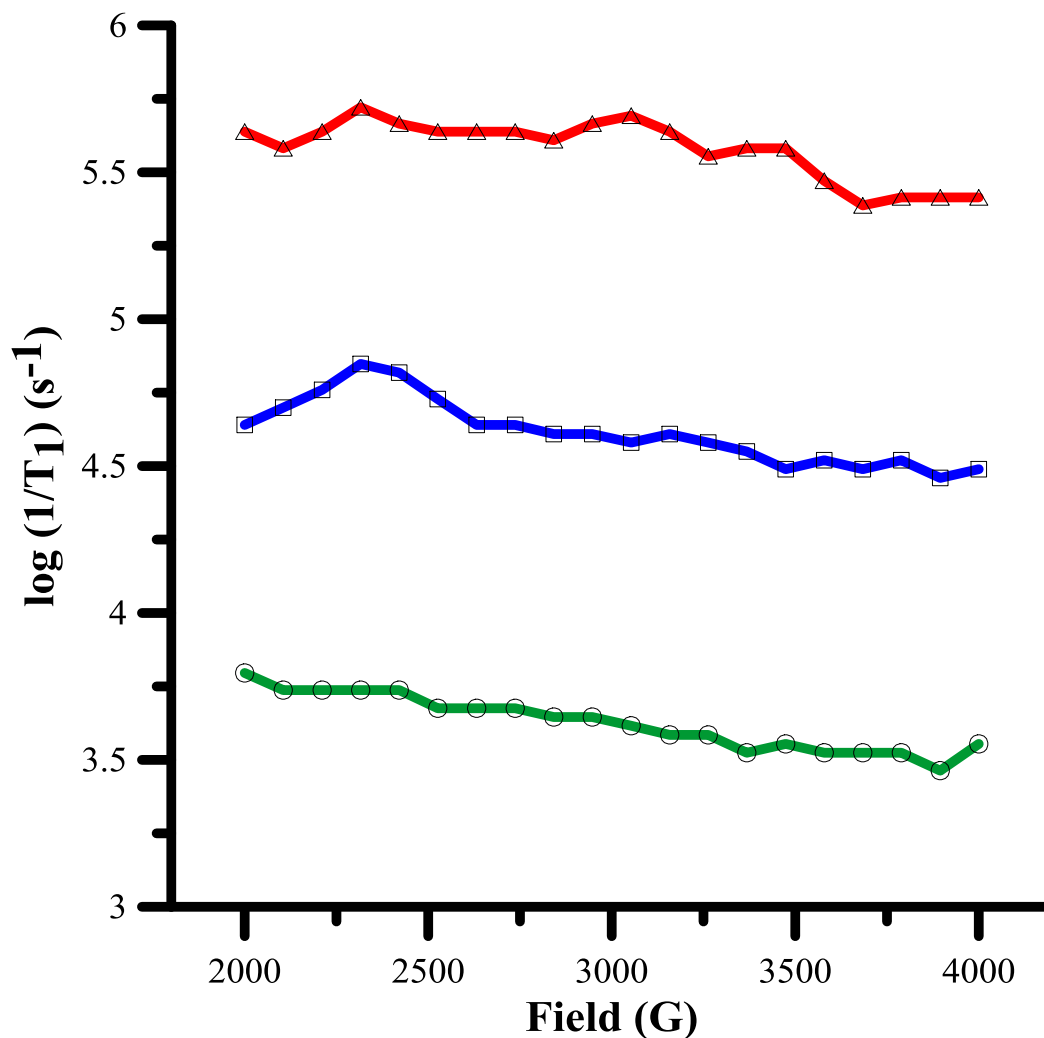


Figure 3.18 Spin-lattice relaxation rate ($1/T_1$) for $\text{Co}(\text{DTPA})^{3-}$ as a function of field. The rates were measured at 5 K (green line), 7 K (blue line) and 10 K (red line).

3.3.5 Gd^{3+} and its complexes

Gd^{3+} has 7 electrons in the 4f shell. The total magnetic angular quantum number for Gd^{3+} is $7/2$, the spin quantum number is $7/2$, the orbital quantum number is 0, and the spectral term for ground state is $^8S_{7/2}$ [1]. Aquo Gd^{3+} has a magnetic moment of 8 Bohr magneton [40]. The relaxation time of aquo Gd^{3+} , measured by NMR linewidths, is in the

range of 10^{-8} to 10^{-9} s in water at room temperature, which is longer than other lanthanide metal ions [27]. CW spectra of Gd^{3+} and its complexes were recorded at 80 K, instead of lower temperatures, because the signals have been reported to saturate very readily at lower temperatures. Q-band was used to increase spectral resolution and because the linewidths of the $m_s = \pm 1/2$ transitions are smaller at Q-band than at X-band. These transitions occur near $g = 2$ and dominate the CW spectra. In Q-band CW spectra at 80 K the $m_s = \pm 1/2$ transitions have a linewidth of 23 G for Gd^{3+} (Figure 3.19) and 62 G for $\text{Gd}(\text{DTPA})^{2-}$ (Figure 3.20).

Fluid solution spectra in aqueous solution at ambient temperature were recorded at X-band. The CW spectra of $\text{Gd}(\text{DTPA})^{2-}$ (Figure 3.23) and $\text{Gd}(\text{DPA})_3$ (Figure 3.24) in water, have some complex features which are not present in spectra of $\text{Gd}(\text{EDTA})^-$ (Figure 3.22) and aquo Gd^{3+} (Figure 3.21). In Benmelouka et al. [43], these complex spectral features of $\text{Gd}(\text{DTPA})^{2-}$ were attributed to the large magnitude of the zero field splitting (ZFS). Since the static ZFS parameters are similar in frozen and fluid solution, the ZFS values are relevant to spin relaxation in aqueous solution. In aqueous solution the linewidth for $\text{Gd}(\text{DTPA})^{2-}$ (Figure 3.23) is between 580 to 604 G, which is similar to 600 G found in Ref. [44]. The linewidth of Gd^{3+} (Figure 3.21) is between 525 to 540 G which is similar to the linewidth found in Refs. [45,46].

Complexes with higher symmetry have narrower linewidth and longer electron T_1 [45,47,48]. Relaxation times are interpreted in terms of static and transient ZFS. Static ZFS arises from the low symmetry of the molecule and transient ZFS is for the vibrations and collisions with the solvent molecules [49]. The relaxation time of Gd^{3+} in solution

depends on the magnetic field also because of the rotational correlation time that matters to slow relaxing species. As shown in Table 3.1, at 80 K at Q-band T_2 for 5 mM and 10 mM Gd^{3+} is between 0.21 and 0.31 μs and T_1 is between 1.2 to 1.4 μs . However, at 80 K at X-band with 7 mM Gd^{3+} , T_2 is 0.241 μs and T_1 is 0.473 μs . For $Gd(DTPA)^{2-}$ at 80 K the T_2 is 0.5 μs and T_1 is 1.5 μs at Q-band whereas at X-band, T_2 is 0.24 μs and T_1 is 0.85 μs . These results show that values of T_1 shown in Table 3.1 are longer at Q-band (34 GHz) than reported previously [25,5025] at X-band (9 GHz). Values of T_1 are not very concentration dependent, but values of T_2 are concentration dependent above 2 mM. According to Table 3.2, T_2 and T_1 are temperature dependent. T_2 and T_1 get shorter with increase in temperature. Values of T_2 and T_1 are in good agreement with unpublished values that were obtained in our lab by Brent Schuchmann for Gd^{3+} and $Gd(DTPA)^{2-}$ species.

Table 3.1 Concentration dependence of T_1 and T_2 for aquo Gd^{3+} and $Gd(DTPA)^{2-}$ at 80 K and 34 GHz in 1:1 water: glycerol.

Concentration	T_2 (μs)	T_1 (μs) ^a
0.1mM Gd^{3+}	0.73	1.7 , 0.70
0.2mM Gd^{3+}	0.69	1.5 , 0.54
0.5mM Gd^{3+}	0.58	1.5 , 0.6
1mM Gd^{3+}	0.50	1.4 , 0.57
2mM Gd^{3+}	0.43	1.60 , 0.67
5mM Gd^{3+}	0.31	1.4 , 0.55
10mM Gd^{3+}	0.21	1.2 , 0.35
20mM Gd^{3+}	0.09	0.96
2mM $Gd(DTPA)^{2-}$	0.50	1.6 , 0.51
20mM $Gd(DTPA)^{2-}$	0.2	1.5 , 0.52
1mM $Gd(DPA)_3$	0.26	1.5, 0.44

^aThe two values are the results from a two-component fit.

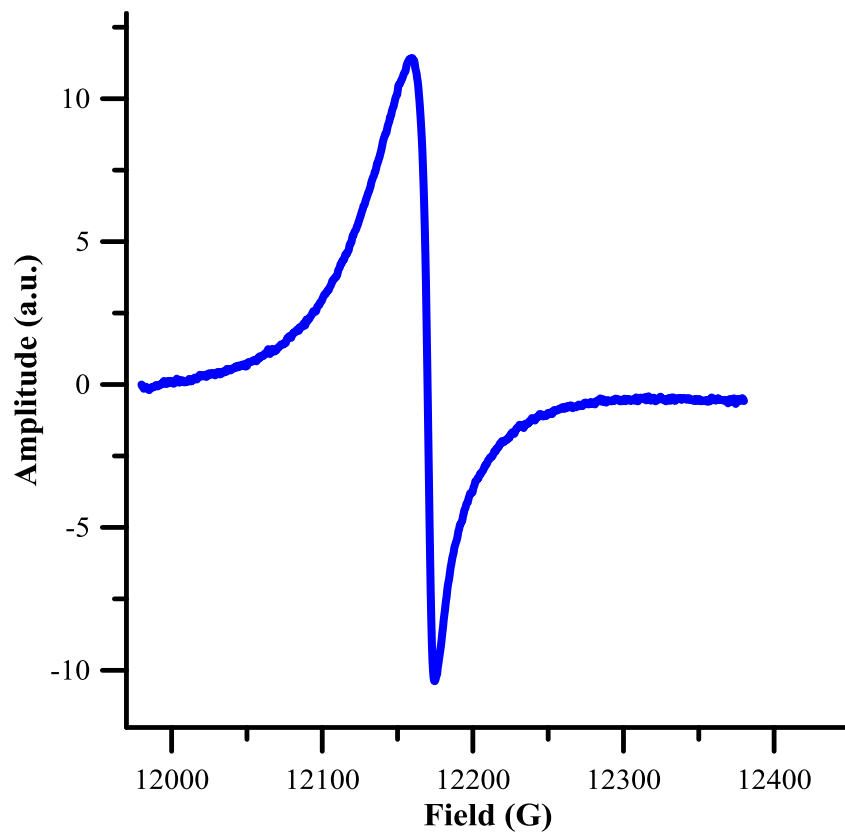


Figure 3.19 Q-band (33.97 GHz) CW spectrum of 1 mM Gd³⁺. The sample was dissolved in 1:1 H₂O: glycerol. The spectrum was taken at 80 K with modulation amplitude of 5 G and 2.37 mW power.

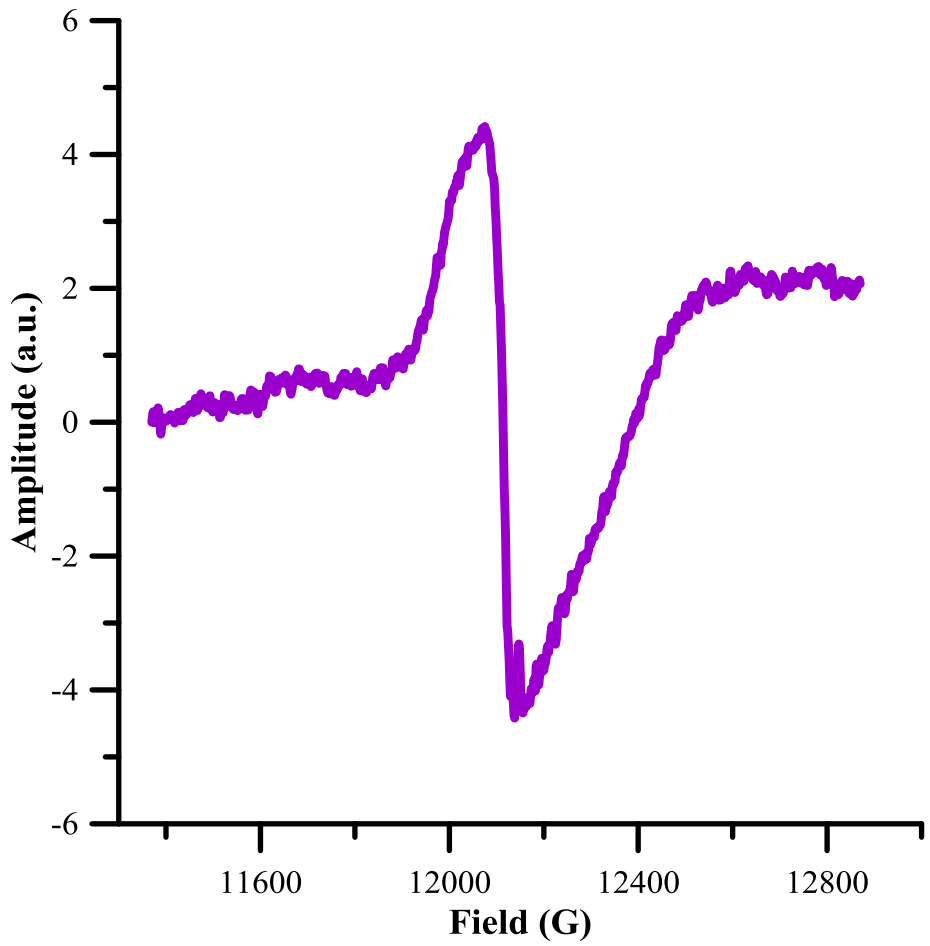


Figure 3.20 Q-band (33.95 GHz) CW spectrum of 2 mM $\text{Gd}(\text{DTPA})^{2-}$.

The sample was dissolved in 1:1 H_2O :glycerol. The spectrum was taken at 80 K with modulation amplitude of 3 G and 0.24 mW power.

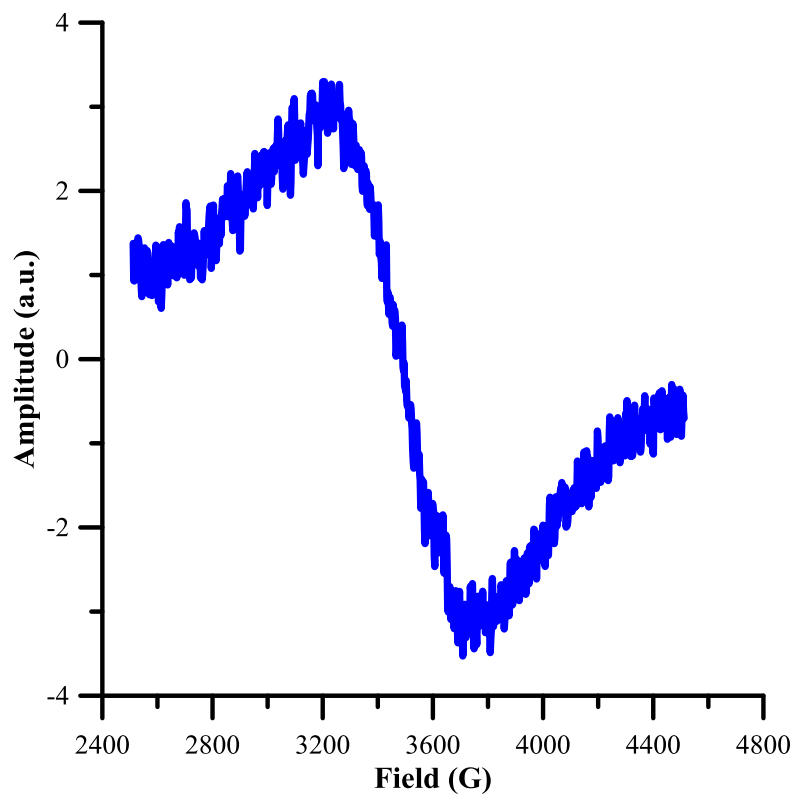


Figure 3.21 X-band (9.84 GHz) CW spectrum of 5 mM Gd³⁺ in water at room temperature.

The spectrum was taken with modulation amplitude of 3 G and at 2.37 mW power.

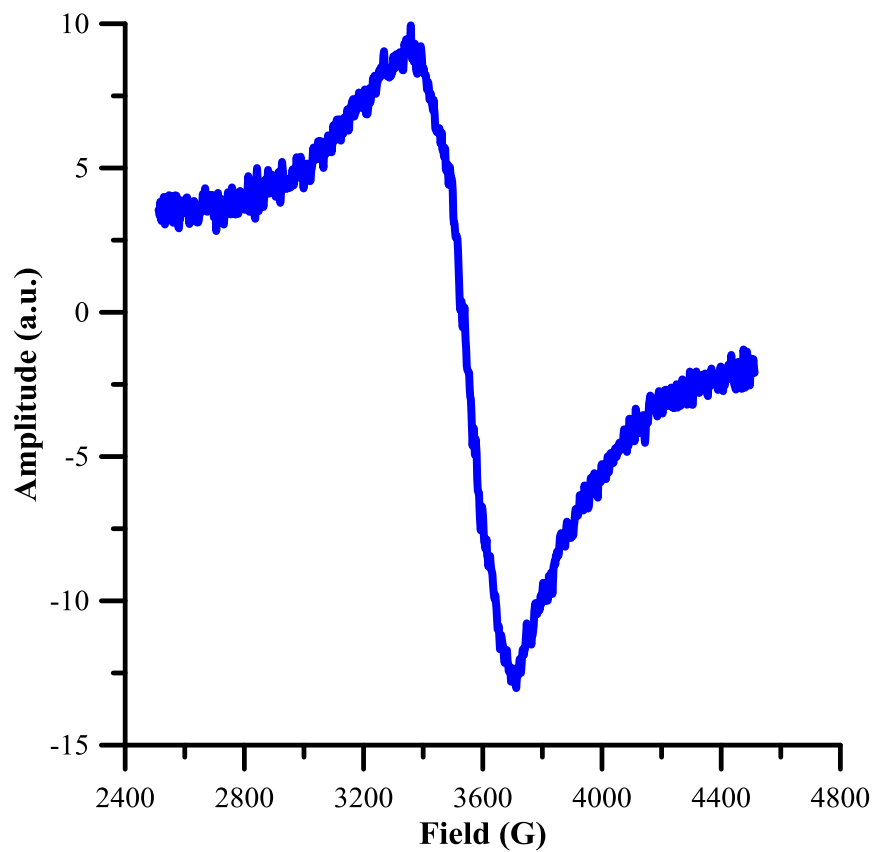


Figure 3.22 X-band (9.84 GHz) CW spectrum of 5 mM Gd(EDTA)⁻ in water at room temperature.

The spectrum was taken with modulation amplitude of 3 G and 2.37 mW power.

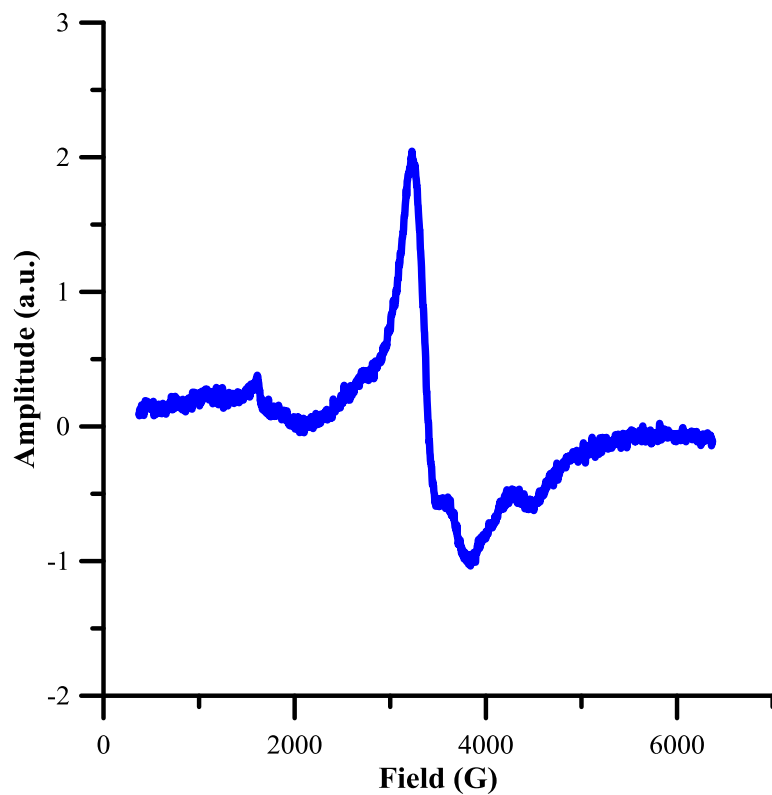


Figure 3.23 X-band (9.84 GHz) CW spectrum of 2 mM Gd(DTPA)²⁻ in water at room temperature.

The spectrum was taken with modulation amplitude of 3 G and 2.37 mW power.

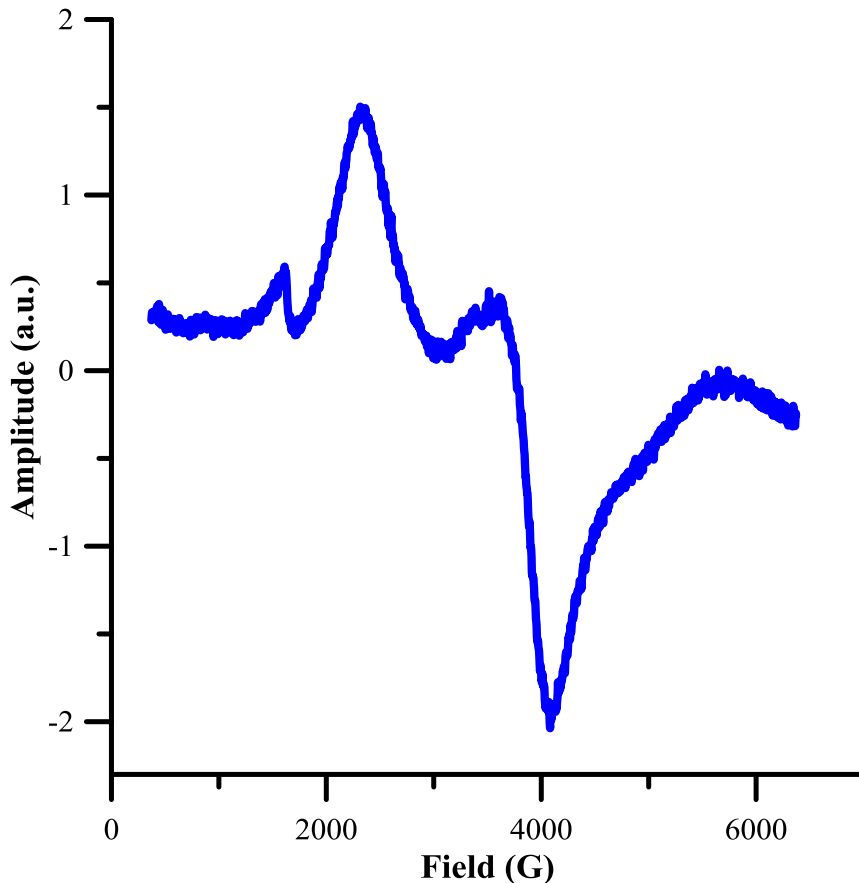


Figure 3.24 X-band (9.84 GHz) CW spectrum of 1 mM Gd(DPA)₃ in water at room temperature.

The spectrum was taken with modulation amplitude of 3 G and 7.56 mW power.

3.4 Overview of Relaxation Times.

A summary of the limited information available for relaxation times of these metals at 5 to 12 K is given in Table 3.3. For Dy³⁺ the relaxation rates are so fast, even at these low temperatures that estimates can only be obtained from the temperature dependent contribution to linewidths. For Er(DTPA)²⁻ 1/T₁ increases by about an order of magnitude between 5 and 7 K. For aquo Co²⁺ and Co(DTPA)³⁺ 1/T₁ increases by about

two orders of magnitude between 5 and 10 K. The strong dependence of relaxation rate on temperature is consistent with observations at lower temperature for these metal ions in ionic lattices [38].

Table 3.2 Temperature dependence of T_1 and T_2 for aquo Gd^{3+} at 9.5 GHz in 1:1 water: glycerol.

Temperature (K)	T_2 (μ s)	T_1 (μ s)
30	2.23	21.6
50	1.09	5.45
70	0.631	1.48

Table 3.3 Overview of Relaxation Times for $Dy(EDTA)^{2-}$, $Er(DTPA)^{2-}$, Co^{2+} and $Co(DTPA)^{3-}$ at 5 to 12 K

Metal Ion	Temperature (K)	T_1 (s)	T_2 (μ s)	Ref.
$Dy(EDTA)^{2-}$	8	2.6×10^{-10}		[32]
	12	1.7×10^{-10}		[32]
$Er(DTPA)^{2-}$	5	5.4×10^{-6} ^a 28×10^{-6}	~ 0.20	
	7	1.3×10^{-6}	~0.10	
Aquo Co^{2+}	5	230×10^{-6}	1.0^b	
	7	17×10^{-6}		
	10	1.5×10^{-6}		
$Co(DTPA)^{3-}$	5	240×10^{-6}	1.2^b	
	7	25×10^{-6}		
	10	2.7×10^{-6}		

^a Biexponential fit. ^b Values of T_2 have substantial uncertainty due to deep proton modulation.

Chapter 4

Effect of Lanthanides and Cobalt Ions on Nitroxide in Mixtures

4.1 Introduction

4.1.1 Intermolecular Effect of Lanthanides and Cobalt ions on the relaxation of nitroxide

A lot of work that has been done on transition metals in the field of EPR, and lanthanides have been studied in the field of NMR more than in EPR. Some of the lanthanides like Dy^{3+} , Gd^{3+} have been studied in EPR but mostly for decreasing power saturation of slowly relaxing radicals and finding distances through DEER, respectively. Most of the lanthanides are fast relaxing as discussed in Chapter 3. At temperatures above about 10 K, their relaxation behavior (other than for Gd^{3+}) cannot be studied directly due to their fast relaxation. Hence, they are studied indirectly by looking at their effects on slow relaxing species. Lanthanides are widely used as shift reagents and in paramagnetic relaxation enhancement experiments in NMR [51]. They have also been used in EPR to reduce the spin-lattice relaxation times of spin probes and spin-labels [5]. According to the Boltzmann distribution, as temperature decreases, the equilibrium nuclear polarization increases, but spin-lattice relaxation times also increase. Lanthanides can speed up solid state NMR experiments by reducing the nuclear spin-lattice relaxation

time (T_{1n}) and various lanthanides work differently in different temperature ranges. They can act as relaxation switches by enhancing relaxation at low temperatures but not on rewarming or dissolution of reagents for dynamic nuclear polarization [51].

In 1969, Leigh did a dipolar interpretation of manganese-nitroxide interactions, and his model was followed by others to explain the interactions between rapidly relaxing metals and slower relaxing radicals. According to his analysis, in the rigid lattice, the interaction is orientation dependent and line broadening is proportional to $\mu_2^2\tau r^{-6}$ where μ_2 , is the metal magnetic moment, τ is the metal electron relaxation time, and r is the distance between the metal and nitroxide electron spins. He also mentioned that for some cases the amplitude of the CW spectrum changes but the lineshape remains the same. His interpretations helped in finding the distances in many proteins [52-54]. However, in Eaton et. al. (1979) [55], it was pointed out that contrary to Leigh's model there was substantial broadening of lines, which can be detected by integrating the first-derivative spectra and calculating the area under the absorption curve.

Dipole-dipole interactions play a larger role than exchange interactions when a fast relaxing metal is present. Rapid metal relaxation averages the dipole-dipole interactions significantly. In the case of an interaction between paramagnetic ions and nitroxide, there is less effect on lineshapes of the nitroxide, than would be seen in an absorption spectrum, because the first-derivative CW lineshape is dominated by the sharpest components.

In some experiments, for example in spin-labeled hemoglobin, iron-nitroxide interactions were quantitated by taking the ratio of the sum of the heights of high- and

low-field lines to the height of the center line of the 3-line nitroxide pattern at 77 K (d_1/d). The value of d_1/d is used to monitor dipolar interaction between the nitroxide label and the iron [52,56].

The dipolar interactions can be calculated by the energy of interactions of two magnetic dipoles at distance r .

$$U = \mu_1\mu_2/r^3 \quad 4.1$$

Where μ_1 and μ_2 are the magnetic moments of dipole 1 and dipole 2 and r is the distance between the two dipoles.

The interaction depends on the orientation of the two dipoles so equation 4.1 can be rewritten as-

$$U = \mu_1\mu_2/r^3 (1-3\cos^2\theta) \quad 4.2$$

Where θ is the angle between the external magnetic field and the line joining the two dipoles. The methods that calculate the changes in spin-lattice rates depend on the square of the dipolar interactions and hence depend on r^{-6} [57]. The Solomon-Bloembergen theory (1956) is used to describe the interaction between two paramagnetic centers.

Bloembergen's model [58] as written by Abragam [59] is as follows-

$$\frac{1}{T_{1s}} = \frac{1}{T_{1s}^0} + S(S+1) \left[\frac{b^2 T_{2f}}{1+(\omega_f-\omega_s)^2 T_{2f}^2 + b^2 T_{1f} T_{2f}} + \frac{c^2 T_{1f}}{1+\omega_s^2 T_{1f}^2} + \frac{e^2 T_{2f}}{1+(\omega_f+\omega_s)^2 T_{2f}^2} \right] \quad 4.3$$

B term
C term
E term

$$b^2 = \frac{8}{3} \left[\frac{-J}{2} - \frac{1}{4} g_s g_f \beta^2 \frac{1-3\cos^2\theta}{hr^3} \right]^2$$

$$c^2 = 3g_s^2 g_f^2 \beta^4 \frac{\sin^2\theta \cos^2\theta}{h^2 r^6}$$

$$e^2 = \frac{3}{2} g_s^2 g_f^2 \beta^4 \frac{\sin^4\theta}{h^2 r^6}$$

where f is fast relaxing spins and s is slow relaxing spins, T_{1s}^0 is T_1 of the slow relaxing species in the absence of interaction, T_{1s} is the T_1 of the slow relaxing species in the presence of interaction, S is the electron spin of fast relaxing center, ω_s and ω_f are the resonant frequencies of slow and fast relaxing spins, respectively, r is the distance between the two spins, J is the electron- electron exchange interaction and θ is the angle between the line joining the two spins and the external field. All the three B, C and E terms are in terms of magnetic moments [60]. One more thing which is important is the product of relaxation time T_1 for the second center and the difference between the resonance frequencies of the two spins ($\Delta\omega$). The second spin interacts with the permanent dipole, when $\Delta\omega^2 T_1^2 \gg 1$ and the interaction is considered weak due to fast relaxation when $\Delta\omega^2 T_1^2 \ll 1$ [28].

The expression given for the pairs that have slow relaxing species with long T_{2s} and T_{1s} and fast relaxing species characterized by $T_{1f}\mu_f/r^3 \ll 1$ is-

$$\Delta \frac{1}{T_{1s}} = \frac{1}{T_{1s}} - \frac{1}{T_{1s}^0} = \frac{\mu_f^2 \gamma^2}{6r^2 T_{1f}^2} \left[\frac{24}{5(\omega_f + \omega_s)^2} + \frac{12}{5\omega_s^2} + \frac{4}{5(\omega_f - \omega_s)^2} \right] \quad 4.4$$

$$\Delta \frac{1}{T_{2s}} = \frac{1}{T_{2s}} - \frac{1}{T_{2s}^0} = \frac{4\mu_f^2 \gamma^2}{15r^6} T_{1f} \quad 4.5$$

All the parameters have the same meaning as in the earlier equations. The effect of fast relaxing metal on the T_{1s} of the slow relaxing species is maximum when $1/T_{1f}$ is equal to the Larmor frequency ($2\pi\nu$) of the slow relaxing species. It can also be maximized if $1/T_2$ of the fast relaxing metal is equal to the difference of the Larmor frequencies of two species [57]. The assumption in equations 4.4 and 4.5 is $T_{1f} = T_{2f}$, $(\omega_f - \omega_s)^2 T_{1f}^2 \gg 1$ and $\omega_s^2 T_{1f}^2 \gg 1$ [13,52]. According to Ref. [60], the three terms reduced to –

$$\frac{1}{2} \left(\frac{T_{1f}}{1 + (\omega_f - \omega_s)^2 T_{1f}^2} \right) : \frac{3}{2} \left(\frac{T_{1f}}{1 + \omega_s^2 T_{1f}^2} \right) : 3 \left(\frac{T_{1f}}{1 + (\omega_f + \omega_s)^2 T_{1f}^2} \right) \quad 4.6$$

These terms explain the behavior of lanthanides as relaxing agents. When the g-value of the metals is high, the C term dominates. If $\omega \approx T_{1f}^{-1} \approx \frac{1}{3} \omega_f$, the ratio of the three terms will be $\frac{1}{10} : \frac{3}{4} : \frac{3}{17}$ and this is what happened in case of Dy^{3+} and Tm^{3+} in Ref. [28]. The metals are arranged in a sequential order in Table 1 of Ref. [28] based on the $P_{1/2}$ values for the radical interacting with the metal. Dy^{3+} and Tm^{3+} are in the middle of the sequence. For the metals listed below Dy^{3+} and Tm^{3+} in the sequence, the last term dominates, for example Pr^{3+} , and they don't act as good relaxing agents. For metals above Dy^{3+} and Tm^{3+} in the sequence, such as Gd^{3+} , the B term dominates. Gd^{3+} has a slow relaxation rate as compared to other lanthanides and hence it is not as good relaxing agent [28, 60].

Likhtenshtein proposed that the dipole-dipole interactions increase $1/T_2$ and $1/T_1$ by the same amount, but $1/T_1$ is more sensitive to the increment because for a slowly relaxing radical in the slow tumbling regime $T_2 \ll T_1$ and thus $1/T_2 \gg 1/T_1$ [61]. The

fast relaxation of metals usually has negligible effect on T_2 and has more effect on T_1 . However, there are additional contributions to $1/T_{2s}$ that are significant when the relaxation rate of the fast relaxing metal is comparable to the dipolar interaction between the two paramagnetic centers [62,63], which is much slower than the rates required for the maximum impact on $1/T_{1s}$. This enhancement of $1/T_{2s}$ has been demonstrated for spin-labeled low-spin iron porphyrins [62], spin-labeled metmyoglobin [64] and spin-labeled myoglobin [65].

The paramagnetic effects of metals on nitroxides can be studied through CW power saturation curves and through relaxation studies. CW power saturation curves depend on the product of T_2 and T_1 , relaxation studies can monitor the two parameters independently [5,6, and 52]. The power saturation of spin labels attached to hemes to find the iron- nitroxide interactions has been shown in Refs. [52,66].

Eq. 4.1 has been proposed as a model to explain the effect of paramagnetic ion. According to Van Vleck et. al. [67], dipolar Hamiltonian was calculated using method of moments. All the moments are concentration dependent, therefore $P_{1/2}$ and relaxation times would be concentration dependent [20,60].

Hyde and Sarna (1978) [68] measured T_1 and T_2 for nitroxide colliding with Cu^{2+} as well as Gd^{3+} and other lanthanides in fluid solution. The three magnetic interactions between nitroxide and paramagnetic metal that one might consider are Heisenberg exchange, dipolar contributions to the spin-lattice relaxation probability and secular dipolar contributions to the linewidth. Hyde and Sarna concluded that the interaction

between Cu^{2+} and nitroxide is predominantly Heisenberg exchange, but that dipole-dipole spin relaxation is the major contribution to broadening of nitroxide in collisions with Gd^{3+} . According to their article, exchange between fast and slow relaxing species contributes equally to T_1 and T_2 . The transition metals and lanthanides show different kinds of interaction with nitroxide radical because of their electronic configurations. Cu^{2+} and Gd^{3+} complexes have about the same rotational correlational times but $S(S+1)$ for Gd^{3+} is greater by a factor of 21. The greater $S(S+1)$ value of Gd^{3+} is due to the number of unpaired electrons. The smaller contribution from exchange interaction for Gd^{3+} is due to the f-orbital contraction for the lanthanides and the fact that the unpaired electrons in a collision are protected by 5s and 5p electrons. An additional contribution might be that the efficiency of collisions leading to Heisenberg exchange is decreased for Gd^{3+} because of steric effects associated with molecules coordinated to the metal ion [68].

This chapter reports my studies of the relaxation effect of lanthanides on nitroxide. The effect of Dy^{3+} , Er^{3+} , Gd^{3+} , Tm^{3+} (and Co^{2+}) in the range of 1 to 30 mM on the relaxation times of 0.2 mM tempone (2, 2, 6, 6-tetramethyl-4-oxo-piperidin-1-oxyl) in 1:1 water: glycerol at pH 6 was studied. The metal ions were selected on the basis of the $P_{1/2}$ values given by Sarna, Hyde, and Swartz, where the larger $P_{1/2}$ means a larger effect of the metal ions on the radical relaxation [28]. Nitroxide T_1 and T_2 in the presence and absence of paramagnetic metal ions were measured by inversion recovery and spin echo dephasing, respectively, between 10 and 295 K.

Another aim of the project was to look for the best metal ion that can increase the spin-lattice relaxation rate with minimal impact on spin-spin relaxation rate. Nitroxide

spin labels are used in DEER experiments for determining distances between two unpaired electrons in biomolecules. DEER is usually done at 80K to maximize nitroxide T_2 and still be able to use liquid nitrogen instead of liquid helium. At this temperature, the motion of the methyl groups in the spin label has relatively little impact on T_2 [69,70]. In DEER, the signal intensity is weak. A lot of signal-averaging time is required to get high enough signal-to-noise for accurate distance distributions. $1/T_1$ limits the pulse repetition rate for the averaging and metal ions can increase the spin-lattice relaxation rate. $1/T_2$ controls the intensity of the DEER signal; and, hence, we don't want any decrease in the spin-spin relaxation rate after the addition of metal ions.

Addition of an appropriate metal ion could permit more averaging in less time and ultimately improve the signal to noise ratio in DEER experiments.

4.2 Experimental Details

4.2.1 Preparation of samples

The stock solutions of metal ions and their complexes were prepared using the same method as in section 3.2.1 of chapter 3. The samples were prepared by mixing appropriate quantities of metal ions or their complexes with a solution of tempone to achieve a final concentration of 0.2 mM tempone. The solvent was a 1:1 water: glycerol mixture which forms a glass when cooled quickly.

4.2.2 Pulsed EPR measurement of electron spin relaxation times at 10 to 80 K

Pulsed EPR experiments were performed at 10 to 200 K at X-band (9.5 GHz) with the same procedure as mentioned in section 3.2.2 of chapter 3. Q-band was performed on a Bruker E580 spectrometer with an ER5107D20602 dielectric resonator. The initial time for data acquisition for both X- and Q- band was 200 ns.

The T_2 decays were fitted using the Bruker Xepr software. The inversion recovery curves were fitted using the uniform penalty method UPEN analysis. UPEN analysis gives the distribution of relaxation times, T_1 [71,72]. The relaxation times distribution is wide, so the median value is reported in this chapter.

Pulse experiments were also done on syntaxin protein labeled with nitroxide with different concentrations of Dy^{3+} , Er^{3+} , $Dy(DTPA)^{2-}$ and $Er(DTPA)^{2-}$. DEER experiments were done on samples prepared by Virginia Meyer and Hilary Weismiller, working in the laboratory of Dr. Martin Margittai at the University of Denver.

4.3 Effect of the lanthanides on the relaxation of tempone

4.3.1 Effect of the rapidly relaxing metals on the spin-lattice relaxation of tempone

The temperature dependence of the spin-lattice relaxation rates ($1/T_1$) for tempone in 1:1 water:glycerol (Figures 4.1- 4.5) is similar to that reported in Ref. [73]. Between about 20 and 100 K the Raman process dominates. As temperature is increased above

100 K, there is increasing contribution from a local mode [73]. Addition of 30 mM Dy^{3+} , Er^{3+} , Tm^{3+} , or Co^{2+} enhances the tempone relaxation over the full range of temperatures studied (Figure 4.1). At X-band (9.5 GHz) the maximum enhancement occurs when $T_{1f} \sim 1.7 \times 10^{-11}$ s (see discussion of Eq. 4.3) and is observed for these metal ion:tempone mixtures at about 35 K for Dy^{3+} , about 40 K for Er^{3+} and about 80 K for Co^{2+} (Figure 4.1). The maximum spin-lattice enhancement increases in the order $\text{Co}^{2+} \sim \text{Er}^{3+} < \text{Dy}^{3+} < \text{Tm}^{3+}$. (Equation 4.3) predicts dependence on g_f . For lanthanides strong spin-orbit coupling means that S is not a good quantum number, so J is also a factor in the relaxation enhancement. For each of these metals the g values are highly anisotropic. The predicted relaxation enhancement (Eq. 4.3) is inversely proportional to r^6 , which is proportional to the square of the dipolar interaction. For a random mixture of ions in solution, r^3 is inversely proportional to concentration, so the relaxation enhancement is predicted to be proportional to the square of the concentration of the paramagnetic ion. The dependence of relaxation enhancement on the square of the concentration has been confirmed for Dy^{3+} [23]. The temperature dependence of the spin-lattice relaxation for 0.2 mM tempone for various concentrations of added metal ions is shown in Figure 4.2 for Dy^{3+} , in Figure 4.3 for Er^{3+} , in Figure 4.4 for Tm^{3+} , and in Figure 4.5 for high-spin Co^{2+} . Analogous data over the limited temperature range of 80 to 200 K are in Figure 4.4 for Tm^{3+} . For each of the metals the relaxation enhancement for tempone increases approximately quadratically with the concentration of the metal ion, as predicted.

It has been shown previously that the half width of an Fe-S signal increased with the decrease in temperature and the increase in concentration of $\text{Dy}(\text{EDTA})^{2-}$ [32]. We

did not see any change in the linewidths of the nitroxide though the linewidth is dominated by the sharpest components. Also, at temperatures below about 80 K the T_1 for nitroxides becomes very long, which makes it difficult to record lineshapes that are free from passage effects.

In Refs. [21,74], they showed that $P_{1/2}$ is linearly dependent on the concentration of $\text{Dy}(\text{EDTA})^{2-}$ and in Ref. [74], derived T_1 from $P_{1/2}$ for nitrogenase by assuming constant T_2 . The relaxation enhancements of tempol by Dy^{3+} were checked in Refs. [24,75]. However, Er^{3+} has not been used as a relaxing agent in other labs. Our findings are consistent with the expectation that relaxation enhancement depends on the concentration of the paramagnetic metal and on temperature [28,60].

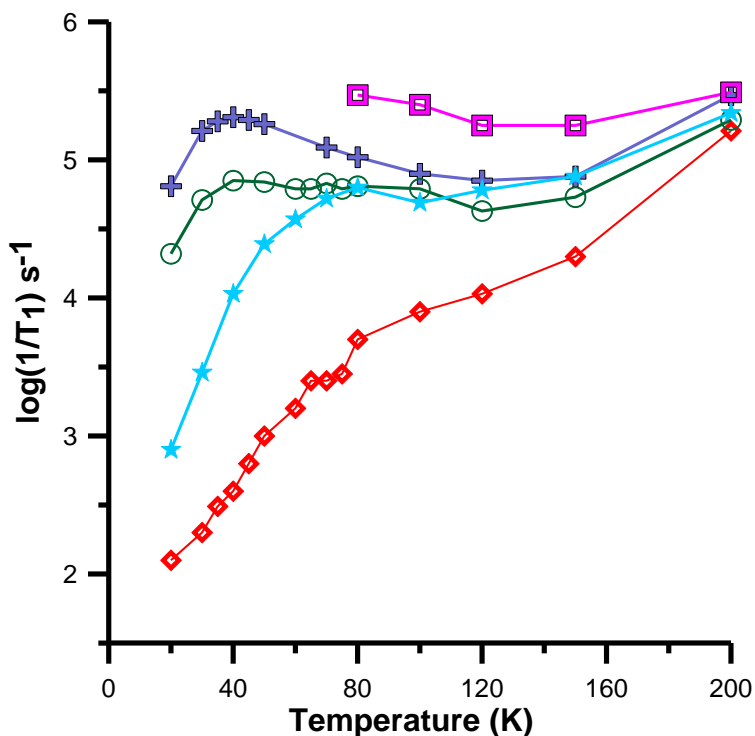


Figure 4.1 Effect of metals on the spin-lattice relaxation rate for 0.2 mM tempone.

The effect of 30 mM Dy^{3+} (\blacktriangle), 30 mM Er^{3+} (\circ), 30 mM Tm^{3+} (\square), 30 mM Co^{2+} (\star) on the spin-lattice relaxation rate for 0.2 mM tempone (\diamond) in 1:1 water:glycerol as a function of temperature at X-band. Uncertainty in relaxation times is about 10%. The lines connect the points.

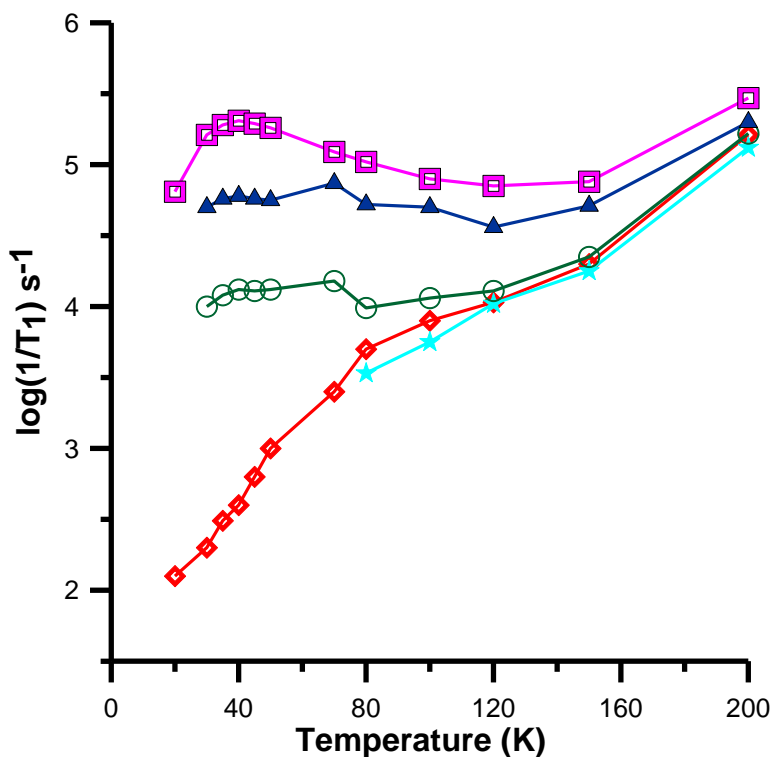


Figure 4.2 Concentration dependence of the effect of Dy^{3+} on the spin-lattice relaxation for 0.2 mM tempone as a function of temperature at X-band.

The sample was dissolved in 1:1 water: glycerol and the concentrations of Dy^{3+} are 0.0 mM (\diamond), 1 mM (\star), 10 mM (\circ), 20 mM (\blacktriangle) and 30 mM (\square). Uncertainty in relaxation times is about 10%. The lines connect the points.

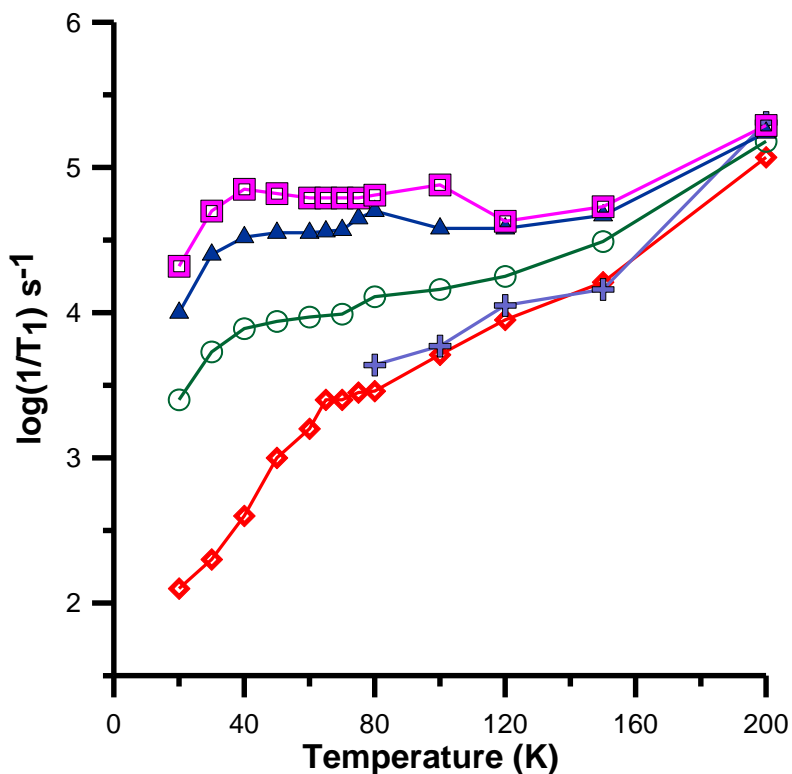


Figure 4.3 Concentration dependence of the effect of Er^{3+} on the spin-lattice relaxation for 0.2 mM tempone as a function of temperature at X-band.

The sample was dissolved in 1:1 water:glycerol and the concentrations of Er^{3+} are 0.0 mM (◇), 5 mM (+), 10 mM (○), 20 mM (▲) and 30 mM (◻). Uncertainty in relaxation times is about 8%. The lines connect the data points.

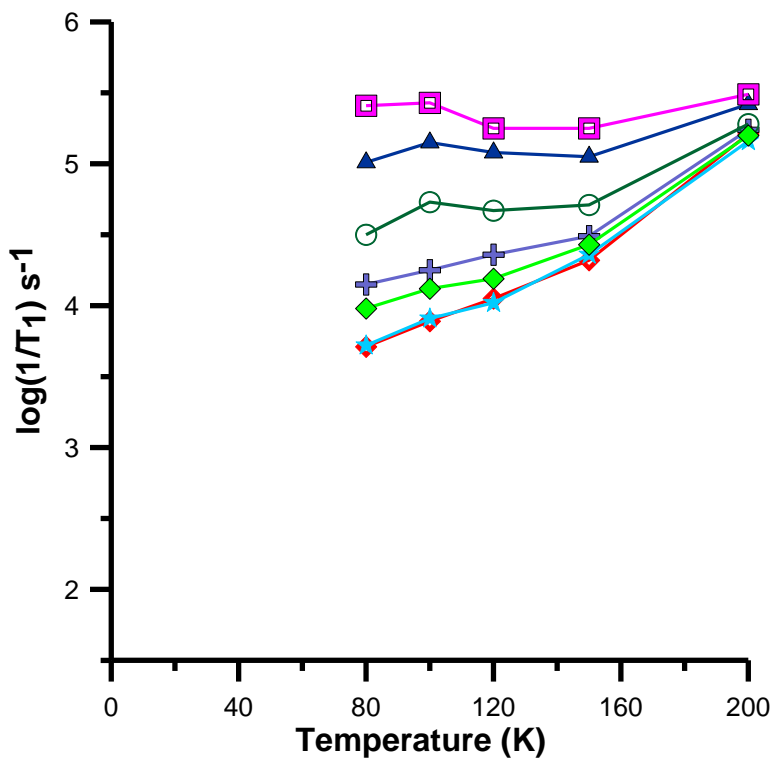


Figure 4.4 Concentration dependence of the effect of Tm^{3+} on the spin-lattice relaxation for 0.2 mM tempone as a function of temperature at X-band.

The sample was dissolved in 1:1 water:glycerol and the concentrations of Tm^{3+} are 0.0 mM (◇), 1 mM (★), 3 mM (◆), 5 mM (⊕), 10 mM (○), 20 mM (▲) and 30 mM (◻). Uncertainty in relaxation times is about 10%. The lines connect the points.

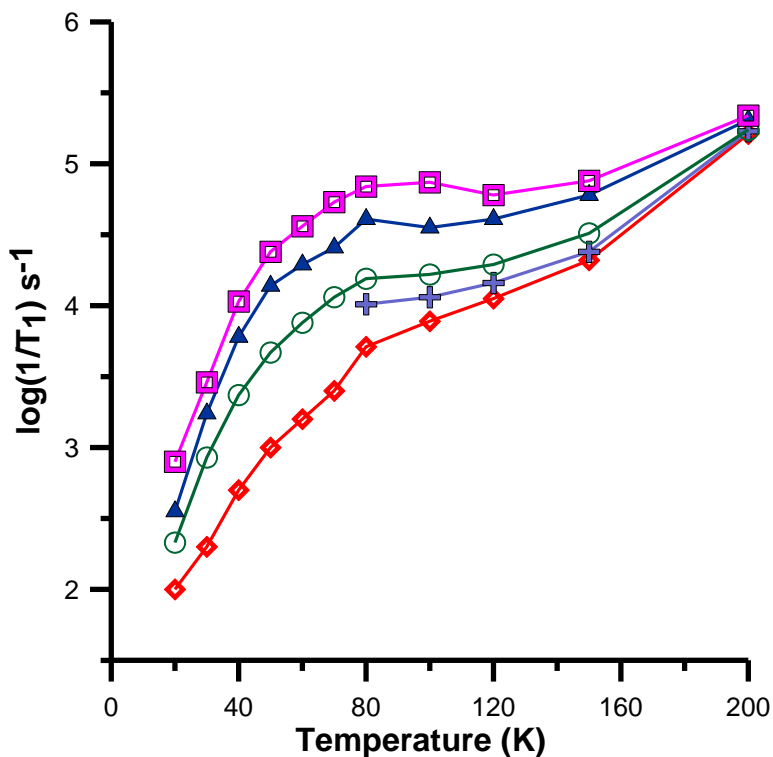


Figure 4.5 Concentration dependence of the effect of Co^{2+} on the spin-lattice relaxation for 0.2 mM tempone as a function of temperature at X-band.

The sample was dissolved in 1:1 water: glycerol and the concentrations of Co^{2+} are 0.0 mM (◇), 5 mM (+), 10 mM (○), 20 mM (▲), and 30 mM (◻). Uncertainty in relaxation times is about 7%. The lines connect the data points.

4.3.2 Effect of the rapidly relaxing metal ions on the spin-spin relaxation of tempone.

The spin-spin relaxation rate ($1/T_2$) for the nitroxide tempone in 1:1 water: glycerol and its dependence on temperature (Figure 4.6- 4.10) are similar to that reported in Ref. [76]. Below about 80 K the relaxation rate is independent of temperature. The echo decay curves below 80 K were fitted with stretched exponentials with $x = 2.3$, which is characteristic of dephasing dominated by nuclear spin diffusion [76]. As the temperature is increased above about 80 K the increasingly rapid rotation of the gem

dimethyl groups enhances spin echo dephasing. Above 80 K the decay curves were fitted with $x = 1$, which is a simple exponential fit, and is characteristic of dephasing that is dominated by a dynamic process that is occurring on the timescale of the spin echo experiment. The effect of different metals on the stretch exponent (x) can be seen in Table 4.2 to 4.5. Enhancement of $1/T_2$ for tempone above about 40 K by the paramagnetic ions is relatively modest (Figures 4.6 – 4.8 and 4.10). For the solutions containing 30 mM metal ions the maximum enhancement of $1/T_2$ above about 40 K is less than a factor of 2. As noted in the introduction to this chapter, $1/T_2$ in this temperature range is much larger than $1/T_1$, so contributions to relaxation that are described by eq. (4.3) are much smaller fractions of $1/T_2$ than of $1/T_1$. Furthermore, the dependence of the enhancement on the concentration of the metal ion between about 40 and 80 K (Figures 4.6 – 4.8, 4.10) is approximately linear in concentration, which suggests that the dominant contribution is different than for $1/T_1$. The enhancement of $1/T_2$ by Dy^{3+} , Er^{3+} and Co^{2+} increases as the temperature is decreased below about 40 K. It is proposed that the mechanism of this enhancement in $1/T_2$ for tempone is similar to that observed for nitroxides in spin-labeled hemoglobins and iron porphyrins [62,64,77]. This enhancement is largest when the metal relaxation rate is comparable to the dipolar interaction between the metal and the nitroxide. In random solutions of metal ions and tempone, this maximum will be broad because of the wide distribution in metal-radical distances. Because of the very fast metal relaxation rates, the tempone dephasing experiments would need to be extended to temperatures much less than 10 K to define the temperature for the maximum effect on $1/T_2$.

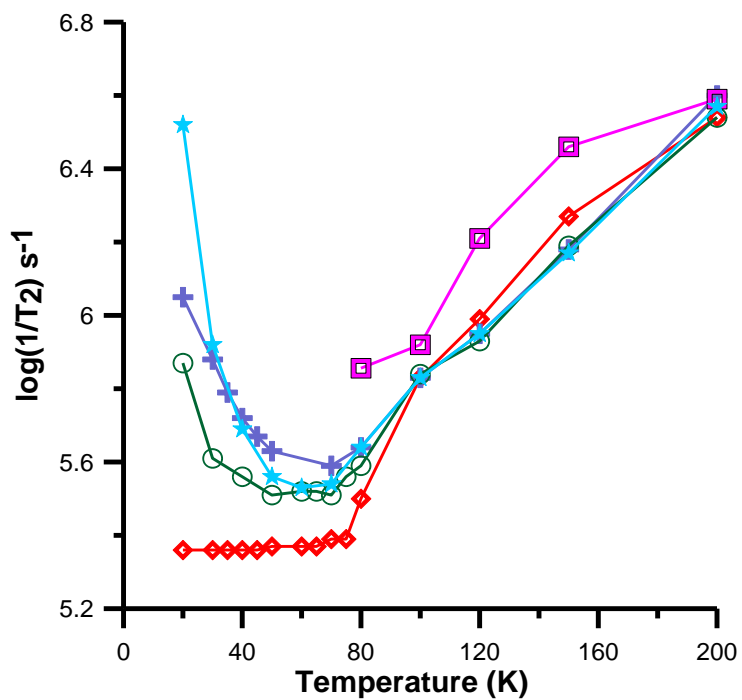


Figure 4.6 Effect of metals on the spin-lattice relaxation rate for 0.2 mM tempone.

The effect of 30 mM Dy³⁺ (+), 30 mM Er³⁺ (○), 30 mM Tm³⁺ (□), and 30 mM Co²⁺ (★) on the spin-spin relaxation for 0.2 mM tempone (◇) in 1:1 water: glycerol as a function of temperature at X-band. Uncertainty in relaxation times is about 5%. The lines connect the data points.

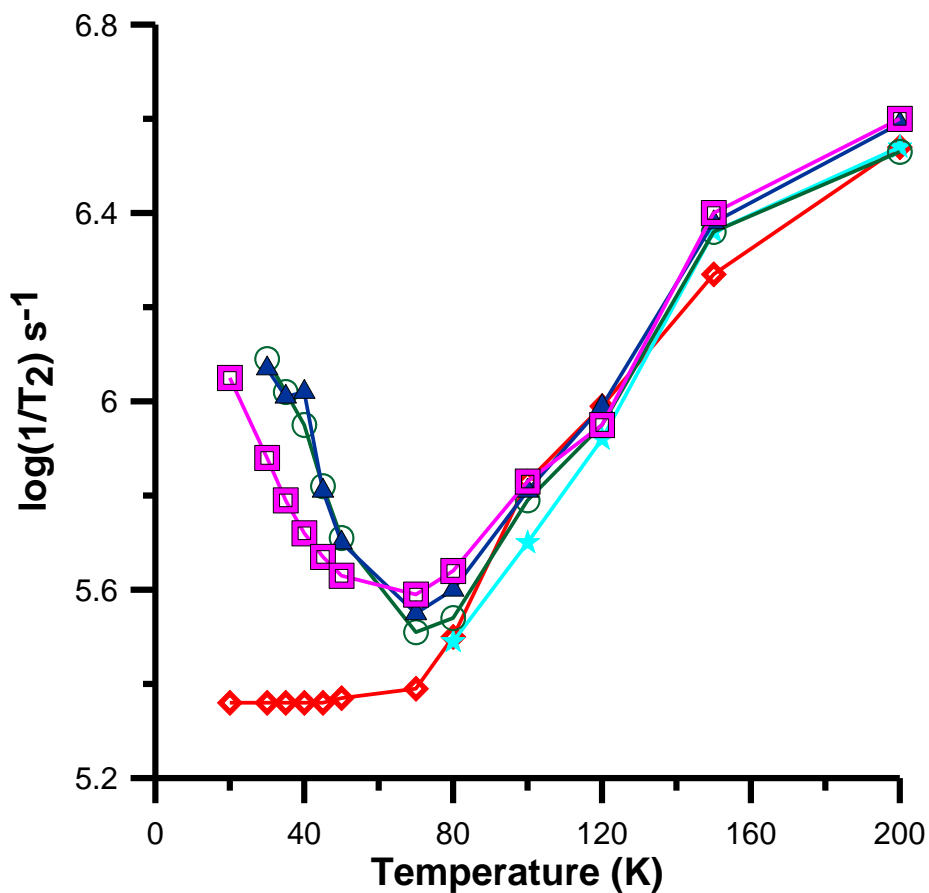


Figure 4.7 Concentration dependence of the effect of Dy^{3+} on the spin-spin relaxation for 0.2 mM tempone as a function of temperature at X-band.

The sample was dissolved in 1:1 water:glycerol and the concentrations of Dy^{3+} are 0 mM (\diamond), 1 mM (\star), 10 mM (\circ), 20 mM (\blacktriangle), and 30 mM (\blacksquare). Uncertainty in relaxation times is about 5%. The lines connect the data points.

Table 4.1 Concentration and temperature dependence of stretched exponential parameter x for solutions of 0.2 mM tempone and Dy^{3+}

Temperature (K)	Tempone	+ 1 mM Dy^{3+}	+ 10 mM Dy^{3+}	+ 20 mM Dy^{3+}	+ 30 mM Dy^{3+}
20-70	2.3		1-1.5	1- 1.37	1
80	1.58	1.59	1.42	1.22	1.16
100- 200	1	1	1	1	1

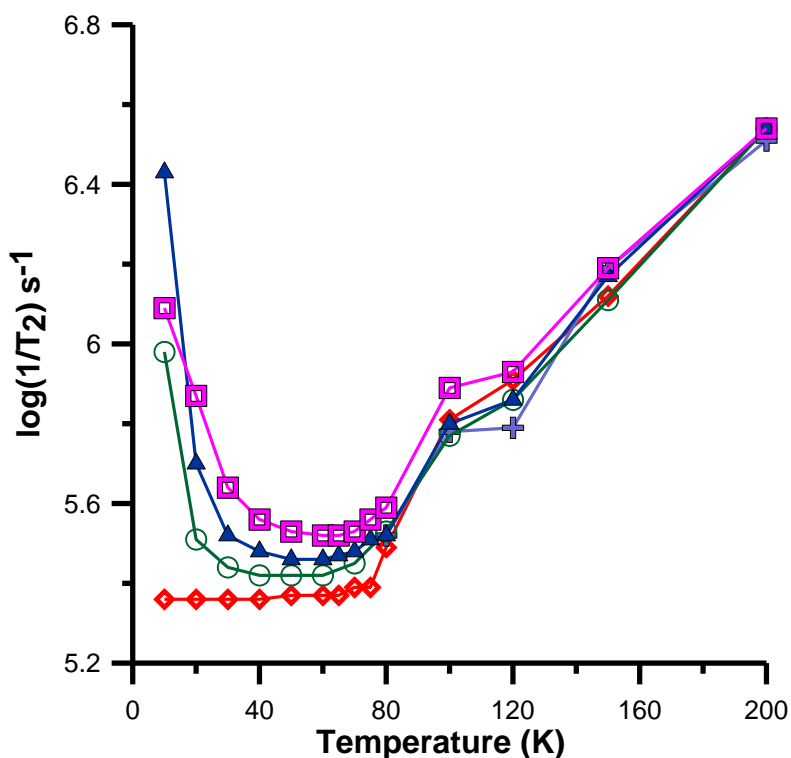


Figure 4.8 Concentration dependence of the effect of Er^{3+} on the spin-spin relaxation for 0.2 mM tempone as a function of temperature at X-band.

The sample was dissolved in 1:1 water:glycerol and the concentrations of Er^{3+} are 0 mM (\diamond), 5 mM ($+$), 10 mM (\circ), 20 mM (\blacktriangle), and 30 mM (\blacksquare). Uncertainty in relaxation times is about 5%. The lines connect the data points.

Table 4.2 Concentration and temperature dependence of stretched exponential parameter x for solutions of 0.2 mM tempone and Er^{3+}

Temperature (K)	Tempone	+ 5 mM Er^{3+}	+ 10 mM Er^{3+}	+ 20 mM Er^{3+}	+ 30 mM Er^{3+}
20-70	2.3			1.1- 1.6	1- 1.4
80	1.58	1.46	1.46	1.62	1.25
100- 200	1	1	1	1	1

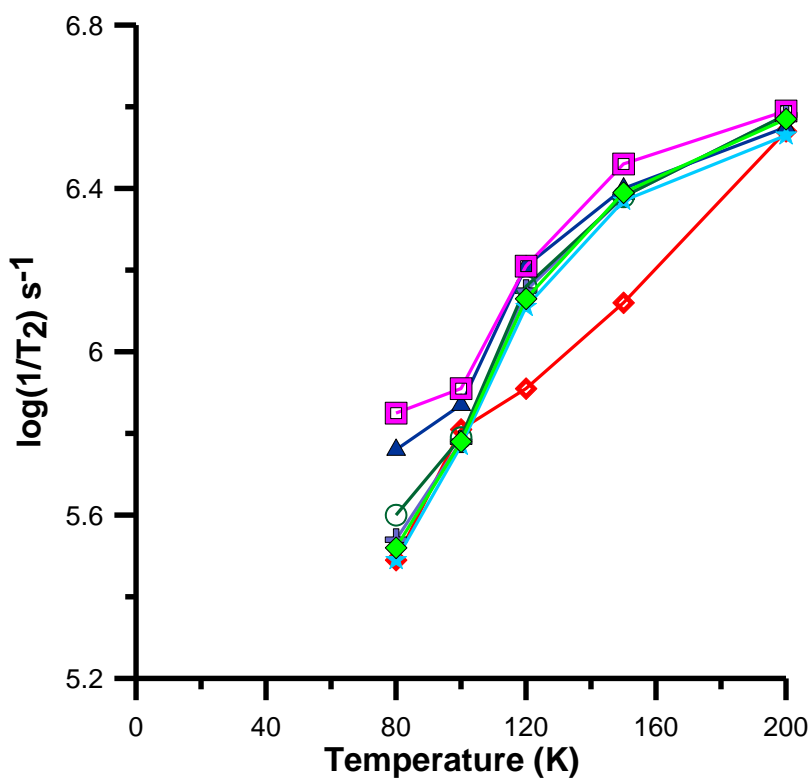


Figure 4.9 Concentration dependence of the effect of Tm^{3+} on the spin-spin relaxation for 0.2 mM tempone at X-band.

The sample was dissolved in 1:1 water:glycerol and the concentrations of Tm^{3+} are 0.0 mM (\blacklozenge), 1 mM (\blackstar), 3 mM (\blacklozenge), 5 mM (\blackplus), 10 mM (\bigcirc), 20 mM (\blacktriangle) and 30 mM (\blacksquare). Uncertainty in relaxation times is about 10%. The lines connect the points.

Table 4.3 Concentration and temperature dependence of stretched exponential parameter x for solutions of 0.2 mM tempone and Tm^{3+}

Temperature (K)	tempone	+ 1 mM Tm^{3+}	+ 3 mM Tm^{3+}	+ 5 mM Tm^{3+}	+ 10 mM Tm^{3+}	+ 20 mM Tm^{3+}	+ 30 mM Tm^{3+}
80	1.58	1.58	1.51	1.41	1.19	1.01	1.03
100- 200	1	1	1	1	1	1	1

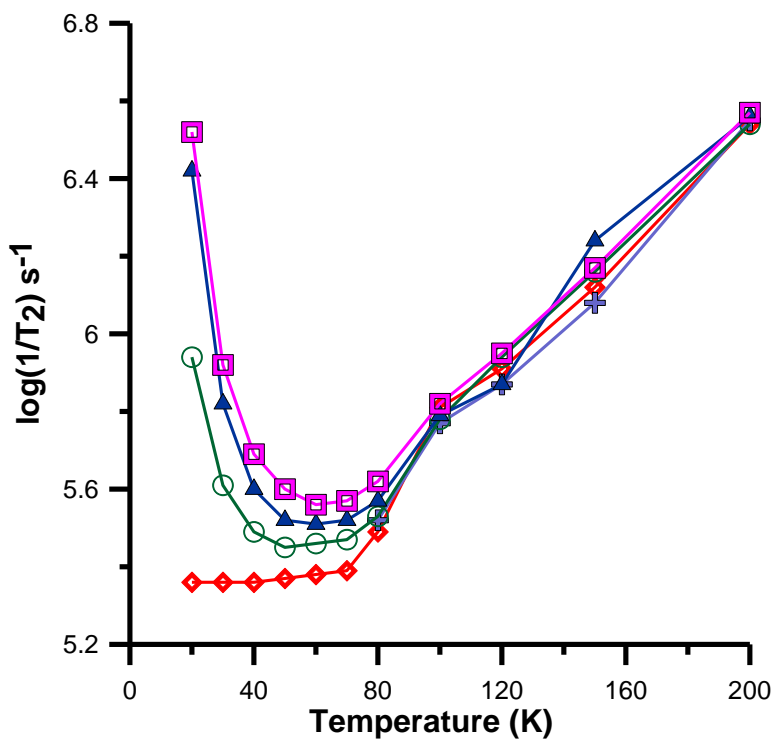


Figure 4.10 Concentration dependence of the effect of Co^{2+} on the spin-spin relaxation for 0.2 mM tempone as a function of temperature at X-band.

The sample was dissolved in in 1:1 water:glycerol and the concentrations of Co^{2+} are 0 mM (\blacklozenge), 5 mM (\blackplus), 10 mM (\bullet), 20 mM (\blacktriangle), and 30 mM (\blacksquare). Uncertainty in relaxation times is about 5%. The lines connect the data points.

Table 4.4 Concentration and temperature dependence of stretched exponential parameter x for solutions of 0.2 mM tempone and Co^{2+}

Temperature (K)	Tempone	+ 5 mM Co^{2+}	+ 10 mM Co^{2+}	+20 mM Co^{2+}	+ 30 mM Co^{2+}
20-70	2.3		1-1.67	1-1.48	1-1.34
80	1.58	1.49	1.45	1.33	1.23
100- 200	1	1	1	1	1

4.3.3 Effect of Lanthanides and their complexes on the spin-lattice relaxation of nitroxide at X-band and Q-band

When $\text{Dy}(\text{DTPA})^{2-}$ is added in place of aquo Dy^{3+} the temperature for the maximum enhancement of the tempone relaxation shifts from about 35 K to about 80 K (Figure 4.11), but the magnitude of the maximum enhancement is unchanged. The relaxation enhancements are similar at X-band and Q-band. These observations suggest that the relaxation rates for the metal in the DTPA complex are substantially slower than for the aquo complex. The relaxation enhancement of a spin label by Dy^{3+} coordinated to the cyclic polydentate chelator DOTA (1,4,7,10-tetraaacyclododecane-1,4,7,10-tetraacetic acid) was maximum at about 80 K [75], which is similar to the maximum shown in Figure 4.11 for $\text{Dy}(\text{DTPA})^{2-}$. In an earlier paper it was reported that the maximum relaxation enhancement for $\text{Dy}(\text{DOTA})^-$ was at about 40 K [24]. However, in Ref. [24] it was stated that the Dy^{3+} and DOTA were mixed several hours prior to performing experiments. Since the rate of reaction of Dy^{3+} with DOTA is relatively slow [78], conversion to the complex may not have been complete. The maximum effect at about 40 K reported in Ref. [24] is similar to the maximum at about 35 K that was observed in our studies for aquo Dy^{3+} . When $\text{Er}(\text{DTPA})^{2-}$ is added to tempone in place of Er^{3+} , the maximum enhancement again shifts to higher temperature (Figure 4.12), which indicates slower relaxation of the metal ion in the DTPA complex than for the aquo ion. In addition, the magnitude of the maximum enhancement is smaller for the complex than for the aquo ion, which may reflect changes in effective g values. For Er^{3+} and

Er(DTPA)²⁻ the relaxation enhancement is similar at X and Q-band at 80 to 150 K (Figure 4.12).

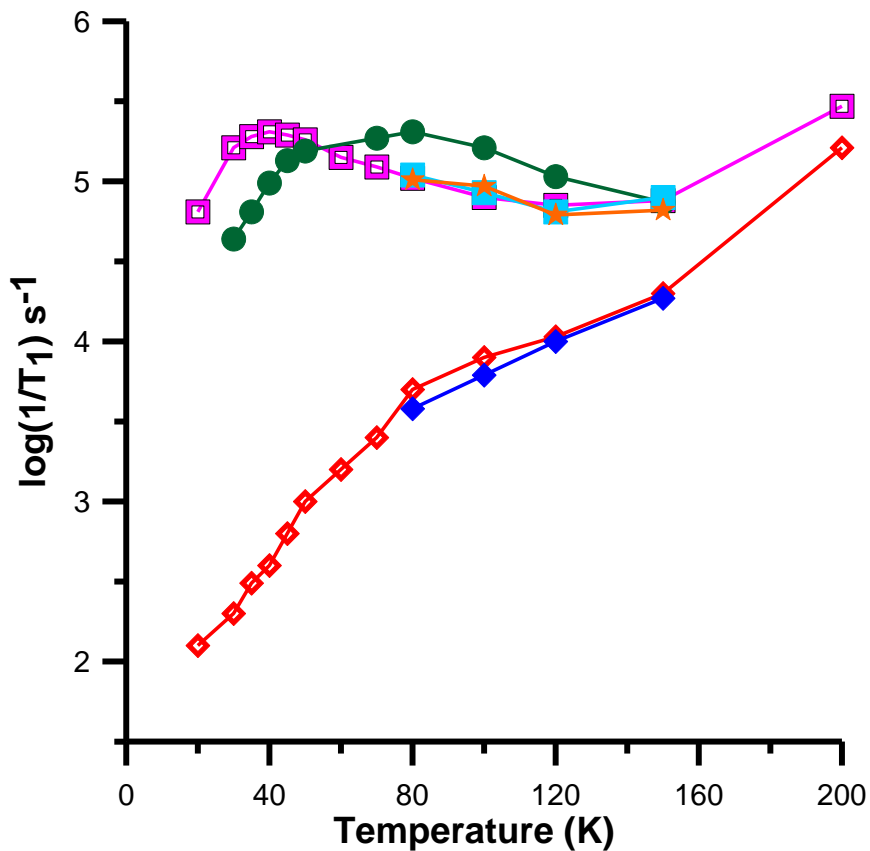


Figure 4.11 Effect of Dy^{3+} and its complex on spin-lattice relaxation rate of nitroxide at X- and Q-band as a function of temperature.

The effect of 30 mM Dy^{3+} (\square), 30 mM Dy(DTPA)^{2-} (\bullet) on nitroxide at X-band (\diamond) and 30 mM Dy^{3+} (\star) and 30 mM Dy(DTPA)^{2-} (\blacksquare) on nitroxide at Q-band (\blacklozenge) spin-lattice relaxation rate ($\log(1/T_1)$) as a function of temperature. Uncertainty is about 8%.

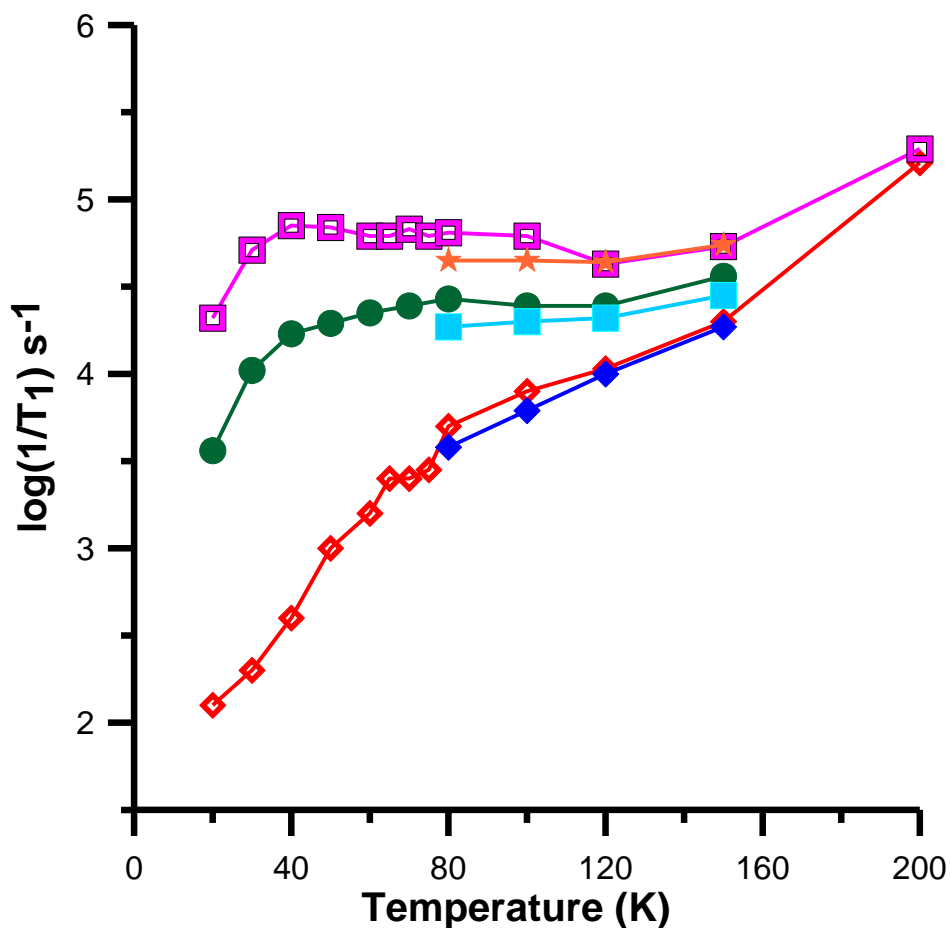


Figure 4.12 Effect of Er^{3+} and its complex on spin-lattice relaxation rate of nitroxide at X- and Q-band as a function of temperature.

The effect of 30 mM Er^{3+} (■), 30 mM $\text{Er}(\text{DTPA})^{2-}$ (●) on nitroxide at X-band (◇) and 30 mM Er^{3+} (★) and 30 mM $\text{Er}(\text{DTPA})^{2-}$ (■) on nitroxide at Q-band (◆) spin-lattice relaxation rate ($\log(1/T_1)$) as a function of temperature. Uncertainty is about 9%.

4.3.4 Effect of Lanthanides and their complexes on the spin-spin relaxation of nitroxide at X-band and Q-band

When $\text{Dy}(\text{DTPA})^{2-}$ is added to tempone in place of aquo Dy^{3+} the enhancements in $1/T_2$ at low temperature are shifted to higher temperature than for Dy^{3+} (Figure 4.13). Analogous to the observations for the enhancements of $1/T_1$ this shift suggests that

relaxation rates are slower for the metal in the DTPA complex than in the aquo ion. When Er(DTPA)^{2-} is added in place of aquo Er^{3+} (Figure 4.14) the enhancement of $1/T_2$ for tempone is decreased, which again is similar to the impact of complexation on the enhancement of $1/T_1$. At Q band, Dy^{3+} and Dy(DTPA)^{2-} , Er^{3+} and Er(DTPA)^{2-} have less effect on the nitroxide rate ($1/T_2$) at 80 to 150 K as compared to X-band at 80 K and there was no significant effect between 100-150K. At Q-band, the global maximum (the center of the spectrum) chosen from the field swept echo is orientation selective, since the signal at this position is mainly for molecules orientated with g_{yy} along the magnetic field. At Q-band molecules with g_{xx} parallel to the field have resonances mainly at the lower field and for g_{zz} resonance is at higher field. The spectra at X-band are less orientation dependent [79].

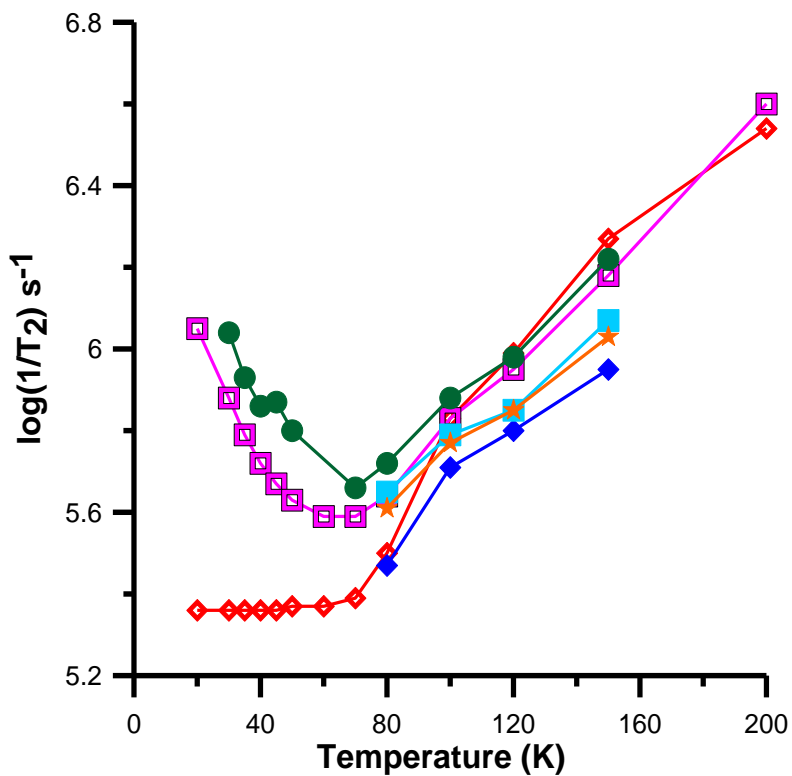


Figure 4.13 Effect of Dy^{3+} and its complex on spin-spin relaxation rate of nitroxide at X- and Q-band as a function of temperature.

Effect of 30 mM Dy^{3+} (□), 30 mM Dy(DTPA)^{2-} (●) on nitroxide at X-band (◇) and 30 mM Dy^{3+} (★) and 30 mM Dy(DTPA)^{2-} (■) on nitroxide at Q-band (◆) spin-spin relaxation rate ($\log(1/T_2)$) as a function of temperature. Uncertainty is about 9%.

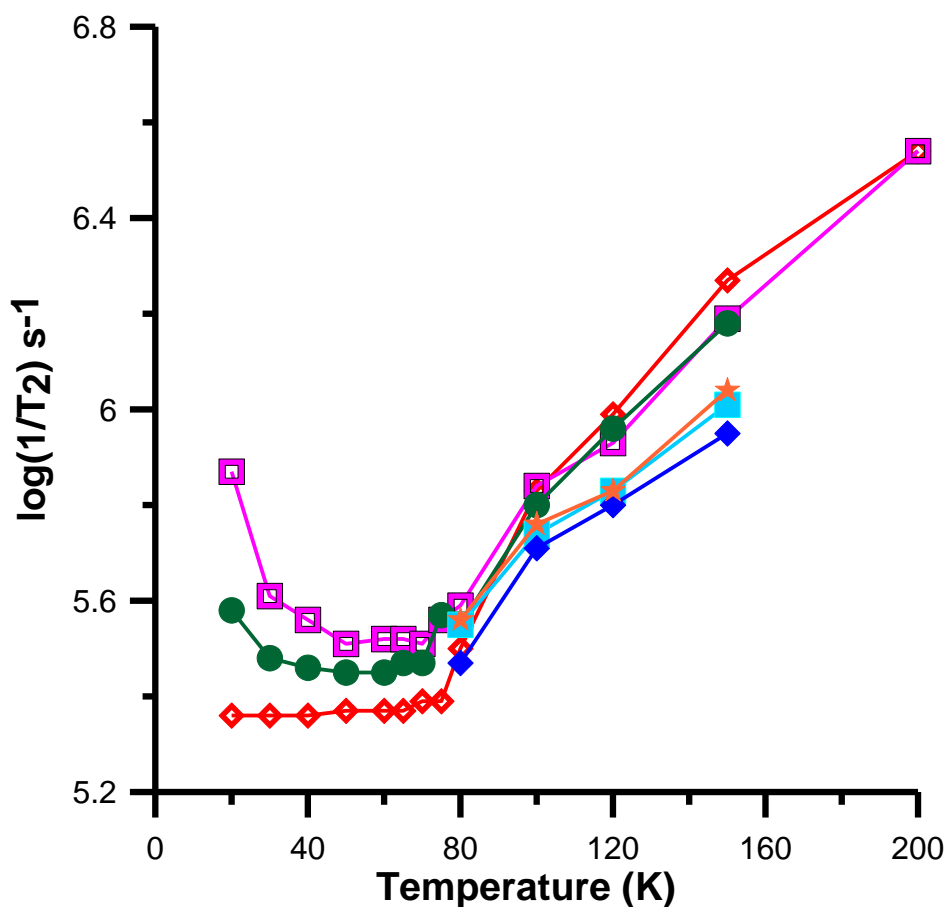


Figure 4.14 Effect of Er^{3+} and its complex on spin-spin relaxation rate of nitroxide at X- and Q-band as a function of temperature.

The effect of 30 mM Dy^{3+} (□), 30 mM $\text{Dy}(\text{DTPA})^{2-}$ (●) on nitroxide at X-band (◇) and 30 mM Dy^{3+} (★) and 30 mM $\text{Dy}(\text{DTPA})^{2-}$ (■) on nitroxide at Q-band (◆) spin-spin relaxation rate ($\log(1/T_2)$) as a function of temperature. Uncertainty is about 5%.

4.3.5 Effect of the more slowly relaxing Gd^{3+} ion on the spin-lattice relaxation of tempone.

The $1/T_1$ rate for tempone increases only at the highest concentration of Gd^{3+} at 80 to 120 K (Figure 4.15). The effect of Gd^{3+} on the spin-lattice relaxation of nitroxide is maximum at about 80 K. As discussed in the introduction to chapter 4, Gd^{3+} did not have large effects on $1/T_1$ because of its slow relaxation as compared to the other lanthanides

studied (see Tables 3.1 and 3.2 in chapter 3). Due to its slow relaxation rates, Eq 4.3 does not apply to Gd^{3+} relaxation enhancement. The effect is too small to claim a dependence on metal concentration.

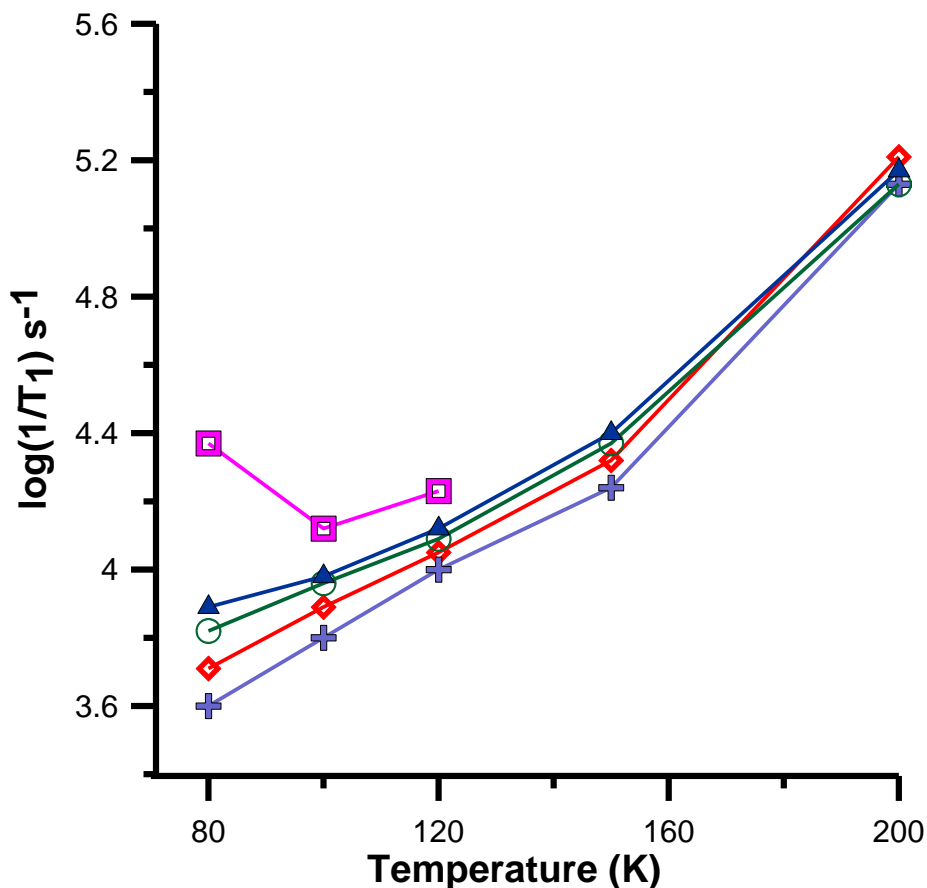


Figure 4.15 Concentration dependence of the effect of Gd^{3+} on the spin-lattice relaxation for 0.2 mM tempone as a function of temperature at X-band.

The sample was dissolved in in 1:1 water:glycerol and the concentrations of Gd^{3+} are 0 mM (◇), 1 mM (+), 2 mM (○), 5 mM (▲), and 7 mM (◻). Uncertainty in relaxation time is about 10%. The lines connect the data points.

4.3.6 Effect of the more slowly relaxing Gd^{3+} ion on the spin-spin relaxation of tempone.

The change in the $1/T_2$ rate of nitroxide under the influence of Gd^{3+} is quadratically concentration dependent. The $1/T_2$ rate of nitroxide became faster at 80 to 200 K (Figure 4.16). The spin-spin relaxation rate was so fast at the highest Gd^{3+} concentration studied (7 mM) Gd^{3+} that an echo for nitroxide was not observable above 150 K. The T_2 values were fit to a single exponential (Table 4.5).

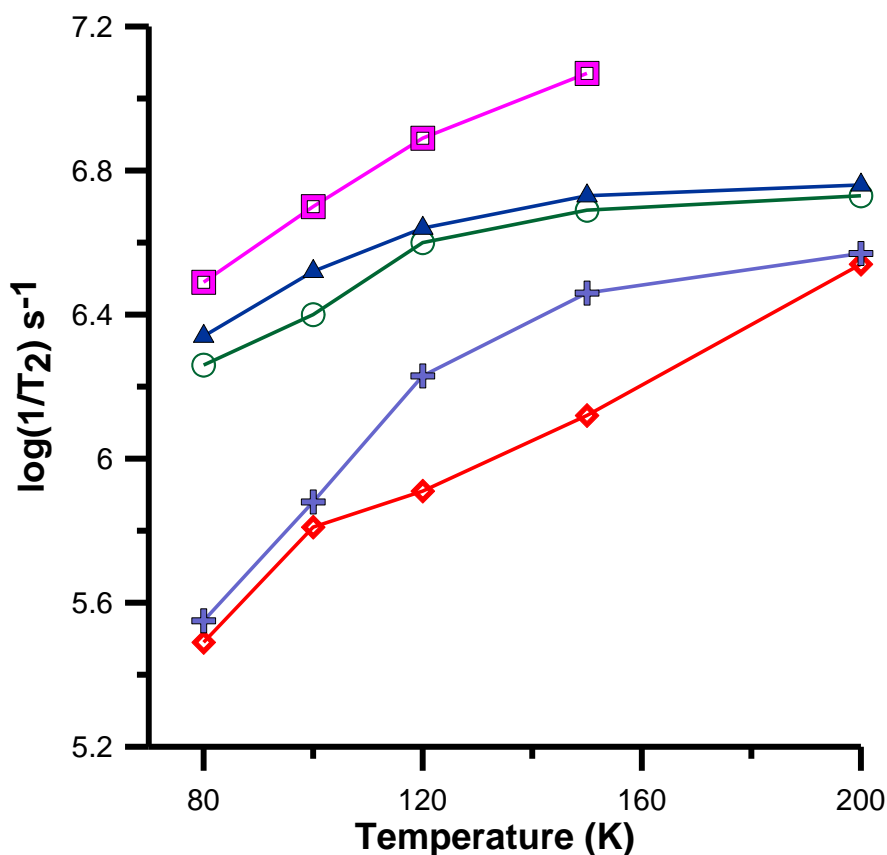


Figure 4.16 Concentration dependence of the effect of Gd^{3+} on the spin-spin relaxation for 0.2 mM tempone as a function of temperature at X-band.

The sample was dissolved in in 1:1 water:glycerol and the concentrations of Gd^{3+} are 0 mM (♦), 1 mM (+), 2 mM (○), 5 mM (▲), and 7 mM (◻). Uncertainty in relaxation time is about 8%. The lines connect the data points.

Table 4.5 Concentration and temperature dependence of stretched exponential parameter x for solutions of 0.2 mM tempone and Co²⁺

Temperature (K)	tempone	+ 1 mM Gd ³⁺	+ 2 mM Gd ³⁺	+ 5 mM Gd ³⁺	+ 7 mM Gd ³⁺
80	1.58	1.52	1.05	1.1	1
100- 200	1	1	1	1	1

4.4 Prediction of signal-to-noise (S/N) improvement for DEER

For a given sample concentration, the S/N for a DEER experiment depends on both $1/T_1$ and $1/T_2$. As $1/T_1$ increases, the shot repetition time can be decreased proportionally, which increases the number of averages per unit time. For white noise the S/N increases proportional to the square root of the number of scans. The impact of $1/T_2$ depends on the extent to which the exponential decay has reduced the intensity of the echo at the fixed time delay (t) at which the echo is measured for the DEER experiment. The echo decay curves were fit to a stretched exponential with exponent x (Table 4.1 to Table 4.5). The longer the value of t, the longer the interspin distance that can be measured. These factors are combined in the following expression

$$S/N = (\exp(-2t/T_2)^x / \exp(-2t/T_{2std})^{xstd}) * (\text{sqrt}(T_{1std}/T_1)) \quad 4.7$$

Where, delay time t, varies with sample, T_2 = spin-spin relaxation time in the presence of metal, T_{2std} = spin-spin relaxation time in the absence of metal (values from figures 4.13 to 4.16), x= stretch exponent (values from Tables 4.1 to 4.4), T_{1std} = spin-lattice relaxation

time in the absence of metal (values from Figures 4.1 to 4.5), T_1 = spin-lattice relaxation time in the presence of metal (values from Figure 4.1 to 4.5).

Equation 4.7 was used to predict the improvement in the signal to noise ratio (S/N) for nitroxide spin labels (Figure 4.17) in DEER experiments. In the comparison calculations $t = 2 \mu\text{s}$ was used. The predicted improvements in S/N were: 30 mM Dy^{3+} and Er^{3+} factors of 18 and 22, respectively at 30 to 40 K; 30 mM Co^{2+} factor of 5 at 40 to 80 K; 7 mM Gd^{3+} no improvement at 80 to 200 K; and 30 mM Tm^{3+} a factor of 3 times improvement. For 30 mM $\text{Er}(\text{DTPA})^{2-}$ and 30 mM $\text{Dy}(\text{DTPA})^{2-}$ a S/N ratio improvement of 10 was predicted at 20 K and about 9 at 40 to 60 K. $\text{Er}(\text{DTPA})^{2-}$ and $\text{Dy}(\text{DTPA})^{2-}$ were selected to improve the S/N ratio for DEER experiments because free aquo ions Dy^{3+} and Er^{3+} can bind to the protein. In the case of nitroxide attached to syntaxin protein, $\text{Er}(\text{DTPA})^{2-}$ and $\text{Dy}(\text{DTPA})^{2-}$ were predicted to improve S/N ratio in DEER experiments at 80 K by factors of 5 and 3, respectively (Figure 4.18). T_2 and T_1 used to find the S/N ratio improvement is given in Tables 4.6 and 4.7, respectively.

Unfortunately, we did not see the predicted S/N ratio improvement in DEER experiments. One possible explanation may be that $\text{Er}(\text{DTPA})^{2-}$ and $\text{Dy}(\text{DTPA})^{2-}$ are attaching to the syntaxin protein because they are charged complexes. In Ref. [80], it has been shown that syntaxin has positively and negatively charged amino acids in its structure. In previous NMR studies an interaction between lanthanides and protein was observed. Ref. [28] reported a decrease in amplitude of CW spectra of melanin (10 mg/ml) after adding 5 mM of lanthanide metals. In Ref. [81] different lanthanides showed different percentage of quenching in the signal of anionic spin-labeled penicillin.

If the metal were to bind close to the spin label, the effective local concentration could be much higher than the range we tested.

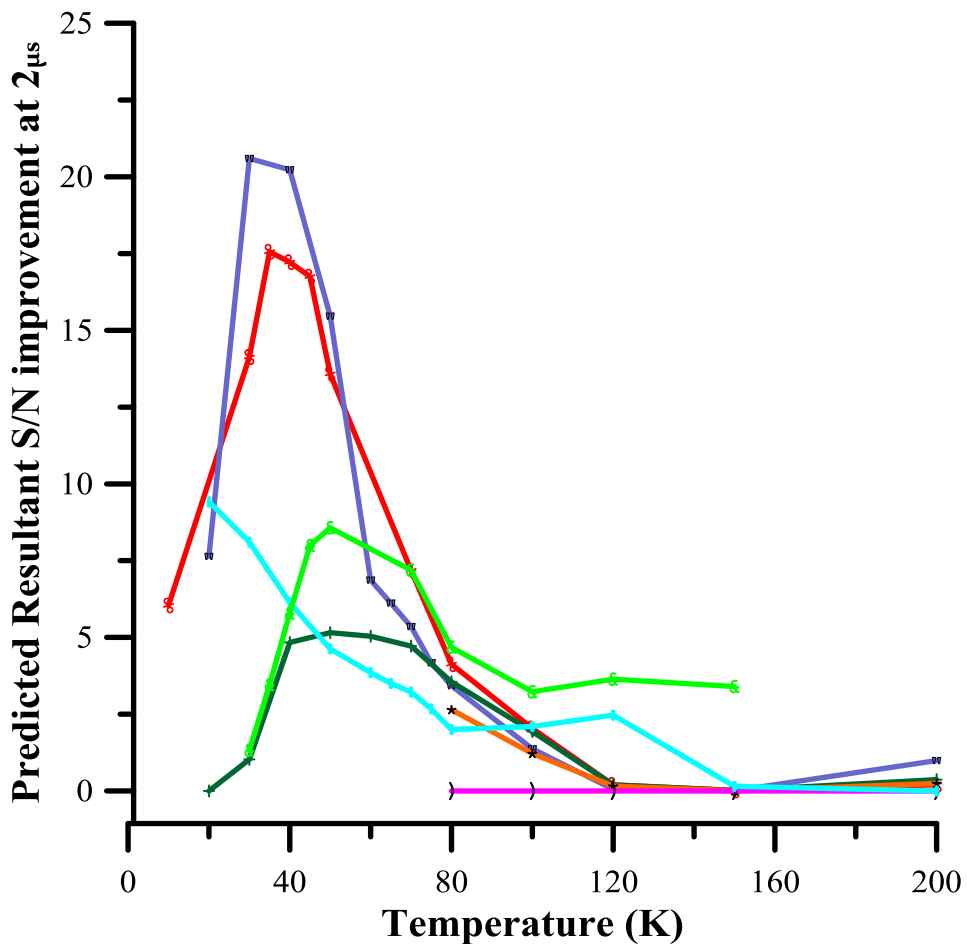


Figure 4.17 Predicted DEER S/N improvement with a 2 μ s spacing between pulses. Calculated effect of 30 mM Dy³⁺ (red), 30 mM Er³⁺ (purple), 30 mM Tm³⁺ (orange), 30 mM Co²⁺ (green), 7 mM Gd³⁺ (pink), 30 mM Dy(DTPA)²⁻ (light green) and 30 mM Er(DTPA)²⁻ (cyan) on S/N ratio at X-band. Uncertainty is 5%.

Table 4.6 T₂ values of spin label on syntaxin with and without metal ions at 30 to 80 K.

Temperature (K)	T ₂ (s) syntaxin * 10 ⁻⁶	T ₂ (s) 1mM Dy-dtpa*10 ⁻⁶	T ₂ (s) 1mM Er-dtpa*10 ⁻⁶	T ₂ (s) 0.5 mM Er-dtpa*10 ⁻⁶	T ₂ (s) 2mM Dy-dtpa*10 ⁻⁶
30	3.71	3.15	1.11	1.57	1.53
40	3.52	2.99	1.18	1.71	2.42
50	3.68	3.16	1.21	1.77	2.81
60	3.59	3.22	1.22	1.82	2.99
70	3.43	3.11	1.25	1.8	2.9
80	3.05	2.64	1.07	1.52	2.62

Table 4.7 T₁ values of spin label on syntaxin with and without metal ions at 30 to 80 K.

Temperature (K)	T ₁ (s) std* 10 ⁻⁶	T ₁ (s) 1mM Dy-dtpa*10 ⁻⁶	T ₁ (s) 1mM Er-dtpa*10 ⁻⁶	T ₁ (s) 0.5mM Er-dtpa*10 ⁻⁶	T ₁ (s) 2mM Dy-dtpa*10 ⁻⁶
30	7980	1600	132	349	1430
40	3600	1040	61.4	217	606
50	1850	645	38	152	356
60	1110	412	32.2	101	230
70	695	308	27	82	167
80	427	229	19.5	71.3	131

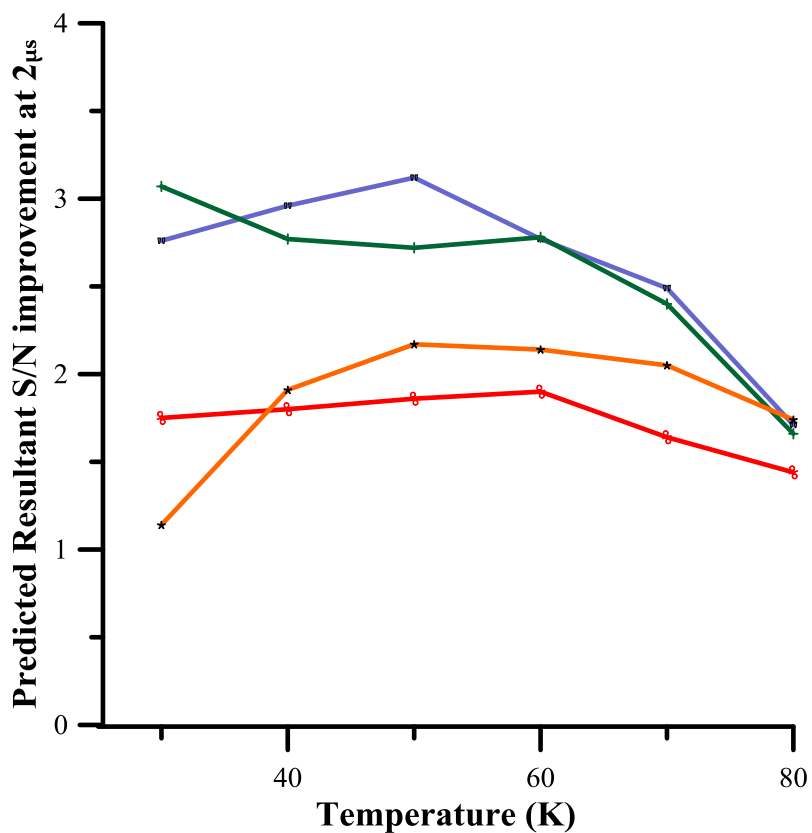


Figure 4.18 Predicted DEER S/N improvement for metals and their complexes for nitroxide attached to syntaxin for a constant pulse spacing of 2 μ s.

Effect of 1 mM Dy(DTPA)²⁻ (red), 2 mM Dy(DTPA)²⁻ (orange), 0.5 mM Er(DTPA)²⁻ (green), 1 mM Er(DTPA)²⁻ (blue) on S/N ratio at Q-band. Uncertainty is 4%.

Chapter 5

Distance between lanthanide and nitroxide

5.1 Introduction

The fundamental question of this research is whether the distance dependence of the enhancement of the relaxation of a nitroxide radical by a lanthanide can be used to measure distances. As a step toward answering this question, a series of molecules was synthesized to contain both a lanthanide and a nitroxide radical. After characterization to estimate the degree of labeling with the lanthanide and nitroxide, relaxation measurements were made by pulsed EPR. Other labs have reported studies related to the results in chapters 4 and 5, as cited below. This effort is part of a multi-pronged development of distance measurements of organic polymers, proteins, nucleic acids, and membrane systems. The wide range of systems requiring distance measurements necessitates a large toolkit of techniques.

Many techniques have been used to characterize and find distances and dynamics in biological molecules. These include X-ray crystallography [82], fluorescence [83], NMR [17], and EPR [5,52,84,85]. X-ray crystallography has been a very powerful tool to study the crystal structure of protein, but sometimes it is hard to get crystals of proteins. In addition, it is well-known that the structure in the crystal can be different from that in

fluid solution. Fluorescence has also been used, but for this technique there can be interference if the solution is opaque. NMR is extensively used to measure distances in proteins in fluid solution and in solids. Short distances are measured in diamagnetic systems. Longer distances can be measured when the protein is labeled with paramagnetic species by using relaxation enhancement. EPR has special advantages in the measurement of distances. In many cases, long distances measured by electron-electron interactions importantly supplement the shorter distances measured by nuclear-nuclear or electron-nuclear interactions. EPR can be used to find distances in fluid and frozen solutions, and in solutions that are opaque. There are no molecular mass limitations for EPR [5].

Many EPR techniques have been used for finding distances. The broadening of hyperfine lines has been used qualitatively to find distances between two paramagnetic centers [5, 6,68,84-87]. Transition metals and lanthanides are used as one of the paramagnetic centers. In many published papers [5,83,84], there is detailed information about metals and nitroxide interactions and the methods used to find the distances and the spin labels that can be used to do these experiments. An important early paper by Taylor et al. [88] on the interaction between Mn^{2+} and nitroxides stimulated numerous studies. Then Likhtenshtein and Kulikov [63] did extensive work to study the interactions between metals and nitroxide. In many of their studies, they used paramagnetic metals to find the depth of immersion of proteins in membrane [5]. According to Leigh, distances can be measured by comparing the amplitude of the nitroxide spectrum in the presence and absence of the metal ion. The decrease in amplitude can give the distance between

nitroxide and metal ion, but the assumptions for this theory are not satisfied for many experiments. The distances were also obtained by relaxation measurements, but power saturation was used to find the relaxation rate ($1/T_1$). As discussed in chapter 4, the d_1/d ratio was also used in finding distances. Half-field transitions and analysis of resolved splitting were also used in the past to find distances [84]. DEER is used widely to find distances between nitroxide- nitroxide, metal- metal and metal- nitroxide [89-92]. DEER is not very useful when metals are fast relaxing; in this case relaxation enhancement proves to be a better method of finding distances. It has been used to find distances in photosystems [93,94], low spin metmyoglobin variants [65], and proteins with iron-sulfur clusters [95,96]. Lueders et al. [23,92] propose that relaxation enhancement is more reliable than DEER and may extend the distance range. In Ref. [92], relaxation enhancement was used to find the distances, which were compared with that found by DEER. Moreover, they were able to increase the accessible distance range. The key point of Ref. [92] was that the Dy-DOTA complex decreases nitroxide T_1 , but only weakly affects T_2 in the 20-100 K temperature range at S, X and Q-band. The Dy-DOTA and nitroxide were attached to WALP23 polypeptides. In Ref. [97] also, relaxation enhancement was used to find distances. They found distances using equation 5.1-

$$\overline{\Delta k} = \frac{1}{\tau_1} = \overline{C} \quad 5.1$$

where τ_1 is the time where the signal has decayed to $1/e$ of its value at $t = 0$ and \overline{C} is an average relaxivity that depends on T_{1f} . Husedt et al. [98], describes the theoretical

simulation of dipolar nitroxide interactions through a tether-in-a-cone model. According to this model, nitroxides at two opposite ends of a tether (linker) attain different distances and orientations. The average distance can be found by this model even when there is a distribution of distances. Equation 4.3 (Ch.4) shows that enhancement of relaxation rates depend on r^{-6} and on orientation in the magnetic field. The resonance frequencies ω_s and ω_r , depends on the orientation of the molecule relative to the external magnetic field, so molecules with different orientations have different relaxation enhancements. The distributions in r also contribute to the distribution of relaxation rates [84].

Data in chapter 4 show the effect of lanthanides on nitroxide in mixtures. In this chapter, metal-nitroxide complexes were made to have particular distances between the lanthanide and nitroxide. Three linkers of different lengths were chosen to calibrate the methods of distance measurement. The three linkers are edta attached to alanine (shortest linker), edta attached to triglycine (medium-length linker), and edta attached to alanine-polyproline peptide (longest linker). Of these three linkers, the peptide alanine with six polyproline chain has two conformations, cis and trans, in different solvents and these conformations have different lengths [99]. The lanthanides were chosen on the basis of results summarized in chapter 4. Dy^{3+} and Er^{3+} exhibited maximum relaxation enhancement of spin-lattice relaxation rate ($1/T_1$) at temperatures below 100 K whereas Gd^{3+} showed less relaxation enhancement. Therefore, Dy^{3+} and Er^{3+} were chosen to see the maximum relaxation enhancement in rigid lattice. Gd^{3+} was chosen as a comparison because it is widely used for relaxation enhancement at room temperature, and La^{3+} was chosen as a control because it is diamagnetic.

5.2 Experimental Details

NMR spectra were obtained on a Bruker 500 MHz spectrometer. The column used for flash chromatography was 4-gram flash column with column volume (CV) of 4.8 ml-18 ml for 20-400mg of sample.

5.2.1 Preparation of Tetraethylester of EDTA (Et₄EDTA)

The following procedure was modeled after that reported in Refs. [89,99]. 5g (0.017mol) of Na₂EDTA, 125 ml ethanol and 0.75 ml concentrated sulfuric acid was refluxed for 24 hr at constant temperature of 70-72°C to make the tetraethyl ester of EDTA (Et₄EDTA). Afterward the solvent was evaporated. A saturated solution of sodium bicarbonate (50 ml) and dichloromethane (250 ml) was added to extract the organic layer. The organic layer was washed three times with sodium-bicarbonate solution and two times with water then dried by adding anhydrous sodium sulfate. The solvent was evaporated and solid was weighed. Product yield was 4.5g (0.011mol) of solid product was obtained. The product was characterized by proton NMR (Figure 5.1) using Bruker 500 MHz spectrometer. Chemical shifts (δ) 1.3 (t, 12H, -CH₂CH₃), 2.9 (s, 4H, -N-CH₂-CH₂-N-), 3.6 (s, 8H, -N-CH₂-COO-), 4.15-4.2 (q, 8H, -CH₂CH₃). A low-resolution mass spectrum was obtained using an Agilent 6100 LCMS system using (Electron spray ionization) ESI ionization mode. Mass spectrum: m/z (M+H)⁺ 405.3 (ESI) (Figure 5.2), Expected: 405.45

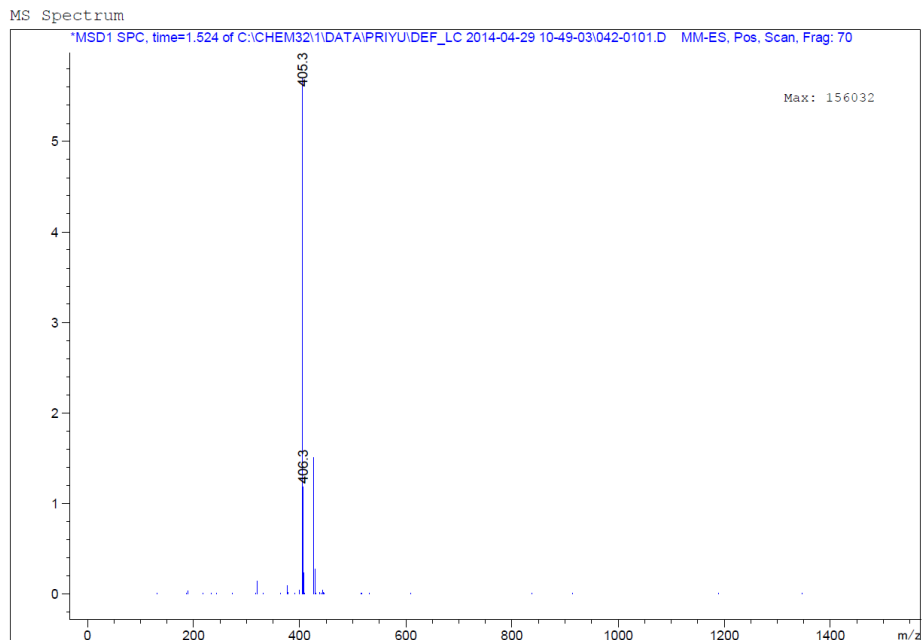


Figure 5.2 Mass spectrum of Et₄EDTA obtained with an Agilent 6100 LCMS system in ESI ionization mode.

5.2.2 Preparation of Triethylester of EDTA (Et₃EDTA)

The following procedure was modeled after that reported previously [88,99]. 4.5 g (0.011 mol) of Et₄EDTA was taken and same number of moles of copper perchlorate was added followed by the addition of 0.011 moles of NaOH. They all were dissolved in 150 ml of water and stirred overnight to complete the reaction. H₂S gas was passed through the solution for 5 hrs, and then the solution was filtered to remove copper sulfide. The filtrate was concentrated, and the product was purified by extraction. The impure product was dissolved in 100 ml chloroform and the impurities extracted with 1N aqueous HCl. The organic layer was dried using anhydrous sodium sulfate and solvent was evaporated. The product was purified by flash chromatography on a silica gel column using 10% methanol in dichloromethane to get 2g (0.0052 mol) of final product. The product was

characterized by TLC and proton NMR (Figure 5.3). Chemical shifts (δ) 1.3 (t, 9H, -CH₂CH₃), 2.9 (d, 4H, -N-CH₂-CH₂-N-), 3.6-3.7 (d, 8H, -N-CH₂-COO-), 4.15-4.2 (q, 6H, -CH₂CH₃). R_f of the product was 0.48. Mass spectrum: m/z (M+H)⁺ 377.1 (ESI) (Figure 5.4), Expected: 377.19

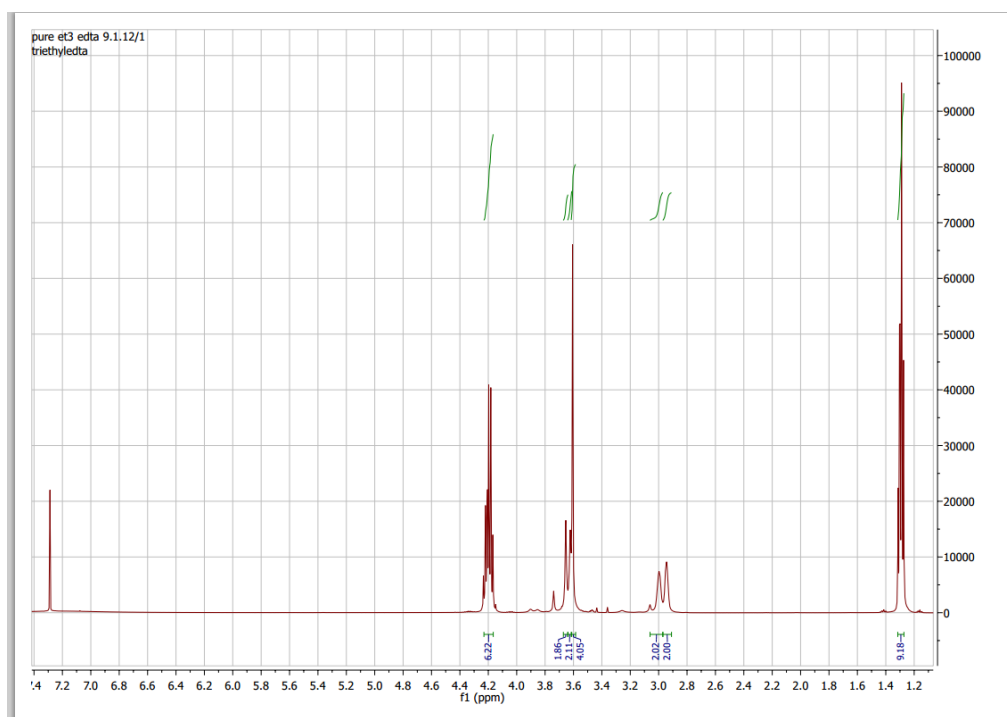
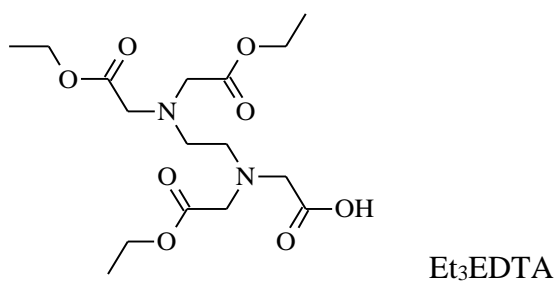


Figure 5.3 NMR of Et₃EDTA in deuterated chloroform.

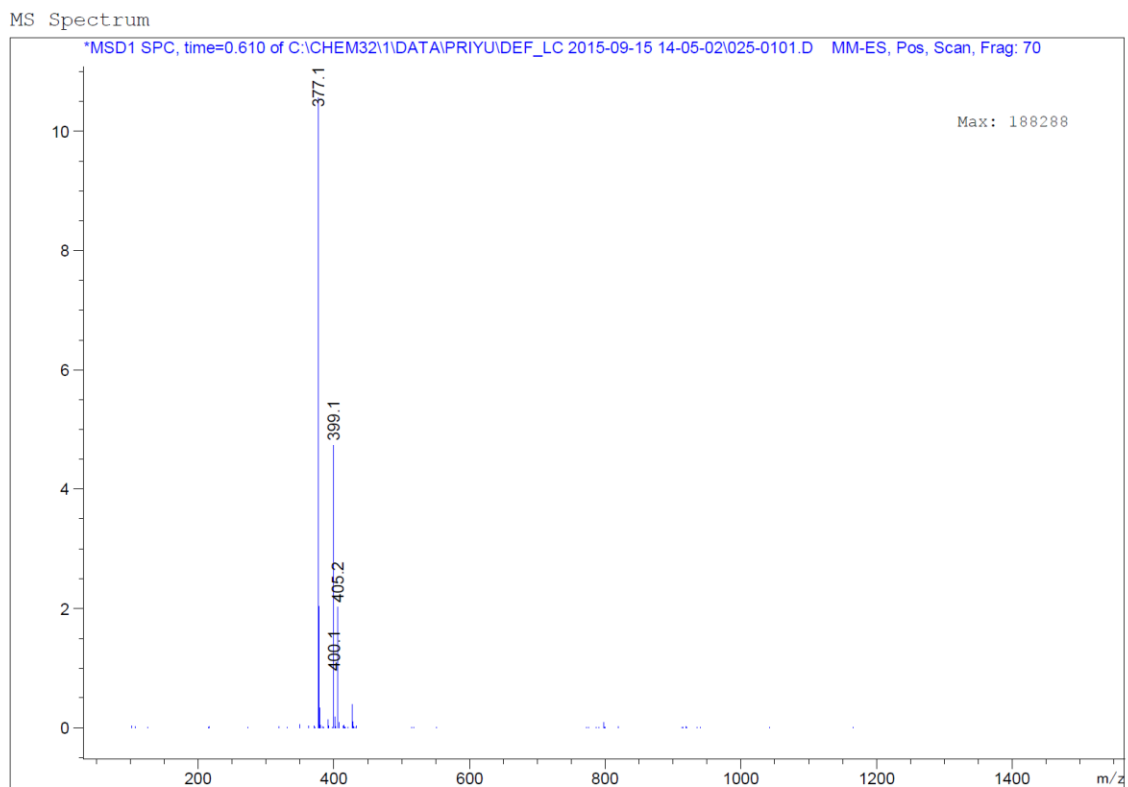
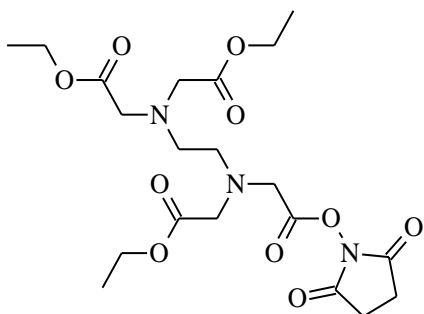


Figure 5.4 Mass spectrum of Et₃EDTA. The spectrum was obtained with an Agilent 6100 LCMS system in ESI ionization mode.

5.2.3 Preparation of N-hydroxy succinimide (NHS) ester of Et₃EDTA

According to previously published procedure [101,102], 0.3 g (0.82 mmol) of Et₃EDTA was combined with the same number moles of NHS and dicyclohexyl-dicarbodiimide (DCC) and dissolved in 1.2 ml of anhydrous tetrahydrofuran (THF). The reaction was stirred overnight at 4°C in the cold room. The reaction mixture was filtered and solvent was evaporated to get product. In the NMR spectrum there was a peak at 2.83 ppm that is characteristic of N-hydroxy succinimide (Figure 5.5). 2-2.6 ppm is the

impurity DCC. Mass spectrum: m/z $(M+H)^+$ 474.3 $(M+Na)^+$ 496.3 (ESI) (Figure 5.6),
Expected: 474.47, 496.47



NHS ester of Et₃EDTA

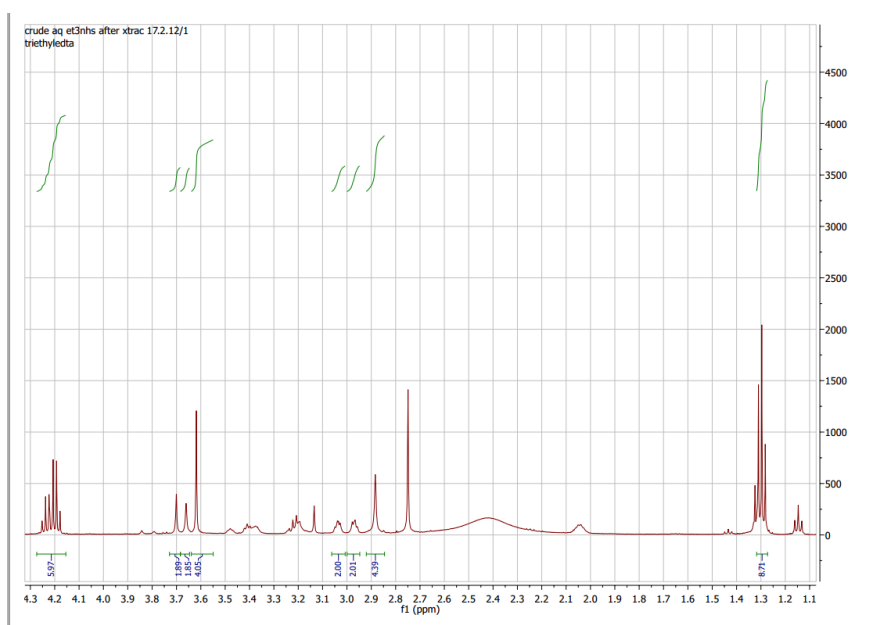


Figure 5.5 NMR of NHS ester of Et₃EDTA in deuterated chloroform.

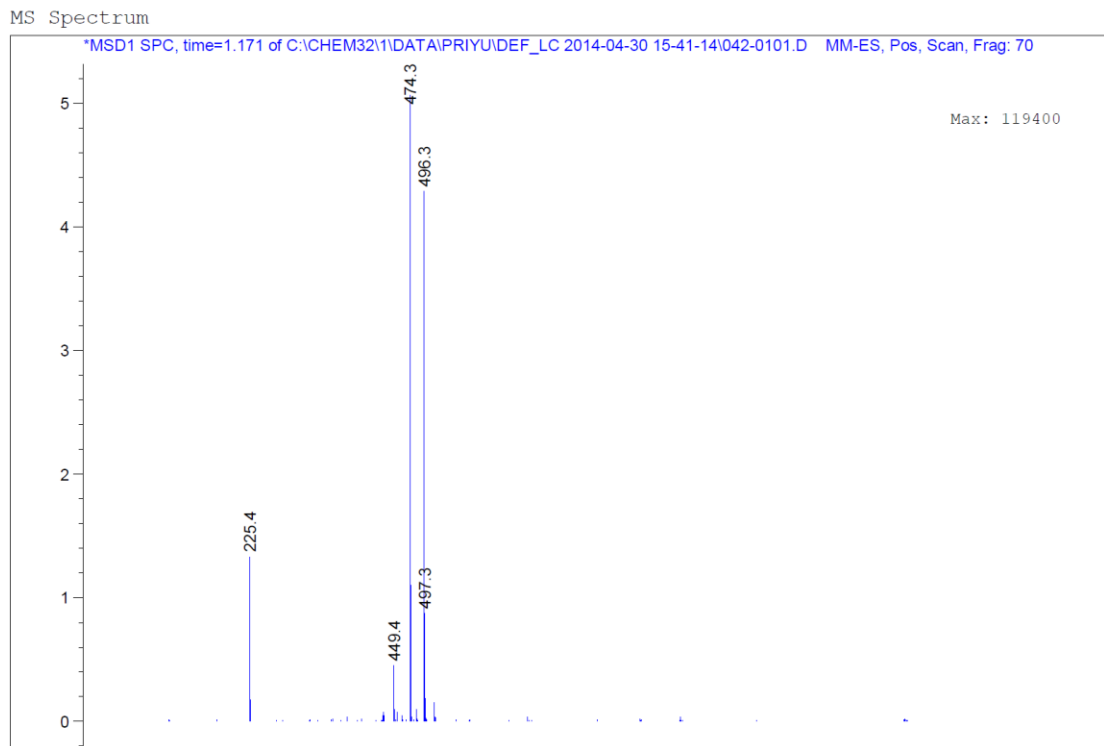
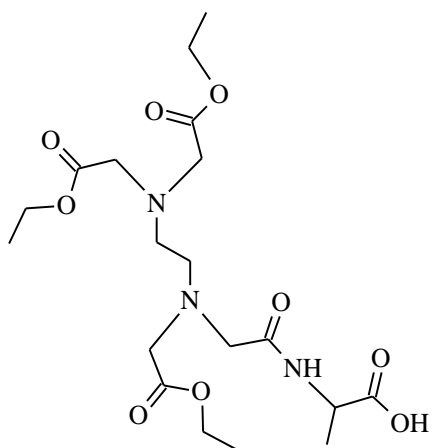


Figure 5.6 Mass spectrum of NHS ester of Et₃EDTA obtained on an Agilent 6100 LCMS system in ESI ionization mode.

5.2.4 Coupling of Et₃EDTA with N-terminus of alanine to make Et₃EDTA-A

The following procedure was modeled after that in Ref. [88]. A solution of 23 mmoles of alanine (Aldrich Chemical Company) and 30 mmoles of NaHCO₃ in 5 ml of water was added to the solution of 23 mmoles of the NHS ester of Et₃EDTA in 10 ml water. The reaction was stirred for 24 hrs at RT. The solvent was evaporated and then the product was extracted using 20 ml of ethyl acetate after mixing it in water. The organic layer was chromatographed on silica gel column using 10% methanol in dichloromethane as an eluting solvent. 1 mmole of product was obtained. The NMR spectrum (Figure 5.7) is consistent with the desired product. Chemical shifts (δ) 1.3 (t, 9H, -CH₂CH₃), 1.4 (d,

3H, -CHCH₃COO-), 2.9 (d, 4H, -N-CH₂-CH₂-N-), 3.6-3.7 (s, 4H, -N-CH₂-COO-), 3.8 (d, 4H, -N-CH₂-COO-), 4.15-4.2 (q, 6H, -CH₂CH₃), 4.3 (q, 1H, NH-CH-CH₃). Mass spectrum: m/z (M+H)⁺ 448.3 (ESI) (Figure 5.8), Expected: 448.23



Et₃EDTA-A

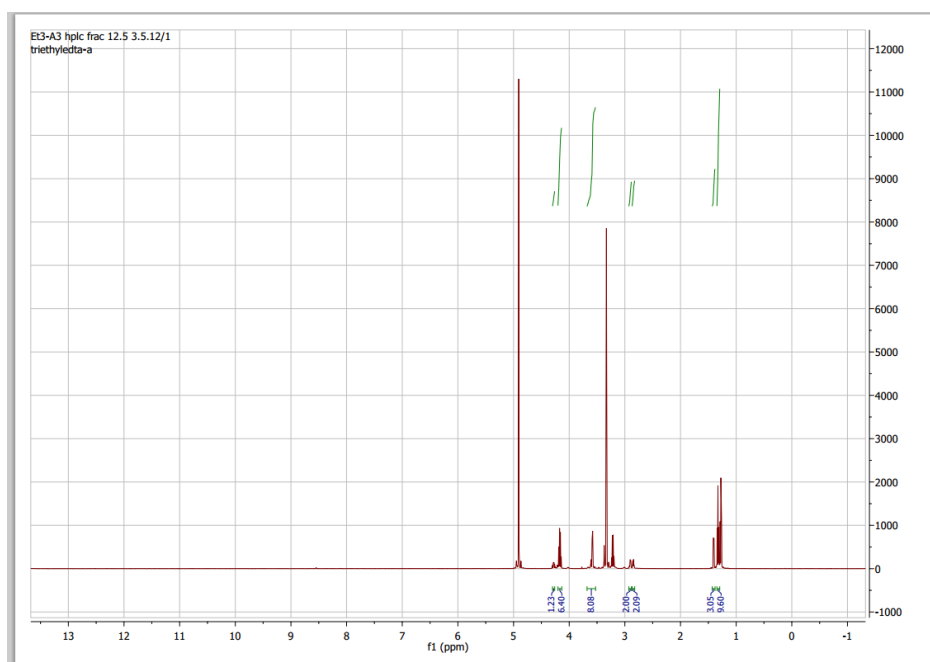


Figure 5.7 NMR of NHS ester of Et₃EDTA.

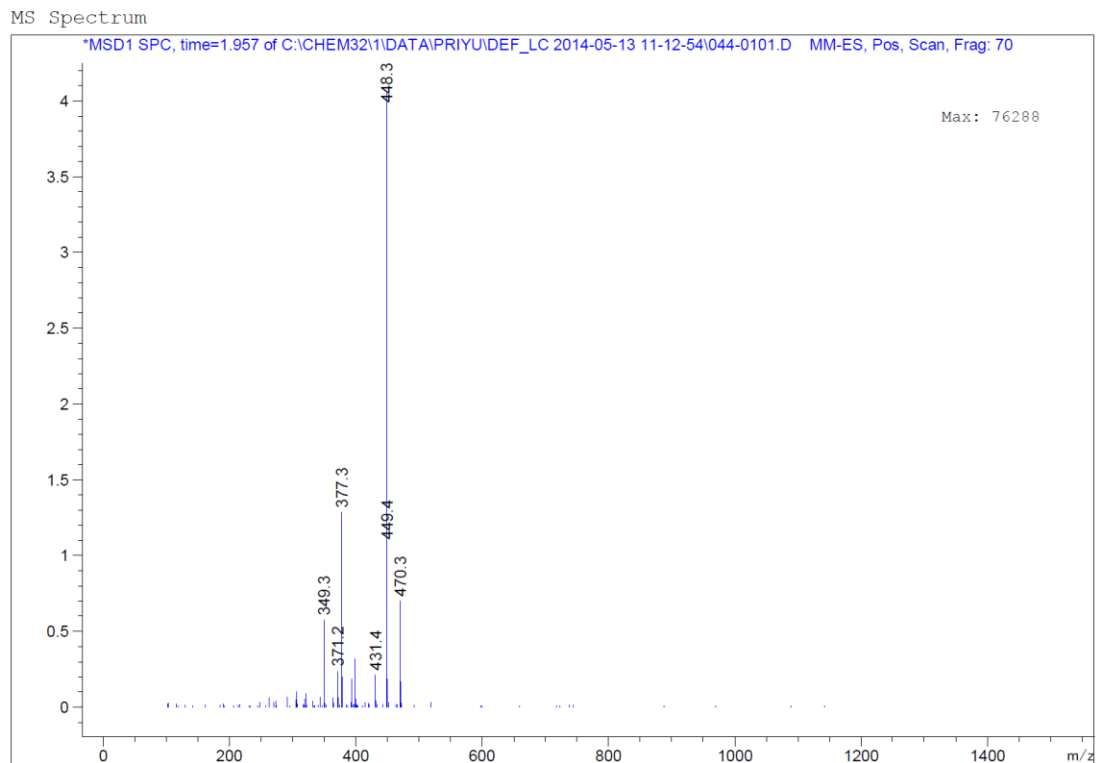
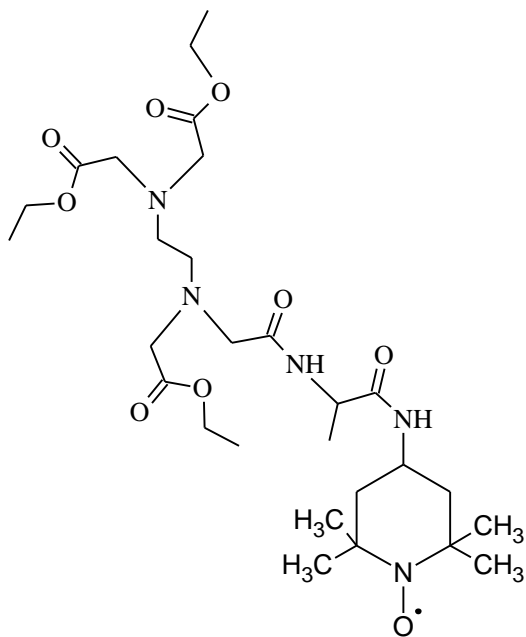


Figure 5.8 Mass spectrum of Et₃EDTA-A obtained using an Agilent 6100 LCMS system in ESI ionization mode.

5.2.5 Spin labeling of the Et₃EDTA-A at the C-terminus of alanine to make Et₃EDTA-A-T

The following procedure is modeled after that in Refs. [103,104]. Et₃EDTA-A was covalently spin-labeled by reacting Tempamine (4-amino-2,2,6,6-tetramethyl-1-piperidinyloxy) with the alanine carboxylic acid residue using 1-ethoxycarbonyl-2-ethoxy-1,2-dihydroquinoline (EEDQ) as the coupling agent. A mixture containing 0.0022 moles of Et₃EDTA-A was incubated with 0.0022 moles of Tempamine for 10 min prior to addition of 0.0044 moles of EEDQ in dichloromethane. The reaction was refluxed for 4 hours at 40°C. TLC was developed in the solvent mixture methanol and

dichloromethane (10:90, v/v) and showed no trace of tempamine or Et₃EDTA-A. 0.0018 moles of product was obtained. Mass spectrum: m/z (M+Na)⁺ 623.5 (ESI) (Figure 5.9),
Expected: 623.7



Et₃EDTA-A-T

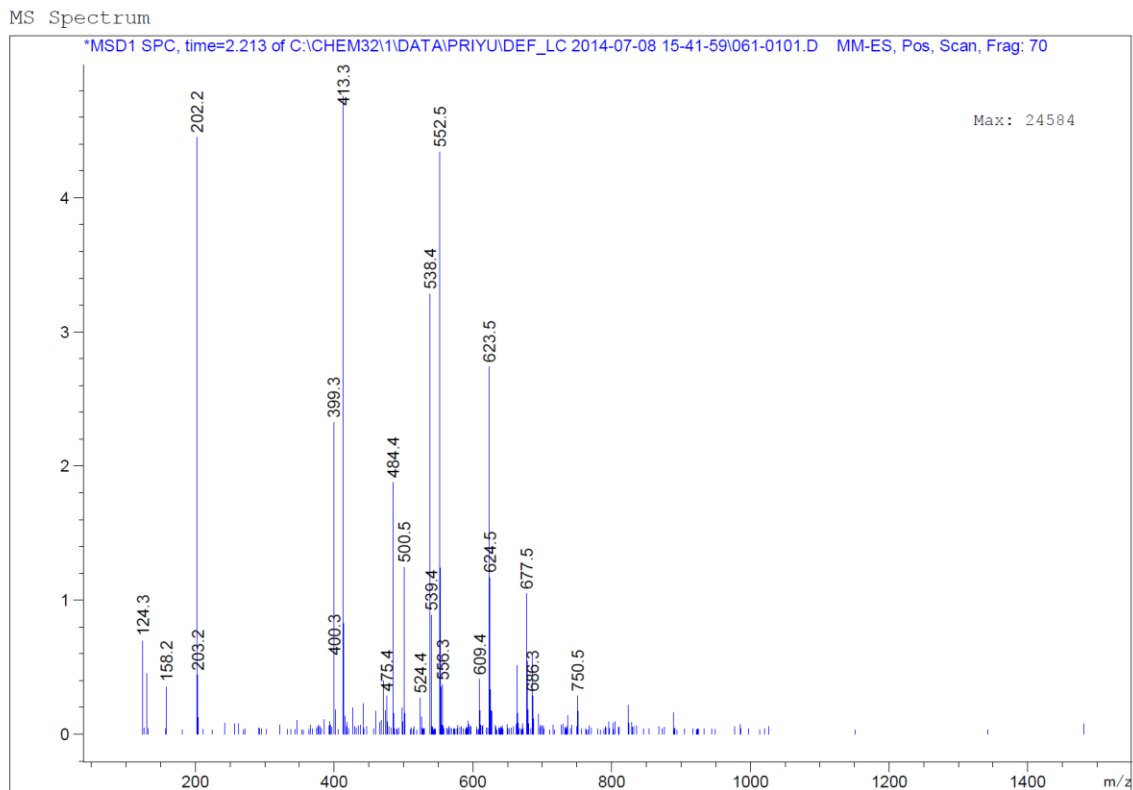
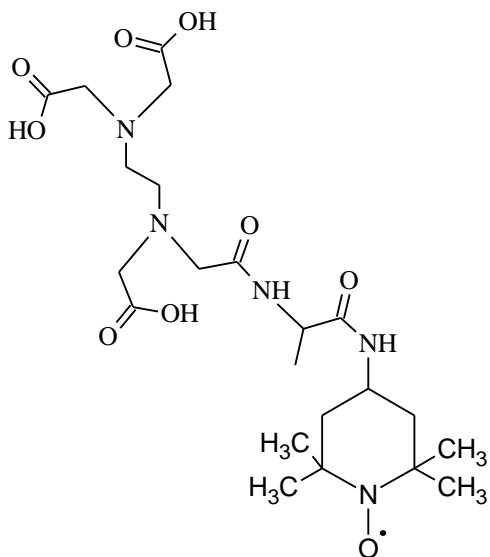


Figure 5.9 Mass spectrum of Et₃EDTA-A-T obtained using an Agilent 6100 LCMS system in ESI ionization mode.

5.2.6 Cleavage of ethyl esters from Et₃EDTA-A-T to make EDTA-A-T

The following procedure is modeled after that in Ref. [88]. A solution of 0.38 mmol LiOH in 5 ml water was added to a 0.13 mmol solution of Et₃EDTA-A-T in 2 ml of ethanol. The mixture was stirred at room temperature for 15 hr. The solvent was removed under vacuum. EDTA-A-T was dissolved in water. The pH was adjusted to 4 using 0.1N HCl. 5 ml of ethyl acetate was used to extract the product. TLC was checked and it showed the expected band for the product, and 0.12 mmol of product was obtained.



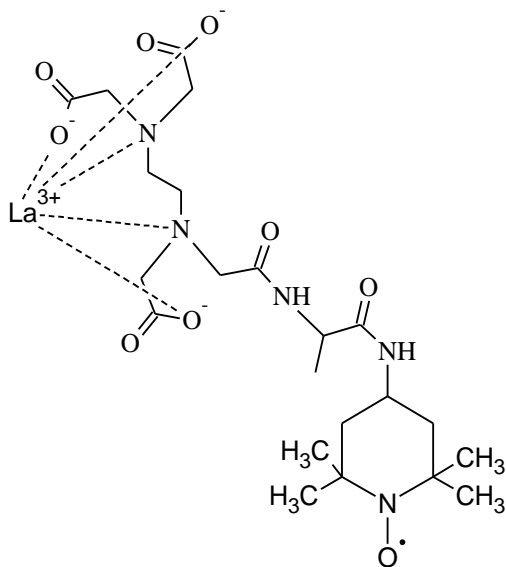
EDTA-A-T

5.2.7 Complexation of lanthanides (La, Gd, Dy and Er) to EDTA-A-T to make MEAT

The following procedure is modeled after that in Ref. [86]. The carboxyl groups of EDTA in EDTA-A-T were complexed with lanthanides at pH 4. The aqueous solution of lanthanide chloride (or nitrate in case of erbium) was mixed with the aqueous solution of EDTA-A-T at pH 4 in 1:1 molar ratio. The complexation progress was checked using arsenazo dye [105]. The pH of the arsenazo dye solution was adjusted with 1 N HCl to pH 4 and was pink in color. pH adjustment is important since the color of the dye changes with pH. As the complexation reaction proceeds, the reaction was checked with the dye solution on the basis of change in colors of the dye solution. When the dye binds to lanthanide the complex is green. When the reaction of lanthanide and EDTA-A-T was

complete excess lanthanide binds to the dye and gives green color. The color of the solution then changes from pink to green due to free lanthanide in the solution.

The samples were purified using size exclusion columns PDminitrapp G-10. These columns can purify small molecules with molecular size greater than 700. The medium was resuspended by shaking the column and then letting it settle down. The storage solution was removed. The column was equilibrated with 8 ml of water. A maximum of 0.3 ml of sample was added to the column, and it was allowed to enter the column completely. Then 0.4 ml of water was added to make a total volume of 0.7 ml. the flow-through was discarded. The product was eluted with water in 0.1 ml fractions. The product was also checked using CW EPR on the EMX spectrometer. Tempamine that is not bound to the peptide can be distinguished from bound radical because the high-field line of the spectrum for the bound radical is broadened by incomplete motional averaging of anisotropic interactions. The mass spectrum was obtained from the Mass Spectrometry Facility of the University of Colorado, Boulder using a Waters Synapt G2 HDMS mass spectrometer operated in resolution mode. Mass spectrum: m/z (M+H)⁺ 653.11 (ESI), Expected: 653.16 (Figure 5.10).



LaEAT

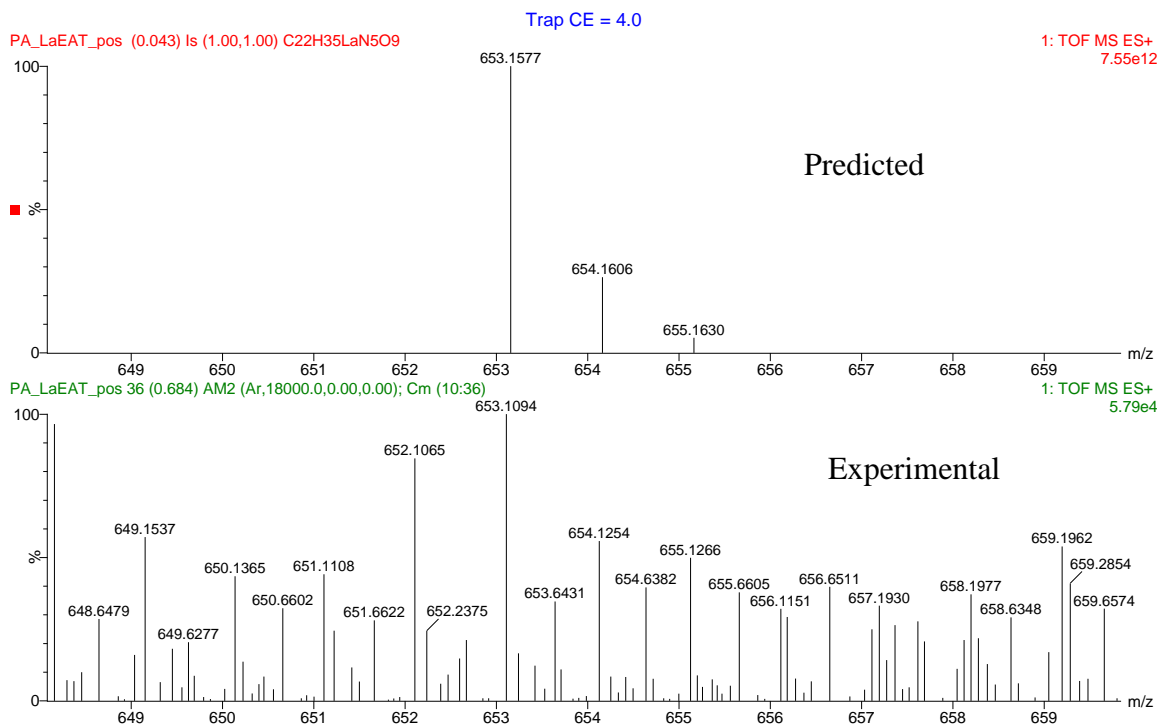
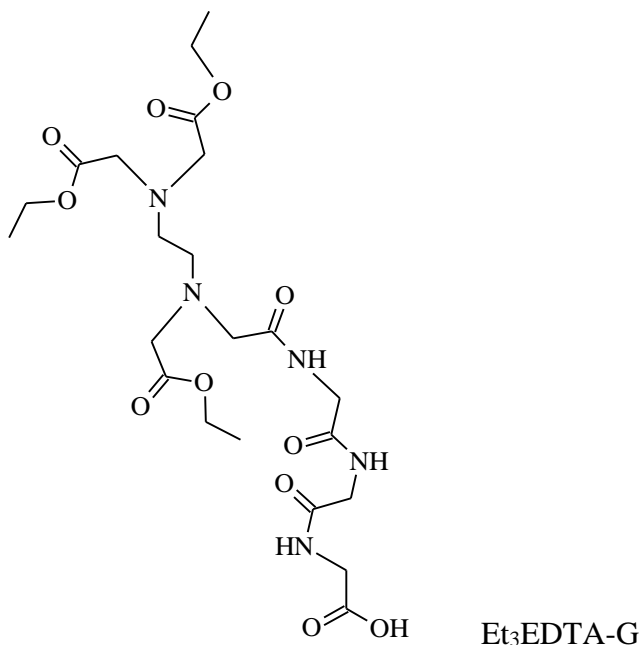


Figure 5.10 Mass spectrum of LaEAT obtained with a Waters Synapt G2 HDMS mass spectrometer operated in resolution mode. The predicted spectrum was calculated for comparison.

5.2.8 Coupling of Et₃EDTA with N-terminus of peptide triglycine to make Et₃EDTA-G

The following procedure is modeled after that in Ref. [88]. A solution of 0.07 mmol of triglycine bought from Lancaster Chemical Company and 0.08 mmol of NaHCO₃ in 5 ml water was added to the solution of 0.07 mmol of NHS ester of Et₃EDTA in 10 ml water. The reaction was stirred for 24 hrs at RT. The solvent was evaporated. The product was extracted using 20 ml of ethyl acetate and water. The ethyl acetate layer showed the impurities Et₃EDTA, NHS ester of Et₃EDTA, Et₄EDTA and DCC. The mass spectrum of the aqueous layer obtained showed the product; 0.05mmol of product was obtained after the evaporation of the solvent. Mass spectrum: m/z (M+H)⁺ 548.2 (ESI) (Figure 5.11) Expected = 548.26.



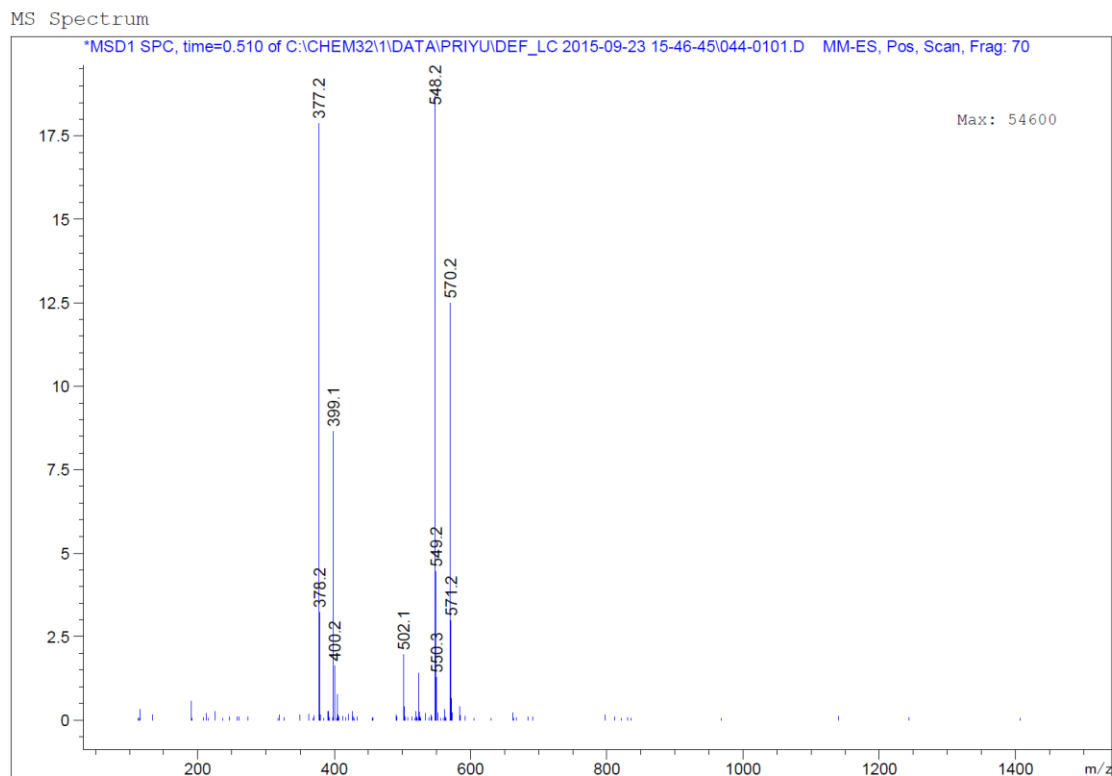
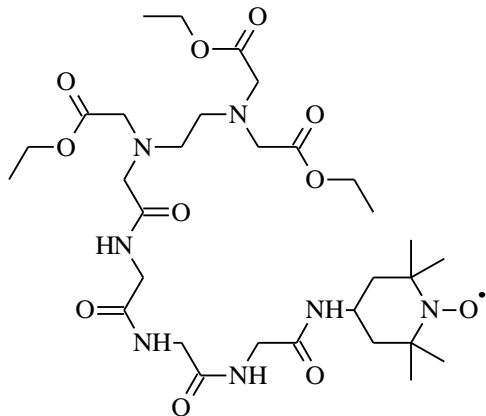


Figure 5.11 Mass spectrum of Et₃EDTA-G obtained with an Agilent 6100 LCMS system in ESI ionization mode.

5.2.9 Spin labeling of Et₃EDTA-G at the peptide C-terminus to form Et₃EDTA-G-T

The following procedure was modeled after that in Refs. [103, 104]. Et₃EDTA-G was covalently spin-labeled by reacting Tempamine with the peptide carboxylic acid residue using 1-ethoxycarbonyl-2-ethoxy-1, 2-dihydroquinoline (EEDQ) as the coupling agent. 0.05 mmol of Et₃EDTA-G was incubated with 0.05 mmol Tempamine for 10 min prior to addition of 0.1 mmol EEDQ in 10 ml of dichloromethane. The reaction was refluxed for 4 hours at 40°C. The solvent was evaporated to get 0.04 mmol of product. Mass spectrum: m/z 723.3 (Figure 5.12), Expected = 723.8



Et₃EDTA-G-T

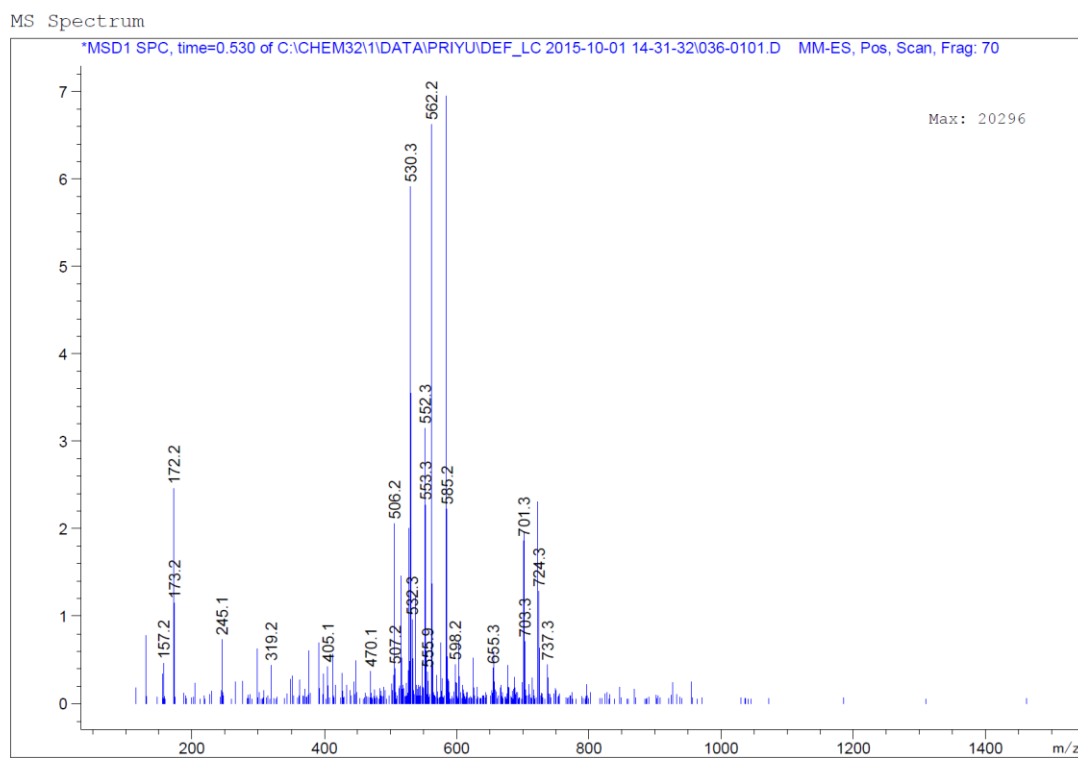
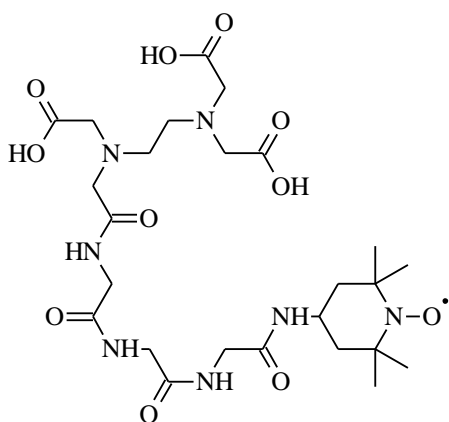


Figure 5.12 Mass spectrum of Et₃EDTA-G-T obtained with an Agilent 6100 LCMS system in ESI ionization mode.

5.2.10 Cleavage of ethyl esters from Et₃EDTA-G-T to make EDTA-G-T

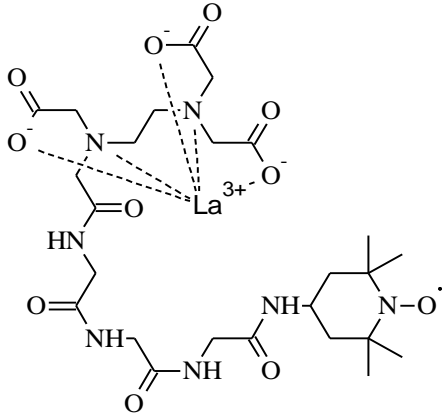
The following procedure was modeled after that in Ref. [88]. A solution of 0.12 mmol of LiOH in 5 ml water was added to 0.04 mmol of Et₃EDTA-G-T in 2 ml of ethanol. The mixture was stirred at room temperature for 15 h. The solvents water and ethanol were removed under vacuum. EDTA-G-T was extracted using 0.1N aqueous HCl at pH of 4 and 10 ml of ethyl acetate. The solvent ethyl acetate was evaporated to get 0.033 mmol of product.



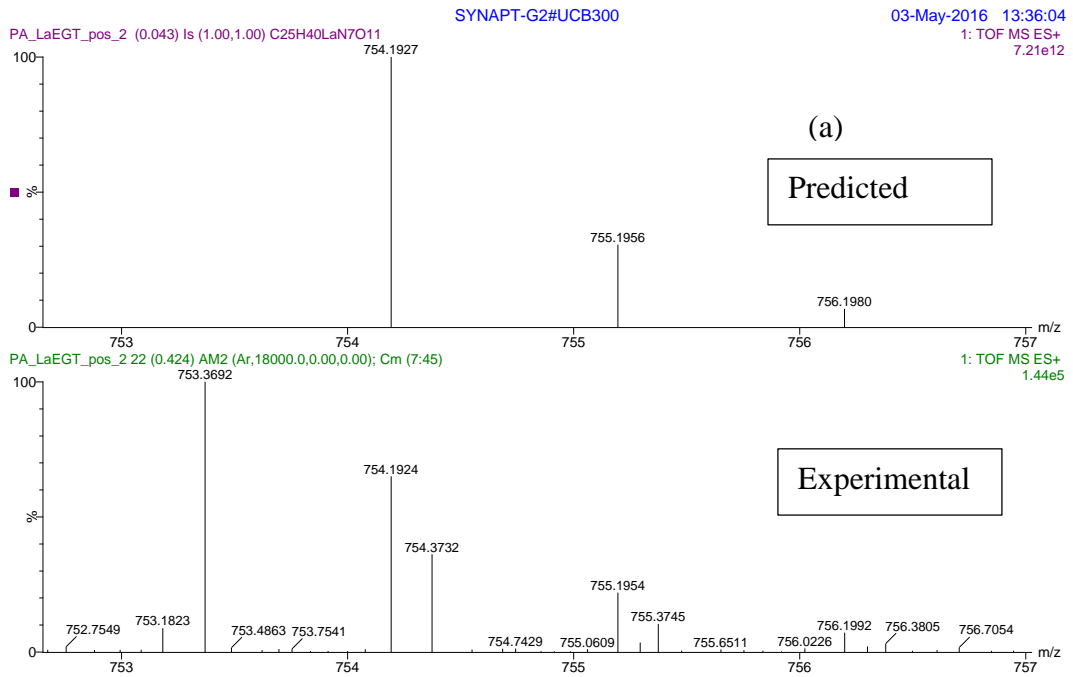
EDTA-G-T

5.2.11 Complexation of lanthanides (La, Gd, Dy and Er) with EDTA-G-T to make MEGT

Complexation and purification of the complex was done as described in section 5.2.7 for EDTA-A-T. Mass spectrum: m/z (M+H)⁺ 754.19 (ESI), Expected: 754.19 (Figure 5.13 a), (M+K)⁺ 791.14 (ESI), Expected: 791.14 (Figure 5.13 b).



LaEGT



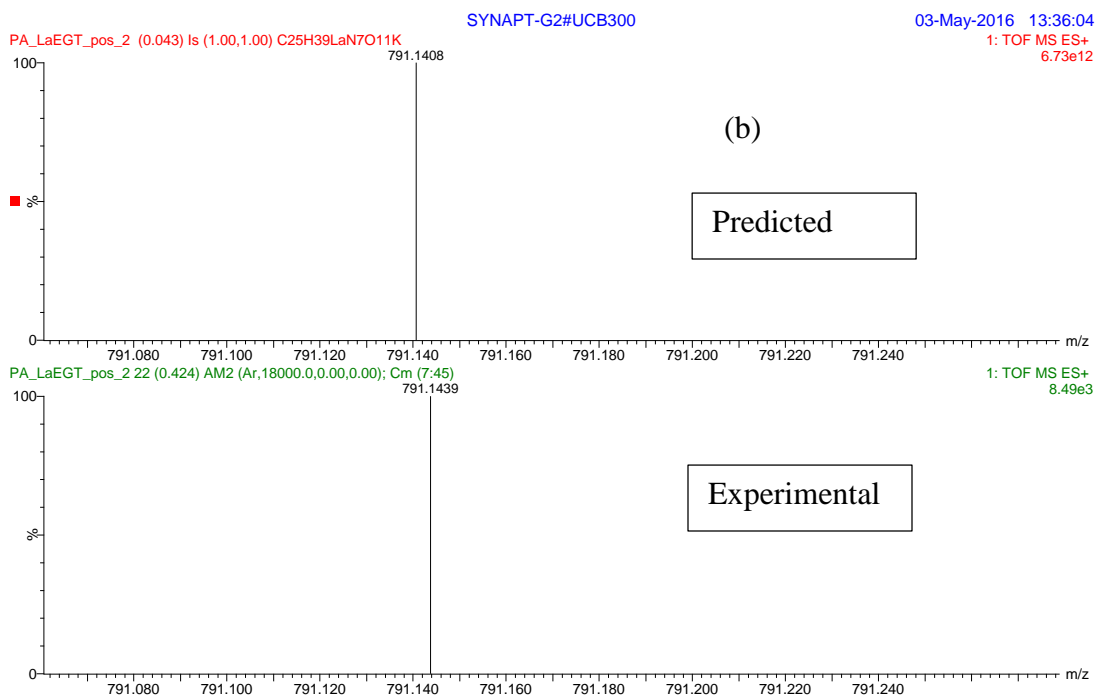
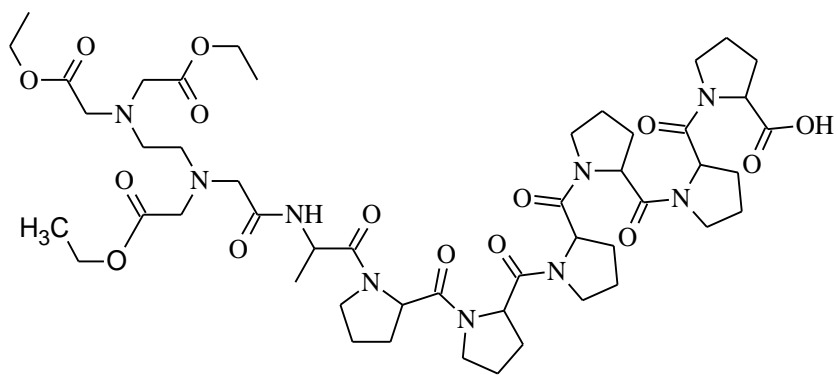


Figure 5.13 Mass spectrum of LaEGT (a) $(\text{LaEGT} + \text{H})^+$ and (b) $(\text{LaEGT} + \text{K})^+$ obtained with a Waters Synapt G2 HDMS mass spectrometer operated in resolution mode. The predicted spectra were calculated for comparison.

5.2.12 Coupling of Et_3EDTA with N-terminus of peptide APPPPPP (alanine with six prolines) to make $\text{Et}_3\text{EDTA-P}$

The following procedure is analogous to that reported in section 5.2.4. A solution of 0.07 mmol of peptide (synthesized by Peptide 2.0 Inc, purity > 98%) and 0.08 mmol of NaHCO_3 in 5 ml water was added to the solution of 0.07 mmol of the NHS ester of Et_3EDTA in 10 ml water. The reaction was stirred for 24 hrs at room temperature. The solvent was evaporated. The product was dissolved in the minimum amount of water and extracted using 20 ml of ethyl acetate. The mass spectrum of the product obtained from the aqueous layer was consistent with product; 0.05 mmol of product was obtained after evaporation of the solvent. Mass spectrum: m/z $(\text{M} + \text{Na})^+$ 1052.6 (ESI) (Figure 5.14), Expected: 1052.17



Et₃EDTA-P

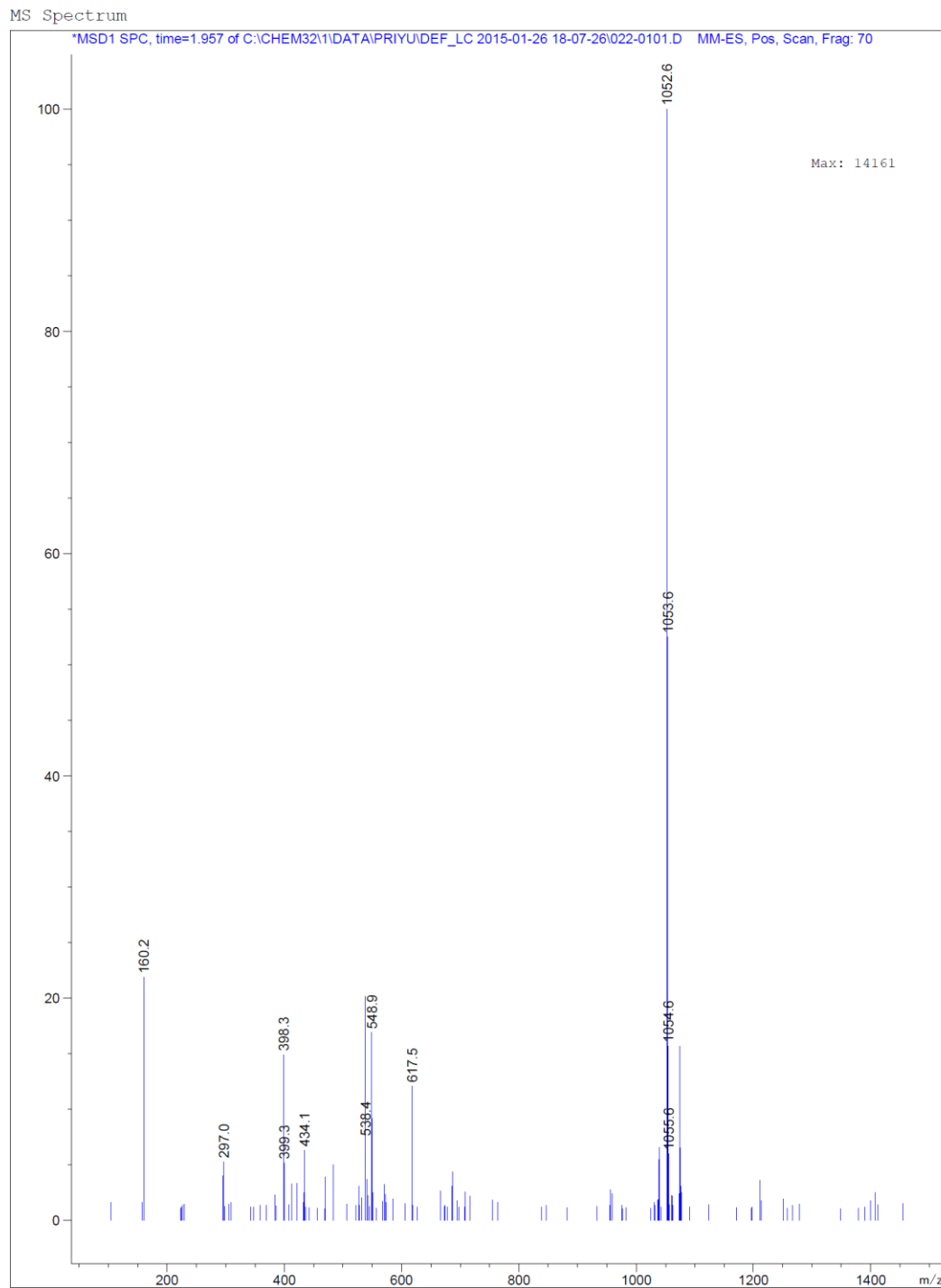
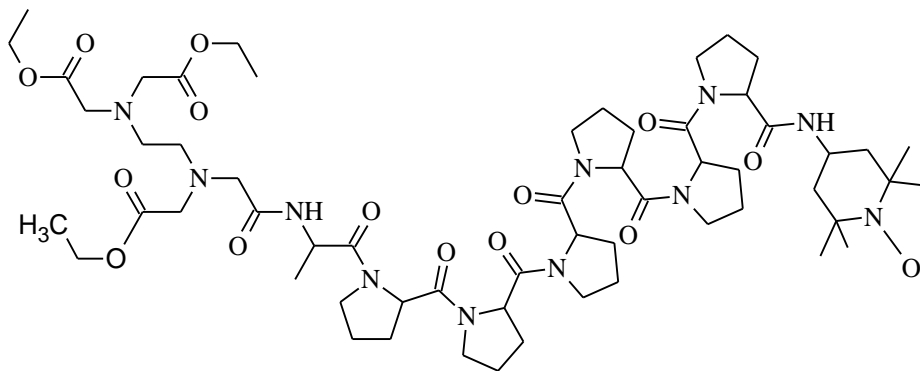


Figure 5.14 Mass spectrum of Et₃EDTA-P obtained with an Agilent 6100 LCMS system in ESI ionization mode.

5.2.13 Spin labeling of Et₃EDTA-P at the peptide C-terminus to make Et₃EDTA-P-T

The following procedure is analogous to that reported in section 5.2.5. Et₃EDTA-P was covalently spin-labeled by reacting Tempamine with the peptide carboxylic acid residue using 1-ethoxycarbonyl-2-ethoxy-1,2-dihydroquinoline (EEDQ) as the coupling agent. The solution contained 0.051 mmol of Et₃EDTA-P was incubated with 0.051 mmol Tempamine for 10 min prior to addition of 0.1 mmol EEDQ in 10 ml of dichloromethane. The reaction was refluxed for 4 hours at 40°C. The solvent was evaporated to get 0.042 mmol of product. Mass spectrum: m/z (M+Na)⁺ 1206.7 (ESI) (Figure 5.15), Expected: 1206.4.



Et₃EDTA-P-T

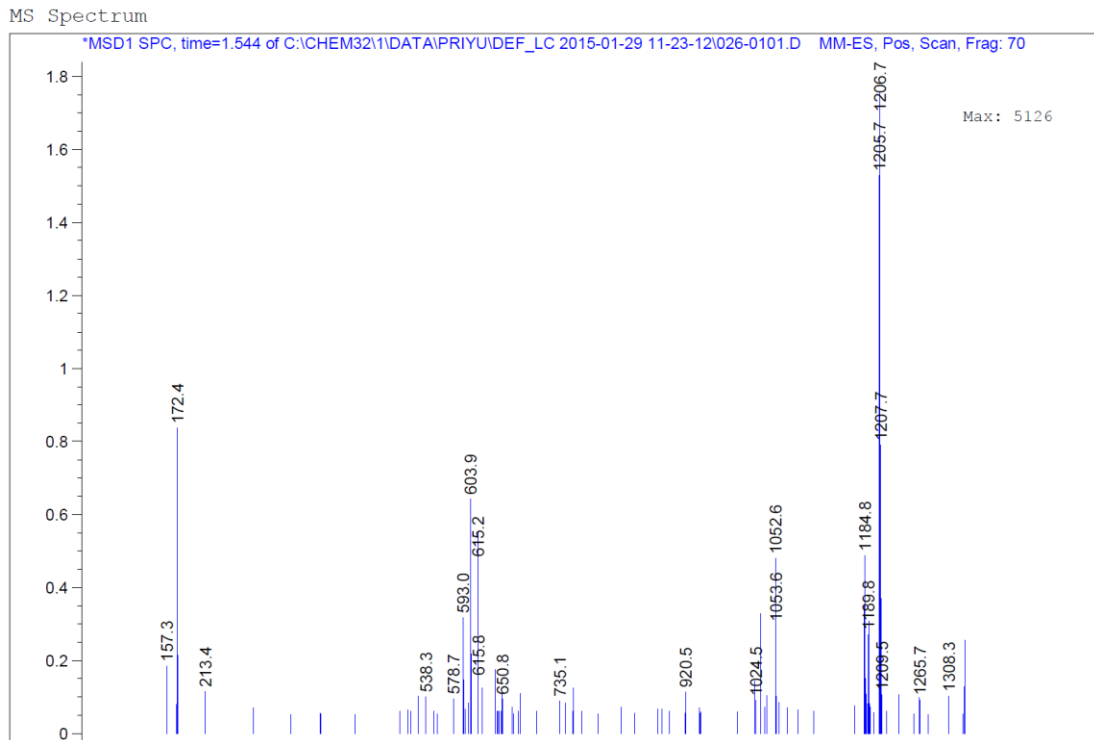


Figure 5.15 Mass spectrum of Et₃EDTA-P-T obtained with an Agilent 6100 LCMS system in ESI ionization mode.

5.2.14 Cleavage of ethyl esters from Et₃EDTA-P-T to make EDTA-P-T

The following procedure is analogous to that reported in section 5.2.6. A solution of 0.12 mmol lithium hydroxide (LiOH) in 5 ml water was added to a 0.04 mmol solution of Et₃EDTA –P-T in 2 ml of ethanol. The mixture was stirred at room temperature for 15 h. The solvent was removed under vacuum. EDTA-P-T was dissolved using a minimum volume of 1N aqueous HCl and diluted with additional water to make pH 3 and extracted using 10 ml of ethyl acetate [88]. The aqueous layer from the extraction was evaporated to get 0.03 mmol of product.

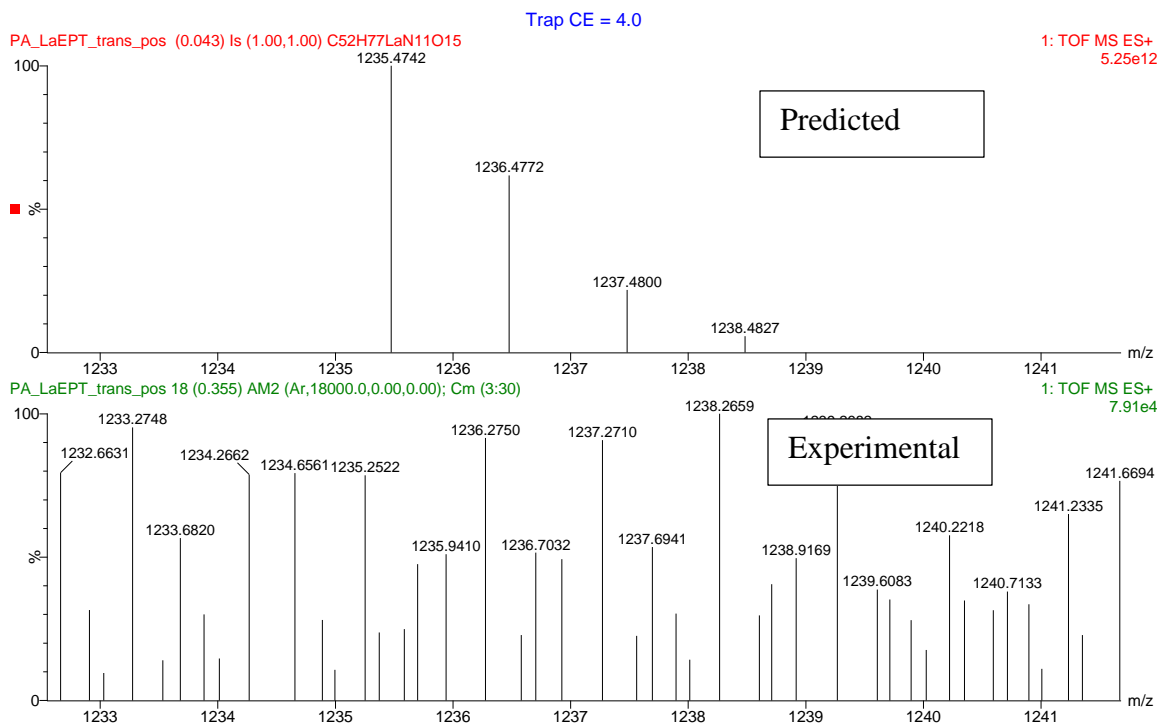


Figure 5.16 Mass spectrum of LaEPT obtained with a Waters Synapt G2 HDMS mass spectrometer operated in resolution mode. The predicted spectrum was calculated for comparison.

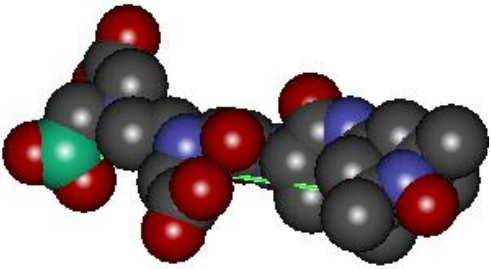
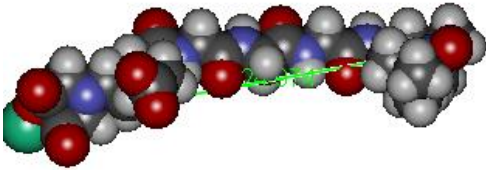
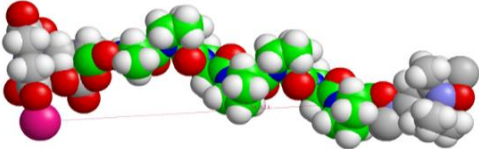
5.2.16 Conversion of trans polyproline to cis and monitoring the conversion using Circular Dichroism (CD)

The final purified MEPT is in water and polyprolines usually have a trans configuration [99], since it is the more stable configuration in water. The pure peptide and purified MEPT were dried and incubated in propanol for 22 days to convert the polyproline from trans to cis configuration [99]. CD spectroscopy was done using the Jasco Model J-810 spectropolarimeter at the Biophysics Core Facility at University of Colorado Anschutz campus. Results are described in section 5.3.1.

5.2.17 Distance calculations using Discovery Studio 2.5

The distance between the metal and the oxygen of nitroxide was measured using Discovery studio 2.5 software. The forcefield CHARMM was applied, CFF was the partial charge used and MM2 energy minimization was done. The distance was measured after the minimization of the energy of the molecule. The distances obtained by the program for the three molecules are M-EAT- 1.6 nm, M-EGT- 2.4 nm and M-EPT with cis-polyproline- 2.4 nm and M-EPT with trans-polyproline- 3.4 nm (Table 5.1). The distance measured in Ref. [106] between Gd-DOTA and a spin label on the 5th proline when 6 prolines in a trans configuration are present as a linker is approximately 2 nm.

Table 5.1 The structure and distances of molecules obtained using Discovery Studio 2.5 software.

	Structure of the molecule	Distance between Metal and Nitroxide	
Gd-EDTA-A-T A = Alanine		1.6 nm	MEAT
Gd-EDTA-G-T G = Triglycine		2.4 nm	MEGT
Gd-EDTA-P-T P = Peptide Alanine(Proline)₆		3.4nm	MEPT

5.2.18 CW EPR spectroscopy

The concentration of nitroxide in each sample was checked using a Bruker EMX CW X-band EPR spectrometer. Tempamine (0.6 mM) in water was used as a standard to find the concentrations of spin label. For room temperature spectra the sample tubes were 0.8 mm i.d. capillaries supported in 4 mm OD quartz tube. The unknown concentration was found by comparing the double integral for the sample to the double integral of the standard sample. The uncertainties in concentrations were ± 0.05 mM. The samples were prepared with the concentration in the range of 0.1 to 0.2 mM and the samples were in 1:1 water : glycerol mixture. For low temperature spectroscopy 100 μ l of sample was in 4 mm tubes. X-band CW power saturation was measured for all of the samples at 80 and 120 K on a Bruker E-580 X-band spectrometer. The CW spectra also were taken for LaEAT, GdEAT, LaEGT, GdEGT, LaEPT and GdEPT at room temperature at 0.05 G modulation amplitude after purging the sample with nitrogen for 1 hour. Spectra were simulated using the ASYM software [107].

The percentage of nitroxide spins detected was calculated by comparing the value of double integration intensity of CW spectra with 200 G sweep widths for the paramagnetic metal (Gd, Er and Dy)-containing complexes with the value for the Lanthanum complexes. The double integration intensity values were obtained using the Cwlv program.

5.2.19 Pulsed EPR measurements of electron spin relaxation times at 30 to 80 K

Pulsed EPR experiments were performed at 30 to 80 K at X-band (9.5 GHz) on a Bruker E580 spectrometer with an ER4118X-MS5 split ring resonator, an Oxford CF935 liquid helium cryostat, and an Oxford ITC503 temperature controller. Spin-spin relaxation times (T_2) were measured by two-pulse spin-echo using a 90° pulse length of 40 ns. Spin-lattice relaxation times (T_1) were measured by inversion recovery using 80ns-40ns-80ns pulses. The spin lattice relaxation rates of the nitroxide in MEAT, MEGT and MEPT compounds were measured at constant times for the two-pulse echo detection sequences (τ) of 200 and 100 ns. The spin-lattice relaxation times T_1 were calculated using the uniform penalty method UPEN analysis. UPEN analysis gives distribution of relaxation times [71,72]. The relaxation times distribution is wide so the median from each UPEN analysis was used in the following discussions. The attenuation of the power from the TWT was selected to give 180 and 90° pulses.

The percentages of nitroxide spins that were detected were calculated by taking the ratios of the amplitude of the maximum peak of the field swept echo spectra of metal complexes (Gd, Dy and Er) to the amplitude of field-swept echo spectra of the corresponding lanthanum complex.

5.3 Results

5.3.1 Conversion of trans-MEPT to cis-MEPT

Polyproline has two conformations: - PP-I has a cis configuration and PP-II has a trans configuration [99]. Polyproline was chosen to be one of the linkers to get two different linker lengths and metal-nitroxide distances by changing the conformation from trans to cis. PP-I with cis configuration is a right handed helix in which dihedral angles are -75° (ϕ), 160° (φ) and 0° (ω), the axial translation is 1.90 \AA , and there are 3.3 residues per turn. On the other hand, PP-II with trans configuration is a left handed helix with an axial translation of 3.20 \AA , 3 residues per turn, and dihedral angles of -75° (ϕ), 145° (φ) and 180° (ω). PP-II is stable in water and PP-I is more stable in aliphatic alcohols, which is the reason why propanol was used to convert trans polyproline to cis polyproline [99]. The conversion of trans to cis is a very slow process and it is always hard to get 100% conversion especially when the peptide length is small [108, 109]. In Figure 5.17, the CD spectrum of ErEPT exhibits the trans-polyproline properties when it is present in 1:1 water/ glycerol. It has a strong negative band at 205 nm and weak positive band at around 225 to 227 nm that is similar to Ref. [99]. The metal-free trans polyproline peptide converted to only partially cis after 7 days of incubation in propanol, and showed a strong negative band at around 200 nm and weak positive band at 217 to 219 nm. If it would convert completely to cis, it would show a large positive band at 217 to 219 nm and negative band at 200 nm. When the metals were bound, LaEPT, ErEPT and DyEPT, the linker did not convert to the cis configuration. In Ref. [110], it was shown that it's hard to

get in-vitro conversion from trans to cis but this conversion can be done faster in vivo by the enzyme peptidyl-prolyl cis-trans isomerase (PPIase). Even after enzyme-catalyzed conversion, there still is a distribution of trans and cis conformations. On the basis of the results obtained by CD, no further attempts were made to convert the trans conformation to cis. Results reported in this dissertation are for the trans conformation.

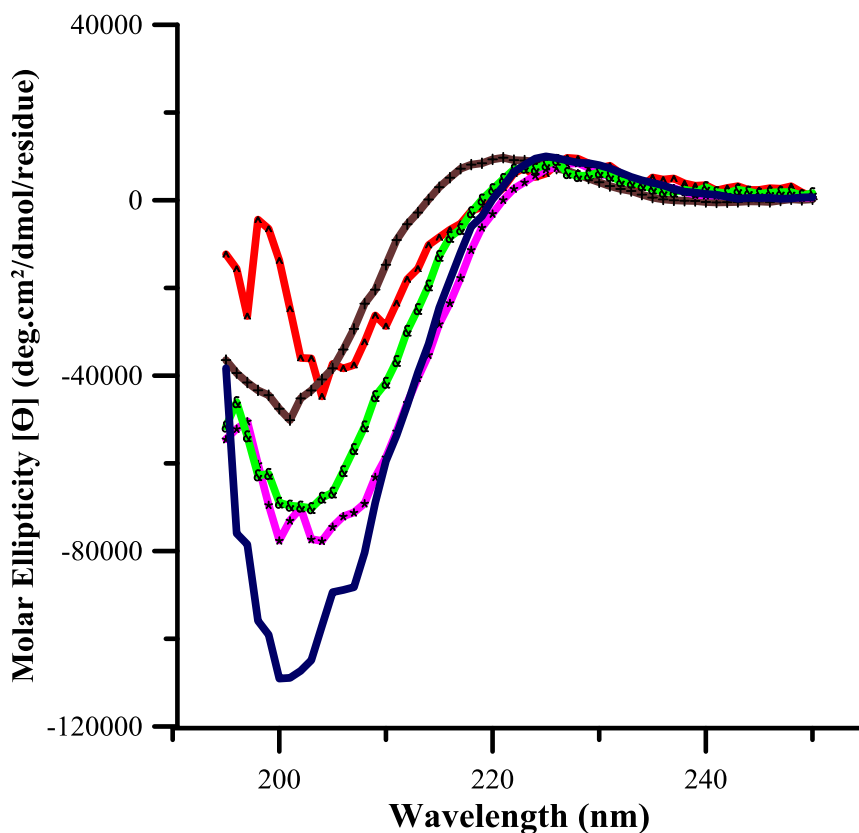


Figure 5.17 CD spectrum of polyproline.

ErEPT in 1:1 water: glycerol (magenta trace), peptide without metal after incubating in propanol for 7 days (brown), LaEPT after incubating in propanol for 22 days (red trace), ErEPT after incubating in propanol for 22 days (green trace) and DyEPT after incubating in propanol for 22 days (blue trace).

5.3.2 Tumbling correlation times (τ_B) of spin-labeled molecules.

Since g and A values for nitroxides are anisotropic, the linewidths in the CW spectra can be analyzed to determine the tumbling correlation time. The linewidth dependence on nitrogen nuclear spin, m_I , can be described as -

$$\text{Linewidth} = A + Bm_I + Cm_I^2$$

Equation 5.2 was used to calculate tumbling correlation times of the spin-labeled molecules. The value of B was obtained from the ASYM program. In the ASYM program, hyperfine values of tempamine from the published work by Windle [111] were used in the simulations. Kivelson's model was applied to find the correlation times [112]. Table 5.2 shows that the tumbling correlation time increases with the increase in the size and molecular weight as expected through the results in Ref. [113]. This correlation confirms that the nitroxide is attached to the probes with varying lengths.

$$\tau_B = \frac{-Blw}{(0.2667 \times b \times delg \times B_0) + (0.1778 \times delg \times B_0 \times \frac{a}{g_0})} \quad 5.2$$

where Blw = value of B obtained from ASYM simulation of CW spectrum

$$b = 0.667 \times 2 \times 3.1416 \times [Az - 0.5 \times (Ax + Ay)] \times 2.8025 \times 10^{10}$$

$$a = 0.333 \times 2 \times 3.1416 \times (Ax + Ay + Az) \times 2.8025 \times 10^{10}$$

$$delg = g_z - 0.5 \times (g_x + g_y), \quad g_0 = 1/3 \times (g_x + g_y + g_z)$$

Table 5.2 Correlation times in water for tempamine attached to different molecules, calculated using the Kivelson model of tumbling

Spin-labeled probe	Tumbling correlation time (τ_B) (ps) ^a	Molar mass
Tempamine	12	171
LaEAT	45	670
LaEGT	48	753
LaEPT	88	1255

^a Uncertainties are about ± 10 ps except for tempamine where the uncertainty is about ± 2 ps.

5.3.3 Effect of lanthanides on $P_{1/2}$ values of nitroxide at 80 and 120 K

The increase in $P_{1/2}$ of the nitroxide due to interaction with a rapidly relaxing metal has been reported in many studies [21, 28,74]. Values of $P_{1/2}$ for each of the spin-labeled metal complexes at 80 and 120 K are summarized in Table 5.3. To facilitate comparisons, $P_{1/2}$ for nitroxide in the paramagnetic metal complexes also is ratioed to that for the diamagnetic La^{3+} analog. The impact of the metal ion increases in the order $\text{Gd}^{3+} \ll \text{Dy}^{3+} < \text{Er}^{3+}$. The much smaller impact for Gd^{3+} is consistent with its relatively slow relaxation at 80 to 120 K and the modest impact on relaxation rates for nitroxide in mixtures (Ch. 4). The larger effect of Er^{3+} than of Dy^{3+} is the reverse of what was observed in mixtures (Ch. 4). For Er^{3+} the impact on $P_{1/2}$ decreases in the order $\text{EAT} > \text{EGT} > \text{EPT}$, which is the order of increasing distances predicted from the calculations

with Discovery Suite (Table 5.1). For Dy³⁺ the impact on P_{1/2} decreases in the order EGT > EPT > EAT, which is not the order of increasing distances predicted from the calculated structures. The position of EAT in the sequence is out of order. This sequence needs to be confirmed.

Table 5.3 P_{1/2} (mW) for nitroxide in complexes with La³⁺, Gd³⁺, Dy³⁺ and Er³⁺ in 1:1 water: glycerol at 80 and 120 K. The uncertainty is about 8 %.

Sample	80 K		120 K	
	P _{1/2}	$\frac{P_{\frac{1}{2}}(M)}{P_{\frac{1}{2}}(La)}$	P _{1/2}	$\frac{P_{\frac{1}{2}}(M)}{P_{\frac{1}{2}}(La)}$
LaEAT	0.13		0.36	
GdEAT	0.13	1.0	0.38	1.1
DyEAT	0.27	2.1	1.5	4.2
ErEAT	9	69	12.3	34
LaEGT	0.16		0.41	
GdEGT	0.22	1.4	0.47	1.1
DyEGT	0.96	6	2.25	5.5
ErEGT	4	25	10.4	25
LaEPT	0.13		0.36	
GdEPT	0.13	1.0	0.41	1.1
DyEPT	0.41	3.1	1.7	4.7
ErEPT	0.74	5.7	1.74	4.8

The percentage of spin detectable for different probes was calculated by comparing the normalized double integrated intensities for CW spectra of samples with coordinated paramagnetic metals to the double integrals of spectra for the La analogs at 80 and 120 K (Table 5.4). Of the 18 values reported in Table 5.4, 5 are less than 80%. The loss of intensity in the CW spectra is surprising. Even if the signal is broadened, its contribution to the integration of a 200 G spectrum would be expected to be maintained. For future experiments it may be useful to compare integrated intensities for 200 and 400 G scan to ensure that all of the interacting spins are included in the integrals. Differences between percentages observed at 80 and 120 K may be an indication of uncertainty in the values. The substantial loss of intensity for DyEAT may be a factor in the smaller than expected impact of Dy³⁺ on P_{1/2} for DyEAT. The spins that are detected in the CW spectra may be predominantly those with orientations that give weaker dipolar interaction.

Table 5.4 Comparison of percentage of spins detectable for different probes in 1:1 water: glycerol at 80 K and 120 K.

Sample	^a Percentage of spins that are detectable at 80 K	^a Percentage of spins that are detectable at 120 K
GdEAT	100	100
DyEAT	30	23
ErEAT	100	100
GdEGT	100	75
DyEGT	100	82
ErEGT	100	100
GdEPT	100	100
DyEPT	100	100
ErEPT	67	72

^a Calculated by comparing normalized integrals of CW spectra with that for the respective La analog. ^bThe uncertainty is about 10 %.

5.3.4 Intensity loss for spin echo detected spectra

The intensities of the echo-detected spectra of the nitroxide in complexes with paramagnetic metals were compared with that for the La analog to find the percentage of spins detectable in the pulse experiments (Figure 5.18). For GdEGT and GdEPT most of the spins were detectable. However, for all of the other complexes, a substantial fraction of the nitroxide spins were not detected under the conditions of these spin echo experiments. The intensity loss was greatest for the short EAT linker (Figure 5.18). For Er³⁺ the intensity loss was greater for EGT than for EPT (longest linker) but for Dy³⁺ the

intensity loss was similar for EGT and EPT. The signal intensity loss has been observed for other experiments when paramagnetic lanthanide metals were present [24,28,81]. The percentages of spin detectable by spin echo (Figure 5.18) are lower than by CW (Table 5.4). Relaxation enhancement may cause the echo signal to decay within the instrument detection deadtime without broadening the CW spectrum beyond the integrated region.

Some of our experiments were done using τ of 100 ns, but we have seen some instrumental artifacts at this value of τ that can cause more uncertainty in the results. For the EAT and EGT complexes, the percent observable at $\tau = 100$ ns are dramatically lower than at $\tau = 200$ ns (Table 5.5 and 5.6). The only explanation we have thought of for the difference is instrumental artifact. The data need to be acquired again before an interpretation is attained.

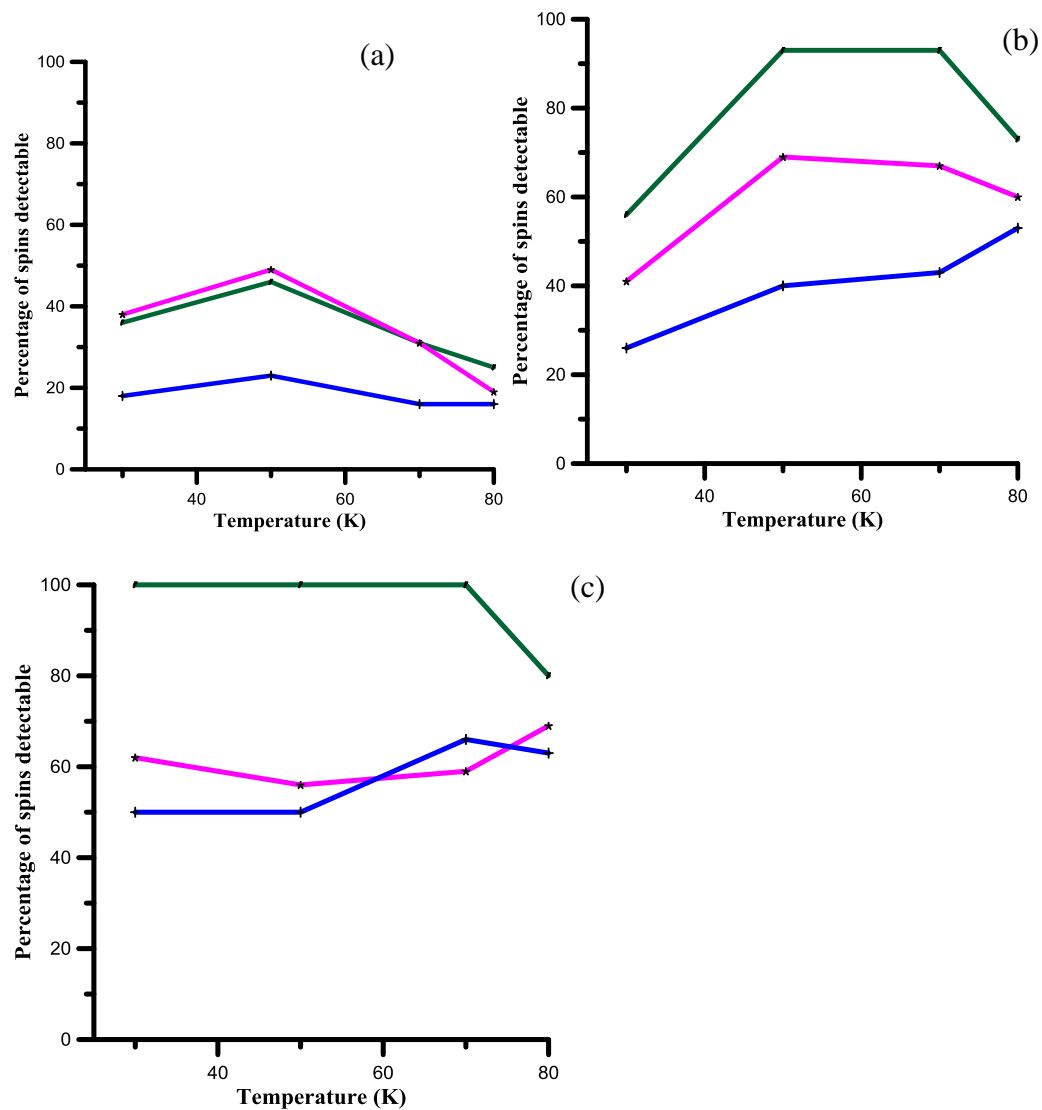


Figure 5.18 Percentage of nitroxide spins detectable in (a) MEAT, (b) MEGT AND (c) MEPT complexes at 30 to 80 K using τ of 100 ns.

M = Gd (green), M = Dy (magenta) and M = Er (blue).

Table 5.5 Nitroxide spins detected^a at τ of 100 ns or 200 ns in 1:1 water: glycerol at 80 K. The uncertainty is about 10 % for τ of 100 ns and 6 to 8 % for τ of 200 ns.

Sample	Intensity ^a for $\tau = 100$ ns	Percent detected ^b	Intensity ^a for $\tau = 200$ ns	Percent detected ^b
LaEAT	3.1		3.2	
GdEAT	1.2	39	2.2	68
DyEAT	1.0	32	1.9	59
ErEAT	0.7	23	2.2	68
LaEGT	3.2		3.7	
GdEGT	2.3	72	3.5	94
DyEGT	1.9	59	2.7	73
ErEGT	1.7	53	2.3	62
LaEPT			3.3	
GdEPT			2.6	79
DyEPT			2.3	69
ErEPT			2.0	61

^a Data were normalized to 60 db video gain, 3 scans and SRT of 2000 μ s. Intensity (divided by 10^6) is reported for the peak of the absorption signal. ^bRelative to the La analog.

Table 5.6 Nitroxide spins detected^a for MEGT complexes at τ of 100 ns or 200 ns in 1:1 water: glycerol at 70 K in field-swept echo-detected spectra. The uncertainty is about 10 % for τ of 100 ns and 6 % for τ of 200 ns.

Sample	Intensity ^a for $\tau = 100$ ns	Percent detected ^b	Intensity ^a for $\tau = 200$ ns	Percent detected ^b
LaEGT	3.3		6.4	
GdEGT	3.0	93	4.1	64
DyEGT	2.2	67	2.4	37
ErEGT	1.4	43	4.1	64

^aData were acquired with 60 db video gain, 3 scans and SRT of 2000 μ s. Intensity (divided by 10^6) is reported for the peak of the absorption signal. ^bRelative to the La analog.

5.3.5 Relaxation enhancement for nitroxides in the metal complexes

In case of MEAT samples, Dy^{3+} and Er^{3+} did not have much appear to effect on spin-lattice relaxation rate ($1/T_1$) (Figure 5.19). However for these metals a large fraction of the spins are not contributing to the echo (Figure 5.18). The effect of these metals on the nitroxide relaxation is seen more clearly on $P_{1/2}$ because more of the spins are detected by CW then by spin echo. Similarly for MEGT samples, there is little difference between $1/T_1$ for the diamagnetic La^{3+} complex and the paramagnetic metal complexes. In the case of MEPT, 61 to 79 % of the spins are detected in the spin echo experiments, so significant relaxation enhancement can be observed directly by measuring $1/T_1$.

In the case of complexes where metal and nitroxide are at fixed distance apart, the relaxation effect at 80 K decreases in the order $\text{Er}^{3+} \sim \text{Dy}^{3+} > \text{Gd}^{3+}$ which is similar to the order that we have observed in the mixtures in chapter 4. In chapter 4, it was observed that the order is $\text{Dy}^{3+} > \text{Er}^{3+} > \text{Gd}^{3+}$.

Data in Figure 5.19 were median values from UPEN [71,72]. The widths of those distribution are summarized in Tables 5.7 and 5.8. The widths of the distributions were calculated as shown in Figure 5.20. Distributions of relaxation times may be present due to two reasons. Firstly, according to the tether-in-a-cone model [98], the tether can acquire different possible angles. These different angles contribute to the intermolecular distribution of distances and relaxation times. Secondly, according to Ref. [24], the g_f values are very anisotropic for lanthanides and have axial symmetry with $g_{\parallel f}$ and $g_{\perp f}$ principal values. Hence g_f can be defined by the equation-

$$g_f = (g_{\perp f}^2 \sin^2 \theta_g + g_{\parallel f}^2 \cos^2 \theta_g)^{1/2} \quad 5.3$$

where θ_g is the angle between the static field and axis of the g tensor of lanthanide. The g-anisotropy gives rise to orientation dependence and hence the B and E terms in equation 4.4 do not reflect the full anisotropy of the interaction. There is lesser effect on C term. [114].

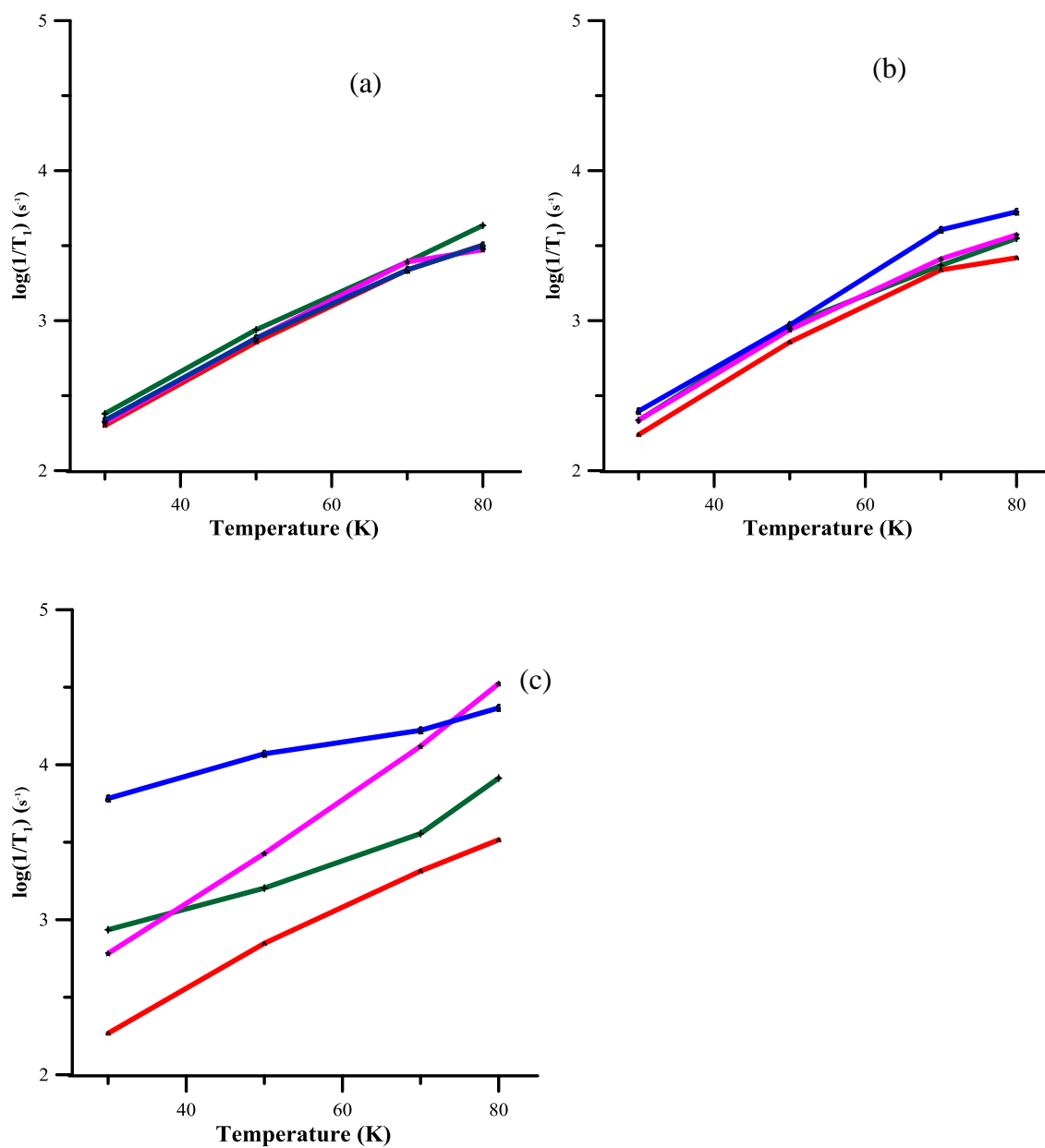


Figure 5.19 Temperature dependence of spin-lattice relaxation rates for nitroxide in (a) MEAT, (b) MEGT and (c) MEPT complexes at 30 to 80 K.

M = La (red), M = Gd (green), M = Dy (magenta) and M = Er (blue). The uncertainty is about 7 %.

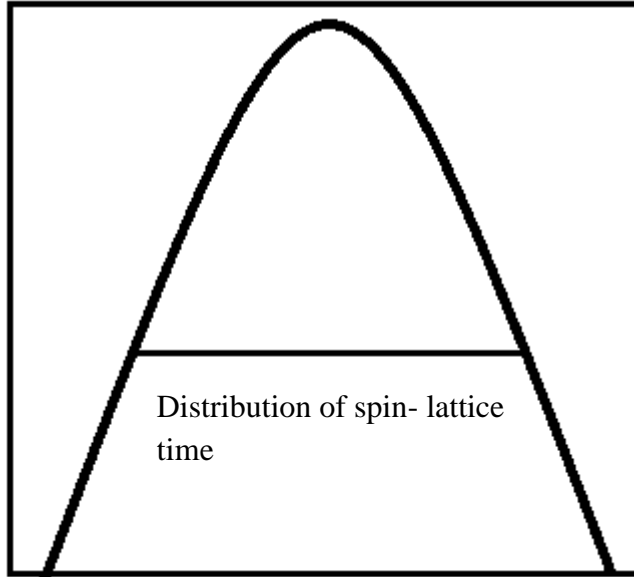


Figure 5.20 The width of distribution of spin-lattice times in the UPEN curve.

Table 5.7 Widths of distribution of spin-lattice times (ms) for nitroxide in different probes as a function of temperature. The uncertainty is about ± 0.5 .

Sample	At 30 K	50 K	70 K	80 K
LaEAT	2.3	1.5	0.4	0.6
GdEAT	6.5	1.1	0.6	0.5
DyEAT	4.3	1.4	0.8	0.8
ErEAT	5.5	1.7	1.0	0.7
LaEGT	6	1.8	0.6	0.4
GdEGT	7.7	1.6	0.6	0.4
DyEGT	6.2	1.4	0.6	0.4
ErEGT	7.9	0.9	0.7	0.4
LaEPT	7.8	1.3	0.8	0.5
GdEPT	6.2	1.8	0.7	0.5
DyEPT	5.3	1.7	0.7	0.5
ErEPT	8.8	1.2	0.7	0.5

Table 5.8 The ratio of the distribution width to the central value of spin-lattice time for nitroxides in probes as a function of temperature. The uncertainty in the ratios is ± 0.3 .

Sample	30 K	50 K	70 K	80 K
LaEAT	0.53	1.0	0.64	0.7
GdEAT	1.2	0.9	1.1	1.0
DyEAT	0.8	1.0	1.8	0.9
ErEAT	1.0	1.1	1.3	0.9
LaEGT	1.0	1.1	1.0	0.7
GdEGT	1.4	1.2	1.1	0.8
DyEGT	1.2	1.0	1.4	0.9
ErEGT	1.3	0.6	1.5	1.0
LaEPT	1.1	1.0	1.1	0.8
GdEPT	1.2	1.2	1.4	0.9
DyEPT	0.8	1.3	1.5	1.0
ErEPT	1.3	1.1	1.1	0.6

For spin-spin relaxation rate ($1/T_2$), there was not much difference in $1/T_2$ of nitroxide when Dy^{3+} and Er^{3+} were coordinated to the other end of the probe but Gd^{3+} increases $1/T_2$. In case of MEAT and MEGT (Figure 5.21), there is not a significant change in $1/T_2$ of nitroxide even with the presence of Gd^{3+} but in case of MEPT (Figure 5.21), Gd^{3+} increases the $1/T_2$ of nitroxide at 30 to 80 K. There is more increase in $1/T_2$ at

80 K as compared to other temperatures. Even Er^{3+} increased the value of $1/T_2$ at 30 K in case of MEPT. The relaxation rate of lanthanide metals is fast at 30 to 80 K, therefore the shape of decay curve depends on the square of dipolar coupling and the value of stretch exponent is equivalent to 2 [65,84]. At temperatures higher than 20 K, Dy^{3+} and Er^{3+} has faster relaxation rates and hence show lesser dipolar coupling, but Gd^{3+} is a slow relaxing lanthanide metal and can affect the echo more and hence increase $1/T_2$ by broadening the signal. The rate $1/T_1$ is affected more by the presence of lanthanides as compared to the values of $1/T_2$ because $1/T_1$ is less affected by the interaction with surrounding magnetic nuclei and hence a smaller relaxation change can be observed [92]. The echo decay curves also may be dominated by the more weakly interacting spins.

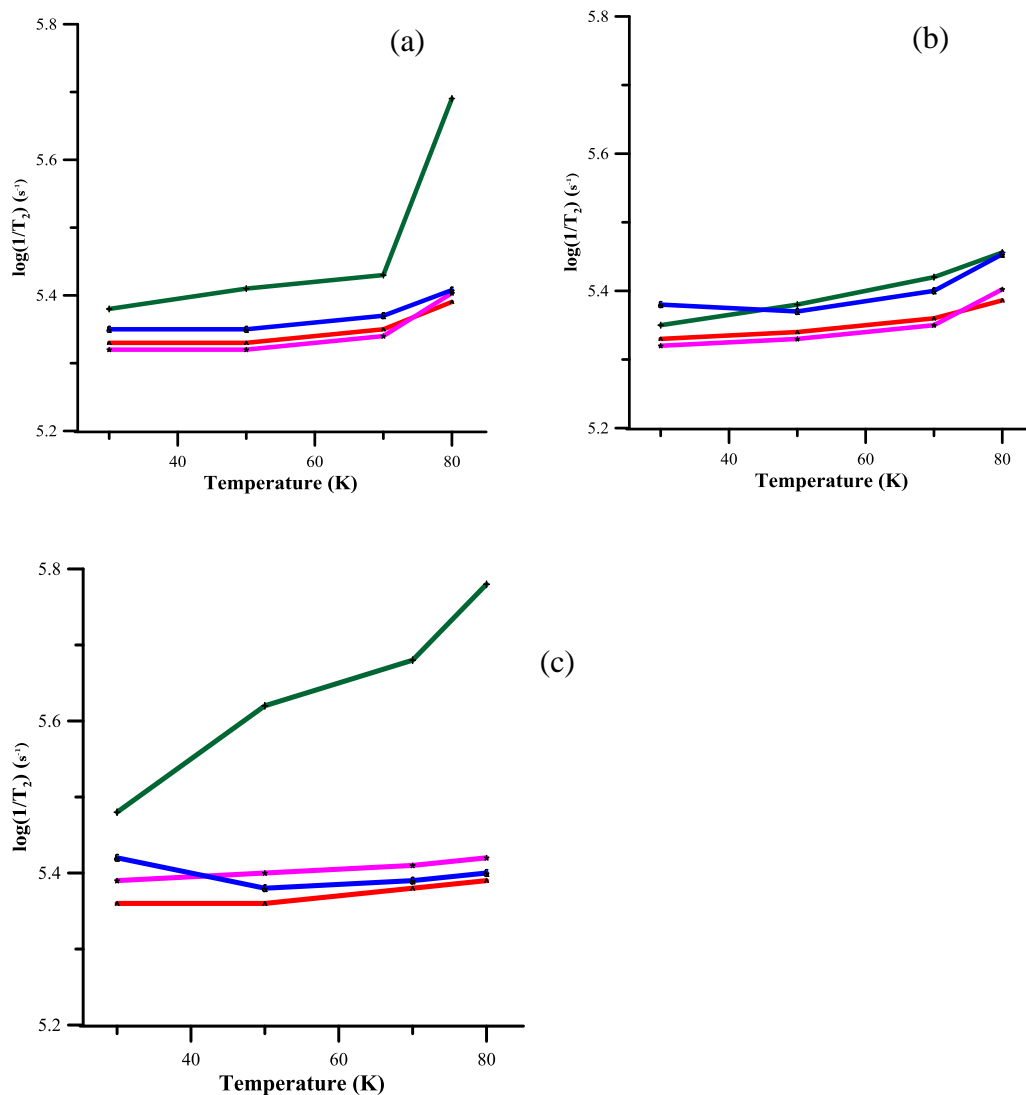


Figure 5.21 Temperature dependence of spin-spin relaxation rates for nitroxide in (a) MEAT, (b) MEGT, and (c) MEPT complexes at 30 to 80 K.

M = La³⁺ (red), M = Gd³⁺ (green), M = Dy³⁺ (magenta) and M = Er³⁺ (blue). The uncertainty is about 5 %.

In conclusion, determination of interspin distances from the relaxation enhancement is complicated by loss of detectable spins under some conditions. The relaxation enhancement at shorter distances from 1.6 to 2.4 nm may be more effectively seen by $P_{1/2}$ measurements. The relaxation enhancement of nitroxide by decreasing T_1 at

60 to 80 K is in the order of $\text{Er}^{3+} \sim \text{Dy}^{3+} > \text{Gd}^{3+}$ for M-EPT with trans- polyproline having distance of 3.4 nm. To better quantify the dependence of relaxation enhancement on the distances, one has to test for detectable spins by checking the difference in amplitude of CW and echo detected spectra when paramagnetic lanthanide is present and when it is absent. One should also check the $P_{1/2}$ in the presence and absence of the paramagnetic lanthanide metals and also it is advisable to check the relaxation times. The combination of all the experiments can give us more useful information about relaxation enhancement of the nitroxide than one measurement alone. The anisotropy of the interaction, and the flexibility of the linkage between the lanthanide and the nitroxide moiety, contribute to the range of interactions observed. Further experiments are needed to explore complementary distance determination methods.

Chapter 6

Gadolinium-loaded P22 virus capsids

6.1 Introduction

Magnetic resonance imaging (MRI) has very low sensitivity. Hence to increase the sensitivity, contrast agents have been used for a very long time. They effect the nuclear relaxation of the water protons present in the tissue and inturn effect the contrast of the image [115]. Relaxivity is the capability of the contrast agents to increase the longitudinal ($1/T_{1n}$ or r_1) or transverse ($1/T_{2n}$ or r_2) relaxation rates of water protons. Most of the contrast agents are Gd^{3+} based because Gd^{3+} has seven unpaired electrons, symmetrical S state, large magnetic moment and long electronic relaxation time. A potential problem is that uncomplexed Gd^{3+} is quite toxic in the blood [116,117]. Mn^{3+} bound to a porphyrin has been used as a contrast agent with reduced toxicity relative to Gd^{3+} [118]. The contrast agents primarily increase the T_1 relaxivity [118-121]. However, for currently available contrast agents T_1 relaxivity decreases with increasing field for fields higher than about 1.5 T. The field used for MRI is increasing and has reached 9.5 T and 11.7 T in various experiments to get a better signal to noise in less time. Hence, there is a need for new MRI contrast agents that work better at higher fields. The contrast

agents that increase the T_2 relaxivity can be better at higher fields because r_2 doesn't decrease with increasing field [122].

The basic requirements to build a good contrast agent are (i) it should not be toxic, (ii) it should have long rotational correlation time and increased relaxivity, (iii) it should be thermodynamically stable. Different people have exploited various approaches to improving contrast agents including dendrimers [121], liposomes [123], and nanoparticles [123]. P22 viral capsids have been used to make improved contrast agents [118,119,124,125]. The bacteriophage P22 viral capsid is bigger than other capsids that have been used such as cowpea mosaic virus (CPMV), cowpea chlorotic virus (CCMV) [120] and bacteriophage MS2 [119]. The benefits of using P22 viral capsids are that their higher molecular weight can decrease the rotational correlation time and increase the relaxivity. The viral capsid is quite stable with temperature change, pH and buffers [119,121]. The P22 capsid is made up of 420 subunits in an icosahedral shape with exterior diameter of 64 nm and internal diameter of 54 nm [119].

The samples that I studied were provided by Dr. Robert Usselman and prepared using a previously published procedure [124]. The P22 virus-like particle protein was expressed in E.coli and self-assembled to give the procapsid (PC) form that had coat protein and scaffold protein. The scaffold protein was removed using guanidine.HCl to give the empty shell (ES) form. The ES form was heated to 65 °C to get the expanded shell (EX). EX was heated further to 75 °C to give the wiffleball form (WB), which did not have pentons at the icosahedral vertices. The P22 viral capsids in the “wiffleball” form have small holes that allow small molecules to diffuse in or out easily [119,124].

The P22 viral capsids were made using site selective polymerization to form encapsulated polymer constrained nanocomposites of 2-aminoethyl methacrylate (AEMA) by atom transfer radical polymerization (ATRP), Figure. 6.1.

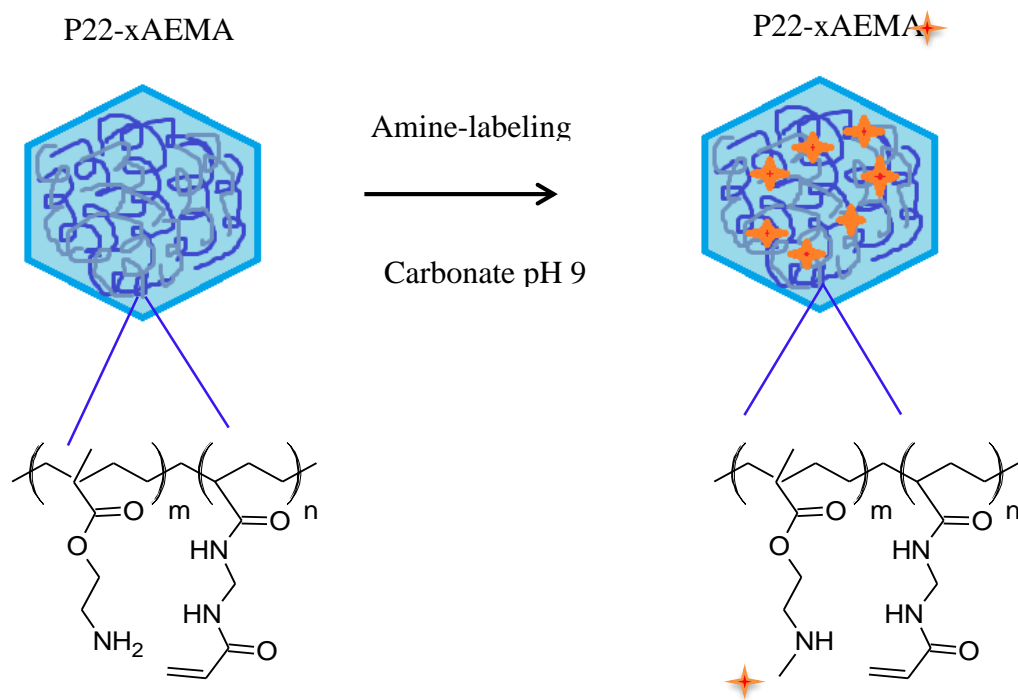
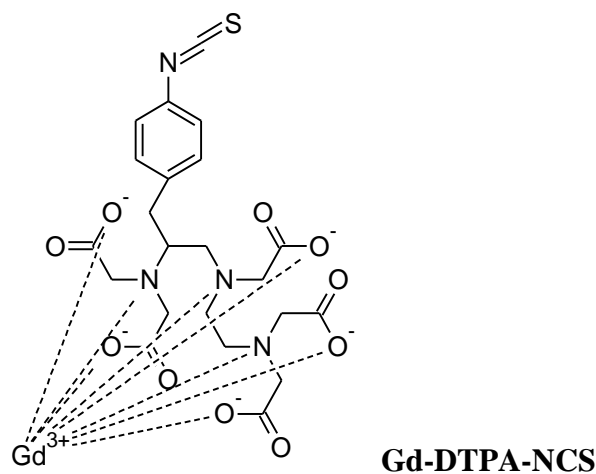


Figure 6.1 Schematic of polymeric P22 particles with spatially confined Gd^{3+} ions. $Gd(DTPA)^{2-}$ was covalently attached to the internal polymer scaffold with loading factors of 1730-10300 $Gd^{3+}/cage$. Figure adapted from Ref. 124 and 125

Gadolinium diethylenetriaminepentaacetate $Gd(DTPA)^{2-}$ was covalently attached to the AEMA polymer network with isothiocyanide linkers to form contrast agents (CAs)

with up to 9100 Gd-DTPA/cage [124]. Polymeric P22-Gd³⁺ constructs have been reported to show enhanced relaxivity and a significantly larger overall particle relaxivity for the polymeric P22-Gd³⁺ than for a P22-Gd³⁺ nanocomposite, comprising shorter oligomers [119]. In these contrast agents, since Gd³⁺ is complexed to DTPA⁵⁻, its toxicity is decreased. These capsids do not grow in size but their mass increases with polymerization, which proves their oligomer growth is mostly confined to the inner part of the capsid and hence most of the Gd (DTPA)²⁻ is attached inside.

In this project, Dr. Robert Usselman did the investigation of nuclear magnetic resonance dispersion (NMRD) and I focused on the EPR of polymeric nanohybrid P22 virus capsids with various Gd³⁺ loading factors [125]. He presented NMRD curves that show these contrast agents behave as enhanced T₁ agents at low magnetic fields and T₂ agents at high magnetic fields. In the NMR results, it can be clearly seen that r₁ relaxivity increased by attaching the contrast agent to the high molecular weight macromolecule, but the r₁ relaxivity decreased at fields greater than 0.49 T. However, the r₂ relaxivity increases with the increase in magnetic field to 7 T [125]. The EPR experiments were done mainly to characterize the P22 viral capsids by exploring the electron relaxation times of the Gd(DTPA)²⁻ attached inside the capsid. The EPR data provide evidence of Gd³⁺-Gd³⁺ dipolar interactions that may lead to enhanced electron spin relaxation. The work performed by Dr. Usselman and reported in Ref. [125] underscores the importance of magnetic field strength and spatial confinement for NMR r₁ and r₂ relaxivity profiles of high density Gd³⁺ paramagnetic nanoparticles. The NMR results presented in Ref.

[125] are of interest to the contrast agent community whose research involves contrast agent design and magnetic field-dependence of relaxivity.

6.2 Experimental Details

6.2.1 Continuous Wave Q-band EPR Spectra at 80 and 150 K

We obtained four samples from Dr. Robert Usselman with different numbers of $\text{Gd}^{3+}/\text{cage}$, which is designated as the loading factor. The samples also had different average (global) concentrations in solution because of the different loading factors (Table 6.1).

Table 6.1 P22 Cage Gd^{3+} loading factors, Gd^{3+} concentrations inside P22 cages, P22 cage concentrations and global Gd^{3+} concentrations.

P22 Loading $\text{Gd}^{3+}/\text{cage}$	Concentration of Gd^{3+} inside P22 cages (mM) ^a	P22 Cage Concentration (nM)	Global Gd^{3+} Concentration (μM)
1.7×10^3	28	102	177
2.9×10^3	46	102	292
4.6×10^3	74	102	469
1.0×10^4	189	22.6	233

^aBased on an interior volume of P22 with the radius of 29 nm.

To estimate the dipolar spin-spin interaction in the P22-Gd³⁺ samples, EPR spectroscopy was used to measure the linewidths as a function of Gd³⁺ loading. Spectra were recorded at 80 or 150 K on a Bruker E580 spectrometer at 34 GHz (Q-band). P22-Gd³⁺ samples for EPR were prepared by adding an equal volume of glycerol to the carbonate buffer (100 mM bicarbonate, 50 mM NaCl, adjusted to pH 9) to ensure glass formation rather than crystallization as the sample was quickly cooled. Samples were transferred into quartz capillaries and centrifuged for 4 min at 1000 X g. Signals were simulated using locally-written software Monmer, based on the equations in Ref. [126].

6.2.2 Power saturation at 80 K

To characterize the changes in electron spin relaxation due to Gd³⁺-Gd³⁺ interactions inside the P22 cages, the amplitudes of the Gd³⁺ EPR signals in the g~ 2 region were recorded at 80 K as a function of microwave power for 2.0 mM Gd(DTPA)²⁻ in pH 9 carbonate buffer: glycerol (1:1) and for P22-Gd³⁺ with 10300 Gd³⁺ /cage. These experiments were performed at X-band (9.7 GHz) because resonator tuning is more reproducible than at the 34 GHz. Signal amplitudes were plotted as a function of \sqrt{P} to obtain a power saturation curve.

6.2.3 Pulsed EPR measurement of Gd³⁺ electron spin relaxation times at 80 K

Pulsed EPR experiments were performed at 80 K on a Bruker E-580 spectrometer at Q- band (34 GHz). Samples of Gd(DTPA)²⁻ in 1:1 water: glycerol and of P22-Gd³⁺ in 1:1 buffer: glycerol were examined. Electron spin-spin relaxation times T_2 were measured by two-pulse spin echo using pulse lengths of 40 and 80 ns for 90° and 180°

pulses, respectively. Incident powers were adjusted to give maximum echo amplitude. The initial time for data acquisition was 200 ns, which is limited by the resonator ring-down. T_1 was measured by inversion recovery using an 80ns-40ns-80ns pulse sequence. T_2 and T_1 were obtained by fitting single or double exponentials to the data using Bruker E-580 software.

6.3 Results

6.3.1 Continuous Wave Q-band EPR Spectra at 80 and 150 K

The EPR spectra extend over hundreds of mT due to zero field splitting (ZFS) of $\text{Gd}(\text{DTPA})^{2-}$. The most prominent features of these spectra are the $m_s = \pm 1/2$ transitions that are observed near $g \sim 2$. These spectral segments are shown in Figure 6.2. After the simulation, we obtained the anisotropic g values: $g_x = 1.964$, $g_y = 1.994$ and $g_z = 1.995$. Within estimated uncertainties, linewidths are the same at 80 and 150 K so average values are shown in Table 6.2. The linewidths probably have contributions from distributions in g values and in ZFS as well as dipolar interactions. The concentration dependent contribution reflects increases in dipolar interactions [122]. Along the g_x and g_y principal axes the linewidths increase dramatically with increasing concentration, consistent with substantial dipolar interactions at these high local concentrations. For the samples with $1.0 \times 10^4 \text{ Gd}^{3+} / \text{cage}$ the linewidths along g_x and g_y are about 9 to 11 mT larger than for $1.7 \times 10^3 \text{ Gd}^{3+} / \text{cage}$, which is a contribution to T_2 of about 1×10^{-10} to 9×10^{-10} s at 80 K. This contribution to T_2 is very large relative to typical T_2 for low concentrations of Gd^{3+} of about 5×10^{-7} s at 80 K (Table 6.3). The strong dipolar

interactions are consistent with the expectations that the Gd^{3+} is concentrated in the interior of the P22 particle [124].

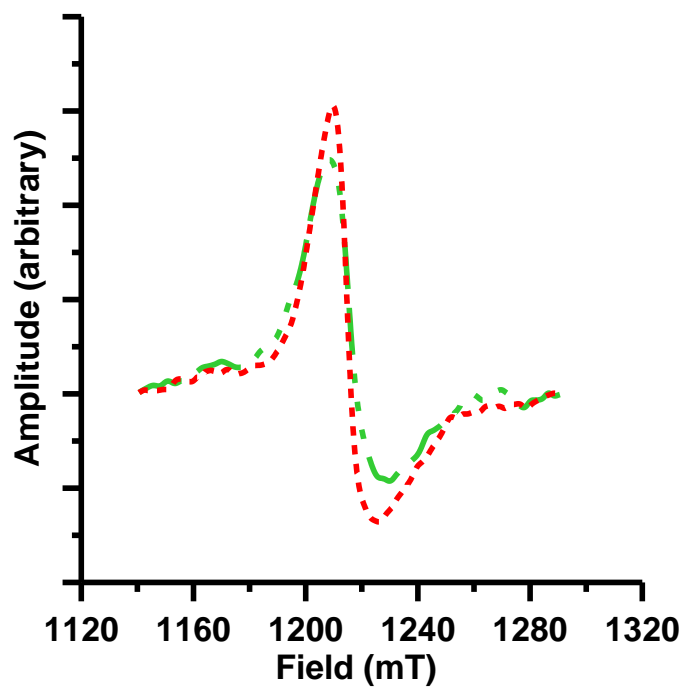


Figure 6.2 Q-band EPR spectra of the $m_s = \pm 1/2$ transitions for P22-Gd³⁺ with 4.6×10^3 Gd³⁺/cage (---) or 1.0×10^4 Gd³⁺/cage (---).

Table 6.2 Average EPR line widths at 80 and 150 K for samples with varying Gd³⁺ concentrations in the P22 cages

P22 Loading Gd ³⁺ /cage	Concentration of Gd ³⁺ inside P22 cages (mM)	P22-Gd ³⁺ EPR Line Widths (mT)		
		g _x	g _y	g _z
1.7x10 ³	28	27	18	7
2.9x10 ³	46	28	23	6
4.6x10 ³	74	34	21	6.3
1.0x10 ⁴	189	36	29	7.2

Uncertainties in line widths are 5%

6.3.2 Power saturation at 80 K

The P22 sample with highest concentration was selected for power saturation experiments, because other samples did not have good enough signal to noise to measure signals at lower powers. The power saturation curve was compared with that for 2 mM Gd (DTPA)²⁻. For the two samples, the highest powers at which the signal increases linearly with \sqrt{P} are shown in Table 6.3. $P_{1/2}$, the power at which the signal amplitude is half of the value predicted in the absence of saturation, also is listed. These measurements indicate that electron spin relaxation at 80 K for the Gd³⁺ in the P22 cages is dramatically

enhanced compared with that for 2.0 mM Gd(DTPA)²⁻. Although the -NCS substituent on the DTPA and attachment to the polymeric framework impacts the local environment such that the ZFS for Gd³⁺ in the P22-DTPA samples is different than for Gd(DTPA)²⁻, the differences in ZFS are likely to cause much smaller changes in relaxation than are caused by the changes in local concentration.

Table 6.3 Power saturation of Gd³⁺ EPR signals at 80 K

Sample	Highest power for linear response	P _{1/2}
2.0 mM Gd(DTPA) ²⁻	0.3 mW	2 mW
1.0 x 10 ⁴ Gd ³⁺ /P22 cage	12 mW	> 200 mW

6.3.3 Pulsed EPR measurement of Gd³⁺ electron spin relaxation times at 80 K

The fit to the inversion recovery curves was substantially better for the sum of two exponentials than for a single exponential, which may reflect overlapping contributions from transitions with different values of m_s . For the P22-Gd³⁺ samples the spin echoes were weak and attributed to small amounts of Gd³⁺ that were not inside the cages. The relaxation times from Gd³⁺ inside the cages were too short to measure by pulsed EPR. Values of T₁ and T₂ for aquo Gd³⁺ and Gd(DTPA)²⁻ are summarized in Table 3.1. Relaxation times are weakly concentration dependent in the range of 0.1 to 2 mM, but become more strongly dependent at higher concentrations.

6.4 Discussion

EPR spectroscopy was used to understand the intra-particle molecular interactions. CW spectra of P22-Gd³⁺ at 80 and 150 K and 35 GHz (1.2 mT) are characteristic of $S = 7/2$ (Fig. 6.2) [125]. The linewidths for the $m_s = \pm 1/2$ transitions increase substantially as the number of Gd³⁺ per cage is increased (Table 6.2), consistent with strong dipole-dipole interactions at the high local concentrations inside the cage. The line broadening indicates large decreases in T_2 . Power saturation curves support the conclusion that the electron spin relaxation rates for P22-Gd are substantially faster than for low concentrations of Gd(DTPA)²⁻ (Table 6.3). The relaxation times for P22-Gd at 80 K are too short to measure by pulsed EPR. Values of T_1 and T_2 for Gd³⁺ and Gd(DTPA)²⁻ at 80 K and 35 GHz obtained by pulsed EPR are about 1 μ s for concentrations in the range of 0.1 to 1 mM, but decrease rapidly at higher concentrations (Table 3.1). These measurements at low temperature suggest that Gd³⁺-Gd³⁺ interactions may also lead to enhanced electron spin relaxation at higher temperatures and magnetic fields. The assumption that T_1 and T_2 are longer than tumbling correlation times is the basis for common models in NMR relaxation enhancement. The two main models that have been used are Curie relaxation and Solomon relaxation and they both have this assumption [120,122]. This assumption however may not be valid for P22 samples especially at high loadings within macromolecular structures. Hence, there is a need for a new model that can actually explain the relaxation in the contrast agents which are inconsistent with this assumption.

Chapter 7

Iron-Sulfur Clusters

7.1 Introduction

Iron is an important transition metal for all three kingdoms of life- bacteria, archaea and eukaryotes. Common oxidation numbers are +2 with $3d^6$ configuration or +3 with $3d^5$ electronic configuration. Iron forms hemes when it is coordinated to porphyrins. It is required for synthesis of chlorophyll in plants. Iron also combines with sulfur to form very important proteins called Iron-Sulfur (Fe-S) proteins. These proteins are the oldest biological cofactors and act as molecular switches in many important functions like catalysis, electron transport and regulatory processes [127-130].

Iron-sulfur clusters were discovered in the 1960s in photosynthetic organisms, nitrogen-fixing bacteria and the mitochondrial fraction of animals. Fe-S clusters have low molecular weight and are water soluble in microorganisms and plants, whereas they are membrane- bound in animals [130]. Iron and sulfur combine in several different molar ratios to form Fe-S clusters. The common Fe-S clusters that were found in the mid-1960's were [2Fe-2S] and [4Fe-4S] that are coordinated to proteins through cysteine residues [129,130]. Their paramagnetic nature was first studied by Sands and Beinert in

1960 using EPR [131,132] in mitochondrial Fe-S clusters of NADH and succinate dehydrogenases enzymes [131,132]. At that time, biochemists could see the Fe-S signal at temperatures ≤ 25 K and found the different components of Fe-S clusters [131]. Fe-S clusters have been extensively studied in vitro because they are easy to assemble in vitro. However, their assembly in vivo is quite complicated because of the multiple biosynthetic pathways and because iron and sulfur both are highly reactive and toxic in vivo. Hence, study of these clusters in vivo has to be done very carefully [128]. Many of the clusters can exist in several oxidation states, so redox potential must be controlled. In addition, some clusters are easily removed from the protein and have to be reconstituted after protein isolation.

All the three kingdoms have multiple pathways for Fe-S clusters assembly. The main component of their assembly is cysteine desulfurase. The cysteine desulfurase enzyme breaks the disulfide bonds of cysteine and helps in releasing sulfur required for the assembly. The cysteine is converted to alanine after donating the sulfur. The sulfur is then taken by the other protein called the scaffold protein where along with iron it forms [2Fe-2S]. Sometimes, [2Fe-2S] is transferred to the target apo-protein to make it active. In some of the other scaffold proteins [2Fe-2S] converts to [4Fe-4S]. Then, [4Fe-4S] clusters move to the target apo-proteins [127,128]. The conversion of [2Fe-2S]²⁺ to [4Fe-4S]²⁺ involves reductive coupling and is a very slow process. One electron reduction and coupling of two adjacent clusters of [2Fe-2S]²⁺ give [4Fe-4S]²⁺. Reductive coupling is mostly an irreversible process, but it has been seen that an [4Fe-4S]²⁺ cluster oxidizes back to [2Fe-2S]²⁺ with exposure to O₂. In vitro, reductive coupling can be done using

dithionite as a reducing agent [127,128]. In some of the hydrogenase, aconitase, and radical S-adenosylmethionine enzymes, $[3\text{Fe-4S}]^+$ clusters were also observed [133-136]. In the 1980s, the $[3\text{Fe-4S}]^+$ cluster was found and studied in beef mitochondrial aconitase. It was also found that EPR active $[3\text{Fe-4S}]^+$ converts to the EPR inactive $[3\text{Fe-4S}]^0$ form at pH greater than 9.5. Then, this $[3\text{Fe-4S}]^0$ can be easily converted to EPR active $[4\text{Fe-4S}]^{2+}$ clusters by reduction in the presence of iron [133,134].

In 2001, S-adenosyl methionine (SAM) was classified as a superfamily of proteins that catalyzes radical reactions. SAM is needed for the activation of many enzymes including pyruvate–formate lyase activating enzyme (PFL-AE), hydrogenase related (HydE and HydF) enzymes, lysine 2,3-aminomutase (LAM) enzyme [136-138], and enzymes that have roles in the Mycofactin (Mft) biosynthetic pathway in *Mycobacterium Tuberculosis* [139]. The SAM superfamily has a characteristic motif $\text{CX}_3\text{CX}_2\text{C}$ where three cysteine molecules bind to three of the four irons of a $[4\text{Fe-4S}]$ cluster. The coordination of the fourth iron varies with the surrounding environment. The fourth iron is labile in these $[4\text{Fe-4S}]$ proteins and in SAM proteins, therefore $[3\text{Fe-4S}]^+$ is also found in some air exposed samples for these proteins [136]. When $[4\text{Fe-4S}]$ binds to SAM, it cleaves SAM and forms 5'-deoxyadenosyl radical ($5'\text{-dA}\cdot$) and methionine. The $5'\text{-dA}\cdot$ radical acts as an oxidizing agent and can oxidize H_2 to form protons [136].

EPR can help in characterizing different types of Fe- S clusters in proteins. It can also tell us about the relaxation behavior of the clusters. In this chapter, I will focus on EPR spectra of several kinds of clusters and their relaxation behavior to know more about the proteins. We received SAM enzyme samples of PFL-AE, HydE and HydF from Dr.

Eric Shepard, Montana State University (MSU) and oxidized and reduced MtfC samples from Dr. John A. Latham, University of Denver.

7.2 PFL-AE, HydE and HydF samples

7.2.1 Experimental Details

The samples were frozen and shipped from MSU in a dry shipper (77 K). The following descriptions of the samples were provided by Dr. Usselman. Samples 1 and 2 are of well-characterized proteins provided as reference materials, and samples 3 and 4 are for a protein (HydF) that the group at MSU seeks to characterize.

1. PFL-AE is a monomeric radical SAM enzyme that contains a single FeS cluster binding site. X-band EPR spectra at MSU had shown that the vast majority of the as-purified enzyme harbors a $[3\text{Fe-4S}]^+$ cluster in this site. The remaining enzyme binds a $[2\text{Fe-2S}]^+$ cluster. The PFL-AE sample has 1.68 mM protein with an Fe number of 2.70 ± 0.10 Fe/protein.
2. Ca HydE, is also a monomeric radical SAM enzyme. It contains two FeS cluster motifs that are located ~ 20 Å apart. The as-reconstituted enzyme binds a $[3\text{Fe-4S}]^+$ in the first motif and a $[2\text{Fe-2S}]^+$ in the second motif. The HydE sample had 344 μM protein with an Fe number of 7.64 ± 0.10 Fe per protein.
3. $\text{HydF}^{\text{AEG}} + \text{DTT}$ is isolated HydF + dithiothreitol. This sample had 207 μM protein with an Fe number of 1.09 ± 0.04 Fe/monomer. Work at MSU showed the presence of $[3\text{Fe-4S}]^+$ and $[2\text{Fe-2S}]^+$.

4. HydF^{ΔEG} Reduced is a reduced sample of the HydF enzyme which exhibits both [2Fe-2S]⁺ and [4Fe-4S]⁺ cluster signals. Two replicate samples were received. Reduced HydF had 1.20 mM protein with an Fe number of 0.57 ± 0.04 Fe per protein monomer.

X-band continuous wave (CW) and pulsed EPR data were acquired on a Bruker E580 spectrometer using a split ring resonator and an Oxford ESR935 cryostat. Spin-spin relaxation times, T_2 , were measured by two-pulse spin echo using a 90°-180° pulse sequence and a 90° pulse length of 40 ns. Field-swept echo-detected spectra were recorded with a constant $\tau = 100$ ns and were background-corrected by subtracting an off-resonance scan. Spin-lattice relaxation was measured by inversion recovery using a 90°-180°-90° pulse sequence and a 90° pulse length of 40 ns. For the [2Fe-2S]⁺ cluster, measurements were performed at $g_{\perp}=2.006$ and at an intermediate g value of 1.99, which is higher than $g_{\parallel} = 1.97$. For the [3Fe-4S]⁺ cluster, measurements were performed at $g_{\perp}=2.02$, and $g = 1.89$ was used for measurements for [4Fe-4S]⁺. There did not appear to be significant anisotropy in T_1 . The spin echo decays and inversion recovery curves were fit to a single exponential, unless otherwise noted. Uncertainties in time constants are about 10%.

The g values and inhomogeneous broadening of the low temperature CW spectra were found by simulation using the locally-written program MONMER that is based on the equations in [126]. The g_{\perp} regions of the temperature-dependent CW spectra at 110 to 150 K were simulated using SATMON in which the line shape is a Gaussian distribution of Lorentzian spin packets characterized by T_2 [140]. In the temperature

range in which line widths are temperature-dependent it was assumed that $T_1 = T_2$ for $[2\text{Fe-2S}]^+$. A detailed description of the calculations is in [141]. The temperature dependence of T_1 for $[2\text{Fe-2S}]^+$ was fit with the function [141]

$$\frac{1}{T_1} = C_{dir} + C_{Ram} \left(\frac{T}{\theta_D}\right)^9 J_8\left(\frac{\theta_D}{T}\right) + C_{orb} \frac{\Delta_{orb}^3}{e^{\Delta_{orb}/T} - 1} \quad (7.1)$$

where T is the temperature in Kelvin, C_{dir} is the contribution from the direct process, C_{Ram} is the coefficient for the contribution from the Raman process, θ_D is the Debye

temperature, J_8 is the transport integral, $J_8\left(\frac{\theta_D}{T}\right) = \int_0^{\theta_D/T} x^8 \frac{e^x}{(e^x - 1)^2} dx$, C_{orb} is the coefficient

for the contribution from the Orbach process, and Δ_{orb} is the energy separation between the ground and excited state for the Orbach process.

7.2.2 CW and Field Swept Echo Detected Spectra

7.2.2.1 PFL-AE

The $[2\text{Fe-2S}]^+$ signal with $g_{\perp} = 2.006$ and $g_{\parallel} = 1.96$ was the only signal seen at 50 - 78 K in the CW spectra (Figure 7.1). The shape of the CW spectra changed at temperatures lower than 50 K. A new peak at $g = 2.02$ was observed at 40 K and below (Figure 7.1) and assigned to $[3\text{Fe-4S}]^+$. The g -value is in accordance with the work of Shepard et. al [142-144]. In the CW spectra, the $[3\text{Fe-4S}]^+$ signal was observed at 40 K and below, but in the field-swept echo-detected spectra, it was not visible above 22 K (Figure 7.2). First integrals of CW spectra and field-swept echo-detected spectra exhibited the same peaks below about 20 K (Figure 7.3). At 21 K and below, the field-swept echo-detected spectrum was dominated by the $[3\text{Fe-4S}]^+$ and the apparent center

shifted from $g = 2.006$ characteristic of $[2\text{Fe-2S}]^+$ toward $g = 2.02$ for the $[3\text{Fe-4S}]^+$ signal that was consistent with previous reports [142-145].

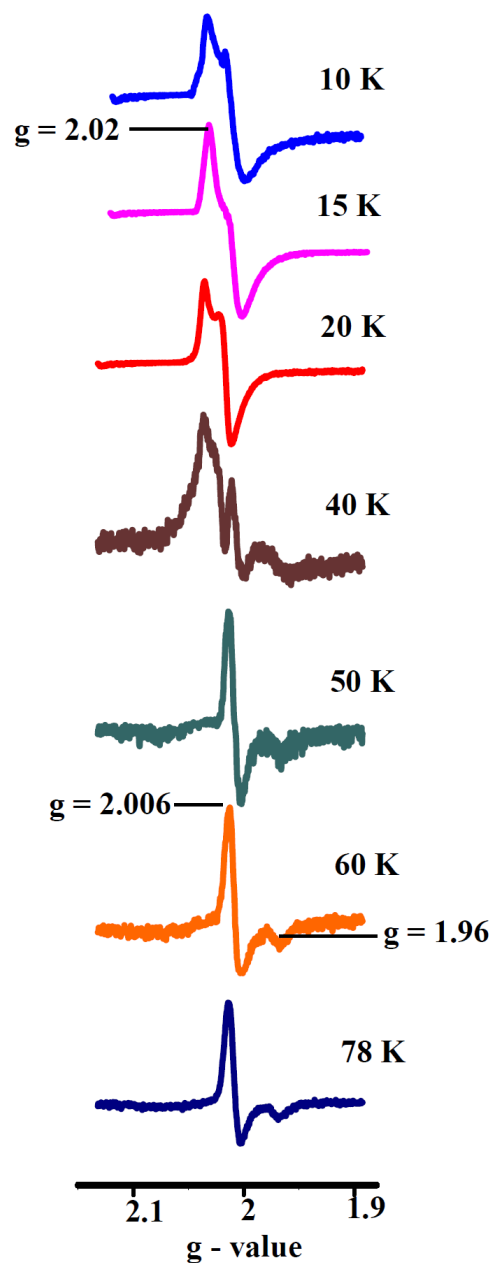


Figure 7.1 X-band (9.42 GHz) CW spectra of PFL-AE at 10 - 70 K.

The spectra were obtained with 1 G modulation amplitude, 400 G sweep width, and 0.755 mW power. The $g = 2.006$ and 1.96 correspond to the $[2\text{Fe-2S}]^+$ signal and $g = 2.02$ corresponds to the $[3\text{Fe-4S}]^+$ signal. The $[2\text{Fe-2S}]^+$ species signal is power saturating at and below 40 K. Signals were plotted with constant y axis amplitude.

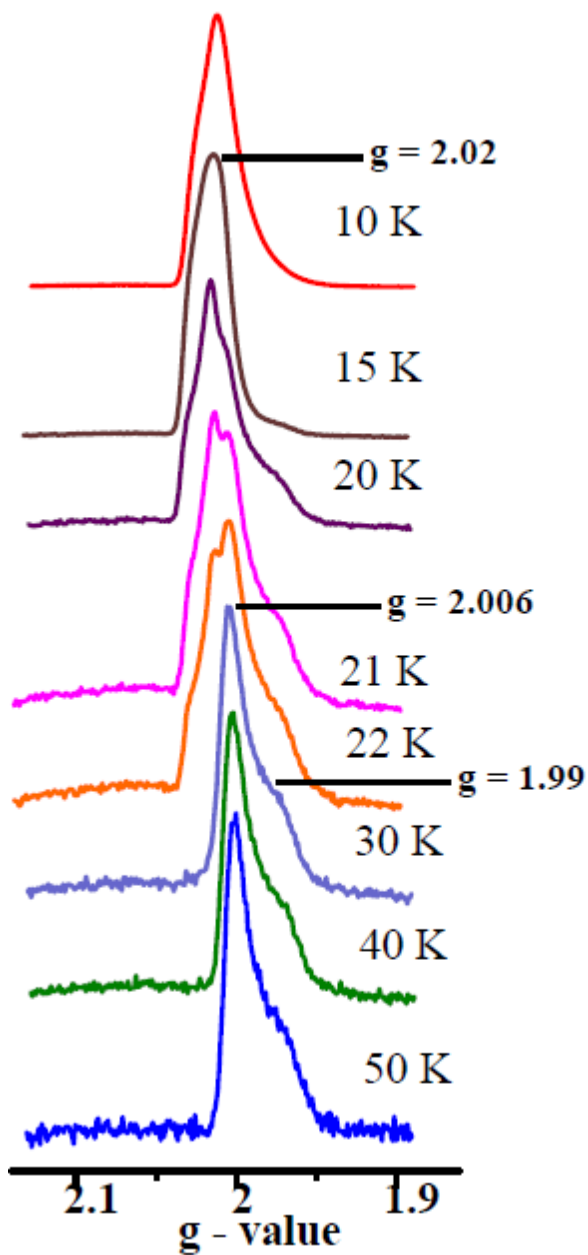


Figure 7.2 X-band (9.424 GHz) two-pulse field-swept echo-detected spectra of PFL-AE at 10 – 50 K.

The spectra were obtained with 400 G sweep width. The echo was weak above 50 K. The shot repetition time (SRT) used for spectra at 30 – 60 K was 800 μ s, 1099 μ s at 20 K and 3000 μ s at 10 - 15 K. Signals were plotted with constant y axis amplitude.

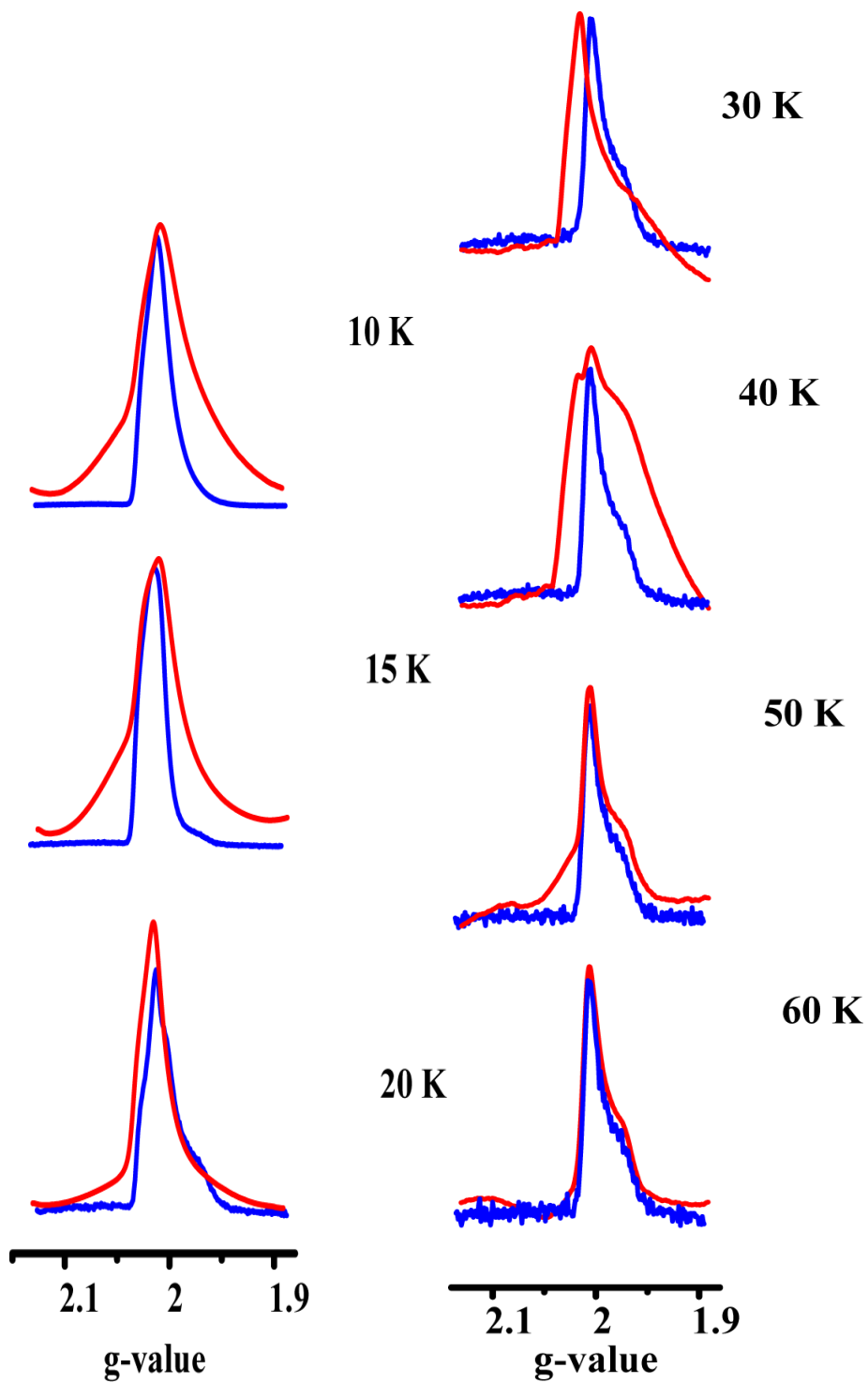


Figure 7.3 Comparison of field-swept echo-detected spectra and integrals of CW spectra at 10 to 70 K for PFL-AE.

The field-swept echo-detected spectra (from Figure 7.2) are in blue and integrals of CW spectra (from Figure 7.1) are in red. Signals were plotted with constant y axis amplitude.

7.2.2.2 *Ca HydE*

The $[2\text{Fe-2S}]^+$ signal at $g_{\perp} = 2.006$ was seen in CW and field-swept echo-detected spectra (Fig 7.4 and 7.5) of *Ca HydE* in the same temperature ranges as for PFL-AE. The signal to noise in the CW spectra is lower than in Figure 7.1 because the concentration of this sample was five times lower than the concentration of the PFL-AE sample. The peak at about 2.06 is due to a resonator background signal. The echo was not strong above 40 K, so field-swept echo and relaxation studies were done at 10 – 40 K. The signal from $[3\text{Fe-4S}]^+$ was too fast relaxing at 10 K to contribute to the echo-detected spectrum.

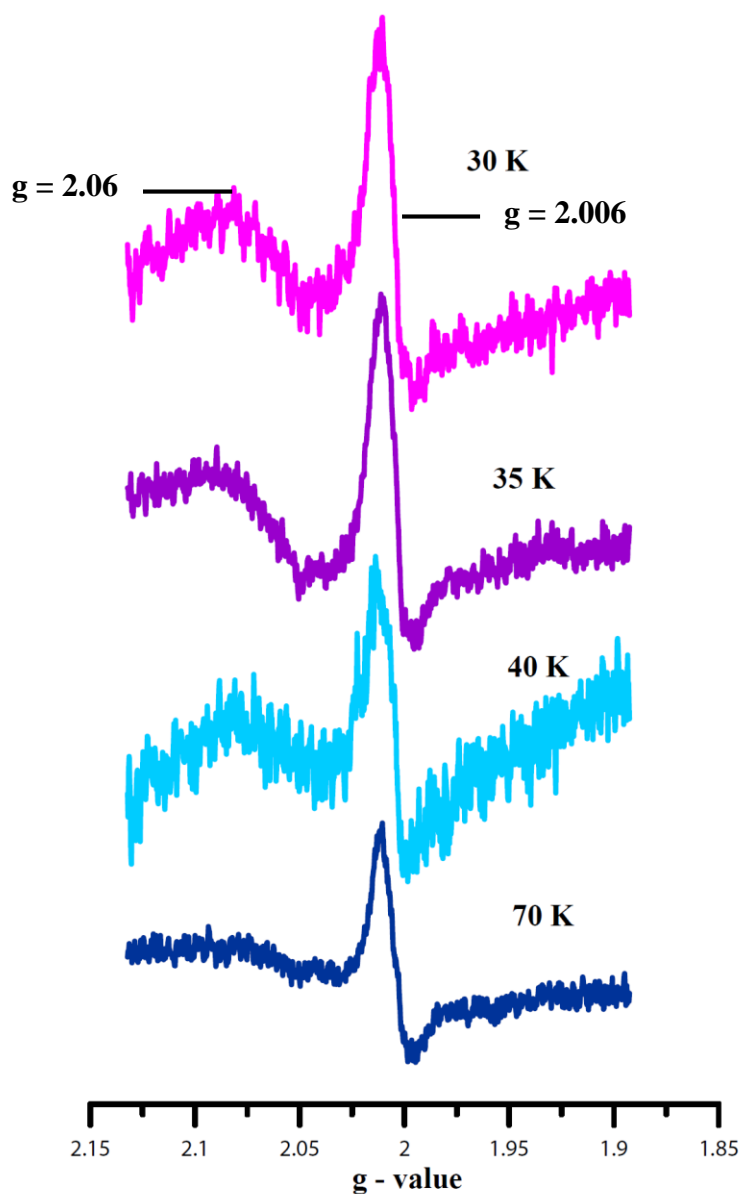


Figure 7.4 CW spectra at X-band of the $[2\text{Fe-2S}]^+$ in Ca HydE, at 30 -70 K.

The spectra were obtained with 1 G modulation amplitude and 400 G sweep width. CW spectra were obtained at 0.755 mW power at all temperatures. The frequency was 9.40 GHz. The signal at $g = 2.06$ is the background signal from the resonator. Spectral amplitude was corrected for differing numbers of scans. Relative amplitudes in the plotted data reflect the temperature dependence of signal amplitude.

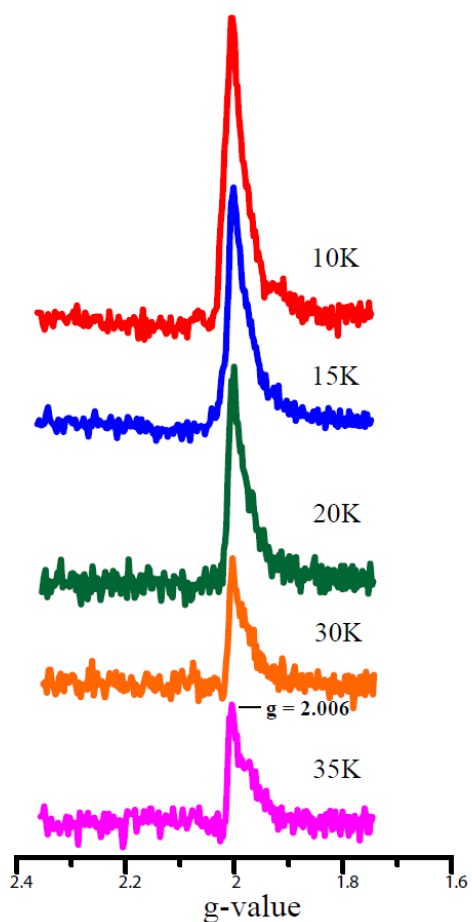


Figure 7. 5 X-band (9.43 GHz) two-pulse field-swept echo-detected spectra of the $[2\text{Fe-}2\text{S}]^+$ in Ca HydD at 10 – 70 K.

The spectra were obtained with 400 G sweep widths. Spectral amplitude was corrected for differing numbers of scans. Relative amplitudes in the plotted data reflect the temperature dependence of signal amplitude.

7.2.2.3 $\text{HydF}^{\text{AEG}} + \text{DTT}$

The $[2\text{Fe-}2\text{S}]^+$ signal at $g_{\perp} = 2.006$ was seen in field-swept echo-detected spectra of $\text{HydF}^{\text{AEG}} + \text{DTT}$ (Figure 7.6). Field-swept echo and relaxation studies were done at 10 – 70 K.

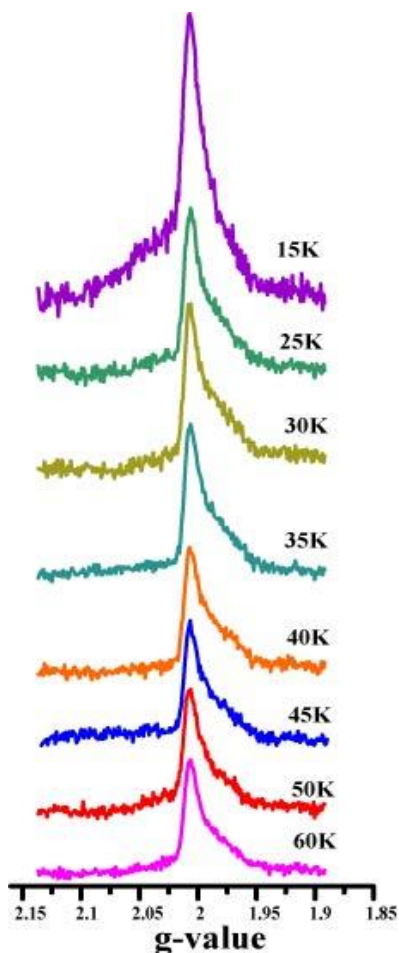


Figure 7. 6 X-band (9.24 GHz) two-pulse field-swept echo-detected spectra of HydF^{ΔEG} + DTT at 10 – 70 K.

The spectra were obtained with 400 G sweep widths. Spectral amplitude was corrected for differing numbers of scans. Relative amplitudes in the plotted data reflect the temperature dependence of signal amplitude.

7.2.2.4 HydF^{ΔEG} Reduced

The [2Fe-2S]⁺ signal with $g_{\perp} = 2.006$ and $g_{\parallel} = 1.96$ was seen at 10 – 40 K in the CW spectra of HydF^{ΔEG} Reduced (Figures 7.7, 7.8). The spectra in Figures 7.7 and 7.8 were taken using different microwave powers. In Figure 7.7, the signal for [2Fe-2S]⁺ was

saturated due to excessive power. The shape of the CW spectra changed at temperatures lower than 30 K (Figure 7.7). A new peak at $g = 1.89$ was observed below 30 K (Figure 7.7, 7.8), which is assigned to the $[4\text{Fe-4S}]^+$. The low g -value shows that all the four irons of the $[4\text{Fe-4S}]^+$ clusters are not linked to cysteine. Three out of four irons are coordinated to cysteines of the SAM motif and one iron is coordinated to some other ligand [144,145]. In field-swept echo-spectra, the $[4\text{Fe-4S}]^+$ signal could be observed at or below 30 K (Figure 7.9) but the signal to noise was very low, because of the low sample concentration. The field-swept echo spectra were taken at longer and shorter Shot Repetition Times (SRT) for better separation of signals from the two species. At shorter SRT, the signal for the faster relaxing species $[4\text{Fe-4S}]^+$ could recover more fully between pulses than the signal for the slowly relaxing species (Figures 7.9 and 7.10).

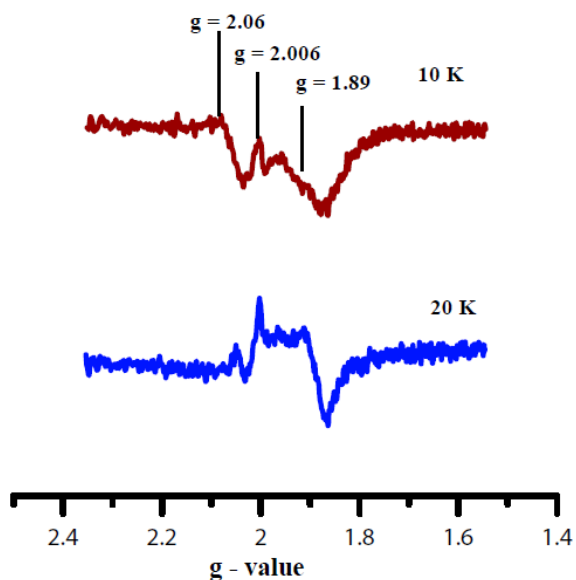


Figure 7.7 X-band CW spectra of HydF^{AEG} Reduced at 10 - 20 K.

The spectra were obtained with 1 G modulation amplitude, 0.76 mW and 2000 G sweep width. Spectra were not background subtracted. At this power the signal for $[2\text{Fe-2S}]^+$ is power saturated.

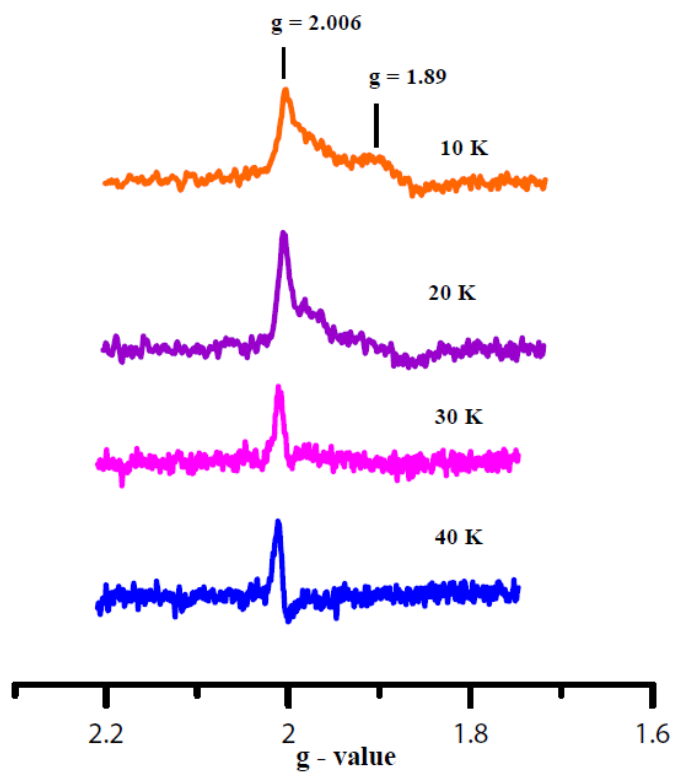


Figure 7.8 X-band (9.43 GHz) CW spectra of HydF^{ΔEG} Reduced at 10 – 40 K. The spectra were obtained with 1 G modulation amplitude and 0.024 mW power. The sweep width is 1000 G.

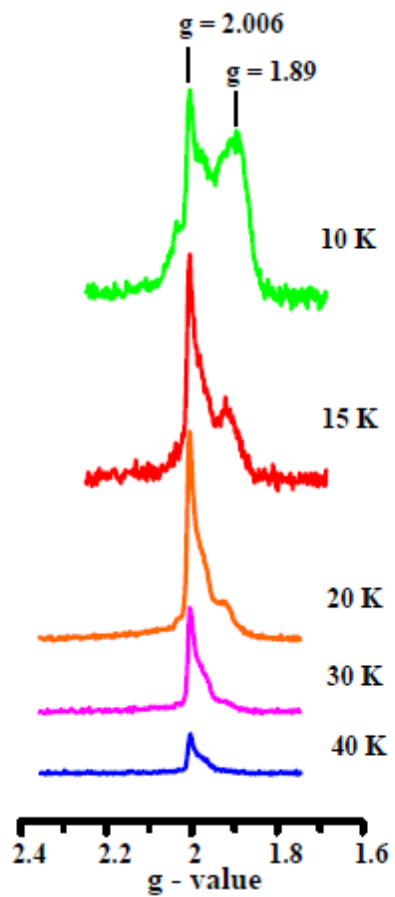


Figure 7.9 X-band (9.43 GHz) two-pulse field swept echo detected spectra of HydF^{ΔEG} Reduced at 10 – 40 K.

The spectra were obtained with 1000 G sweep widths. The shot repetition time (SRT) was 775 μs at 40 K, 1499 μs at 30 K, 1999 μs at 20 K, 15995 μs at 15 K and 30998 μs

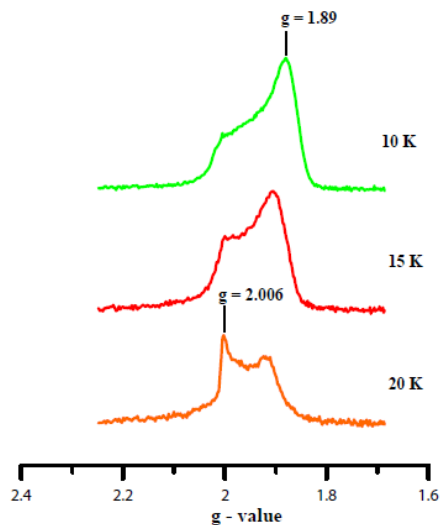


Figure 7.10 X-band (9.43 GHz) two-pulse field-swept echo-detected spectra of HydF^{ΔEG} Reduced at 10 – 20 K.

The spectra were obtained with 1000 G sweep widths. The shot repetition time (SRT) was 49.98 μs.

7.2.3 Electron Spin Relaxation

7.2.3.1 Comparison of relaxation rates of [2Fe-2S]⁺ clusters

Direct measurements of T_1 and T_2 for [2Fe-2S]⁺ in HydF and related samples were obtained by inversion recovery and spin echo decay at temperatures below about 60 K. Below about 20 K, overlap with the much broader signals from [4Fe-4S]⁺ or [3Fe-4S]⁺ made it difficult to distinguish contributions to the pulse EPR signals. The temperature dependence of $1/T_2$ measured by spin echo is shown in Figure 7.11. Values of T_2 below 40 K are approximately independent of temperature and T_2 is between about 1.5 and 1.9 μs, which is in the range that is found for many $S = 1/2$ species at relatively low spin concentrations [141]. The temperature independence below about 40 K suggests that the spin-spin relaxation is dominated by nuclear spin diffusion among the many proton spins in the vicinity of the iron-sulfur clusters. Above about 40 K the values

of T_2 become strongly temperature dependent due to the increasingly fast spin-lattice relaxation and its contribution to T_2 .

The temperature dependence of $1/T_1$ for $[2\text{Fe-2S}]^+$ in HydF and related samples is summarized in Figure 7.12. Values of T_1 below about 60 K were obtained by inversion recovery, and values above about 150 K were obtained by analysis of the temperature dependent contributions to the CW lineshapes. The relaxation rates for the four samples studied are similar. The relaxation rates for these clusters are more than an order of magnitude slower than have been reported previously for $[2\text{Fe-2S}]^+$ clusters [146]. The relaxation rates for PFL-AE and off-column HydF + dithiothreitol were modeled as the sum of contributions from the Raman and Orbach processes (Eq. 7.1). There is substantial uncertainty in the Debye temperatures because there is a relatively narrow temperature range (about 15 to 35 K) in which the Raman process dominates. The Orbach process dominates at higher temperatures. The Orbach energies for the $[2\text{Fe-2S}]^+$ clusters in PFL-AE and in HydF are 500 ± 50 K (350 ± 35 cm^{-1}) which is approximately in the middle of the range of previously reported values [146-148]. The coefficients for the Raman process, C_{Ram} , that were used to generate the fit lines shown in Figure 7.20 are about 10^7 $\text{s}^{-1} \text{K}^{-9}$ which is several orders of magnitude smaller than the $\sim 10^{10}$ $\text{s}^{-1} \text{K}^{-9}$ reported for other $[2\text{Fe-2S}]^+$ clusters [146]. Similarly, the values of C_{orb} for HydF are about 15 $\text{s}^{-1} \text{K}^{-3}$, which is more than an order of magnitude smaller than the $\sim 10^3$ $\text{s}^{-1} \text{K}^{-3}$ reported for other $[2\text{Fe-2S}]^+$ clusters [146]. The smaller coefficients are expected because the rates are so much slower. Small spin-orbit coupling leads to slower electron spin relaxation [146,149]. The g-value anisotropy for the $[2\text{Fe-2S}]^+$ in HydF is

only $2.006 - 1.96 = 0.046$, which is very much smaller than reported for other $[2\text{Fe-2S}]^+$ such as the Rieske cluster from cytochrome bc_1 ($2.0265 - 1.7670 = 0.2595$) [146]. Smaller g anisotropy indicates smaller spin-orbit coupling. It has also been proposed that the coefficients for the Raman and Orbach processes are smaller for more rigid systems [113,146]. The very small values of C_{Ram} and C_{orb} for the $[2\text{Fe-2S}]^+$ clusters in HydF and related proteins suggests that the environment of the cluster in these systems is relatively rigid.

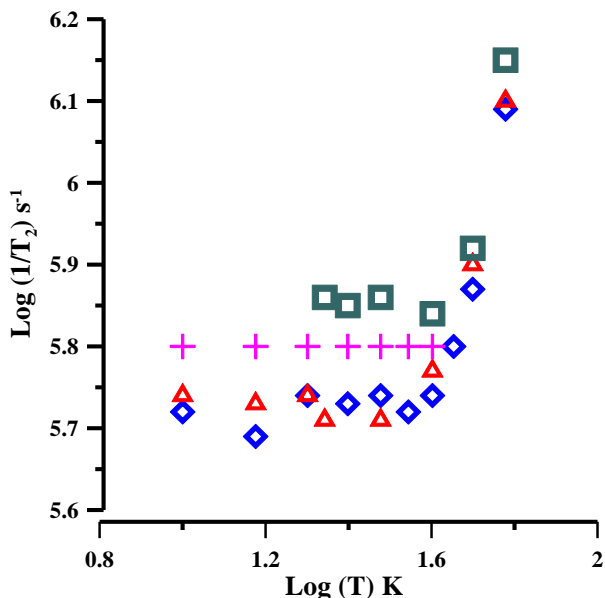


Figure 7.11 Temperature dependence of X-band spin-spin relaxation rates at $g = 2.006$ for $[2\text{Fe-2S}]^+$ in the different proteins.

The proteins are: PFL-AE (■), HydE (+), Photoreduced HydF (△) and Off-column HydF + dithiothreitol by (◇).

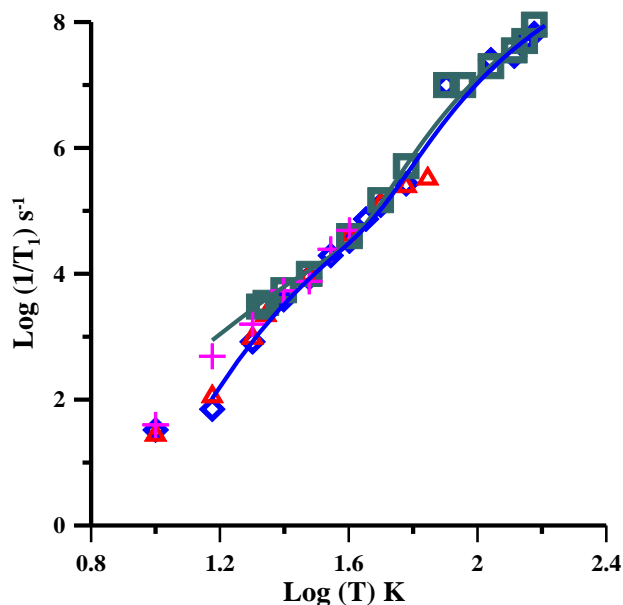


Figure 7.12 Temperature dependence of X-band spin-lattice relaxation rates at $g = 2.006$ for $[2\text{Fe-2S}]^+$ in the different proteins.

The proteins are: PFL-AE (\square), HydE ($+$), photoreduced HydF (Δ) and Off-column HydF + dithiothreitol (\diamond). The solid lines are the modeling of the relaxation rates for PFL-AE (—) and off-column HydF + dithiothreitol (—) as the sum of contributions from the Raman and Orbach processes.

7.2.3.2 Comparison of relaxation rates for $[2\text{Fe-2S}]^+$, $[3\text{Fe-4S}]^+$, and $[4\text{Fe-4S}]^+$

The relaxation times for the two clusters in PFL-AE below 25 K are shown in Table 7.1 and for HydF^{AEg} Reduced in Table 7.2.

Table 7.1 T_2 and T_1 at $g = 2.006$ ($[2\text{Fe-2S}]^+$) and at $g = 2.02$ ($[3\text{Fe-4S}]^+$) in PFL-AE^a

	$[2\text{Fe-2S}]^+$ $g=2.006$	$[2\text{Fe-2S}]^+$ $g=2.006$	$[3\text{Fe-4S}]^+$ $g=2.02$	$[3\text{Fe-4S}]^+$ $g=2.02$
Temperature (K)	T_2 (μs)	T_1 (μs)	T_2 (μs)	T_1 (μs)
10	1.25 ^b	2350 ^b	1.3	1040
15	0.934 ^b	851 ^b	1.01	461
20	1.43	630		

^a Uncertainty is 9%. ^b Overlap with the signal from $[3\text{Fe-4S}]^+$ introduces uncertainty for these values. It is difficult to distinguish the contributions to the echo decay and recovery curves from the two species.

Table 7.2 T_2 and T_1 at $g = 2.006$ ($[2\text{Fe-2S}]^+$) and 1.89 ($[4\text{Fe-4S}]^+$) in $\text{HydF}^{\Delta\text{EG}}$ Reduced.^a

	$[2\text{Fe-2S}]^+$ $g = 2.006$	$[2\text{Fe-2S}]^+$ $g = 2.006$	$[4\text{Fe-4S}]^+$ $g = 1.89$	$[4\text{Fe-4S}]^+$ $g = 1.89$
Temperature (K)	T_2 (μs)	T_1 (μs)	T_2 (μs)	T_1 (μs)
10	1.82	36000	1.7	263
15	1.86	9000	1.8	186
20	1.82	1050	0.71	81
22	1.95	454	0.36	22

^a Uncertainty is 7%

The relaxation rate differences between $[2\text{Fe-2S}]^+$ and $[3\text{Fe-4S}]^+$ in PFL-AE also explain the differences between the field-swept echo spectra and integrals of CW spectra at different temperatures. The $[3\text{Fe-4S}]^+$ signal at 40 K was not seen in the field-swept echo-detected spectra of PFL-AE because it was relaxing very fast (Figure 7.3). Analysis of the shapes of inversion recovery curves at and below 20 K, indicated that there was a very fast relaxing component. The fast relaxing component might be spectral diffusion between different clusters and enhanced by the relatively high concentration of $[3\text{Fe-4S}]^+$. Fitting to the initial portions of the inversion recovery curves suggests spectral diffusion time constants of 5 - 8 μs at both $g = 2.006$ and 2.02.

T_2 and T_1 relaxation times at $g = 2.006$ and 1.89 for $\text{HydF}^{\Delta\text{EG}}$ Reduced were also measured. Values of T_2 and T_1 in Table 7.2 show that the $[2\text{Fe-2S}]^+$ clusters ($g = 2.006$ and 1.99) relaxed more slowly than $[4\text{Fe-4S}]^+$ ($g = 1.89$) in the range of 10-22 K. The relaxation of the $[2\text{Fe-2S}]^+$ in PFL-AE is similar to that for the analogous radicals in other SAM proteins (Fig. 7.12) and there is no indication of relaxation enhancement by the faster relaxing $[4\text{Fe-4S}]^+$.

7.2.4 Discussion

In these three SAM proteins, we have seen three different kinds of clusters: $[2\text{Fe-2S}]^+$, $[3\text{Fe-4S}]^+$ and $[4\text{Fe-4S}]^+$. In all three proteins, the $[2\text{Fe-2S}]^+$ has g values of 2.006 and 1.96, $[3\text{Fe-4S}]^+$ has $g = 2.02$ and $[4\text{Fe-4S}]^+$ has $g = 1.89$ which are the characteristic g values for the respective clusters [142-145]. The presence of $[3\text{Fe-4S}]^+$ in PFL-AE suggests that this sample might be an air-exposed sample. If the fourth iron of the $[4\text{Fe-4S}]^+$ cluster did not bind to a cysteine of SAM that iron might be labile and form $[3\text{Fe-4S}]^+$ [136]. The low g -value ($g = 1.89$) of the $[4\text{Fe-4S}]^+$ that differs from the standard g value of 1.94 [144] suggests that this Fe-S cluster is not completely coordinated to cysteines [145]. One of the irons of the cluster is linked to some other ligand that is not cysteine. The spin-lattice relaxation rates of the three clusters increased in the order- $[2\text{Fe-2S}]^+ < [3\text{Fe-4S}]^+ < [4\text{Fe-4S}]^+$ [150]. We observe spin diffusion in the case of PFL-AE, which is attributed to the higher concentration of $[3\text{Fe-4S}]^+$ species. This can explain the faster spin-lattice relaxation rate for $[3\text{Fe-4S}]^+$ cluster than $[4\text{Fe-4S}]^+$. They both have faster relaxation rate than $[2\text{Fe-2S}]^+$ cluster, which is in accordance with Ref. [150].

The temperature dependence of T_2 for $[2\text{Fe-2S}]^+$ can be explained by nuclear spin diffusion below about 40 K and domination of spin-lattice relaxation above about 40 K. In case of spin-lattice relaxation, Raman and Orbach processes determine the temperature dependent behavior. The Raman process dominates at 15 to 35 K and above 35 K the Orbach process dominates. The smaller g -anisotropy of the cluster and the rigid environment makes the spin-orbit coupling smaller and hence the cluster has slower spin-relaxation rate than other studied clusters [146].

7.3 MftC SAM enzyme

7.3.1 Experimental Details

Preparation of recombinant MftC was done by Bulat Khaliulin in Dr.Latham's lab, who provided a brief description of preparation. *E. coli* gene synthesis was done using the amino acid sequence of mftC from *Mycobacterium ulcerans* Agy99 and it was cloned into pET28a. The mftC/pET28a plasmid was used to transform BL21. An overnight culture was used to inoculate LB (Luria-Bertani) broth and incubated at 37 °C aerobically. The temperature was decreased to 22 °C, after getting the cell density of 0.6 at OD 600. Sodium fumarate and FeCl₃ were added to the culture and it was sealed for 20 mins. The culture was induced by adding 1 mM IPTG (Isopropyl β-D-1-thiogalactopyranoside) to produce His₆-MftC (herein known as MftC). The flasks were then resealed and incubated overnight. Cells were harvested by centrifugation at 6,500 rpm for 5 min and transferred to an anaerobic chamber. The cells were lysed and purified using HisTrap FF column (GE Lifesciences) using an FPLC (GE Lifesciences) located in the anaerobic chamber. Fractions were monitored for purity by SDS-PAGE. Fractions containing the His-tagged MftC were desalted using a HiTrap Desalting column (GE Lifesciences) and concentrated. The MftC was reconstituted using 50 mM Hepes, 100 mM NaCl, and 10 mM DTT (dithiothreitol) (pH 7.5), 1.2 mM FeCl₃ and stirred at room temperature for 30 min. 1.2 mM Na₂S was added to the solution and stirred at room temperature for 3 h. The reconstituted protein was purified further using PD-10 column and fractions containing oxidized MftC were concentrated and flash frozen. The oxidized

MftC was then reduced by incubating it with dithionite. UV-Vis spectroscopy showed that MftC has two $[4\text{Fe-4S}]^+$ clusters. EPR was done on oxidized and reduced samples.

X-band (~ 9.5 GHz) continuous wave (CW) EPR spectra were recorded on a Bruker E580 spectrometer with an ER4118X-MS5 split ring resonator, an Oxford CF935 liquid helium cryostat, and an Oxford ITC503 temperature controller. Samples were in 4 mm OD quartz tubes. Spectra were acquired with 0.4 mT modulation amplitude at 100 kHz and 0.76 mW microwave power. The resonator has a Cu(II) background signal, which overlaps the $g\sim 2.05$ region of the signal from the protein. Resonator background spectra were acquired for a sample of the oxidized protein, which is diamagnetic. Background spectra were subtracted using the Bruker XEPR software, after x-axis offset to correct for differences in the microwave frequencies at which data were acquired. Field-swept echo-detected spectra were obtained with a two-pulse $90^\circ\text{-}\tau\text{-}180^\circ\text{-}\tau\text{-echo}$ sequence using 40 ns 90° pulses and a shot repetition time (SRT) of 1000 μs . The electron spin relaxation times for the background signal are very different from those for the signal from the protein, so the background signal does not contribute to the echo-detected spectrum at the SRT selected for the experiment. The first derivative of the echo-detected absorption spectrum was calculated numerically with subsequent filtering to reduce high frequency noise. The g -values were determined by simulation of the spectra using the locally written program Monmer, which is based on the equations in Ref. [126]. Uncertainties in the background subtraction cause greater uncertainty in the value for g_z than for g_x or g_y .

Values of T_1 and T_2 were obtained by a three-pulse inversion recovery sequence or a two-pulse electron spin echo, respectively, using 40 ns 90° pulses at $g = 1.94$. The inversion recovery curves were not single exponential. The data were fit to the sum of two exponentials, which may be a surrogate for a distribution.

7.3.2 Results

7.3.2.1 CW experiments

EPR spectra of the dithionite-reduced MtfC sample are shown in Figure 7.13. There is good agreement between the first derivative of the field-swept echo-detected spectrum at 10 K and the CW spectrum at 25 K. The positions of the low-field signal maximum ($g = 2.05$) and the zero-crossing point ($g = 1.93$) marked on the spectra are similar to the g values reported recently for the $[4\text{Fe-4S}]^+$ center in the reduced state of radical SAM enzymes including WhiD (2.06 and 1.94) [151], RimO (2.04, 1.93) [152], PqqE (2.05, 1.94) [153], and MiaB [143,144,154,155]. The simulated spectrum (Figure 7.13) was obtained with $g_x = 1.89 \pm 0.005$, $g_y = 1.93 \pm 0.005$, and $g_z = 2.03 \pm 0.01$. Spectra as a function of temperature (Figure 7.14) were obtained by subtraction of a strong background signal, which causes substantial uncertainty in the lineshape in the vicinity of $g \sim 2.02$. The amplitude of the peak at $g \sim 1.93$ changes with temperature which says that it is $1/T$ dependent (Figure 7.14). However the amplitude of peak at $g \sim 2.02$ exhibits substantially less temperature dependence, which may be due to imperfections in the background subtraction (Figure 7.14). The lineshapes at 20 and 30 K differ substantially from the spectrum in Fig. 7.13 at 25 K. These differences may be due to imperfections in

the background subtraction or to changes in sample preparation. The spectra will be reproduced for subsequent preparations. The signal broadens rapidly as temperature is increased due to increasing rates of electron spin relaxation, which is typical of $[4\text{Fe-4S}]^+$ clusters with $S = \frac{1}{2}$ ground states [156].

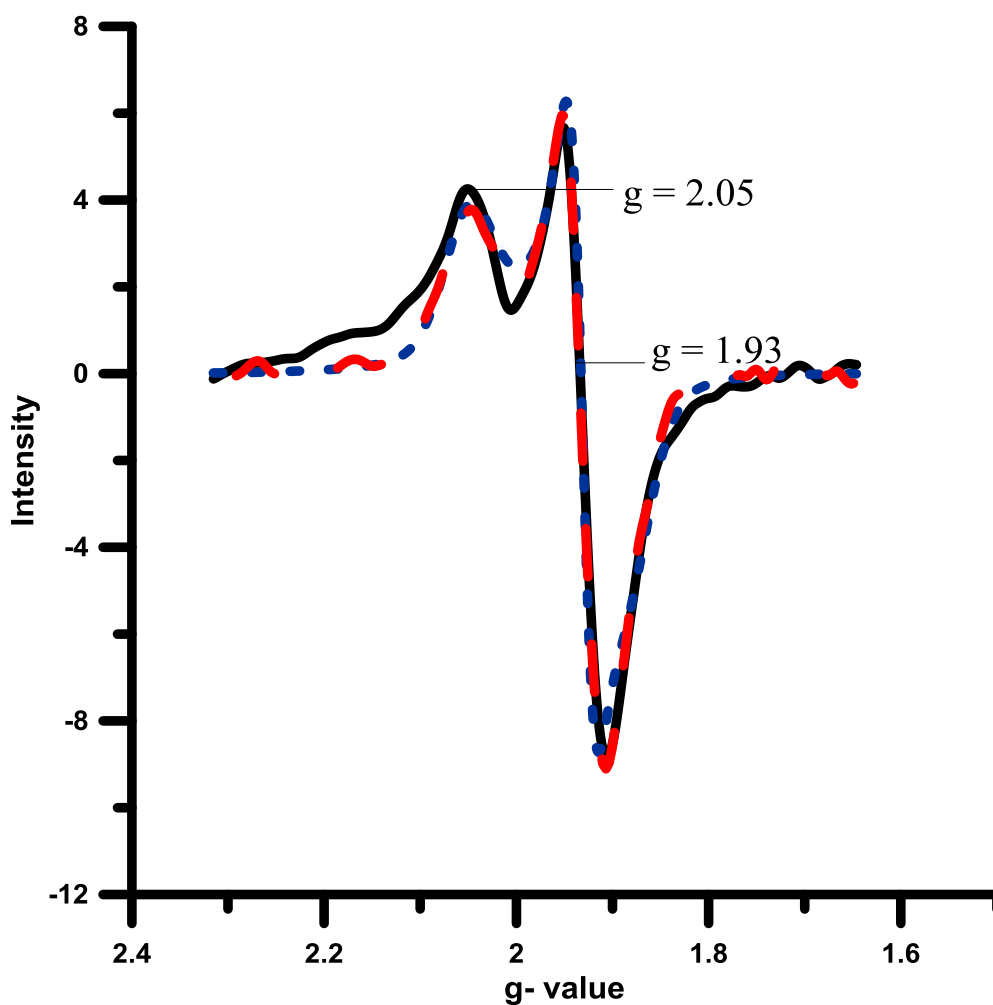
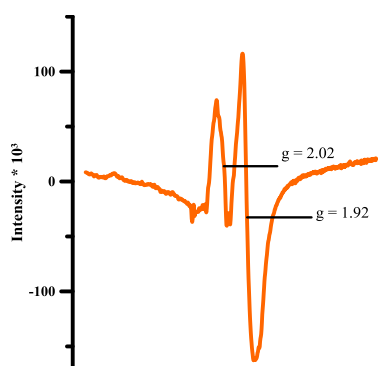
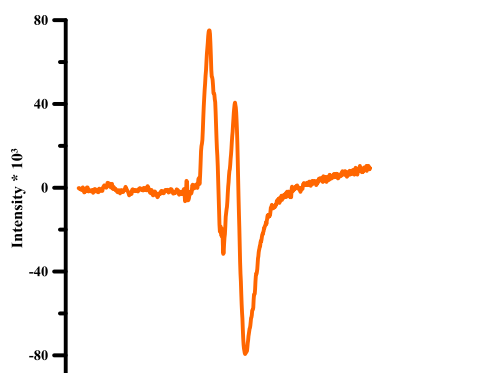


Figure 7.13 X-band spectra of reduced MtfC.

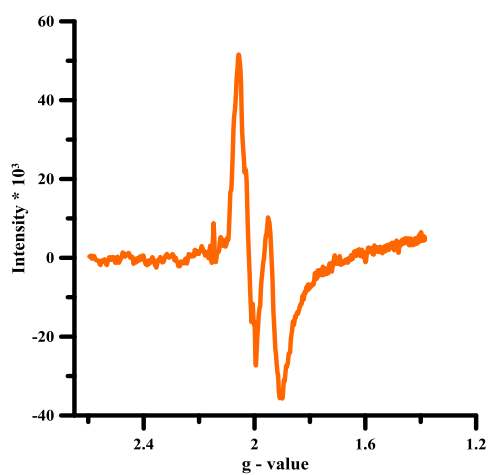
The background corrected spectrum at 25 K (solid black line) is superimposed on the first derivative of the field-swept echo-detected spectrum at 10 K (dashed red line). The dashed blue line is a simulation calculated with the local program Monmer.



20 K



30 K



40 K

Figure 7.14 Spectra for reduced sample of MtfC after subtracting oxidized spectra at 20, 30 and 40 K.

Spectra were obtained with 0.76 mW power and 4 G modulation amplitude at 100 kHz.

7.3.2.2 Pulse experiments

Values of T_2 (Table 7.3) at $g = 1.93$ are $1.7 \pm 0.1 \mu\text{s}$ between 10 and 30 K, which is much shorter than T_1 (Table 7.4). The negligible temperature dependence of T_2 in this temperature region is similar to that observed in the HydE samples and is consistent with domination by nuclear spin diffusion [141]. The long component of the two-component fits to the inversion recovery curve recorded at $g = 1.93$ decreased from $T_1 = \sim 1 \text{ ms}$ at 10 K to $\sim 35 \mu\text{s}$ at 30 K. The strong temperature dependence is typical for $[\text{4Fe-4S}]^+$ [96,156]. Values of T_2 decrease rapidly above about 30 K as T_1 approaches T_2 . The strong temperature dependence of T_1 and its impact on T_2 above about 30 K are consistent with the rapid broadening of the CW spectra as temperature is increased above about 30 K.

Table 7.3 T_2 at $g = 1.93$ for reduced MtfC sample.

Temperature (K)	T_2 (μs) ^a
10	1.7
15	1.8
20	1.7
25	1.6
30	1.7

^aUncertainty is 8%.

Table 7.4 T_1 at $g = 1.93$ for Reduced MftC.

Temperature (K)	T_1 (μ s) with weightings of components ^a
10	1026 (49%) and 186 (51%)
15	222 (29%) and 35.5 (71%)
20	121(26%) and 11.5(74%)
25	61.5 (35%) and 6.36 (65%)
30	36.4(38%) and 3.2 (62%)

^aUncertainty is 7%.

7.3.3 Discussion

In the oxidized sample, only the background signal was present whereas in the reduced sample, there were two peaks at different g -values ($g = 2.05$ and $g = 1.93$). These g -values correspond to $[4\text{Fe-4S}]^+$ clusters [143,144,151-155,157]. This shows that in the SAM enzyme, EPR inactive $[4\text{Fe-4S}]^{2+}$ with $S = 0$ is reduced to EPR active $[4\text{Fe-4S}]^+$ with $S = \frac{1}{2}$ by reaction with dithionite. The g -value of the $[4\text{Fe-4S}]^+$ cluster is in accordance with the standard g -value for these kinds of clusters [143,144,151-155,157] which means all the irons in the cluster are coordinated to cysteine as their ligand [145]. The CW and echo detected signals were observed at 10 K to 30 K, but not above 40 K, which is consistent with fast relaxation, which is another characteristic of the $[4\text{Fe-4S}]^+$ cluster [151,158]. This is the first EPR result demonstrating that MftC is a member of the SAM superfamily and contains an $[4\text{Fe-4S}]^+$ cluster, consistent with the bioinformatics findings in Haft et al. [139].

7.3.4 Comparison of [4Fe-4S]⁺ cluster in HydF^{ΔEG} Reduced and MtfC

In the CW spectrum of HydF^{ΔEG} Reduced, a peak at $g = 1.89$ was observed below 30 K (Figure 7.7, 7.8) that represents [4Fe-4S]⁺ [142-145] whereas in MtfC, the [4Fe-4S]⁺ cluster has $g = 2.05$ and $g = 1.93$ (Figure 7.13 and 7.14) [143,144,151-155]. The g -values in HydF^{ΔEG} Reduced are similar to that of proteins in which all four irons of [4Fe-4S]⁺ clusters are not linked to cysteine [144,145] whereas in case of MtfC, the g -value for the [4Fe-4S]⁺ cluster are similar to that for other proteins in which all the irons are coordinated to cysteine.

There is a difference in the relaxation times between the proteins. In case of HydF^{ΔEG} Reduced, the [4Fe-4S]⁺ clusters have shorter T_2 at 20 to 22 K (Table 7.2) than [4Fe-4S]⁺ clusters in MtfC enzyme (Table 7.3). The T_1 relaxation time is also shorter for [4Fe-4S]⁺ clusters of HydF^{ΔEG} Reduced at 10 to 22 K (Table 7.2) than clusters of MtfC (Table 7.4). The differences in relaxation times may reflect differences in local environment.

Chapter 8

Conclusion and Future Work

8.1 Conclusion

The dissertation is divided into two main parts. The first part concerned the interaction between rapidly relaxing metal ions and nitroxide radicals in glassy solutions. The lanthanides and complexes that were studied are Dy^{3+} , $\text{Dy}(\text{DTPA})^{2-}$, Er^{3+} , $\text{Er}(\text{DTPA})^{2-}$, Gd^{3+} , $\text{Gd}(\text{EDTA})^-$, $\text{Gd}(\text{DTPA})^{2-}$, $\text{Gd}(\text{DPA})_3$, Tm^{3+} and transition metal Co^{2+} and its complex $\text{Co}(\text{DTPA})^{3-}$. Relaxation times were measured by electron spin echo or inversion recovery for $\text{Er}(\text{DTPA})^{2-}$, Tm^{3+} , Co^{2+} and $\text{Co}(\text{DTPA})^{3-}$ at 5 K to 10 K. For Dy^{3+} , Er^{3+} , Tm^{3+} , Co^{2+} and their complexes the metal relaxation rates are so fast that CW spectra could not be observed at temperature above about 15 K. The relaxation rates are much slower for Gd^{3+} than for other lanthanides and values of T_1 and T_2 were measured at 80 K.

The impact of the metal ions on the relaxation times, T_1 and T_2 , for the nitroxide radical tempone (0.2 mM) in 1:1 water:glycerol were studied in mixtures between 20 and 150 K. For concentrations of the metal ion between 5 and 30 mM, the enhancement of the nitroxide relaxation rate $1/T_1$ by the metal ions is quadratically dependent on the concentration of the metal ion. The relaxation enhancement for nitroxide $1/T_1$ decreases in the order $\text{Dy}^{3+} > \text{Er}^{3+} \sim \text{Co}^{2+} > \text{Gd}^{3+}$. However, the enhancement of the nitroxide $1/T_2$ is

linearly dependent on the concentration of the metal ion. The nitroxide $1/T_2$ rate increases at lower temperatures in the presence of Dy^{3+} , Er^{3+} , Co^{2+} and Gd^{3+} .

We also studied the intramolecular interactions between lanthanide and nitroxide. Three complexes with different distances were made. MEAT was the shortest complex with 1.6 nm distance, MEGT with 2.4 nm and MEPT, the longest one had a distance of 3.4 nm. For each of these complexes the 'E' represent EDTA that was a chelator for the lanthanides. The spin label that was used in the experiment was tempamine and the four different lanthanides used were Er^{3+} , Dy^{3+} , Gd^{3+} and La^{3+} . It seems that the intermolecular and intramolecular effect of different metals are different. In the complexes where metal and nitroxide are at fixed distance apart, the analysis of relaxation effect are complicated by the decrease in number of spins detectable in various experiments. For finding distances by relaxation enhancement experiments, we need to take into consideration the percentage of spin detectable, as well as $P_{1/2}$ and relaxation rates. This has not been done in the previous reports by other people. Results for the intramolecular interactions need to be replicated before drawing conclusions.

The second part of the thesis explored three different types of Fe-S clusters $[2Fe-2S]^{2+}$, $[3Fe-4S]^+$ and $[4Fe-4S]^+$. These clusters have been studied in different types of proteins previously. The study of these clusters helped in the understanding of the redox reactions of proteins and in turn can give better understanding of these classes of proteins. In this thesis, I have studied the Fe-S clusters in pyruvate-formate lyase activating enzyme (PFL-AE), enzymes related to hydrogenase synthesis (HydE and HydF) and Mycofactocin (Mft) in *Mycobacterium Tuberculosis*. The EPR experiments

helped to characterize three different clusters and to differentiate the same kind of clusters in different proteins. The $[2\text{Fe-2S}]^+$ showed the characteristic g values of 2.006 and 1.96, $[3\text{Fe-4S}]^+$ has $g = 2.02$ (PFL-AE and HydE and HydF proteins) and $[4\text{Fe-4S}]^+$ (HydF reduced protein) has $g = 1.89$ and the $[4\text{Fe-4S}]^+$ cluster has $g = 2.05$ and $g = 1.93$ (MtfC). The temperature dependence of T_2 and T_1 for $[2\text{Fe-2S}]^+$ was studied. The T_2 and T_1 relaxation times were shorter for the $[4\text{Fe-4S}]^+$ clusters in case of HydF^{ΔEG} Reduced, than $[4\text{Fe-4S}]^+$ clusters in MtfC enzyme.

The CW, $P_{1/2}$ and pulse measurements of P22 viral capsids with $\text{Gd}(\text{DTPA})^{2-}$ at low temperature suggest that Gd^{3+} - Gd^{3+} interactions leads to enhanced electron spin relaxation at higher temperatures and magnetic fields.

8.2 Future work

The conclusions of my thesis are helpful in planning future experiments with lanthanides efficiently. The relaxation properties of lanthanides can help us in finding the best metal ion or their complexes that can increase the $1/T_1$ rate with minimal effect on the $1/T_2$ rate of the slow relaxing nitroxides. Many nitroxides are so slowly relaxing that it's hard to get their CW spectra at low temperatures, but relaxation enhancement by adding small amount of Er^{3+} and $\text{Er}(\text{DTPA})^{2-}$ or Dy^{3+} and $\text{Dy}(\text{DTPA})^{2-}$ can make it possible to record undistorted CW spectra. Dy^{3+} and $\text{Dy}(\text{EDTA})^-$ have been used for these purposes previously, but my work showed that Er^{3+} is also a good candidate for these kind of experiments. The work in this dissertation focused on the relaxation enhancement by different lanthanides in rigid lattice. These results can give us insights for planning the future distance relaxation enhancement experiments for proteins with

different lanthanides. The work in this dissertation gave preliminary results for further experiments. Lanthanides can replace Ca^{2+} in some proteins with retention of function, hence one end can have the lanthanide and the other end can have the nitroxide attached that we can do by spin labelling. The qualitative studies of the effects of lanthanides on the nitroxide with different distances are reported here. In the future, these studies should be extended to quantitative distances measurements. We can find the distances by looking at the relaxation enhancement between lanthanide and the nitroxide which can be a great technique to find distances efficiently and in less time than DEER.

Zaripov et al. [159] and Pivtsov et al. [160] used a holmium (Ho) complex to shorten the relaxation time of a nitroxide in frozen solution. They did not report any decrease in intensity of the field-swept, echo-detected EPR spectra. Although T_1 was reduced by about a factor of 25, T_2 was reduced a little more than a factor of 2 by the Ho complex at 20 mM concentration. In the future, we should add Ho to the set of metals studied.

References

1. C. Huang and Z. Bian, Chapter 1 in C. Huang, Rare Earth Coordination Chemistry, Fundamentals and Applications, John Wiley and Sons, Singapore (2010)
2. L. Sorace and D. Gatteschi, Electronic structure and magnetic properties of lanthanide molecular complexes, *in* Lanthanides and Actinides in Molecular Magnetism, 1 - 26 (2015)
3. J. A. Weil and J. R. Bolton, Electron Paramagnetic Resonance, Wiley Interscience. Hoboken, NJ (2007)
4. G. N. La Mar, W. Dew. Horrocks, Jr. and R. H. Holm, NMR of Paramagnetic Molecules, Academic Press, New York (1973)
5. G. I. Likhtenshtein, Spin Labeling Methods in Molecular Biology. Wiley-Interscience (1976)
6. S. S. Eaton and G. R. Eaton, Distance measurements in biological systems by EPR, G. R. Eaton, S. S. Eaton, and L. J. Berliner, eds., *Biol. Magn. Reson.* 19, 100 - 114 (2000)
7. A. Schweiger and G. Geschke, Principles of Pulse Paramagnetic Resonance, Oxford University Press, Oxford (2001).
8. M. D. Murphy, EPR (Electron Paramagnetic Resonance) spectroscopy of polycrystalline oxide systems, *in* Metal Oxide Catalysis, Wiley (2009)
9. S. A. Dikanov and A. R. Crofts, Electron Paramagnetic Resonance Spectroscopy, Chapter 3 (2006)
10. G. R. Eaton, S. S. Eaton, D. P. Barr and R. T. Weber, Quantitative EPR, Springer, New York (2010)
11. E. L. Hahn, Spin Echoes, *Phys. Rev.* 80, 1 – 6 (1950)
12. W. Froncisz and J. S. Hyde, The Loop-Gap Resonator: A new microwave lumped circuit ESR sample structure, *J. Magn. Reson.* 47, 515 - 521 (1982)
13. A. I. Potapov, D. V. Stass, E. Yu. Fursova, N. N. Lukzen, G. V. Romanenko, V. I. Ovcharenko and Yu. Molin, Searching for the exchange shift: a set of test systems, *Appl. Magn. Reson.* 35, 43 - 55 (2008).

14. C. Das, S. Vaidya, T. Gupta, J. M. Frost, M. Righi, E. K. Brechin, M. Affronte, G. Rajaraman and M. Shanmugam, Single-molecule magnetism, enhanced magnetocaloric effect, and toroidal magnetic moments in a family of Ln₄ squares, *Chem. Eur. J.* 21, 15639 – 15650 (2015)
15. S. Aime, M. Botta, M. Fasano, M. P. M. Marques, C. F. G. C. Geraldes, D. Pubanz and A. E. Merbach, Conformational and coordination equilibria on DOTA complexes of lanthanide metal ions in aqueous solution studied by ¹H-NMR Spectroscopy, *Inorg. Chem.* 36, 2059 - 2068 (1997)
16. C. N. Relley and B. W. Good and F. Desreux, Structure-independent method for dissecting contact and dipolar nuclear magnetic resonance shifts in lanthanide complexes and its use in structure determination, *Anal. Chem.* 47, 2110-3116 (1975)
17. G. Pintacuda, M. John, X.-C. Su and G. Otting, NMR structure determination of protein-ligand complexes by lanthanide labeling, *Acct. Chem. Res.* 40, 206 - 212 (2007)
18. J. Gordon, S. B. Fain, and I. J Rowland, Effect of lanthanide ions on dynamic nuclear polarization enhancement and liquid state T₁ relaxation, *Magn. Reson. Med.* 68, 1949 – 1954 (2012)
19. J. Bargon, Chemically induced dynamic nuclear polarization in the presence of paramagnetic shift reagents, *J. Amer. Chem. Soc.* 95, 941 – 942 (1973)
20. W. E. Antholine, J. S. Hyde and H. M. Swartz, Use of Dy³⁺ as a free-radical relaxing agent in biological tissues, *J. Magn. Reson.* 29, 517 - 522 (1978).
21. S. W. Meinhardt and T. Ohnishi, Determination of the position of the Qi- quinone binding site from the protein surface of the cytochrome bc₁ complex in *Rhodobacter capsulatus* chromatophores, *Biochim. Biophys. Acta* 1100, 667 - 74 (1992)
22. H. Blum, J. S. Leigh and T. Ohnishi, Effect of dysprosium on the spin-lattice relaxation time of cytochrome c and cytochrome a. *Biochim. Biophys. Acta* 626, 31-40 (1980).
23. P. Lueders, S. Razzaghi, H. Jager, R. Tschaggelar, M. A. Hemminga, M. Yulikov and G. Jeschke; Distance determination from dysprosium induced relaxation enhancement: a case study on membrane-inserted WALP23 polypeptides, *Mol. Phys.* 111, 2824 - 2833 (2013)
24. H. Jager, A. Koch, V. Maus, H. W. Spiess and G. Jeschke, Relaxation-based distance measurements between a nitroxide and a lanthanide spin label, *J. Magn. Reson.* 194, 254 – 263 (2008)

25. D. J. Hirsh, J. McCracken, R. Biczko and K-A. Gesuelli, Saturation-recovery EPR with nitroxide radical-Dy(III) spin pairs: distances and orientations, *J. Phys. Chem. B* 117, 11960 - 11977 (2013)
26. G. Jeschke, DEER distance measurements on proteins, *Annu. Rev. Phys. Chem.* 63, 419 – 446 (2012)
27. I. Bertini, G. Martini and C. Luchinat, Relaxation Data Tabulation. Chapter IV in *Handbook of Electron Spin Resonance*, edited by C. P. Poole, Jr., and H. A. Farach, AIP Press, New York (1994)
28. T. Sarna, J. S. Hyde and H. M. Swartz, Ion-exchange in melanin: an electron spin resonance study with lanthanide probes, *Science* 192, 1132 - 1134 (1976)
29. V. Martinez and F. de M. Ramirez, Synthesis, spectroscopic and magnetic behavior of dysprosium bis (tetraphenylporphyrinate) and bis dysprosium tris (tetraphenylporphyrinate), *Polyhedron* 617, 965-973 (1994)
30. J. W. Walton, R. Carr, N. H. Evans, A. M. Funk, A. M. Kenwright, D. Parker, D. S. Yufit, M. Botta, S. De Pinto and K.-L. Wong, Isostructural series of nine-coordinate chiral lanthanide complexes based on triazacyclononane, *Inorg. Chem.* 51, 8042 – 8056 (2012)
31. H. Blum, J. R. Bowyer, M. L. A. Cusanovich, A. J. Waring and T. Ohnishi, Spin-lattice relaxation rates of iron-sulfur proteins and heme proteins affected by dysprosium complexes and temperature, *Biochim. Biophys. Acta*, 748, 418 - 428 (1983)
32. H. Blum, M. A. Cusanovich, W. V. Sweeney and T. Ohnishi, Magnetic interactions between dysprosium complexes and two soluble iron-sulfur proteins, *J. Biol. Chem.* 256, 2199 - 2206 (1981)
33. J. Reuben and D. Fiat, Nuclear magnetic resonance studies of solutions of the rare-earth ions and their complexes. IV. Concentration and Temperature Dependence of the Oxygen-17 Transverse Relaxation in Aqueous Solutions, *J. Chem. Phys.* 51, 4918-4927 (1969)
34. P. D. Burns and G. N. LaMar, Proton spin relaxation for the nonlabile coordinated chelate in lanthanide shift reagents, *J. Magn. Reson.* 46, 61-68 (1982)
35. M. B. Schulz and C. D. Jeffries, Paramagnetic resonance and relaxation of some rare- earth ions in $YCl_3 \cdot 6H_2O$, *Phys. Rev.* 159, 277-284 (1967)
36. R. Leones, M. Fernandes, F. Sentanin, I. Cesarino, J. F. Lima, V. de Zea Bermudez, A. Pawlicka, C. J. Magon, J. P. Donoso and M. M. Silva, Ionically conducting Er^{3+} -doped DNA-based biomembranes for electrochromic devices, *Electrochimica Acta* 120, 327 - 333 (2014)
37. I. X. Cantarelli, M. Pedroni, F. Piccinelli, P. Marzola, F. Boschi, G. Conti, A. Sbarbati, P. Bernardi, E. Mosconi, L. Perbellini, L. Marongiu, M. Donini, S. Dusi, L. Sorace, C. Innocenti, E. Fantechi, C. Sangregorio and A. Speghini,

- Multifunctional nanoprobe based on upconverting lanthanide doped CaF₂: towards biocompatible materials for biomedical imaging, *Biomater. Sci.* 2, 1158 (2014)
38. K. J. Standley and R. A. Vaughn, *Electron Spin Relaxation Phenomena in Solids*, Plenum Press, New York 199 - 239 (1969)
 39. P. C. Kang, G. R. Eaton and S. S. Eaton, Pulsed electron paramagnetic resonance of high spin cobalt (III) complexes, *Inorg. Chem.* 3, 3660-3665 (1994)
 40. E. Wiberg, N. Wiberg, A. F. Holleman, *Holleman- Wiberg Inorganic Chemistry* Academic Press, San Diego, 1701 (2001)
 41. L. E. Iton and J. Turkevich, Electron paramagnetic resonance of rare earth ions in the zeolites, *J. Phys. Chem.* 81, 435 - 449 (1977)
 42. S. K. Hoffmann, J. Goslar and S. Lijewski, Electron paramagnetic resonance and electron spin echo studies of Co²⁺ coordination by nicotinamide adenine dinucleotide (NAD⁺) in water solution, *Appl. Magn. Reson.* 44, 817 - 826 (2013)
 43. M. Benmelouka, J. V. Tol, A. Borel, S. Nellutla, M. Port, L. Helm, L-C. Brunel and A. E. Merbach, Multiple frequency and variable-temperature EPR study of Gadolinium (III) complexes with polyaminocarboxylates: analysis and comparison of the magnetically dilute powder and the frozen- solution spectra, *Helv. Chim. Acta*, 92, 2173 - 2185 (2009)
 44. A. Borel, E. Toth, L. Helm, A. Janossy and A. E. Merbach, EPR on aqueous Gd³⁺ complexes and a new analysis method considering both linewidths and shifts, *Phys. Chem. Chem. Phys.* 2, 1311- 1317 (2000)
 45. E. J. Werner, S. Avedano, M. Botta, B. P. Hay, E. G. Moore, S. Aime and K. N. Raymond, *J. Amer. Chem. Soc.* 129, 1870 - 1871 (2007)
 46. S. Rast, A. Borel, L. Helm, E. Belorizky, P. H. Fries and A. E. Merbach, EPR spectroscopy of MRI-related Gd(III) complexes: simultaneous analysis of multiple frequency and temperature spectra, including static and transient crystal field effects *J. Amer. Chem. Soc.* 123, 2637 - 2644 (2001)
 47. S. K. Sur and R. G. Bryant, Nuclear and electron-spin relaxation rates in symmetrical iron, manganese and gadolinium ions, *J. Phys. Chem.* 99, 6301 - 6308 (1995)
 48. S. K. Sur and R. G. Bryant, Ionic association and electron spin relaxation rates in aquo Gadolinium (III) complexes, *J. Magn. Reson. B* 111, 105 - 108 (1996)
 49. S. Rast, P. H. Fries and E. Belorizsky, Theoretical study of electronic relaxation processes in hydrated Gd³⁺ complexes in solution, *J. Chim. Phys.* 96, 1543 - 1550 (1999)
 50. V. A. Atsarkin, V. V. Demidov, G. A. Vasneva, B. M. Odintsov, R. L. Belford, B. Raduchel and R. B. Clarkson, Direct measurement of fast electron spin-lattice

- relaxation: method and application to nitroxide radical solutions and Gd^{3+} contrast agents, *J. Phys. Chem. A* 105, 9323 - 9327 (2001)
51. D. T. Peat, A. J. Horsewill, W. Kockenberger, A. J. Perez Linde, D. G. Gadian and J. R. Owers-Bradley, Achievement of high nuclear spin polarization using lanthanides as low-temperature NMR relaxation agents, *Phys. Chem. Chem. Phys.* 15, 7586-7591 (2013)
 52. S. S. Eaton and G. R. Eaton, Interaction of Spin Labels with Transition Metals, *Coord. Chem. Rev.* 26, 207 - 262 (1978)
 53. J. S. Taylor, J. S. Leigh, Jr. and M. Cohn, Magnetic resonance studies of spin-labeled creatine kinase system and interaction of two paramagnetic probes, *Proc. Natl. Acad. Sci. U.S.A.* 64, 219-226 (1969)
 54. J. S. Leigh, Jr., ESR rigid-lattice line shape in a system of two interacting spins, *J. Chem. Phys.* 52, 2608-2612 (1970)
 55. S. S. Eaton, M. L. Law, J. Peterson, G. R. Eaton and D. J. Greenslade, Metal-Nitroxyl Interactions. 7. Quantitative aspects of EPR spectra resulting from dipolar interactions, *J. Magn. Reson.* 33, 135 - 141 (1979)
 56. A. I. Kokorin, K. I. Zamarayev, G. L. Grigoryan, V. P. Ivanov and E. G. Rozantsev, Measurements of the distance between the paramagnetic centers in solid solutions of nitroxide radicals, biradicals, and spin-labeled proteins. *Biofizika*, 17, 34-41 (1972)
 57. S. S. Eaton and G. R. Eaton, Distance Measurements by CW and Pulsed EPR, in *Distance Measurements in Biological Systems by EPR*, G. R. Eaton, S. S. Eaton, and L. J. Berliner, eds., *Biol. Magn. Reson.* 19, 1 - 27 (2000)
 58. N. Bloembergen, On the interaction of nuclear spins in a crystalline lattice, *Physica* 15, 386-426 (1949)
 59. A. Abragam, Overhauser effect in nonmetals, *Phys. Rev.* 98, 1729-1735 (1955)
 60. J. S. Hyde and K. V. S. Rao, Dipolar-induced electron spin-lattice relaxation in unordered solids, *J. Magn. Reson.* 29, 509 - 516 (1978)
 61. S. S. Eaton and G. R. Eaton, Relaxation times of organic radicals and transition metal ions, *Biol. Magn. Reson.* 19, 29 - 154 (2000)
 62. M. H. Rakowsky, K. M. More, A.V. Kulikov, G.R. Eaton and S. S. Eaton, Time-domain electron paramagnetic resonance as a probe of electron-electron spin-spin interaction in spin-labeled iron porphyrins, *J. Amer. Chem. Soc.* 117, 2049 - 2057 (1995)

63. A.V. Kulikov and G. I. Likhtenshtein, The use of spin relaxation phenomena in the investigation of the structure of model and biological systems by the method of spin labels, *Adv. Mol. Relax. and Interact. Proc.* 10, 47 - 69 (1977)
64. M. Seiter, V. Budker, J.-L. Du, G. R. Eaton and S. S. Eaton, Interspin Distances Determined by Time Domain EPR of Spin-Labeled High-Spin Methemoglobin, *Inorg. Chim. Acta* 273, 354 - 366 (1998)
65. D. Ulyanov, B. E. Bowler, G. R. Eaton and S. S. Eaton, Electron-Electron Distances in Spin-Labeled Low-Spin Metmyoglobin Variants by Relaxation Enhancement, *Biophys. J.* 95, 5306 – 5316 (2008)
66. A. V. Kulikov, Determination of distance between label and paramagnetic center spins from the parameters of saturation curves of the ESR spectrum at 77 K, *Molek. Biol.* 10, 109-116 (1976)
67. J. H. Van Vleck, The dipolar broadening of magnetic resonance lines in crystals, *Phys. Rev.* 74, 1168 (1948)
68. J. S. Hyde and T. Sarna, Magnetic interactions between nitroxide free radicals and lanthanides or Cu^{2+} in liquids, *J. Chem. Phys.* 68, 4439-4447 (1978)
69. I. D. Sahu, R. M. McCarrick, K. R. Troxel, R. Zhang, H. J. Smith, M. M. Dunagan, M. S. Swartz, P. V. Rajan, B. Kroncke, C. R. Sanders and G. A. Lorigan, DEER EPR measurements for membrane protein structures via bi-functional spin labels and lipodisq nanoparticles, *Biochemistry* 52, 6627 – 6632 (2013)
70. M. A. Swanson, V. Kathirvelu, T. Majtan, F. E. Frerman, G. R. Eaton and S. S. Eaton, Electron transfer flavoprotein domain II orientation monitored using double electron-electron resonance between an enzymatically reduced, native FAD cofactor, and spin labels, *Protein Science* 20, 610- 620 (2011)
71. G. C. Borgia, R. J. S. Brown, and P. Fantazzini, Uniform-penalty inversion of multiexponential decay data. II. Data spacing, T_2 data, systemic data errors, and diagnostics, *J. Magn. Reson.* 147, 273-285 (2000)
72. G. C. Borgia, R. J. S. Brown, and P. Fantazzini, Uniform-penalty inversion of multiexponential decay data, *J. Magn. Reson.* 132, 65 - 77 (1998)
73. H. Sato, S. E. Bottle, J. P. Blinco, A. S. Micallef, G. R. Eaton and S. S. Eaton, Electron spin-lattice relaxation of nitroxyl radicals in temperature ranges that span glassy solutions to low-viscosity liquids, *J. Magn. Reson.* 191, 66 – 77 (2008)
74. M. E. Oliver and B. J. Hales, Using dysprosium complexes to probe the nitrogenase paramagnetic centers, *Biochem.* 32, 6058 - 6064 (1993)

75. P. Lueders, H. Jager, M. A. Hemminga, G. Jeschke and M. Yulikov, Multiple pathway relaxation enhancement in the system composed of three paramagnetic species: nitroxide radical-Ln³⁺-O₂, *J. Phys. Chem. Lett.* 3, 1336 - 1340 (2012)
76. A. Zecevic, G. R. Eaton, S. S. Eaton and M. Lindgren, Dephasing of electron spin echoes for nitroxyl radicals in glassy solvents by non-methyl and methyl protons, *Mol. Phys.* 95, 1255- 1263 (1998)
77. D. Ulyanov, B. E. Bowler, G. R. Eaton and S. S. Eaton, Electron-electron distances in spin-labeled low-spin metmyoglobin variants by relaxation enhancement, *Biophys. J.* 95, 5306 - 5316 (2008)
78. J. F. Desreux, Nuclear magnetic resonance spectroscopy of lanthanide complexes with a tetraacetic tetraaza macrocycle. unusual conformation properties, *Inorg. Chem.* 19, 1319 - 1324 (1980)
79. Y. Polyhach, E. Bordignon, R. Tschaggelar, S. Gandra, A. Godt and G. Jeschke, High sensitivity and versatility of the DEER experiment on nitroxide radical pairs at Q-band frequencies, *Phys. Chem. Chem. Phys.* 14, 10762 – 10773 (2012)
80. I. Fernandez, J. Ubach, I. Dulubova, X. Zhang, T. C. Sudhof and J. Rizo, Three-dimensional structure of an evolutionarily conserved N-terminal domain of Syntaxin 1A, *Cell* 94, 841 – 849 (1998)
81. D. Cookson, R. J. P. Williams, B. T. Golding and P. V. Ioannou, Interaction between spin-labelled penicillins and lanthanide ions, *J. Inorg. Nucl. Chem.* 41, 1089-1091 (1979)
82. M. S. Smyth and J. H. J. Martin, X Ray crystallography, *J Clin Pathol: Mol Pathol* 53, 8 –14 (2000)
83. Y. Yan and G. Marriott, Analysis of protein interactions using fluorescence technologies, *Curr. Opin. Chem. Biol.* 7, 635 - 640 (2003)
84. S. S. Eaton and G. R. Eaton, Determination of distances based on T₁ and T_m effects in Distance measurements in biological systems by EPR, G. R. Eaton, S. S. Eaton, and L. J. Berliner, eds., *Biol. Magn. Reson.* 19, 350-378 (2000).
85. S. S. Eaton and G. R. Eaton, Interaction of Spin Labels with Transition Metals. Part 2, *Coord. Chem. Rev.* 83, 29 - 72 (1988).
86. K. M. More, G. R. Eaton and S. S. Eaton, Metal-nitroxyl interactions. 47. EPR spectra of two-spin-labeled derivatives of EDTA coordinated to paramagnetic metal ions, *Inorg. Chem.* 25, 2638 - 2646 (1986)
87. T. D. Yager, G. R. Eaton, and S. S. Eaton, (Cr(oxalate)₃)³⁻ as a broadening agent in nitroxyl spin probe studies, T. D. Yager, G. R. Eaton and S. S. Eaton, *J. C. S. Chem. Commun.* 944 - 945 (1978).

88. J. S. Taylor, P. G. Schultz and P. B. Dervan, DNA affinity cleaving sequence specific cleavage by distamycin-EDTA-Fe (II) and EDTA-distamycin-Fe (II), *Tetrahedron* 40, 457-465 (1984)
89. J. C. Taylor, J. S. Leigh and M. Cohn, Magnetic resonance studies of spin-labeled creatine kinase system and interaction of two paramagnetic probes, *Proc. Natl. Acad. Sci. U. S.* 64, 219-226 (1969)
90. G. Luca, E. Bordignon, E. K. Brooks, W. L. Hubbell, G. Jeschke, and M. Yulikov, Orthogonal spin labeling and Gd(III)-nitroxide distance measurements on bacteriophage T4-lysozyme, *J. Phys. Chem. B* 117, 3145 – 3153 (2013)
91. P. Lueders, G. Jeschke and M. Yulikov, Double electron-electron resonance measured between Gd³⁺ ions and nitroxide radicals, *J. Phys. Chem. Lett.* 2, 604 – 609 (2011)
92. P. Lueders, H. Jager, M. A. Hemminga, G. Jeschke and M. Yulikov, Distance measurements on orthogonally spin-labeled membrane spanning WALP23 polypeptides, *J. Phys. Chem. B* 117, 2061 – 2068 (2013)
93. K. V. Lakshmi and G. W. Brudvig, Pulsed electron paramagnetic resonance methods for macromolecular structure determination. *Curr. Opin. Struct. Biol.* 11, 523 – 531 (2001)
94. G. I. Likhtenshtein, Depth of immersion of paramagnetic centers in biological systems. *Biol. Magn. Reson.* 19, 309–346 (2000)
95. A. J. Fielding, R. J. Usselman, N. Watmough, M. Simkovic, F. E. Frerman, G. R. Eaton and S. S. Eaton.. Electron paramagnetic resonance characterization and interspin distance measurement of electron transfer flavoprotein ubiquinone oxidoreductase (ETF-QO), *J. Magn. Reson.* 190, 222 – 232 (2008)
96. R. J. Usselman, A. J. Fielding, F. E. Frerman, G. R. Eaton and S. S. Eaton. Impact of mutations on the midpoint potential of the [4Fe-4S]⁺ cluster and on the catalytic activity in electron transfer flavoprotein-ubiquinone oxidoreductase (ETF-QO), *Biochemistry* 47, 92 – 100 (2008)
97. H. Jäger, A. Koch, V. Maus, H. W. Spiess and G. Jeschke, Relaxation-based distance measurements between a nitroxide and a lanthanide spin label, *J. Magn. Reson.* 194, 254 – 263 (2008)
98. E. J. Hustedt, R. A. Stein, L. Sethaphong, S. Brandon, Z. Zhou and S. C. DeSensi, Dipolar coupling between nitroxide spin labels: the development and application of a tether-in-a-cone model, *Biophys. J.* 90, 340 – 356 (2006)
99. S. Kakinoki, Y. Hirano and M. Oka, On the stability of Polyproline- I and II structures of proline oligopeptides, *Polymer Bulletin* 53, 109 – 115 (2005).
100. P. G. Schultz, J. S. Taylor and P. B. Dervan, Design synthesis of a sequence specific DNA cleaving molecule.(Distamycin-EDTA) iron(II), *J. Amer. Chem. Soc.* 104, 6861-6863 (1982)

101. G. W. Anderson, J. E. Zimmerman and F. M. Callahan, The use of N-hydroxysuccinimide in peptide synthesis, *J. Amer. Chem. Soc.* 86, 1839-1842 (1964)
102. D. L. Boger and J. Zhou, CDPI3-enediyne and CDPI3-EDTA conjugates: a new class of DNA cleaving agents, *J. Org. Chem.* 58, 3018-3024 (1993)
103. B. Zacharie, T. P. Connolly and C. L. Penney, A simple one-step conversion of carboxylic-acids to esters using EEDQ, *J. Org. Chem.* 60, 7072 - 7074 (1995)
104. J.M. Herzs, R. J. Mehlhorn and L. Packer, Topographic Studies of Spin-labeled Bacteriorhodopsin, evidence for buried carboxyl residues and immobilization of the COOH-terminal tail, *J. Biol. Chem.* 258, 9899 - 9907 (1983)
105. O.P. Shvoeva, V. P. Dedkova and S. B. Savvin, Complexation reactions between lanthanum, gadolinium, and ytterbium and reagents of arsenazo III group on the surface of fibrous materials loaded with a chelex 100 ion exchanger, *J. Anal. Chem.* 66, 590 – 594 (2011)
106. L. Garbuio, B. Lewandowski, Patrick Wilhelm, L. Ziegler, M. Yulikov, H. Wennemers and G. Jeschke, Shape persistence of Polyproline II helical oligoprolines, *Chem. Eur. J.* 21, 10747 - 10753 (2015)
107. S. S. Amin, K. Cryer, B. Zhang, S. K. Dutta, S. S. Eaton, O. P. Anderson, S. M. Miller, B. A. Reul, S. M. Brichard and D. C. Crans, Chemistry and Insulin Mimetic Properties of Bis (acetylacetonate) oxovanadium (IV) and Derivatives, *Inorg. Chem.* 39, 406 - 416 (2000)
108. G. Fischer and F. X. Schmid, The mechanism of protein folding. Implications of in vitro refolding models for de novo protein folding and translocation in the cell, *Biochemistry* 29, 2205-2212 (1990)
109. L. Shi, A. E. Holliday, N. Khanal, D. H. Russell and D. E. Clemmer, Configurationally-coupled protonation of polyproline-7, *J. Amer. Chem. Soc.* 137, 8680 – 8683 (2015)
110. M. Qi, A. Gro, G. Jeschke, A. Godt and M. Drescher, Gd(III)-PyMTA label is suitable for in-cell EPR, *J. Amer. Chem. Soc.* 136, 15366 – 15378 (2014)
111. J. J. Windle, Hyperfine coupling constants for nitroxide spin probes in water and carbon tetrachloride, *J. Magn. Reson.* 45, 432 - 439 (1981)
112. D. Kivelson, Theory of EPR (electron paramagnetic resonance) line widths of free radicals, *J. Chem. Phys.* 33, 1094 – 1106 (1960)
113. H. Sato, V. Kathirvelu, A. Fielding, J. P. Blinco, A. S. Micallef, S. E. Bottle, S. S. Eaton and G. R. Eaton, Impact of molecular size on electron spin relaxation

- rates of nitroxyl radicals in glassy solvents between 100 and 300 K, *Mol. Phys.* 105, 2137 – 2151 (2007)
114. Y. Degliannakis, Electron paramagnetic relaxation enhancement produced on T_1 by anisotropic g-tensors in rigid systems, *Mol. Phys.* 105, 2095 – 2108 (2005)
115. P. Caravan, J. J. Ellison, T. J. McMurry and R. B. Lauffer, Gadolinium(III) chelates as MRI contrast agents: Structure, dynamics, and applications, *Chem. Rev.* 99, 2293 – 2352 (1999)
116. M. Botta and L. Tei, Relaxivity Enhancement in Macromolecular and Nanosized Gd III-Based MRI Contrast Agents, *Eur. J. Inorg. Chem.* 12, 1945 - 1960 (2012)
117. G. L. Davies, I. Kramberger and J. J. Davis, Environmentally responsive MRI contrast agents, *Chem. Commun.* 49, 9704 - 9721 (2013)
118. S. Qazi, M. Uchida, R. Usselman, R. Shearer, E. Edwards and T. Douglas, Manganese (III) porphyrins complexed with P22 virus-like particles as T_1 -enhanced contrast agents for magnetic resonance imaging, *J. Biol. Inorg. Chem.* 19, 237 – 246 (2014)
119. S. Qazi, L. O. Liepold, M. J. Abedin, B. Johnson, P. Prevelige, J. A. Frank and T. Douglas, P22 Viral Capsids as Nanocomposite High-Relaxivity MRI Contrast Agents, *Mol. Pharm.* 10, 11-17 (2013)
120. L. Liepold, S. Anderson, D. Willits, L. Oltrogge, J. A. Frank, T. Douglas and M. Young, Viral capsids as MRI contrast agents, *Magn. Reson. Med.* 58, 871 – 879 (2007)
121. X.G. Lei, S. Jockusch, N. J. Turro, D. A. Tomalia and M. F. Ottaviani, EPR characterization of gadolinium(III)-containing-PAMAM-dendrimers in the absence and in the presence of paramagnetic probes, *J. Colloid. Interf. Sci.* 322, 457 - 464 (2008)
122. P. Caravan, C. T. Farrar, L. Frullano and R. Uppal, Influence of molecular parameters and increasing magnetic field strength on relaxivity of gadolinium- and manganese-based T_1 contrast agents, *Contrast Media Mol. Imaging* 4, 89 - 100 (2009)
123. M. F. Ferreira, B. Mousavi, P. M. Ferreira, C. I. O. Martins, L. Helm, J. A. Martins and C. F. G. C. Geraldes, Gold nanoparticles functionalised with stable, fast water exchanging Gd^{3+} chelates as high relaxivity contrast agents for MRI, *Dalton Trans.* 41, 5472 – 5475 (2012)
124. J. Lucon, S. Qazi, M. Uchida, G. J. Bedwell, B. LaFrance, P. E. Prevelige and T. Douglas, Using the interior cavity of the P22 capsid for site specific initiation of atom transfer radical polymerization with tremendously increased cargo loading, *Nature Chem.* 4, 781 (2012)

125. R. J. Usselman, S. Qazi, P. Aggarwal, S. S. Eaton, G. R. Eaton, S. Russek and T. Douglas, Gadolinium-loaded viral capsids as magnetic resonance imaging contrast agents, *Appl. Magn. Reson.* 46, 349 - 355 (2015)
126. A.D. Toy, S. H. H. Chaston, J. R. Pilbrow and T. D. Smith, Electron spin resonance study of the copper(II) chelates of certain monothio- β -diketones and diethyldithiocarbamate, *Inorg. Chem.* 10, 2219 - 2225 (1971)
127. S. Bandyopadhyay, K. Chandramouli and M. K. Johnson, Iron-Sulfur cluster biosynthesis, *Biochem Soc Trans.* 36, 1112 - 1119 (2008)
128. C. Ayala-Castro, A. Saini and F.W. Outten, Fe-S cluster assembly pathways in bacteria, *Microbiol. Mol. Biol. Rev.* 72, 110 - 125 (2008)
129. R. Lill, Function and biogenesis of iron-sulfur proteins, *Nature* 460, 831 - 838 (2009)
130. H. Beinert, R. H. Holm and E. Munck, Iron-sulfur clusters: nature's modular, multipurpose structures, *Science* 277, 653 - 659 (1997)
131. H. Beinert, Chapter 3, Iron-Sulfur centers of the mitochondrial electron transfer system- recent developments, *in* Iron-sulfur Proteins. volume (III). Structure and Metabolic Mechanisms, Walter Lovenberg, New York (1977)
132. R. H. Sands and H. Beinert, Studies of mitochondria and submitochondrial particles by paramagnetic resonance (EPR) spectroscopy, *Biochem. Biophys. Res. Commun.* 3, 47 - 52 (1960).
133. R. Bingemann and A. Klein, Conversion of the central [4Fe-4S] cluster into a [3Fe-4S] cluster leads to reduced hydrogen-uptake activity of the F420-reducing hydrogenase of *Methanococcus voltae*, *Eur. J. Biochem.* 267, 6612 - 6618 (2000)
134. T. A. Kent, J.-L. Dreyer, M. C. Kennedy, B. H. Huynh, M. H. Emptage, H. Beinert and E. Munck, Mossbauer studies of beef heart aconitase: Evidence for facile interconversions of iron-sulfur clusters, *Proc. Natl. Acad. Sci. U. S.* 79, 1096 - 1100 (1982)
135. M. C. Kennedy, T. A. Kent, M. Emptage, H. Merkle, H. Beinert and E. Munck, Evidence for the formation of a linear [3Fe-4S] cluster in partially unfolded aconitase, *J. Biol. Chem.* 259, 14463 - 14471 (1984)
136. J.B. Broderick, B. R. Duffus, K. S. Duschene and E. M. Shepard, Radical S-adenosylmethionine enzymes, *Chem. Rev.* 114, 4229 - 431 (2014)
137. R.C. Driesener, M. R. Challand, S. E. McGlynn, E. M. Shepard, E. S. Boyd, J. B. Broderick, J. W. Peters and P. L. Roach, [FeFe]-hydrogenase cyanide ligands derived from S-Adenosylmethionine-Dependent Cleavage of Tyrosine *Angew. Chem., Int. Ed.* 49, 1687 - 1690 (2010)
138. E. M. Shepard, B. R. Duffus, S. J. George, S. E. McGlynn, M. R. Challand, K. D. Swanson, P. L. Roach, S. P. Cramer, J. W. Peters and J. B. Broderick, [FeFe]-

- hydrogenase maturation: HydG-catalyzed synthesis of carbon monoxide, *J. Amer. Chem. Soc.* 132, 9247 - 9249 (2010)
139. H. Daniel, Bioinformatic evidence for a widely distributed, ribosomally produced electron carrier precursor, its maturation proteins, and its nicotinoprotein redox partners, *BMC Genomics* 12 - 21 (2011)
140. M. H. Rakowsky, A. Zecevic, G. R. Eaton and S. S. Eaton, Determination of high-spin iron(III)-nitroxyl distances in spin-labeled porphyrins by time-domain EPR, *J. Magn. Reson.* 131, 97 - 110 (1998)
141. S. S. Eaton and G. R. Eaton, Relaxation times of organic radicals and transition metal ions, *Biol. Magn. Reson.* 19, 29 - 154 (2000)
142. E. M. Shepard, S. E. McGlynn, A. L. Bueling, C. S. Grady-Smith, S. J. George, M. A. Winslow, S. P. Cramer, J. W. Peters and J. B. Broderick, Synthesis of the 2Fe subcluster of the [FeFe]-hydrogenase H cluster on the HydF scaffold, *PNAS*, 107, 10448- 10453 (2010)
143. I. Czeck, A. Silakov, W. Lubitz and T. Happe, The [FeFe]-hydrogenase maturase HydF from *Clostridium acetobutylicum* contains a CO and CN- ligated iron cofactor, *FEBS Lett.* 584, 638 - 42 (2010)
144. R. C. Conover, A. T. Kowal, W. Fu, J. B. Park, S. Aono, M. W. Adams and M. K. Johnson, Spectroscopic characterization of the novel iron-sulfur cluster in *Pyrococcus furiosus* ferredoxin, *J. Biol. Chem.* 265, 8533 – 8541 (1990)
145. X. Brazzolotto, J. K. Rubach, J. Gaillard, S. Gambarelli, M. Atta and M. Fontecave, The [FeFe]-hydrogenase maturation protein HydF from *Thermotoga maritima* is a GTPase with an iron-sulfur cluster, *J. Biol. Chem.* 281, 769 – 774 (2006)
146. M. Sarewicz, M. Dutka, R. Pietras, A. Borek and A. Osyczka, Effect of H bond removal and changes in the position of the iron-sulfur head domain on the spin-lattice relaxation properties of the [2Fe-2S]²⁺ Rieske cluster in cytochrome bc₁, *Phys. Chem. Chem. Phys.* 17, 25297 - 25308 (2015)
147. P. Bertrand, J. P. Gayda, J. A. Fee, D. Kuila and R. Cammack, Comparison of the spin-lattice relaxation properties of the two classes of [2Fe-2S] clusters in proteins, *Biochim. Biophys. Acta* 916, 24 - 28 (1987)
148. P. Bertrand, G. Roger and J. P. Gayda, Measurement of the spin-lattice relaxation time from the broadening of the EPR spectrum of a randomly-oriented systems with S = 1/2: Application to iron-sulfur proteins, *J. Magn. Reson.* 40, 539 – 549 (1980)
149. H. Rupp, A. de la Torre and D.O. Hall, The electron spin relaxation of the electron acceptors of photosystem I reaction center studied by microwave power saturation. *Biochim. Biophys. Acta* 548, 552-564 (1979)

150. R. Cammack and F. MacMillan, Electron magnetic resonance of iron-sulfur proteins in electron-transfer chains: resolving complexity. Chapter 2 in *Biol Magn. Reson.* 29, (2010)
151. P. Jakimowicz, M. R. Cheesman, W. R. Bishai, K. R. Chater, A. J. Thomson and M. J. Buttner, Evidence that the streptomyces development protein WhiD, a member of the WhiB family, binds a [4Fe-4S] cluster, *J. Biol. Chem.* 280, 8309 - 8315 (2005)
152. K.-H. Lee, L. Saleh, B. P. Anton, C. L. Madinger, J. S. Benner, D. F. Iwig, R. J. Roberts, C. Krebs and S. J. Booker, Characterization of RimO, a new member of the methylthiotransferase subclass of the radical SAM superfamily, *Biochemistry* 48, 10162 - 10174 (2009)
153. S. R. Wecksler, S. Stoll, H. Tran, O. T. Magnusson, S.-H. Wu, D. King, R. D. Britt and J. P. Klinman, Pyrroloquinoline quinone biogenesis: demonstration that PqqE from *Klebsiella pneumoniae* is a radical S-Adenosyl-L-Methionine Enzyme, *Biochemistry* 48, 10151 - 10161 (2009)
154. H. L. Hernandez, F. Pierrel, E. Elleingrand, R. Garcia-Serres, B. H. Huynh, M. K. Johnson, Fontecave, M. and M. Atta, MiaB, A bifunctional radical-S-Adenosylmethionine enzyme involved in the thiolation and methylation of tRNA, contains two essential [4Fe-4S] clusters, *Biochemistry* 46, 5140 - 5147 (2007)
155. T. Yano, J. Sklar, E. Nakamaru-Ogiso, Y. Takahashi, T. Yagi and T. Ohnishi, Characterization of cluster N5 as a fast-relaxing [4Fe-4S] cluster in the Nqo3 subunit of the proton-translocating NADH-ubiquinone oxidoreductase from *Paracoccus denitrificans*, *J. Biol. Chem.* 278, 15514 - 15522 (2003)
156. P. Bertrand, J. P. Gayda and K. K. Rao, Electron spin-lattice relaxation of the 4Fe-4S ferredoxin from *Bacillus stearothermophilus*. Comparison with other iron proteins, *J. Chem. Phys.* 76, 4715 - 4719 (1982)
157. E. C. Duin, M. E. Lafferty, B. R. Crouse, R. M. Allen, I. Sanyal, D. H. Flint and M. K. Johnson, [2Fe-2S] to [4Fe-4S] cluster conversion in *Escherichia coli* Biotin Synthase, *Biochemistry* 36, 11811–11820 (1997)
158. W. H. Orme-Johnson, and R. H. Sands, in *Iron-Sulfur Proteins* (Lovenberg, W., ed) 2, 194–217, Academic Press, New York (1973)
159. R. B. Zaripov, V. I. Dzhabarov, A. A. Knyazev, Yu. G. Galyametdinov and L. V. Kulik, Use of additional fast-relaxing paramagnetic species for improvement of RIDME performance, *Appl. Magn. Reson.* 40, 11–19 (2011)
160. A. V. Pivtsov, L. V. Kulik, N. V. Surovtsev, S. V. Adichtchev, I. A. Kirilyuk, I. A. Grigor'ev, M. V. Fedin and S. A. Dzuba, Temperature dependence of hyperfine interaction for ¹⁵N nitroxide in a glassy matrix at 10–210 K, *Appl. Magn. Reson.* 41, 411 – 429 (2011)